

**WL-TR-97-4118**



**THE PHASE EVOLUTION, CREEP AND  
TENSILE BEHAVIOR OF TWO-PHASE  
ORTHORHOMBIC TITANIUM ALLOYS**

**CARL BOEHLERT**

**UES, INC.  
4401 DAYTON XENIA ROAD  
DAYTON, OH 45432-1894**

**DECEMBER 1997**

**FINAL REPORT FOR PERIOD AUGUST 1993 - SEPTEMBER 1997**

Approved for public release; distribution unlimited

**MATERIALS AND MANUFACTURING DIRECTORATE  
AIR FORCE RESEARCH LABORATORY  
AIR FORCE MATERIEL COMMAND  
WRIGHT PATTERSON AFB OH 45433-7817**

**19980220 120**

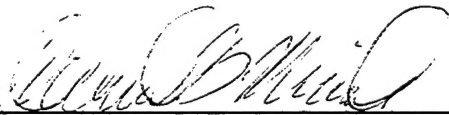
UNCLASSIFIED

## NOTICE

WHEN GOVERNMENT DRAWINGS, SPECIFICATIONS, OR OTHER DATA ARE USED FOR ANY PURPOSE OTHER THAN IN CONNECTION WITH A DEFINITELY GOVERNMENT-RELATED PROCUREMENT, THE UNITED STATES GOVERNMENT INCURS NO RESPONSIBILITY OR ANY OBLIGATION WHATSOEVER. THE FACT THAT THE GOVERNMENT MAY HAVE FORMULATED OR IN ANY WAY SUPPLIED THE SAID DRAWINGS, SPECIFICATIONS, OR OTHER DATA, IS NOT TO BE REGARDED BY IMPLICATION OR OTHERWISE IN ANY MANNER CONSTRUED, AS LICENSING THE HOLDER OR ANY OTHER PERSON OR CORPORATION, OR AS CONVEYING ANY RIGHTS OR PERMISSION TO MANUFACTURE, USE, OR SELL ANY PATENTED INVENTION THAT MAY IN ANY WAY BE RELATED THERETO.

THIS REPORT IS RELEASABLE TO THE NATIONAL TECHNICAL INFORMATION SERVICE (NTIS). AT NTIS, IT WILL BE AVAILABLE TO THE GENERAL PUBLIC, INCLUDING FOREIGN NATIONS.

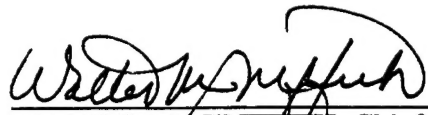
THIS TECHNICAL REPORT HAS BEEN REVIEWED AND IS APPROVED FOR PUBLICATION.



DANIEL B. MIRACLE, Project Engineer  
Metals Development & Materials  
Processing Branch  
Metals, Ceramics & NDE Division



KATHERINE A. STEVENS, Actg Chief  
Metals Development & Materials  
Processing Branch  
Metals, Ceramics & NDE Division



WALTER M. GRIFFITH, Chief  
Metals, Ceramics & Nondestructive  
Evaluation Division  
Materials and Manufacturing Directorate

IF YOUR ADDRESS HAS CHANGED, IF YOU WISH TO BE REMOVED FROM OUR MAILING LIST, OR IF THE ADDRESSEE IS NO LONGER EMPLOYED BY YOUR ORGANIZATION, PLEASE NOTIFY, AFRL/MLLM, WRIGHT-PATTERSON AFB OH 45433-7817 TO HELP US MAINTAIN A CURRENT MAILING LIST.

COPIES OF THIS REPORT SHOULD NOT BE RETURNED UNLESS RETURN IS REQUIRED BY SECURITY CONSIDERATIONS, CONTRACTUAL OBLIGATIONS, OR NOTICE ON A SPECIFIC DOCUMENT.



REPORT DOCUMENTATION PAGE			FORM APPROVED OMB NO. 0704-0188	
Public reporting burden for this collection of information is estimated to average 1 hour per response, including the time for reviewing instructions, searching existing data sources, gathering and maintaining the data needed, and completing and reviewing the collection of information. Send comments regarding this burden estimate or any other aspect of this collection of information, including suggestions for reducing this burden, to Washington Headquarters Services, Directorate for Information Operations and Reports, 1215 Jefferson Davis Highway, Suite 1204, Arlington, VA 22202-4302 and to the Office of Management and Budget, Paperwork Reduction Project (0704-0188), Washington, DC 20503.				
1. AGENCY USE ONLY (Leave blank)		2. REPORT DATE DECEMBER 1997		3. REPORT TYPE AND DATES COVERED Final for Aug 93 - Sep 97
4. TITLE AND SUBTITLE THE PHASE EVOLUTION, CREEP AND TENSILE BEHAVIOR OF TWO-PHASE ORTHORHOMBIC TITANIUM ALLOYS			5. FUNDING NUMBERS F33615-96-C-5258 PE 62102F PR 2306 TA B0 WU 02	
6. AUTHOR(S) CARL BOEHLERT				
7. PERFORMING ORGANIZATION NAMES(S) AND ADDRESS(ES) UES, INC. 4401 DAYTON XENIA ROAD DAYTON, OH 45432-1894			8. PERFORMING ORGANIZATION REPORT NUMBER	
9. SPONSORING/MONITORING AGENCY NAMES(ES) AND ADDRESS(ES) MATERIALS AND MANUFACTURING DIRECTORATE AIR FORCE RESEARCH LABORATORY AIR FORCE MATERIEL COMMAND WRIGHT-PATTERSON AFB OH 45433-7734 (POC: Dan Miracle 937-255-9833)			10. SPONSORING/MONITOR- ING AGENCY REPORT NUMBER  WL-TR-97-4118	
11. SUPPLEMENTARY NOTES				
12a. DISTRIBUTION/AVAILABILITY STATEMENT APPROVED FOR PUBLIC RELEASE; DISTRIBUTION IS UNLIMITED			12b. DISTRIBUTION CODE	
13. ABSTRACT (Maximum 200 words) The phase evolution, creep, and tensile behavior were studied for near Ti <sub>2</sub> AlNb and Ti <sub>12</sub> Al-38Nb O+BCC alloys. Monolithic materials were produced through conventional thermomechanical processing techniques. Heat treatment and TEM studies estimated the temperature ranges for the respective phase fields and a pseudobinary diagram based on Ti=50at.% was constructed. The aging-transformation behavior was studied in detail. O-phase precipitation within BCC-dominated microstructures resulted in significant room-temperature (RT) strengthening. The BCC phase was vital for imparting RT ductility. The deformation observations and calculated creep exponents and activation energies suggested that three creep mechanisms are dominating the secondary creep behavior. For low applied stress, Coble creep characteristics were exhibited. For intermediate stresses, the minimum creep rates were proportional to $\sigma^2/GS$ and fiducial-line experiments revealed grain boundary sliding and grain boundary cavitation. For high stresses, the stress exponents were greater than or equal to 3.5 and a high density of dislocations were observed, indicative of a dislocation climb mechanism. Overall, the sub-transus processed and heat-treated microstructures contained much smaller grain sizes than super-transus microstructures and this resulted in worse creep resistance. For targeted low-to-intermediate stress and intermediate temperature applications, grain size is the dominant microstructural feature influencing the creep behavior of O+BCC alloys.				
14. SUBJECT TERMS ORTHORHOMBIC TITANIUM-ALUMINUM-NIOBIUM ALLOYS MONOLITHIC MATERIALS			15. NUMBER OF PAGES 255	
			16. PRICE CODE	
17. SECURITY CLASSIFICATION OF REPORT UNCLASSIFIED	18. SECURITY CLASSIFICATION OF THIS PAGE UNCLASSIFIED	19. SECURITY CLASSIFICATION OF ABSTRACT UNCLASSIFIED	20. LIMITATION OF ABSTRACT SAR	

## TABLE OF CONTENTS

LIST OF ILLUSTRATIONS.....	v
LIST OF TABLES.....	xix
LIST OF SYMBOLS/ABBREVIATIONS.....	xxi
PREFACE.....	xxv
ACKNOWLEDGMENTS.....	xxvi
INTRODUCTION.....	1
CHAPTER	
1. BACKGROUND.....	3
1.1 Constituent Phases.....	3
1.2 Phase Evolution.....	6
1.3 Mechanical Behavior.....	11
1.3.1 Creep Behavior.....	12
1.3.2 Tensile Behavior.....	21
1.4 Deficiencies in Understanding.....	30
1.4.1 Phase Evolution.....	30
1.4.2 Creep Behavior.....	31
1.4.3 Tensile Behavior.....	34
2. OBJECTIVES AND APPROACH.....	36
2.1 Objectives.....	36
2.2 Approach.....	37
2.3 Summary.....	41
3. EXPERIMENTAL METHODS.....	42
3.1 Processing Methods.....	42
3.1.1 Forging and Rolling Procedures.....	43
3.1.2 Induction-Heating Procedures.....	53
3.2 Material Preparation.....	57
3.3 Characterization Methods.....	61
3.3.1 Testing.....	61
Creep Experiments.....	61
Tensile Experiments.....	67
3.3.2 Metallography.....	68
4. RESULTS.....	73

4.1	Phase Evolution.....	73
4.1.1	Near Ti <sub>2</sub> AlNb Alloys.....	74
	Solution-Treatment Study.....	79
	Aging Study.....	87
	Super-transus Processed Near Ti <sub>2</sub> AlNb Alloy..	106
4.1.2	Ti-12Al-38Nb.....	107
4.2	Creep Behavior.....	118
4.2.1	Near Ti <sub>2</sub> AlNb Alloys.....	119
	Aging and Tension/Compression Effects.....	120
	Mechanical Properties.....	123
	Deformation Behavior.....	136
4.2.2	Ti-12Al-38Nb.....	147
	Grain Size Effects.....	147
	Mechanical Properties.....	148
	Deformation Behavior.....	150
4.2.3	Summary.....	153
4.3	Tension Behavior.....	155
4.3.1	Elevated-Temperature Properties.....	155
4.3.2	RT Tension Behavior.....	157
	Constituent Phase Properties.....	157
	Second-Phase Strengthening.....	159
	Deformation Behavior.....	162
	Interstitial Oxygen and Aging Effects.....	165
	Grain size and Morphological Effects.....	168
4.3.3	Summary.....	170
5.	ANALYSIS AND DISCUSSION.....	173
5.1	Phase Evolution of O+BCC Alloys.....	173
5.1.1	Equilibria.....	173
5.1.2	Cellular Precipitation.....	178
5.1.3	Super-transus Microstructures.....	182
5.1.4	Ti-12Al-38Nb and the Pseudobinary Diagram.....	185
5.2	Creep Behavior.....	188
5.2.1	Creep Mechanisms and Modeling.....	188
5.2.2	Microstructural Dependence of the Creep Mechanisms	199
5.2.3	Aging Effects.....	201
5.2.4	Microstructure-Property Trends.....	203
5.3	Tension Behavior.....	205
5.3.1	Temperature Dependence.....	205
5.3.2	RT Tensile Behavior.....	206
6.	SUMMARY AND CONCLUSIONS.....	209
6.1	Summary.....	209
6.2	Conclusions.....	216
6.2.1	Processing.....	217
6.2.2	Phase Evolution.....	217
6.2.3	Creep Behavior.....	219
6.2.4	Tension Behavior.....	220
6.3	Recommendations.....	221
	BIBLIOGRAPHY.....	225

## LIST OF ILLUSTRATIONS

1.1	The basal planes of the (a) $\alpha_2$ and (b) O lattices and (c) the crystal structure (AB) of the ordered B2 structure. In Ti-Al-Nb alloys rich in titanium, A sites of the B2 structure are occupied by Ti and B sites by Al and Nb atoms randomly (Banerjee <i>et al.</i> 1987).....	5
1.2	Figure 1.2 900°C isothermal ternary slice taken from Rowe <i>et al.</i> (1993) where the bold line highlights the range of O+BCC compositions containing Ti=50at.%. The nominal compositions of the alloys investigated in this work, which lie along the bold line, are marked X.....	6
1.3	The Ti-25Al-xNb vertical section taken from Sagar <i>et al.</i> (1996).....	8
1.4	Grain boundary cracking between $\alpha_2$ grains for a RT tensile deformed Ti-25Al-17Nb specimen.....	24
1.5	RT tensile fracture surface of a Ti-25Al-17Nb specimen showing the fracture characteristics of the constituent phases.....	25
1.6	Slip compatibility between adjacent O and B2 grains for a RT deformed Ti-25Al-17Nb specimen. Note the wavy slip traces in the B2 phase and lack of slip transfer to the $\alpha_2$ phase.....	25
1.7	A bar chart taken from Rowe (1993b) depicting the elevated-temperature creep, RT fracture toughness, and RT tensile properties as a function of nominal alloy composition.....	30
3.1	Size comparison of the (a) forged and (b) forged and rolled Ti <sub>2</sub> AlNb cigar-melted ingots.....	44

3.2	Low magnification photograph of the three as-rolled Ti <sub>2</sub> AlNb sheets.....	46
3.3	As-rolled microstructures of sheets (a) A, (b) B, and (c) C. These SEM images were taken from the thickness section and the rolling direction is horizontal.....	48
3.4	The (a) top and (b) side views of the can assembly after the first forging run for Ti-12Al-38Nb.....	48
3.5	The (a) top and (b) side views of the can assembly after the first forging run for Ti-25Al-25Nb. Note the non-uniform deformation.....	49
3.6	The Ti-25Al-25Nb can assembly after the interrupted forging run. Note the initiation of buckling.....	49
3.7	The (a) top and (b) side views of the extracted workpiece after the second forging for Ti-12Al-38Nb.....	50
3.8	Comparison of the Ti-12Al-38Nb (a) as-cast and (b) forged microstructures. The forging direction was vertical. Note the reduction in grain size after forging...	51
3.9	Comparison of the Ti-23Al-27Nb (a) as-cast and (b) forged microstructures. The forging direction was vertical.....	51
3.10	The (a) top, (b) bottom and (c) side views of the sheared Ti-25Al-25Nb workpiece after the initial forging run.....	55
3.11	The (a) top and (b) side views of the can assembly of the uniformly deformed Ti-25Al-25Nb after the second forging runs.....	56
3.12	Comparison of the Ti-25Al-25Nb (a) as-cast and (b) forged microstructures. The forging direction was vertical.....	56
3.13	The (a) can assembly prior to rolling and the (b) extracted workpiece after rolling for Ti-12Al-38Nb.....	57
3.14	The (a) can assembly prior to rolling and the (b) extracted workpiece after rolling for Ti-23Al-27Nb.....	58
3.15	The post-rolled (a) can assembly and (b) extracted workpiece for Ti-25Al-25Nb.....	59

3.16	As-rolled microstructures of the (a) Ti-25Al-25Nb, (b) Ti-23Al-27Nb, and (c) Ti-12Al-38Nb sheets. These SEM images were taken from the thickness section and the rolling direction is horizontal.....	60
3.17	The as-fabricated near Ti <sub>2</sub> AlNb rod which was induction heated for five days using a Crystalox machine specially designed for producing single crystals.....	60
3.18	Specimen mapping for the (a) Ti-23Al-27Nb and (b) Ti-25Al-25Nb sheets. Sections were cut along the bold lines and the numbered regions represent the blanks from which specimens were machined.....	62
3.19	A typical specimen geometry, containing a cylindrical gage section, used for the tension and tensile-creep experiments.....	63
4.1	DTA plot of temperature difference versus temperature for the heating curves of (a) Ti-23Al-27Nb, (b) Ti-25Al-24Nb and (c) Ti-25Al-23Nb sheets. The heating rate was 15°C/minute.....	77
4.2	As-rolled (a) Ti-23Al-27Nb, (b) Ti-25Al-24Nb, and (c) Ti-25Al-23Nb microstructures. The rolling direction is vertical.....	78
4.3	Microstructures of Ti-23Al-27Nb solution treated and water quenched samples. Solution-treatment temperatures were (a) 1090°C, (b) 1025°C, (c) 1000°C, and (d) 900°C.....	81
4.4	XRD plot of Intensity versus 2θ for a Ti-25Al-24Nb heat-treated (1090°C/0.5h/WQ) fully-B2 microstructure.....	82
4.5	SADPs taken from neighboring (a) α <sub>2</sub> +B2 and (b) O+B2 grains for 1025°C/40h/WQ and 900°C/45h/WQ solution treatments, respectively, of Ti-23Al-27Nb. The ORs are: [11 $\bar{2}$ 0]α <sub>2</sub> //[1 $\bar{1}$ 1]B2; (0001)α <sub>2</sub> //(011)B2, [ $\bar{1}$ 11]B2//[1 $\bar{1}$ 0]O and (110)B2//(001)O. (c) Verification of the ordered B2 structure in a 900°C solution-treated sample depicting super-lattice reflections from a [001] zone axis	84

4.6	Super-transus heat-treated Ti-23Al-27Nb microstructures: (a) 1150°C/0.5h/CC at 15°C/min. to RT and (b) 1090°C/0.5h/WQ/900°C/8h/WQ; containing large prior B2 grains with O and $\alpha_2$ precipitates.....	86
4.7	Comparison of the Ti-23Al-27Nb (a) $\alpha_2$ +B2 solution-treated (HT:1025°C/200h/WQ) microstructure with (b) that for the solution-treated microstructure after subsequent heating within the O+B2 field (HT:1025°C/200h/WQ/925°C/2h/WQ). Note the $\alpha_2$ phase remained and Widmanstätten O precipitated in (b).....	88
4.8	Near Ti <sub>2</sub> AlNb microstructures which have been solution treated at 875°C: (a) Ti-25Al-24Nb, (b) Ti-25Al-23Nb, and (c) Ti-23Al-27Nb. These images show the effect of alloy composition, in particular Al content, on O phase volumes.....	89
4.9	Ti-25Al-24Nb heat-treated sheet microstructures: (a) 875°C/100h/WQ/900°C/8h/WQ and (b) 975°C/100h/WQ. These microstructures exhibit the effect of heat treatment on morphology.....	89
4.10	Effect of aging temperature on microstructure. Comparison of a Ti-23Al-27Nb solution-treated (a) (950°C/45h/WQ) microstructure with solution-treated and aged microstructures. The specimens were aged at (b) 850°C, (c) 750°C, and (d) 650°C for 13 hours followed by water quenching. The arrows indicated in (c) and (d) represent the initiation of discontinuous precipitation.....	90
4.11	Effect of aging time on microstructure. These Ti-23Al-27Nb specimens were solution-treated at 950°C and then aged at 650°C for (a) 24 hours, (b) 48 hours, (c) 100 hours, and (d) 304 hours followed by water quenching.....	92
4.12	Ti-23Al-27Nb microstructures obtained by (a) solution treatment at 1025°C/45h/WQ and (b) solution treatment at 1025°C/45h/WQ plus aging at 650°C/610h/WQ. The majority of B2 phase has undergone discontinuous precipitation.....	93

4.13	CBED patterns taken from the discontinuous precipitating region for a Ti-23Al-27Nb 950°C/45h/WQ/650°C/373h/WQ heat-treated sample. The patterns are identified as (a) $[00\bar{1}]O$ and (b) $[01\bar{1}]\beta$ .....	93
4.14	Dark field images of the (a) O phase and (b) O+ $\beta$ phase platelets corresponding to the CBED patterns of Figure 4.13. (c) SADP taken from the same region depicting the corresponding OR: $[01\bar{1}]\beta//[00\bar{1}]O$ , $(\bar{2}11)\beta//(110)O$ .....	94
4.15	(a) Lower and (b) higher magnification bright field images of transformation misfit dislocations at O/ $\beta$ interfaces for a Ti-23Al-27Nb 950°C/45h/WQ/650°C/66h/WQ heat-treated sample.....	94
4.16	Solution treated and aged microstructures for (a) Ti-25Al-24Nb (975°C/100h/WQ/650°C/300h/WQ) and (b) Ti-25Al-23Nb (950°C/45h/WQ/650°C/304h/WQ). The microstructures exhibited discontinuous precipitation at prior B2 grain boundaries.....	95
4.17	A transformed B2 region containing the $\beta$ , B2, and O phases for a Ti-23Al-27Nb 875°C/40h/WQ/650°C/320h/WQ heat-treated sample.....	96
4.18	SEM micrograph of a transformed B2 region containing only small volumes of discontinuous precipitation for a Ti-23Al-27Nb 875°C/40/h/WQ/650°C/288/WQ heat-treated sample.....	96
4.19	Ti-23Al-27Nb super-transus solution-treated samples (1090°C/0.5h/WQ) which were aged at 650°C for (a) 2, (b) 9 and (c) 100 hours, followed by water quenching. Precipitates coarsened at (transformed-B2)/(transformed-B2) boundaries.....	99
4.20	Microstructures of a Ti-25Al-23Nb (a) super-transus solution-treated sample (1090°C/0.5h/WQ) which had been aged at 650°C for (b) 2, (c) 9 and (d) 100 hours, followed by water quenching. Precipitates coarsened at (transformed-B2)/(transformed-B2) boundaries.....	100



4.21	XRD plot of Intensity versus $2\theta$ for a Ti-23Al-27Nb (a) super-transus solution-treated sample (1090°C/0.5h/WQ) which had been aged at 650°C for (b) 0.25 and (c) 2 hours, followed by water quenching.....	101
4.22	A high-magnification BSD SEM image of the aligned grain-boundary precipitates for a heat-treated (1090°C/0.5h/WQ/650°C/9h/WQ) Ti-23Al-27Nb sample.....	102
4.23	High magnification BSD image of a 1090°C solutionized Ti-23Al-27Nb sample which was aged at 650°C for 681 hours. Discontinuous precipitation is identified by the unlabeled arrows.....	103
4.24	Microdiffraction patterns identifying the (a) $[\bar{1}22]B2$ and (b) $[100]O$ structures within precipitated regions of a 1090°C solutionized Ti-23Al-27Nb sample which was aged at 650°C for 681 hours. The OR between the phases ( $[\bar{1}11]B2//[1\bar{1}0]O$ and $(110)B2//(001)O$ ) is depicted in (c).....	103
4.25	Microstructure of a 1090°C solutionized Ti-23Al-27Nb sample which was aged at 650°C for 670 hours depicting discontinuous precipitation resulting in coarser platelets at O/O boundaries.....	104
4.26	Heat-treated microstructures of (a) Ti-23Al-27Nb (HT:1090°C/1h/WQ/650°C/9h/WQ/900°C/8h/WQ) and (b) Ti-25Al-23Nb (HT:1090°C/1h/WQ/650°C/2h/WQ/900°C/8h/WQ).....	105
4.27	TEM image of the Ti-25Al-27Nb microstructure containing O and B2 laths; the longitudinal rod direction is horizontal.....	108
4.28	The (a) $\{001\}$ pole figure of the as-processed Ti-25Al-27Nb microstructure taken from a section perpendicular to the longitudinal rod direction. A (b) stereographic projection of O on (001) taken from Banerjee (1995). These figures indicate that the O phase was textured close to $(\bar{1}31)O$ .....	109
4.29	SADP taken from the $[011]B2$ zone axis for a Ti-25Al-27Nb sample aged at 650°C for 670 hours.....	109

4.30	The (a) as-rolled Ti-12Al-38Nb microstructure; the rolling direction was vertical. The (b) SADP of the [011] $\beta$ zone axis for as-rolled Ti-12Al-38Nb.....	110
4.31	DTA plot of temperature difference versus temperature for the heating curve of the as-rolled Ti-12Al-38Nb sheet. The heating rate was 3°C/minute between 600- 1000°C.....	110
4.32	Ti-12Al-38Nb microstructures of samples aged at 650°C for 24 hours followed by heating at (a) 850°C, (b) 800°, and (c) 750°C for 5 hours followed by water quenching. The $\beta \rightarrow \beta+O$ transus was close to 800°C.....	111
4.33	Effect of aging time on microstructure. These images depict the as-rolled Ti-12Al- 38Nb microstructure after aging at 650°C for (a) 24 hours, (b) 50 hours, (c) 100 hours, and (d) 304 hours, followed by water quenching.....	112
4.34	Microdiffraction patterns of the O and $\beta$ structures for a heat-treated (650°C/435h/WQ) Ti-12Al-38Nb sample illustrating the (a) $[00\bar{1}]O$ zone axis and the (b) [011] $\beta$ zone axis. (c) SADP of the O/ $\beta$ OR: $[\bar{1}11]B2//[\bar{1}\bar{1}0]O$ ; $(110)B2//(001)O$ .....	113
4.35	(a) Lower and (b) higher magnification bright-field TEM images of transformation misfit dislocations at O/ $\beta$ interfaces for a Ti-12Al-38Nb 650°C/411h/WQ heat- treated sample.....	113
4.36	Microstructures of Ti-12Al-38Nb solution treated and water quenched samples. Solution-treatment temperatures were (a) 900°C, (b) 950°C, and (c) 1200°C. These images depict the effect of solution-treatment temperature on $\beta$ grain size.....	115
4.37	A plot of $\ln k$ vs $(1/T)$ , based on equations 4.1 and 4.2, depicting the $\beta$ grain growth for heat-treated Ti-12Al-38Nb.....	116
4.38	SEM image of a 900°C solutionized Ti-12Al-38Nb sample which was aged at 650°C for less than 5 hours. The O phase precipitated initially at the $\beta$ grain boundaries.....	117

4.39	Grain boundary precipitates for a heat-treated (900°C/5h/WQ/650°C/62h/WQ) Ti-12Al-38Nb sample.....	117
4.40	Creep strain versus time plot for the as-rolled Ti-25Al-24Nb sheet material depicting the three stages of creep. The tangential line used in the 'onset method' to determine $\epsilon_p$ and $t_p$ is indicated.....	119
4.41	Creep strain vs time curves for solution treated (950/45/WQ) and solution treated and aged (950°C/45h/WQ/650°C/304h/WQ) Ti-23Al-27Nb specimens.....	121
4.42	Ti-23Al-27Nb samples which were solution-treated at 950°C. One sample (a) was crept at 650°C/172 MPa for 66 hours and the other (b) was heat treated at 650°C for 50 hours.....	121
4.43	Comparison of a Ti-25Al-23Nb solution-treated (a) (910°C/8h/WQ) microstructure with a solution-treated and aged (b) (910°C/8h/WQ/650/218h/WQ) microstructure.....	122
4.44	Creep strain vs time curves for solution treated (910°C/8h/WQ) and solution treated and aged (910°C/8h/WQ/650°C/218h/WQ) Ti-25Al-23Nb specimens.....	122
4.45	Creep strain vs time curves for tension and compression loadings of Ti-23Al-27Nb specimens which were solutionized at 875°C and then aged at 650°C. The creep conditions were 650°C/172 MPa.....	123
4.46	Examples of the creep strain versus life behavior for single-specimen experiments, which were (a) incrementally loaded from 50 to 442 MPa in steps while the temperature remained constant (650°C), or (b) the temperature was increased from 705°C to 760°C in steps while the load was held constant (i.e. stress = 50 MPa). Note that the load or temperature was changed only after the secondary stage was reached. An identical heat treatment (1090°C/0.5h/WQ/650°C/112h/WQ) was performed on each specimen prior to testing.....	126

4.47	Creep plots for three Ti-23Al-27Nb microstructures, represented by their solution-treatment temperatures; (a) stress dependence of $\dot{\epsilon}_{\min}$ at $T=650^{\circ}\text{C}$ and (b) temperature dependence of $\dot{\epsilon}_{\min}$ for $\sigma = 50 \text{ MPa}$ .....	127
4.48	Creep plots for the super-transus Ti-23Al-27Nb microstructure. (a) $\text{Log } \dot{\epsilon}_{\min}$ vs $\text{log } \sigma$ curves at $650^{\circ}\text{C}$ and $760^{\circ}\text{C}$ . (b) Arrhenius plot of $\ln \dot{\epsilon}_{\min}$ vs $10^4/T$ for an applied stress of 50 MPa, where the $650\text{-}705^{\circ}\text{C}$ data exhibited a lower $Q_{\text{app}}$ than the $705\text{-}760^{\circ}\text{C}$ data.....	129
4.49	$\ln (\dot{\epsilon}_{\min})$ vs $(1/T)$ for similar Ti-23Al-27Nb and Ti-25Al-23Nb microstructures at $\sigma = 50\text{MPa}$ . The heat treatments used to obtain the similar microstructures were $875^{\circ}\text{C}/45\text{h}/\text{WQ}/650^{\circ}\text{C}/304\text{h}/\text{WQ}$ for Ti-23Al-27Nb and $650^{\circ}\text{C}/116\text{h}/\text{WQ}$ for Ti-25Al-23Nb.....	135
4.50	Creep strain versus time plot for Ti-25Al-24Nb specimens at $650^{\circ}\text{C}/172 \text{ MPa}$ . The average GS of the specimens are depicted next to each curve.....	135
4.51	$\text{Log } \dot{\epsilon}_{\min}$ vs $\text{log } \sigma$ for Ti-23Al-27Nb and Ti-25Al-27Nb microstructures, which are represented by their grain sizes.....	136
4.52	A Ti-23Al-27Nb $875^{\circ}\text{C}$ heat-treated sample containing fiducial marks; (a) prior to creep and after (b) 4% creep, and (c) 9.8% creep at $650^{\circ}\text{C}/172 \text{ MPa}$ . Arrows indicate displacement offsets at grain boundaries. Cracks nucleated at O/O boundaries, marked 'a' in (b) and (c), aligned normal to the loading axis (horizontal).....	139
4.53	SEM image of local grain boundary offsets (indicated by arrows) for the $875^{\circ}\text{C}$ heat-treated Ti-23Al-27Nb specimen depicted in Figure 4.52c, which deformed to 9.8% creep.....	140

4.54	The deformed, sub-surface microstructures of Ti-23Al-27Nb 875°C/45h/WQ/650°C/304h/WQ heat-treated tension specimens which were unloaded within the secondary creep regime. Grain boundary cracking is indicated by the arrows. The respective loading conditions and creep strains were (a) 650°C/172 MPa; 9.8% and (b) 650°C/100 MPa; >20%.....	140
4.55	Severe grain boundary cracking at the surface for a Ti-23Al-27Nb 875°C/45h/WQ/650°C/304h/WQ heat-treated specimen which exhibited 9.8% creep strain before unloading within the secondary creep stage. The loading conditions was 650°C/172 MPa.....	141
4.56	The deformed, sub-surface microstructure of the Ti-23Al-27Nb 875°C/24h/WQ/650°C/218h/WQ heat-treated compression specimen which exhibited 9.8% creep. The specimen was unloaded in the secondary creep regime after being incrementally loaded from 172-250 MPa at 650°C.....	141
4.57	Elevated temperature creep cracking and slip for a heat treated (930°C/100h/WQ) Ti-25Al-25Nb specimen crept to 2.1% at 650°C/172 MPa. (a) O/O grain boundary cracks were blunted by B2. (b) Planar slip in the O phase (arrow a), slip transmittability between O and B2 grains (arrow b), and surface cracks (arrow c) were evident next to the specimen's edge.....	142
4.58	SEM (a) secondary electron and (b) BSD images of the same location illustrating a surface crack which was retarded inside a transformed B2 grain and continued along primary O grain boundaries for a sub-transus Ti-23Al-27Nb specimen tested at 650°C/100 MPa.....	143
4.59	The (a) surface and (b) cross-sectional views of the environmentally-assisted surface cracking for a 875°C/45h/WQ/650°C/304h/WQ Ti-23Al-27Nb specimen, which exhibited over 20% creep strain at 650°C/100 MPa. The specimen was unloaded after 283 hours.....	144

4.60	The post-creep microstructure of a 950°C/45h/WQ heat-treated Ti-23Al-27Nb specimen which exhibited more than 6% creep strain at 650°C/100 MPa. Dislocations formed preferentially at (a) O/β interfaces although this was also observed in heat-treated samples which were not creep deformed. A limited number of dislocations were observed within equiaxed O grains, see (b) and (c). In some cases the dislocations piled up at a (equiaxed O)-(equiaxed O) interfaces, see (c).....	145
4.61	The deformed Ti-25Al-27Nb as-processed microstructure tested at 394 MPa/760°C. Dislocations formed within O grains in slip bands.....	146
4.62	Bright-field TEM images of a post-crept Ti-23Al-27Nb super-transus microstructure containing (a) B2 platelets which are saturated with dislocations and (b) piled-up dislocations near a grain boundary for a specimen crept at 650°C/442 MPa.....	146
4.63	Creep strain versus time plots for the three Ti-12Al-38Nb heat-treated microstructures, represented by their average prior β grain size, tested at 650°C/50 MPa.....	149
4.64	Creep plots for three heat-treated Ti-12Al-38Nb microstructures. (a) Log $\dot{\epsilon}_{\min}$ vs log $\sigma$ curves at T = 650°C, where the data indicates a transition in creep exponent at 135 MPa. (b) Temperature dependence of $\dot{\epsilon}_{\min}$ for $\sigma = 50$ MPa.....	150
4.65	Creep fracture surface of step-loaded (a) Ti-12Al-38Nb (HT:650°C/55h/WQ) and (b) Ti-23Al-27Nb (HT:1090°C/0.5h/WQ/650°C/112h/WQ) specimens crept at 650°C. The Ti-12Al-38Nb failed at 172 MPa after 350 hours and 3% strain, while the Ti-23Al-27Nb specimen failed at 442 MPa after 600 hours and 2% strain. Note the environmental affected zone was much larger for the Ti-12Al-38Nb specimen.....	152

4.66	Higher magnification SEM images of the Ti-12Al-38Nb creep fracture surface depicted in Figure 4.65a. These photos were taken from the regions marked (a) b, (b) c, and (c) d.....	152
4.67	TEM image of a post-crept Ti-12Al-38Nb 650°C heat-treated microstructure which failed after reaching 8% creep at $\sigma=50$ MPa.....	153
4.68	Log $\dot{\epsilon}_{min}$ vs log $\sigma$ curves at 650°C for selected near Ti <sub>2</sub> AlNb and Ti-12Al-38Nb microstructures, represented by the average equiaxed grain size of the corresponding solution treatments.....	154
4.69	Stress vs strain plot for selected (a) Ti-25Al-24Nb and (b) Ti-12Al-38Nb specimens, including those heat treated to obtain fully-O, fully-B2 and fully- $\beta$ microstructures. Also depicted are curves for O+BCC microstructures, represented by the volume and morphology of the O phase, which show the strengthening effect of the O phase within the BCC matrix.....	161
4.70	Fracture surfaces of the heat-treated (a) fully-O Ti-25Al-24Nb and (b) fully- $\beta$ Ti-12Al-38Nb microstructures.....	163
4.71	Fracture surfaces of the heat-treated fully-B2 (a) Ti-25Al-24Nb and (b) Ti-23Al-27Nb microstructures.....	163
4.72	(a) Lower and (b) higher magnification SEM images illustrating the slip behavior of the fully- $\beta$ Ti-12Al-38Nb microstructure, obtained from surface observations. The photo in (b) indicates slip traces were interconnected within grains.....	164
4.73	The fracture surface of the as-rolled Ti-25Al-24Nb microstructure which exhibited cleaved and faceted fracture in O grains and dimples in B2 regions.....	165
4.74	A RT tensile deformed O+B2 Ti-25Al-24Nb microstructure which was heat treated at 975°C/100h/WQ. Planar slip is illustrated in the O phase (a) and wavy slip is seen the B2 phase (b). Slip compatibility of the two phases is also illustrated (c). O/O grain boundary cracks were blunted by B2 grains (d).....	166

4.75	The deformation behavior for a heat treated (900°C/5h/WQ/650°C/55h/WQ) Ti-12Al-38Nb microstructure which was strained to more than 12% at RT. Wavy $\beta$ slip traces readily transgressed O-phase platelets, indicated by the arrows.....	167
4.76	A RT deformed Ti-25Al-27Nb specimen exhibiting concentrated (Luder) deformation bands along its (a) face and (b) edges.....	170
4.77	A RT deformed Ti-25Al-27Nb specimen exhibiting a greater dislocation build-up within the B2 phase compared with the O phase.....	172
4.78	A RT deformed fully-lenticular O+B2 microstructure which exhibited a localized fracture where cracks transgressed B2 laths.....	172
5.1	Figure 5.1 The Ti-22Al isopleth with the current data overlaid for a Nb composition of 27at.%.....	175
5.2	Discontinuous precipitation (indicated by arrows) for super-transus Ti-23Al-27Nb samples which were aged within the O+B2 region. The corresponding heat treatments were (a) 1090°C/0.5h/WQ/900°C/8h/WQ and (b) 1090°C/0.5h/WQ/650°C/9h/WQ/900°C/8h/WQ.....	182
5.3	Super-transus heat-treated Ti-23Al-27Nb microstructure (1150°C/0.5h/cooled at 15°C/min. to RT) which was subsequently aged at 650°C for 100 hours followed by water quenching. No cellular precipitation was evident.....	184
5.4	Ternary diagrams for the Ti-Al-Nb system. (a) The 900°C isothermal ternary slice taken from Rowe <i>et al.</i> (1993) where selected alloys of this work are represented along the constant Ti=50at.% tie-line. Ti-12Al-38Nb borders the BCC/BCC+O phase regimes at the left-hand-side of this line. (b) The schematic representation of a 650°C isothermal ternary slice depicting the lateral shift in the BCC/BCC+O boundary.....	185
5.5	The pseudobinary section of the Ti-Al-Nb system at 50 at.% Ti taken from Bendersky <i>et al.</i> (1991) with data from the Ti-25Al-24Nb, Ti-23Al-27Nb, and Ti-12Al-38Nb alloys superimposed.....	187



5.6	The calculated grain boundary sliding rate versus $\sigma^2/GS$ for the Ti-23Al-27Nb microstructures judged to be within the grain boundary sliding regime at 650°C. Also indicated are the measured minimum creep rates for these microstructures..	194
5.7	The calculated grain boundary sliding rate versus $\sigma^2/GS$ for all the near Ti <sub>2</sub> AlNb and Ti-12Al-38Nb microstructures judged to be within the grain boundary sliding regime at 650°C. Also indicated are the measured minimum creep rates for these microstructures.....	196

## LIST OF TABLES

1.1	Orthorhombic Alloy Testing Conditions and Corresponding Creep Parameters.....	21
1.2	Orthorhombic Alloy RT Tensile Properties.....	29
3.1	Rolling Procedures and Parameters for the Ti <sub>2</sub> AlNb cigar-melted Ingots.....	45
3.2	Lattice Parameters of the Different Phases.....	71
4.1	Chemical Analysis of the near Ti <sub>2</sub> AlNb Alloys.....	75
4.2	The Measured Average Grain Sizes, Phase Volume Percents and Compositions for the Ti-23Al-27Nb Heat-Treated Microstructures.....	78
4.3	The Measured Average Grain Sizes, Phase Volume Percents and Compositions for the Ti-25Al-24Nb, Ti-25Al-23Nb, and Ti-25Al-27Nb Microstructures.....	80
4.4	Chemical Analysis of the As-rolled Ti-12Al-38Nb Sheet Material.....	109
4.5	Ti-12Al-38Nb Heat Treatments and Measured Average Grain Sizes, Phase Volume Percents and Compositions .....	115
4.6	Creep Properties for Heat-Treated Ti-23Al-27Nb Microstructures.....	125
4.7	Measured Creep Exponents and Apparent Activation Energies for Heat-Treated Ti-23Al-27Nb Microstructures.....	127
4.8	Creep Properties for Heat-Treated Ti-25Al-27Nb, Ti-25Al-23Nb, and Ti-25Al-24Nb Microstructures.....	132
4.9	Measured Creep Exponents and Apparent Activation Energies for Heat-Treated Ti-25Al-23Nb and Ti-25Al-27Nb Microstructures.....	133
4.10	Creep Properties for Heat-Treated Ti-12Al-38Nb Microstructures.....	148
4.11	Measured Creep Exponents and Apparent Activation Energies for Heat-Treated Ti-12Al-38Nb Microstructures.....	149

4.12.	The Heat Treatments and 650°C Tensile Properties for Selected near Ti <sub>2</sub> AlNb and Ti-12Al-38Nb Microstructures.....	157
4.13	The Heat Treatments and RT Tensile Properties for Selected near Ti <sub>2</sub> AlNb and Ti-12Al-38Nb Microstructures.....	158
4.14	Chemical Analysis of the Lower-Oxygen and Higher-Oxygen Ti-23Al-27Nb Sheet Materials.....	167
5.1	Comparison of Creep Parameters for Different Ti-Alloys.....	200

## LIST OF SYMBOLS/ABBREVIATIONS

A	dislocation creep constant
$A_{gbs}$	grain boundary sliding creep constant
$\alpha$	alpha phase titanium
$\alpha_2$	alpha-2 phase titanium
Ag	silver
Ar	argon
Al	aluminum
ASTM	American Society for Testing and Materials
at. %	atomic percent
ATS	Applied Test Systems, Inc.
AQ	air quench
b	burgers vector
BCC	Body-Centered Cubic
$\beta$	disordered BCC phase titanium
B2	ordered BCC phase titanium
BC	brick cooled
BSD	back-scatter detector
C	carbon or Coble creep
CC	control cooling
$^{\circ}\text{C}$	degrees Celsius
cm	centimeter
$\text{cm}^3$	cubic centimeters
d	average planar grain size determined by the line-intercept method
CBED	convergent beam electron diffraction
Cu	copper
CRSS	critical resolved shear stress

$D_0$	frequency factor for grain boundary diffusion
$D_l$	frequency factor for volume diffusion
DTA	differential thermal analysis
$E$	elastic modulus
$E_{BCC}$	elastic modulus of the constituent BCC phase
$E_O$	elastic modulus of the constituent O phase
$\epsilon_c$	Coble creep rate
$\epsilon_{dc}$	dislocation climb creep rate
EDM	electron discharge machine
$\epsilon_f$	elongation-to-failure
$\epsilon_g$	creep strain contribution from within the grains
$\epsilon_{gbs}$	creep strain attributed to grain boundary sliding
$\epsilon_{gbs}$	grain boundary sliding creep rate
$\dot{\epsilon}_{min}$	minimum creep rate
$\dot{\epsilon}_{ss}$	steady-state creep rate
$\epsilon_{tot}$	total measured creep strain
exp	exponent
$\epsilon_p$	primary creep strain
FCC	Face-Centered Cubic
Fe	iron
FC	furnace cool
g	gram
$G$	shear modulus
GPa	Giga Pascal
$\gamma$	gamma phase titanium
GS	average spatial grain size
$GS_0$	the pre-heat treatment grain size used in the equation for grain growth
$GS_{eff}$	effective grain size for diffusional creep used in the equation for Coble creep
h	hour
H-D	Harper-Dorn creep
HCP	Hexagonal Close Packed
H	hydrogen
IBM	International Business Machines
JEOL	Japan Electro Optics Limited
k	Boltzmann's constant or the grain growth constant

K	Kelvin (absolute temperature)
kg	kilogram
kJ	kilojoule
kN	kilonewton
kV	kilovolt
LVDT	linear variable differential transformers
m	meter
mA	milliampere
min	minute
mm	millimeter ( $10^{-3}$ m)
MMC	metal matrix composite
Mo	molybdenum
mol	mole
MPa	mega pascal
MTS	Mechanical Testing Systems
n	creep exponent or grain growth exponent
N	nitrogen
Nb	niobium
N-H	Nabarro-Herring creep
NIST	National Institute for Standards and Technology
nm	nanometer ( $10^{-9}$ m)
O	Orthorhombic phase titanium
$\Omega$	activation volume
OR	orientation relationship
OM	optical microscopy
OQ	oil quench
PC	personal computer
pj	probability of finding a jog on a dislocation
ppm	parts per million
PST	polysynthetically twinned
Qapp	apparent activation energy
R	gas constant
rpm	revolutions per minute
s	second
$\sigma$	applied creep stress
SADP	selected area diffraction pattern

SEM	scanning electron microscopy
SiC	silicon carbide
t	time
T	temperature
TEM	transmission electron microscopy
Ti	titanium
T <sub>m</sub>	melting temperature
TMC	titanium matrix composite
TMF	thermomechanical fatigue
t <sub>p</sub>	primary creep transient time
μ	Poisson's ratio
UTS	ultimate tensile strength
V	vanadium
v <sub>o</sub>	volume fraction of the O phase
V <sub>p</sub>	volume percent
vs	versus
W	grain boundary width
wt. %	weight percent
WQ	water quenched
XRD	X-ray diffraction
YS	yield strength
z	coordination number

## PREFACE

This technical report presents the results of a systematic study of the physical metallurgy of orthorhombic titanium-aluminum-niobium alloys. The main objective of this work was to understand microstructure-creep relationships. The phase evolution, creep, and tensile behavior were studied for near Ti<sub>2</sub>AlNb and Ti-12Al-38Nb O+BCC alloys. Monolithic materials were produced through conventional thermomechanical processing techniques. Phase evolution studies showed that these alloy may contain several constituent phases including:  $\alpha_2$  (ordered hexagonal close-packed DO<sub>19</sub> structure), B2 (ordered body-centered-cubic (bcc)),  $\beta$  (disordered bcc), and O (ordered orthorhombic based on Ti<sub>2</sub>AlNb). Heat treatment and TEM studies estimated the temperature ranges for the respective phase fields and a pseudobinary diagram based on Ti=50at.% was constructed. The aging-transformation behavior was studied in detail. O-phase precipitation within BCC-dominated microstructures resulted in significant room-temperature (RT) strengthening. As the phase volume of the O phase increased, lower room-temperature strains-to-failure were exhibited and the fully-O microstructures exhibited poor ductility. The BCC phase is vital for imparting RT ductility to O+BCC alloys. In terms of the creep behavior, unaged microstructures, which transformed during the creep experiments, exhibited larger creep strains than long-term aged microstructures and the creep load did not significantly effect the transformation behavior. The deformation observations and calculated creep exponents and activation energies suggested that three creep mechanisms are dominating the secondary creep behavior. The creep mechanisms were dependent on microstructure and stress. For low applied stresses, Coble creep characteristics were exhibited. For intermediate stresses, the minimum creep rates were proportional to  $\sigma^2/GS$  and fiducial-line experiments revealed grain boundary sliding and grain boundary cavitation. For high stresses, the stress exponents were greater than or equal to 3.5 and a high density of dislocations were observed, indicative of a dislocation climb mechanism. Overall, the sub-transus processed and heat-treated microstructures contained much smaller grain sizes than super-transus microstructures and this resulted in worse creep resistance. For targeted low-to-intermediate stress and intermediate temperature applications, grain size is the dominant microstructural feature influencing the creep behavior of O+BCC alloys.



## ACKNOWLEDGMENTS

The experimental work of this study was funded by the UES, Inc. Dayton, Ohio contracts F33615-91-C-5663 and F33615-C-96-5258 to the United States' Government through the Materials and Manufacturing Directorate at Wright-Patterson Air Force Base, Fairborn, Ohio. The laboratory tasks and experimental testing were performed at the Materials and Manufacturing Directorate under the provisions of the UES contracts.

I thank Drs. Bhaskar Majumdar, Venkat Seetharaman, S. Krishnamurthy, and Madan Mendiratta of UES, Inc. and Dr. Daniel Miracle of Wright Laboratory for their guidance throughout the development of this work. I also thank Drs. Daniel Eylon and Deborah Thebert-Peeler of the University of Dayton for reviewing this document.

Special thanks are due to Dr. Andrew Rosenberger, Miss Debbie Garner, Miss Stephanie Luetjering, and Messrs Daniel Knapke and David Maxwell of the University of Dayton Research Institute (UDRI) and Miss Sonya Boone and Messrs Michael Scott and George Cornish of UES, Inc. for their technical assistance with the elevated temperature tension and creep testing.

I am grateful to Dr. Robert Wheeler of UES for teaching me the intricacies of transmission electron microscopy (TEM). I am also grateful to the technical staff of the UES off-site contract for their excellent technical assistance. I would especially like to thank Mark Dodd, Joe Henry, Joe and Travis Brown, Tom Jones, Tom Goff, Eric Fletcher, Scott Apt, Tim Shock, Marlin Cook, Luann Piazza, Cheryl Heidenreich, Judy Paine, Lou Henrich, and Pam Lloyd.

I also appreciate the guidance and encouragement of Mr. Paul Smith and Dr. Mary Lee Gambone of the Materials and Manufacturing Directorate.

## INTRODUCTION

Today, within the aerospace industry, there is a need for materials with high strength and stiffness and low density, especially for high-temperature applications. Titanium (Ti) alloys and their composites are examples of such materials which have found use in a variety of elevated temperature applications because of their high specific strength and stiffness as well as their creep and oxidation resistance. Major applications for Ti alloys have been in the aerospace industry, and research and development efforts to increase their temperature and strength capabilities have been sustained throughout the last 30 years. Efforts have been directed toward developing binary alloys based on the intermetallics of titanium such as  $\text{Ti}_3\text{Al}$   $\alpha_2$ -based and  $\text{TiAl}$   $\gamma$ -based alloys. More recently, alloy development efforts have been directed almost exclusively towards intermetallics because of a significant potential increase in temperature capability. The superior properties of alloys based on intermetallic compounds arise from their greater degree yield strength and elastic modulus retention with temperature and lower diffusivities resulting in enhanced creep-stress rupture properties and lower creep rates. However, these superior properties are balanced against their typically low ductility and fracture toughness at ambient temperatures. For many applications, especially for matrices within titanium matrix composites (TMCs), the latter properties are unacceptable.

In an effort to improve the fracture toughness and ductility of  $\alpha_2$ -based intermetallics, ternary alloying additions of niobium (Nb) have been explored by Blackburn and Smith (1989). A large range of alloy compositions has since been examined and alloys with higher room-temperature (RT) elongations and enhanced

temperature capabilities are now available. The interest in Nb-rich Ti<sub>3</sub>Al alloys has led to several breakthroughs. One important recent discovery was the existence of an orthorhombic (O) phase, based on the compound Ti<sub>2</sub>AlNb. Because of the attractive properties associated with O phase, titanium alloys containing a significant amount of the O phase (henceforth termed O alloys) are being considered for use in structural applications both as monolithic materials as well as matrix alloys in continuously reinforced metal matrix composites (MMCs). The intermetallic alloy based on the O phase, Ti-25Al-25Nb(at.%), is one of the most recent of the O alloys being considered. Other O alloys, such as Ti-23Al-27Nb(at.%) and Ti-12Al-38Nb(at.%), containing the O and Body-Centered Cubic (BCC) phases are also being considered. Due primarily to the high Nb content in such alloys, the two-phase O+BCC regimes have a wider temperature range than the  $\alpha_2$ +B<sub>2</sub>,  $\alpha_2$ +B<sub>2</sub>+O, and O phase fields. Hence such alloys are termed "O+BCC" alloys. The research presented in this technical report was intended to further develop our understanding in the areas of O+BCC titanium alloys and is centered on these ternary alloy systems. In particular, the phase evolution, creep, and tensile behavior were investigated.

## CHAPTER 1

### BACKGROUND

Although the database for the O class of titanium alloys is much smaller than that for the more studied,  $\alpha+\beta$ ,  $\alpha_2$ , and  $\gamma$ -based systems, a relatively high percentage of the literature on Ti alloys has involved O alloys since the discovery of the O phase nearly a decade ago (Banerjee *et al.* 1988). This chapter is devoted to this recent influx of O-alloy literature and in particular the existing knowledge of phase equilibria, creep, tension, and microstructure-property relations of O alloys. Due to the similarities between the  $\alpha_2$ -based and O-based systems, whenever relevant, the existing knowledge of the more studied  $\alpha_2$  systems will also be presented. The purpose of this chapter is to provide the reader with an accurate description of the work performed in these areas as well as identify where a bridge between the current understanding and a more advanced stage is needed. The topics of interest include the nature of the constituent phases which are present in O alloys, microstructural evolution and phase stability, microstructure-property trends, and deformation behavior. Special emphasis will be placed on the creep behavior of O alloys, which was chosen to be the main focus of this work. This chapter concludes with an assessment of the deficiencies in our knowledge of the behavior of O alloys.

#### 1.1 Constituent Phases

The O phase, discovered in a Ti-25Al-12.5Nb(at.%) (All compositions will be reported in atomic percent henceforth.) alloy which also contained the hexagonal close packed (HCP)  $\alpha_2$  phase and the ordered BCC B2 phase, was first identified by Banerjee

*et al.* (1988) using TEM, convergent beam electron diffraction (CBED), and channeling enhanced microanalysis. The precise atomic coordinates and quantified sublattice occupancies for the Ti, aluminum (Al), and Nb atoms were later determined by Mozer *et al.* (1990). The O phase (Cmcm symmetry based on  $\text{Ti}_2\text{AlNb}$ ) is similar in nature to  $\alpha_2$  ( $\text{Ti}_3\text{Al}$ ,  $\text{DO}_{19}$  structure), yet differs by the lattice arrangement of Nb with respect to Ti. The Nb and Ti atoms are more randomly distributed in the  $\alpha_2$  phase compared with the O structure. The atomic positions on the basal planes of the  $\alpha_2$  and O lattices, based on the findings of Mozer *et al.* (1990), are sketched to scale in Figure 1.1a and b, which shows how the ordered arrangement of the different-sized Nb and Ti atoms has destroyed the hexagonal symmetry of the  $\alpha_2$  phase. The O phase has since been identified in Ti alloy compositions ranging from 20-30 Al and 12.5-30 Nb thus encompassing the lower Nb range of the BCC phase. The stability of the BCC phase extends from the Nb-rich end into the ternary system as shown by Shyue *et al.* (1993) in alloys Ti-14Al-75Nb and Ti-17Al-45Nb. The crystal structure of the ternary ordered B2 phase (CsCl symmetry based on  $\text{Ti}_2\text{AlNb}$ ) is depicted in Figure 1.1c. Banerjee *et al.* (1987) have shown that Nb and Al occupy one sublattice while Ti occupies the other sublattice. Note that the BCC structure is relatively open compared with that of O and  $\alpha_2$ . An isothermal (900°C) ternary slice taken from Rowe *et al.* (1993) illustrating the range of compositions of the three phases is depicted in Figure 1.2. The bold line depicts the range of O+B2 compositions with constant Ti=50at.%. Each of the alloys investigated in this work are marked with an X. The Ti-25Al-25Nb alloy borders the single-phase O and two-phase O+BCC regimes while Ti-12Al-38Nb borders the single-phase BCC and O+BCC regimes. Ti-23Al-27Nb lies within the O+BCC regime between the single-phase O and single-phase BCC regions.

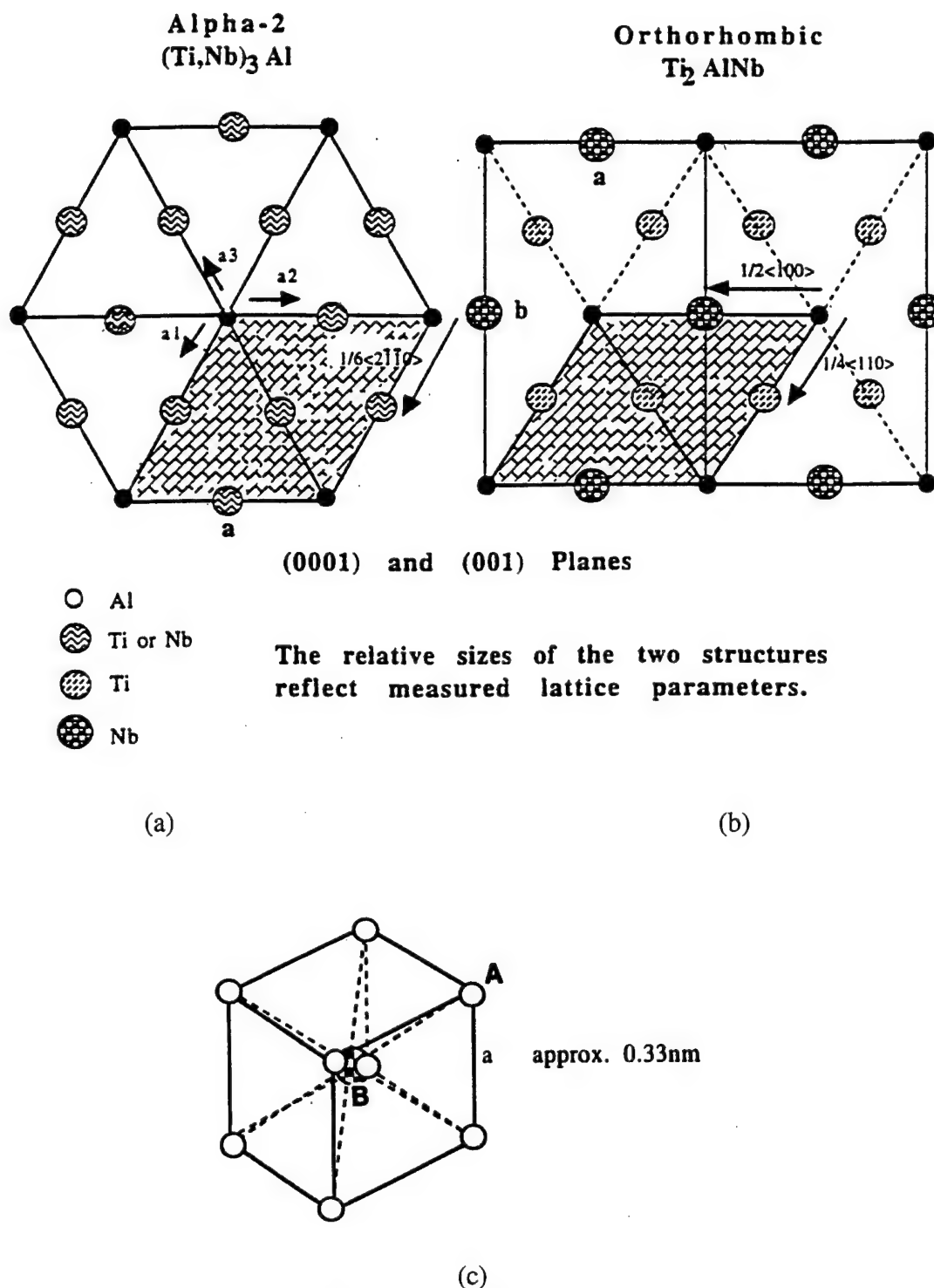


Figure 1.1 The basal planes of the (a)  $\alpha_2$  and (b) O lattices and (c) the crystal structure (AB) of the ordered B2 structure. In Ti-Al-Nb alloys rich in titanium, A sites of the B2 structure are occupied by Ti and B sites by Al and Nb atoms randomly (Banerjee *et al.* 1987).

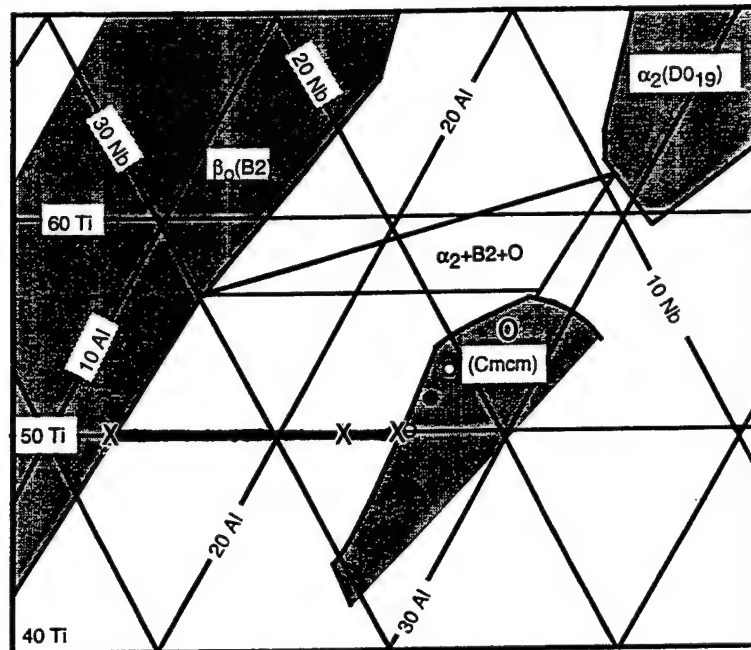


Figure 1.2 900°C isothermal ternary slice taken from Rowe *et al.* (1993) where the bold line highlights the range of O+BCC compositions containing Ti=50at.%. The nominal compositions of the alloys investigated in this work, which lie along the bold line, are marked X.

### Phase Evolution

An extensive amount of work on the phase equilibria of O alloys has been performed by Muraleedharan (1995). From his efforts and others' (Banerjee *et al.* 1989, Muraleedharan *et al.* 1990 1992a,b 1995a,b, Bendersky *et al.* 1991, Bendersky and Boettinger 1993, Rowe *et al.* 1993) a definitive understanding of the phase equilibria involving the O phase has been obtained. The crystallographic features of the product O phase have been explained by the phenomenological theory of martensitic transformations. The evolution of microstructure in the course of the transformations is governed by strain energy minimization (Bendersky *et al.* 1991, Muraleedharan 1995). The limited amount of phase evolution examined in this work was performed to aid in the understanding of microstructure-property relationships. The pertinent observations of the

previously mentioned works, in particular the phase transformations and long term stability of O alloys, are described in the following paragraphs.

Muraleedharan (1995) has examined alloys spanning a range of Nb contents up to 25at.% with Al ranging from 24-28at.%. The sub-transus phase fields for such alloys include  $\alpha_2$ +B2,  $\alpha_2$ +B2+O, O+B2, O+ $\beta$  ( $\beta$  is the disordered BCC phase), and O. The Ti-25Al-xNb vertical section (Muraleedharan 1995, Sagar *et al.* 1996) depicting the different phase regimes is given in Figure 1.3. Above the transus, single-phase BCC microstructures exist and the  $\beta$ -B2 ordering transformation is assumed to be a second order transformation. For alloys containing close to 25Al, the ordered B2 structure, which exists as high as 1400°C at 25Nb, is more stable with increasing Nb contents (Bendersky *et al.* 1991, Muraleedharan 1995, Vasudevan *et al.* 1996). By cooling rapidly from above the transus through the  $\alpha_2$ +B2 and  $\alpha_2$ +B2+O fields,  $\alpha_2$  formation may be prevented and only the O+BCC phases will coexist. However, slow cooling or solutionizing in the  $\alpha_2$ +B2 or  $\alpha_2$ +B2+O regimes will promote the formation of  $\alpha_2$ . Upon subsequent aging in the  $\alpha_2$ +B2+O, O+B2, O+ $\beta$ , or O regimes, a 'rim O' phase will develop at the periphery of the equiaxed  $\alpha_2$ . This 'rim O' phase is suggested to act as a barrier thereby preventing the  $\alpha_2$  phase from transforming when aged in the lower temperature fields even for very long times (Muraleedharan, 1995). This significantly affects the stability of O alloys at lower temperatures as high concentrations of  $\alpha_2$  may appear stable even though it is not an equilibrium phase.

BCC diffusion kinetics are more rapid than those for  $\alpha_2$ . At Nb contents greater than 11%, metastable B2 is retained on quenching from the single-phase B2 field. In addition metastable B2 is also retained on quenching from the  $\alpha_2$ +B2,  $\alpha_2$ +B2+O, or O+B2 fields. The metastable B2 phase can be decomposed to  $\alpha_2$  and/or O through three distinct transformation modes. The processing, solutionizing, and aging temperatures as well as the alloy compositions are important variables for determining the type of mechanism governing the B2 decomposition.



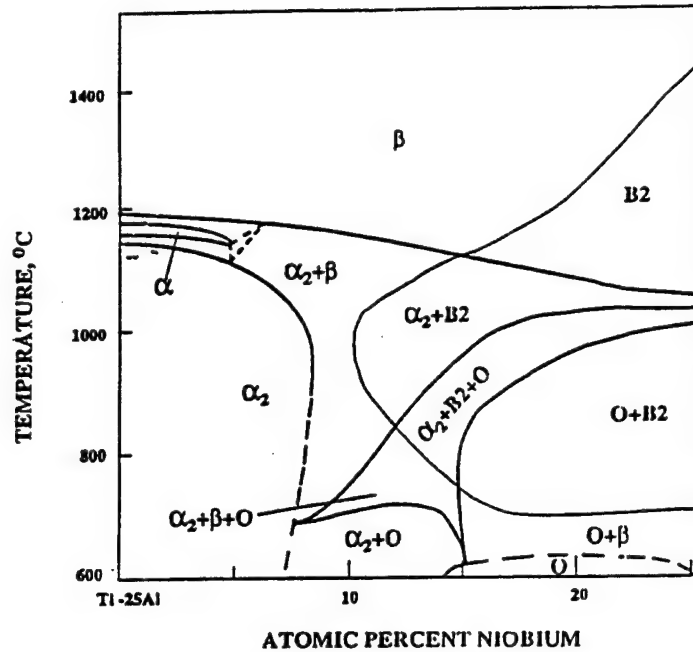


Figure 1.3 The Ti-25Al-xNb vertical section taken from Sagar et al. (1996).

The first transformation mechanism is the conventional Widmanstatten precipitation of  $\alpha_2$  or O, depending on the aging temperature. For super-transus processed or sub-transus processed then super-transus annealed microstructures, this precipitation mode occurs between 800°C and the transus temperature for alloys containing between 23-25Al (Majumdar *et al.* 1994 1995, Banerjee 1994, Boehlert *et al.* 1997a,d,e). The lowest temperature at which Widmanstatten precipitation initiates, which corresponds to the BCC transus temperature, decreases with decreasing Al content (Bendersky *et al.* 1991, Shyue *et al.* 1993). This is a result of the lower transus temperatures for lower Al-containing alloys. For sub-transus processed microstructures, which contain equiaxed B2 grains, of alloys containing between 23-25Al, the lowest temperature in which Widmanstatten O precipitation initiates is 875°C (Boehlert *et al.* 1997e). Thus the range of temperatures in which the B2 phase is decomposed to  $\alpha_2$  or O through Widmanstatten precipitation is dependent on both the processing and annealing temperatures.

A second decomposition mode is through a composition invariant mechanism which rapidly transforms the super-transus parent B2 to either a metastable  $\alpha_2$  phase at low Nb contents (Gogia 1990) or metastable O at higher Nb levels (Bendersky *et al.* 1991, Muraleedharan 1995). With continued aging, equilibration of the structure occurs by reprecipitation of B2 in the matrix which is now  $\alpha_2$  or O. This decomposition mode occurs at aging temperatures ( $T < 800^\circ\text{C}$ ) lower than those for which conventional Widmanstätten precipitation is observed. The tendency for the composition invariant mechanism decreases with decreasing Al content (Bendersky *et al.* 1991).

A third decomposition mode is through discontinuous precipitation of B2 to  $\alpha_2 + \text{BCC}$  or  $\text{O} + \text{BCC}$  which replaces fine intragranular matrix precipitation (Mishra and Banerjee 1990, Rowe and Gigliotti 1990, Rowe and Hall 1991, Rowe 1991, Rowe 1993, Rowe and Larsen 1996, Boehlert *et al.* 1997c-e). Composition and temperature effects on this decomposition mode are described in detail in the aging sub-section of the phase-evolution results section in Chapter 4. It is noted that at temperatures below  $900^\circ\text{C}$ , the B2 phase undergoes a composition induced disordering resulting in the disordered  $\beta$  structure (Kestner-Weykamp *et al.* 1989, Bendersky *et al.* 1991, Rhodes 1997, Boehlert *et al.* 1997d,e). This is attributed to the decreasing Al and increasing Nb content of the B2 phase in the ternary system as the temperature decreases. The exact order/disorder temperature is dependent on alloy composition.

During the phase transformations, orientation relationships (ORs) develop between each of the constituent phases involved. In all cases the  $\alpha_2$  phase forms from B2 with the same OR described by Burgers (1934) for the  $\alpha$  and  $\beta$  phases:  $[1\bar{1}20]\alpha_2//[1\bar{1}1]\text{B2}$ ;  $(0001)\alpha_2//(110)\text{B2}$ . Sagar *et al.* (1996) have reported that for a Ti-22Al-25Nb alloy, the  $\alpha_2$  and B2 particles undergo dynamic recrystallization when thermomechanically processed in the  $\alpha_2 + \text{B2}$  field and this destroys the Burgers OR. The OR formed between the B2 and O structures is:  $[1\bar{1}1]\text{B2}//[110]\text{O}$ ;  $(110)\text{B2}//(001)\text{O}$  (Muraleedharan *et al.* 1992b). The manner in which the O phase forms at the rim of the

$\alpha_2$  phase is described as:  $[0001]\alpha_2//[001]O$ ;  $(10\bar{1}0)\alpha_2//(110)O$  (Banerjee *et al.* 1988). Finally, for alloys of close to a  $Ti_4AlNb_3$  composition, the OR and habit planes of O precipitates within the  $\beta$  matrix have been characterized by Bendersky *et al.* (1991). The O phase grows from fully- $\beta$  microstructures with the following OR:  $[011]\beta//[001]O$ ;  $(\bar{2}11)\beta//(110)O$  (for the first variant) and  $(\bar{2}1\bar{1})\beta//(1\bar{1}0)O$  (for the second variant). This is identical to the previously described OR between O and B2. Based on the similarity between the  $\alpha_2$  and O phases this OR is identical to that described by Burgers (1934) for the  $\alpha$  and  $\beta$  phases. This OR gives 12 orientational variants of the O phase in the  $\beta$  matrix (two rotated  $\pm 3^\circ$  around each of the 6  $\langle 110 \rangle_\beta$  matrix phase directions). These ORs are important not only for describing the microstructure but also in relationship to mechanical behavior as is described in the tensile behavior sub-section of this chapter.

Another microstructural aspect which has proven to be important to mechanical behavior is interstitial content. The interstitial elements oxygen, carbon, nitrogen, and hydrogen play an important role in the experimental determination of phase equilibria. In particular, oxygen shifts the phase equilibria by raising the BCC-transus and increases the  $\alpha_2$ -phase content in two-phase microstructures (Szaruga *et al.* 1992, Rhodes *et al.* 1993, Boehlert *et al.* 1997a,c,d, Takag and Ouchi 1997). For  $Ti_2AlNb$  alloys, an increase in the B2 transus temperature from 1030-1070°C has been observed with increasing oxygen levels between 280-980 weight parts per million (ppm) (Boehlert *et al.* 1997c,d). An increase in the B2 transus temperature with increasing oxygen between 710-1800 ppm has also been observed for Ti-25Al-10Nb-3V-1Mo (Szaruga *et al.* 1992). A greater rate of increase in the transus temperature was noted for increasing oxygen contents between 710-1000 ppm, while a lower rate of increase was noted between 1000-1800 ppm oxygen. Interestingly, the order/disorder temperature of the BCC phase was also affected by oxygen content. Oxygen effects on the O-phase stability have been studied by Rhodes *et al.* (1993) in Ti-22Al-23Nb and Ti-22Al-27Nb alloys. At temperatures between 800-900°C, the equilibrium phases in Ti-22Al-23Nb, with more than 980 ppm oxygen, are

$\alpha_2$ +B2+O. In the same alloy containing 220 ppm oxygen and in the Ti-22Al-27Nb alloy with 260-1120 ppm oxygen, the equilibrium phases in the same temperature range are B2 and O. They have also reported that oxygen has a concomitant effect on the BCC-transus temperature in both these alloys (1020-1125°C in Ti-22Al-23Nb and 980-1010°C in Ti-22Al-27Nb). Carbon has also been shown to increase  $\alpha_2$  stability (Krishnamurthy and Miracle 1997a). Similarly, the introduction of hydrogen has reportedly increased the stability of the O phase by increasing the O-phase volume fraction (Saqib *et al.* 1995). Thus interstitial contents are important to the phase evolution of O alloys and must be considered when evaluating microstructures. They also must be considered when evaluating mechanical behavior as described in the tensile behavior results and discussion sections.

### 1.3 Mechanical Behavior

Orthorhombic titanium alloys have potential for high-temperature applications. They possess good creep resistance and reasonable RT ductility, dependent on microstructure, making them attractive over  $\gamma$ -based TiAl alloys for use in the temperature range 500°C-700°C. One major application area for such alloys is as a matrix in continuous fiber-reinforced titanium matrix composites, where  $\gamma$ -based TiAl alloys are unsuitable because of their poor ductility. It has been demonstrated that matrix ductility, which is dependent on the heat treatment and its associated microstructure, significantly influences efficient utilization of fiber strength during longitudinal loading of MMCs (Boehlert *et al.* 1997a), while matrix creep resistance is particularly important for off-axis MMCs because of very low fiber-matrix bond strengths (Majumdar *et al.* 1992, Krishnamurthy and Miracle 1997b, Woodard and Pollock 1997). In addition, advantages of O alloys include enhanced specific tensile strength and stiffness, fracture toughness, longitudinal and transverse creep, fatigue crack growth resistance, and thermomechanical fatigue (TMF) resistance compared with the more familiar Ti-24Al-

11Nb and Ti-25Al-10Nb-3V-1Mo  $\alpha_2$  and super  $\alpha_2$ -based alloys, respectively (Rowe 1991, Balsone *et al.* 1993, Smith *et al.* 1994a,b, Foster *et al.* 1995, Russ *et al.* 1995, Majumdar *et al.* 1994 1995, Woodfield 1996, Krishnamurthy and Miracle 1997b, Boehlert *et al.* 1997a). Due to their importance in terms of MMC performance, the monolithic matrix creep and tension behavior were investigated in this work. The following sections discuss the literature involving creep and tension for O alloys.

### 1.3.1 Creep Behavior

Several studies have involved the creep behavior of a wide variety of O-alloy compositions and microstructures (Rowe 1991 1993a,b, Rowe *et al.* 1991,1992, Austin *et al.* 1992, Nandy *et al.* 1993 1995, Smith *et al.* 1993, Chesnutt *et al.* 1993, Majumdar *et al.* 1994 1995, Smith *et al.* 1994a,b 1995, Rowe and Bendersky 1995, Woodfield 1996, Rowe and Larsen 1996, Woodard *et al.* 1996, Hayes 1996, Dary *et al.* 1996, Woodard and Pollock 1997, Boehlert *et al.* 1997b-e). In terms of microstructure-property relationships, creep studies on first-generation O alloys such as Ti-25Al-17Nb and Ti-22Al-23Nb, which contain the  $\alpha_2$ , BCC, and O phases, showed a strong creep-microstructure correlation. The creep resistance increased with increasing volume percent of the O phase and decreased with decreasing volume percent of the  $\alpha_2$  phase (Majumdar *et al.* 1994 1995, Smith *et al.* 1994a,b 1995, Woodard *et al.* 1996). This observation was made after comparing the creep behavior of several different microstructures under one creep condition, 650°C/172 MPa. As a first attempt, the observations may be explained by the superior creep resistance found for fully-O microstructures (Nandy *et al.* 1993) compared with fully- $\alpha_2$  microstructures (Mendiratta and Lipsitt, 1980). Judging from the similarities of the fully-O and fully- $\alpha_2$  (i.e. They both contain equiaxed grains of between 88-100 $\mu$ m grain size.), this appears to be a fair comparison. However, this result may be misleading as the fully-O microstructure was tested in compression while the fully- $\alpha_2$  microstructure was tested in tension, where

cavitation may lead to significantly higher strain rates. In addition, this comparison may not explain the trends of the three-phase microstructures because the fully-O microstructure was examined under much higher applied stresses,  $\sigma > 172$  MPa, and therefore the dominant secondary creep mechanism may have been different. In particular, the strain rate versus applied stress behavior of the fully- $\alpha_2$  microstructure suggested that a transition in mechanism occurs at lower applied stresses. Typically, the microstructural features most influential to the secondary creep behavior are related to the dominant secondary creep mechanism. For example, grain size is considered to be more influential in Coble creep than in dislocation climb creep. With this respect, grain-size effects, which have proven to be important in other studies (Mishra and Banerjee 1990, Rowe and Larsen 1996), may be significant. Interestingly, the microstructures containing a higher volume of O phase also contained larger prior B2 grains. Also important are morphological effects (Eylon *et al.* 1976, Miller *et al.* 1987, Mishra and Banerjee 1990 1995, Worth *et al.* 1995), which may have played a role as the O phase was typically in a lenticular morphology, while the  $\alpha_2$  phase was equiaxed. A fourth possibility is that the order/disorder nature of the BCC phase, which depends on alloy content and heat treatment, is important. In particular, the BCC phase chemistry determines ordering, where at lower Al and higher Nb contents the B2 structure undergoes a composition induced disordering which preferentially occurs during long aging times at low temperatures (Kestner-Weycamp *et al.* 1989, Bendersky *et al.* 1991, Rhodes 1997). Composition induced disordering is of practical importance in view of the substantially higher diffusivity expected for the disordered  $\beta$  phase compared with B2, as this will adversely effect the creep resistances of these alloys during anticipated application at such temperatures. As a result of these studies it was determined that in order to more thoroughly understand microstructure-creep relationships a better understanding of the creep mechanisms involved was necessary. In particular, the range of temperatures and stresses dominated by certain mechanisms would be useful.

The literature reporting creep exponent ( $n$ ) and apparent activation energy ( $Q_{app}$ ) values for O alloys, although limited, has indicated the possibility of several different mechanisms (Nandy *et al.* 1993 1995, Smith *et al.* 1993, Hayes 1996, Woodard *et al.* 1996, Rowe and Larsen 1996, Woodard and Pollock 1997). For low applied stresses,  $\sigma < 100$  MPa, Smith *et al.* (1993) and Woodard and Pollock (1997) have obtained steady-state creep exponents of 1.4 and 1.3, respectively. These studies were performed on a three-phase Ti-22Al-23Nb alloy between 650-760°C. Values of  $n$  close to unity typically indicate that stress-directed diffusion of vacancies is the dominant mechanism (Evans and Wilshire 1985). If diffusion occurs through the bulk, a Nabarro-Herring (N-H) mechanism (Herring 1950) is suggested and the activation energies are typically close to those for lattice self-diffusion. If diffusion occurs along grain boundaries, a Coble creep mechanism (Coble 1963) is suggested and the activation energies are typically close to those for grain boundary diffusion. The activation energy for grain boundary diffusion is typically 0.5-0.6 times that for lattice self-diffusion. Therefore, whenever a stress exponent close to unity is observed, the measured apparent activation energy frequently is used to identify the mechanism. Although, Smith *et al.* (1993) did not measure the activation energy in this regime, the apparent activation energy reported by Woodard and Pollock (1997) for a constant applied stress of  $\sigma = 69$  MPa was 187 kJ/mol, which is lower than that expected for lattice self-diffusion as will be described shortly. In studies of  $\alpha_2 + B_2$  Ti-24Al-11Nb, Mishra and Banerjee (1990) and Smith *et al.* (1993) also obtained low creep exponents,  $n=1$  and  $n=0.9$ , respectively, for stresses below 80 MPa and temperatures between 575-760°C. Mishra and Banerjee (1990) obtained activation energies between 107-120 kJ/mol, which correspond closely to those values obtained for the creep regime considered to be dominated by grain boundary diffusional creep in pure  $\alpha$ -Ti (Malakondaiah and Rao 1981). It is noted that no activation energy values for grain boundary diffusion in  $\alpha$ -Ti are available. Mishra and Banerjee (1990) concluded that the steady-state low-stress regime corresponds to Coble creep and this conclusion was

supported by the lack of significant dislocation activity within the  $\alpha_2$  grains. Earlier works on Ti-25Al-10Nb-3V-1Mo (Cho *et al.* 1990) and Ti-24Al-11Nb (Hayes 1989) did not report a diffusional creep regime and in their work on single-phase  $\alpha_2$ , Mendiratta and Lipsitt (1980) only speculate on the existence of such a domain. A later work on Ti-25Al-10Nb-3V-1Mo (Hayes 1991) did, however, suggest that a diffusional creep regime exists as the creep exponent was unity for stresses below 70 MPa at 760°C. It was also concluded by Mishra and Banerjee (1990) that diffusion along (equiaxed  $\alpha_2$ )-(aged  $\beta$ ) interfaces results in the shape changes leading to creep strain. This finding was based on the relationship between equiaxed  $\alpha_2$  grain size (GS) and the steady-state creep rate as for Coble creep, the steady-state creep rate is proportional to  $GS^{-3}$ . A large decrease in the steady-state creep rate was observed for the super-transus heat-treated microstructure compared with the sub-transus heat-treated microstructures, and the diffusion along (lath  $\alpha_2$ )- $\beta$  interfaces was suggested to be responsible for this. A direct correlation with lath size and strain rate was not attempted due to the difficulties in estimating the grain size of the lath structures. The size of the large prior  $\beta$  grains was not correlated with the strain rate in their work. In summary, the low-stress,  $\sigma < 100$  MPa, creep parameters of both O and  $\alpha_2$ -based alloys suggest that Coble creep is the dominant mechanism, and although the relationship between lath size or prior  $\beta$  grain size and creep rate is not well understood, grain size is suggested to be a significant microstructural parameter.

For Ti-22Al-23Nb, Smith *et al.* (1993) obtained a high creep exponent,  $n \sim 8$ , for stresses between 100-172 MPa. Creep exponent values larger than 3.5 suggest a dislocation climb mechanism is rate-controlling. The creep behavior of the same three-phase O alloy has been examined by Hayes (1996) for  $69 \text{ MPa} < \sigma < 172 \text{ MPa}$  and  $650 < T < 760^\circ\text{C}$ . Hayes reported a temperature compensated creep exponent of  $n = 2.8$ , which is intermediate to those measured for the low-stress and higher-stress regimes of Smith *et al.* (1993). The data taken from Woodard *et al.* (1996) also revealed an intermediate exponent,  $n \sim 2.4$ , for a Ti-21Al-21Nb alloy between 69-172 MPa at 650°C.



It should be noted that an intermediate exponent would be expected had Smith *et al.* (1993) calculated the stress exponent at the intermediate-stress levels, i.e. between 60-100 MPa. Similar behavior is evident for  $\alpha_2$ -based alloys. In studies of Ti-24Al-11Nb, Mishra and Banerjee (1990) and Smith *et al.* (1993) noted a transition in exponent in going from low stresses, where  $n \sim 1$ , to high stresses, where  $n \sim 3.3-5.0$ . In both studies, for the region between 60-200 MPa, an intermediate slope existed. (The exact ranges of intermediate slope depended on the creep temperature.) This is important as a gradual change in slope from  $n \sim 1$  to  $n \sim 3.3-8.0$  indicates that a transition region exists between the diffusion and dislocation-controlled regions. The relatively broad range of stresses within this transition region suggests that another creep mechanism is significantly contributing to the strain rates for applied stresses between the low and high-stress creep regimes. For example, creep exponents close to two have been correlated to a grain boundary sliding mechanism for metals and alloys (Langdon 1970, Crossman and Ashby 1975, Evans and Wilshire 1985). In the transition region between  $n \sim 1$  and  $n \sim 5$ , dislocations were observed to pile-up at (equiaxed  $\alpha_2$ )-(aged  $\beta$ ) boundaries and decrease rapidly towards the center of the equiaxed  $\alpha_2$  grains (Mishra and Banerjee 1990). This would be expected to occur if a grain boundary sliding mechanism, as proposed by Langdon (1970), was significantly contributing. Thus both the microstructural observations of deformed specimens and the measured creep exponents suggest that grain boundary sliding is occurring for intermediate applied stresses. The activation energy for grain boundary sliding has been correlated to the activation energy for lattice self-diffusion (Langdon 1970, Crossman and Ashby 1975, Evans and Wilshire 1985). An activation energy of  $Q_{app} = 327$  kJ/mol for an O alloy within the intermediate stress regime ( $\sigma = 172$  MPa) was obtained by Hayes (1996). This is significantly larger than the activation energy ( $Q_{app} = 187$  kJ/mol) measured by Woodard and Pollock (1997) within the low-stress regime. Therefore the creep parameters obtained by Hayes (1996) suggest that a grain boundary sliding mechanism is active. The creep exponent extrapolated from

Smith *et al.* (1993) is also suggestive of grain boundary sliding. Thus, indications of grain boundary sliding exist for O-based alloys, yet no conclusive evidence based on the deformation behavior has been provided. In addition, the authors of the mentioned works have failed to speculate on the existence of grain boundary sliding. In order to definitively describe the creep mechanisms, especially for applied stresses near  $n$ -transition regions, both microstructural observations of the deformation behavior and calculated creep parameters based on the steady-state creep rate need to be made.

Based on the observed deformation characteristics, where preferential cracking occurred at O/O grain boundaries, Rowe and Larsen (1996) have reported grain boundary sliding for a Ti-25Al-23Nb at 650°C/310 MPa. The strain rate behavior between 310-380 MPa indicated a similar stress exponent,  $n \sim 2.8$ , to that observed by Hayes (1996) and the finer-grained microstructure exhibited worse creep resistance than the super-transus solutionized then aged microstructure. This is expected within a grain boundary sliding regime based on the relationship between grain size and steady-state creep rate,  $\dot{\epsilon}_{ss} \propto G S^{-1}$  projected in grain boundary sliding models (Langdon 1970, Crossman and Ashby 1975, Evans and Wilshire 1985). Within the intermediate-stress regime, Dary *et al.* (1996) have also noted grain boundary sensitivity as severe grain boundary cracking was observed. Grain boundary sliding is sometimes accompanied by grain boundary cracking (Langdon 1970). To the author's knowledge these are the only deformation observations suggesting grain boundary sliding exists for O alloys. In studies of  $\alpha_2$ -based alloys (Mendiratta and Lipsitt 1980, Thompson and Pollock 1991, Albert and Thompson 1991, Smith *et al.* 1993), creep exponents close to two have been obtained for applied stresses between 40-200 MPa at temperatures above 700°C, and grain boundary sliding has been speculated to exist. This along with the observations of Mishra and Banerjee (1990) suggest that a grain boundary sliding mechanism is active for  $\alpha_2$ -based alloys. In addition, for an  $\alpha+\beta$  alloy, Ti-6Al-2Nb-1Ta-0.8Mo, sliding along  $\alpha/\beta$  interfaces, colony

boundaries, and prior  $\beta$  grain boundaries has contributed to the creep strains and rupture process (Miller *et al.* 1987).

Overall, the intermediate-stress,  $100 < \sigma < 380$  MPa, creep parameters and deformation behavior of both O and  $\alpha_2$ -based alloys suggest that grain boundary sliding is contributing to the secondary creep rates, and similar to that noted for the Coble creep regime, grain size appears to be an important microstructural parameter. After considering the data from Smith *et al.* (1993), Woodard and Pollock (1997), Woodard *et al.* (1996), Hayes (1996), and Rowe and Larsen (1996), a more thorough investigation is necessary to confirm the creep mechanisms and/or define the stresses and temperatures of the respective mechanisms in the low-to-intermediate applied stress regimes.

Nandy *et al.* (1993) have examined the high-stress compression creep characteristics of equiaxed, single-phase O microstructures for Ti-27Al-21Nb. They reported a steady-state creep rate, at  $T=650^\circ\text{C}$  and  $\sigma=363$  MPa, of  $\dot{\epsilon}_{ss}=5 \times 10^{-9} \text{ s}^{-1}$ , which is lower than conventional  $\alpha_2$  and  $\alpha_2+\beta$  (Mendiratta and Lipsitt 1980), super  $\alpha_2$  (Hayes 1991), and even some  $\gamma$  (Schwenker and Kim 1995) microstructures. For applied stresses between 240-500 MPa and temperatures between  $650-750^\circ\text{C}$ , the stress exponents obtained were between 5-6. The activation energy obtained was  $Q_{app}=340 \text{ kJ/mol}$ . Accounting for the back stresses, a  $Q_{app}$  equal to  $230 \text{ kJ/mol}$  was obtained. The creep exponents and the relatively high activation energies, representative of lattice self-diffusion, are indicative of a dislocation climb mechanism. In addition, Nandy *et al.* (1995) have found similar creep exponents,  $n \sim 4.3$ , for high stresses applied to lighter O alloys, Ti-27Al-16Nb and Ti-24Al-16Nb. They reported a significant decrease in the creep resistance, and in particular an approximately one order of magnitude increase in steady-state creep rate, with the small decrease in nominal Al content. The measured activation energies,  $Q_{app}=371-376 \text{ kJ/mol}$ , were consistent with the behavior of Ti-27Al-21Nb. In their deformation studies, Nandy *et al.* (1995) have shown a greater density of twins within the O-phase laths for specimens deformed in the high-stress regime. Rowe

and Larsen (1996) reported creep exponents of  $n=5.3$  for Ti-22Al-27Nb between 175-380 MPa at 650°C. For  $\alpha_2$ -based alloys, the calculated creep exponents,  $n>4.3$ , for stresses above 200 MPa and temperatures between 650-760°C, also suggest a dislocation climb mechanism (Mendiratta and Lipsitt 1980, Hayes 1989, Mishra and Banerjee 1990, Cho *et al.* 1990, Thompson and Pollock 1991, Albert and Thompson 1991 1992, Soboyejo *et al.* 1997). The activation energies obtained within this regime have varied from 206 kJ/mol for single-phase Ti<sub>3</sub>Al  $\alpha_2$  microstructures (Mendiratta and Lipsitt 1980), which is close to that of lattice self-diffusion in  $\alpha$ -Ti (Conrad *et al.* 1973), to 324 kJ/mol for  $\alpha_2+\beta$  Ti-25Al-10Nb-3Mo-1V microstructures (Hayes 1991). Although there is some overlap, the generally higher activation energy of O alloys compared with  $\alpha_2$  alloys has been attributed to slower diffusion kinetics resulting from greater Nb concentrations. Thus, the better creep resistance of O alloys compared to  $\alpha_2$  alloys is believed to be partially due to the ternary ordering of the Ti and Nb atoms, see Figures 1.1a and b.

The dislocation structures between the low and high-stress regimes are quite different for  $\alpha_2$  alloys (Mishra and Banerjee 1990). Only very isolated dislocation activity within the equiaxed  $\alpha_2$  grains was observed at low stresses in the Coble creep regime and networks of higher dislocation densities were observed for higher stresses within the dislocation climb regime. The effect of morphology on creep, when dislocation-climb is the rate-controlling mechanism, is expected to be related to effective slip lengths which are dictated by spacing of potential slip barriers such as grain boundaries. This is true for Widmanstätten  $\alpha+\beta$  microstructures, where larger slip lengths lead to worse creep resistance (Eylon *et al.* 1976, Miller *et al.* 1987). In addition,  $\alpha_2+\beta$  lath structures are stronger in both primary and secondary creep than equiaxed structures which have been related to the lower mean-free slip path (Blackburn and Smith 1989, Mishra and Banerjee 1990 1995). The dislocation observations from O alloys within the dislocation climb regime have yet to be reported.

Table 1.1 lists the creep parameters and the testing conditions for the respective O alloys studied. Combining the stress exponent data taken from all the mentioned studies on O alloys, indications of Coble creep are present for stresses below 100 MPa, grain boundary sliding is suggested between 100-360 MPa, and dislocation climb characteristics are present above 360 MPa, with some overlap between regimes. Comparing the activation energy data, within the low-stress regime suggested to be controlled by Coble creep, the lowest activation energy,  $Q_{app}=187$  kJ/mol (see row 15 of Table 1.1), is obtained. Within the dislocation climb regime, the highest activation energies,  $Q_{app}=340-376$  kJ/mol, are obtained. This range corresponds with values which are twice that of the activation energy taken within the low-stress Coble creep regime. Thus the data suggests that the activation energy for grain boundary diffusion is close to 187 kJ/mol and the activation energy for lattice self-diffusion is between 340-376 kJ/mol. Within the intermediate-stress regime, suggested to include grain boundary sliding, an intermediate activation energy is obtained ( $Q_{app}=327$  kJ/mol), which is closer to that expected for lattice self-diffusion than that expected for grain boundary diffusion.

Extrapolation of the measured strain rates does not correlate between the studies. This is expected to be due to the several different compositions and microstructures investigated. In addition, the testing conditions varied. The low-to-intermediate stress work was all performed in tension while the high-stress work on the fully-O microstructure was examined only in compression. Although the effect of the different loading conditions has not been studied, testing in compression may prevent harmful cracking effects and benefit with reduced secondary creep rates. Half of the studies included testing in air environments, while the other half included testing in vacuum or inert environments. Environmental effects on creep of O alloys indicate that higher creep rates are obtained in air compared to an inert environment (Woodard *et al.* 1996, Dary *et al.* 1996). Examination of the post air-crept specimens' surfaces revealed a discontinuous surface oxide scale, approximately 50 $\mu$ m thick, following a 268 hour creep exposure at

760°C. The extent of the scale in the crept specimens was notably larger than that found following static exposure, suggesting a dynamic cracking/scale formation process. This results in a reduction of the load bearing cross-sectional area and higher creep rates. Therefore the creep rates of tests performed in vacuum or argon are expected to be lower than those of tests performed in air.

Table 1.1 Orthorhombic Alloy Testing Conditions and Corresponding Creep Parameters

Alloy Composition (reference)	Heat Treatment	Test Conditions $\sigma$ (MPa)/Temp(°C)	n	Qapp, kJ/mol
Ti-27Al-21Nb (Nandy <i>et al.</i> (1993))	1170°C/OQ + 900°C/AQ	240-500/650-750 air	5-6	340
Ti-24Al-16Nb (Nandy <i>et al.</i> (1995))	1150°C/2.5°C/s + 750°C/AQ	150-540/700-750 air	4.2-4.3	371
Ti-27Al-16Nb (Nandy <i>et al.</i> (1995))	1170°C/2.5°C/s + 750°C/AQ	240-660/700-750 air	4.2-4.3	376
Ti-21Al-22Nb (Smith <i>et al.</i> (1993))	na	30-90/650-760 air	1.4	na
Ti-21Al-22Nb (Smith <i>et al.</i> (1993))	na	90-172/650-760 air	8.2	197
Ti-22Al-23Nb (Hayes (1996))	996°C/1h/AQ	69-172/650-760 air+argon	2.8	327
Ti-21Al-21Nb (Woodard <i>et al.</i> (1996))	na	69-172/650 vacuum	2.4	na
Ti-22Al-23Nb (Woodard and Pollock (1997))	na	69-110/650 air+vacuum	1.3	187
Ti-22Al-27Nb (Rowe and Larsen (1996))	815°C/1hr	310-380/650 argon	5.3	na
Ti-22Al-27Nb (Rowe and Larsen (1996))	1090°C/1h/Ar + 815°C/1h	175-310/650 argon	5.3	na
Ti-25Al-23Nb (Rowe and Larsen (1996))	815°C/1hr	175-310/650 argon	2.8	na
Ti-25Al-23Nb (Rowe and Larsen (1996))	1065°C/1h/Ar + 815°C/1h	310-380/650 argon	2.8	na

AQ: air quench; OQ: oil quench; Ar: cooling performed in static argon gas; na: not available.

### 1.3.2 Tensile Behavior

Compared with the creep literature, studies involving microstructure-tension relations for O alloys have been more numerous (Rowe *et al.* 1991, Rowe 1991 1993a,b,

Gogia *et al.* 1992, Rowe and Larsen 1992, Banerjee *et al.* 1993, Chesnutt *et al.* 1993, Majumdar *et al.* 1994 1995, Smith *et al.* 1994a,b 1995, Popille and Douin 1996, Woodfield 1996, Dary and Pollock 1996, Dary *et al.* 1996, Emura *et al.* 1996, Thomas *et al.* 1996, Popille-Puissochet *et al.* 1997, Boehlert *et al.* 1997a-d). Only a portion of the studies are discussed here. Similar to the creep observations, work on three-phase alloys has noted phase volume fraction effects on RT tension properties (Majumdar *et al.* 1994 1995, Smith *et al.* 1994a,b 1995, Boehlert 1997a). The strength and elongation-to-failure were enhanced by those microstructures containing a greater volume of O and a lesser volume of  $\alpha_2$ , while the B2 content remained relatively constant. In these studies and others (Gogia *et al.* 1992, Boehlert *et al.* 1997b), it was discovered that  $\alpha_2/\alpha_2$  grain boundaries provide crack initiation sites which lead to failure and are detrimental to strength and elongation. In one study (Boehlert *et al.* 1997a), a greater than 2.5 times increase in strain-to-failure was achieved, without loss in strength, by reducing the concentration of  $\alpha_2/\alpha_2$  grain boundaries through post-processing heat treatment. A micrograph taken from that study which shows grain boundary cracking for a Ti-25Al-17Nb specimen is provided in Figure 1.4. Several  $\alpha_2/\alpha_2$  boundaries were cracked and the B2 phase blunted such cracks. A typical fracture surface taken from that study shows the cleaved fracture of  $\alpha_2$ , ductile dimpling in B2, and the rough and faceted fracture of O, see Figure 1.5.

In addition to fracture observations, surface slip traces have also provided useful insight into the deformation behavior. The stress necessary to initiate slip as well as the slip character of each of the three constituent phases differ. O and B2 slip deformation has been suggested to occur prior to  $\alpha_2$  (Akkurt *et al.* 1991). Planar slip has been identified in the  $\alpha_2$  and O phases, while the B2 slip character is wavy (Majumdar *et al.* 1994 1995, Banerjee 1995, Boehlert 1997a). Transmission of slip from the O to the B2 phase has been found whenever O and B2 grains lie adjacent. Slip traces have been shown to transmit from O to B2 to O without deflection as well as to be jogged at B2

laths before transmission back to O (Majumdar *et al.* 1994 1995). This slip compatibility, see Figure 1.6, not evident between  $\alpha_2$ /B2 grains, can be explained by the ORs identified between the O and B2 structures. Banerjee (1995) has found O basal slip occurs on [110](001). B2 deformation, characterized in a two phase  $\alpha_2$ +B2 Ti-24Al-11Nb microstructure (Banerjee *et al.* 1990), consists of  $\langle 111 \rangle \{110\}$  slip, which can be shown to provide sufficient independent slip systems to satisfy von Mises criterion (Akkurt 1990). Banerjee *et al.* (1988) determined that the close-packed planes in O, (001), grow parallel to the close-packed planes in B2,  $\{110\}$ . In addition, the directional relationship observed between the O and B2 phases are  $\langle 111 \rangle_{B2} // \langle 110 \rangle_O$ . Therefore the  $\langle 111 \rangle \{110\}_{B2}$  slip is considered to be readily transmissible to [110](001) O slip and the OR is compatible with the active slip systems observed in the O and B2 structures. Such slip transmissibility is thought to reduce stress concentration effects which are usually heightened at grain boundaries, and this is partially responsible for the reduced cracking in adjacent O+B2 grain boundaries. In the event that cracks develop, the B2 phase has proven to be an excellent crack blunter, see Figure 1.4. Thus due to its wavy slip and ductile dimpling characteristics along with its crack blunting capability, the B2 phase plays a critical role in imparting ductility to O alloys. It is with this respect that B2 provides a unique combination of both strengthening and toughening for O alloys. However, those alloys heat treated above the B2 transus then quenched, which contain fully-B2 microstructures, have proven to be exceptionally strong, yet they exhibit a brittle-type failure representative of low energy intergranular cleavage (Hertzberg 1976) and reach failure strains less than 1 percent (Majumdar *et al.* 1994 1995, Boehlert *et al.* 1997a). Thus by simply increasing the B2 phase volume, elongation-to-failure is not always increased.

Although the  $\alpha_2$  and O structures are quite similar, their deformation characteristics differ significantly. Banerjee (1995) compared deformation of Ti-26Al-21Nb O-based and Ti-27Al-10Nb  $\alpha_2$ -based alloys and reported that all possible  $\langle a \rangle$  and



$\langle c+a \rangle$  O slip systems were active while no  $\langle c+a \rangle$  slip was evident in  $\alpha_2$ . Thereby it was suggested that a lower critical resolved shear stress (CRSS) existed for the  $\langle c+a \rangle$  slip mode in the O structure. In addition the OR existing between the  $\alpha_2$  and O phases does not appear to be favorable for slip transfer. Predominant slip systems in  $\alpha_2$  include  $\langle 1120 \rangle$  dislocations on the prismatic  $\{1010\}$  plane, with very little chance of cross slip onto basal or pyramidal planes. The lack of cross slip is expected to contribute to an increase in stress concentration from dislocation pile-ups at grain boundaries. For the O phase, basal plane slip primarily occurs on  $[100](001)$  (with cross slip onto  $(041)$ ). The primary slip plane for  $[110]$  dislocations is the prismatic  $(110)$ , although  $[110]$  slip also occurs on  $(001)$ . Slip on the pyramidal system  $[114]$  or  $[102]$ ,  $(\bar{2}\bar{2}1)$  is also evident and an extensive amount of cross slip has also been reported for 'c' component dislocations at  $650^\circ\text{C}$  (Banerjee *et al.* 1991, Banerjee and Rowe 1993, Banerjee 1995). Thus a greater number of independent slip systems are active for O compared with  $\alpha_2$ .

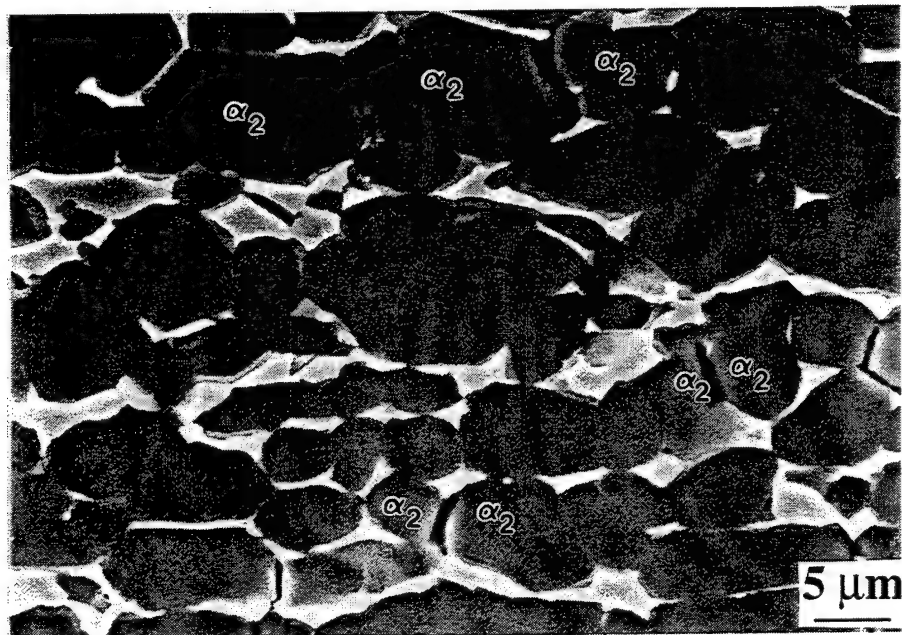


Figure 1.4 Grain boundary cracking between  $\alpha_2$  grains for a RT tensile deformed Ti-25Al-17Nb specimen.

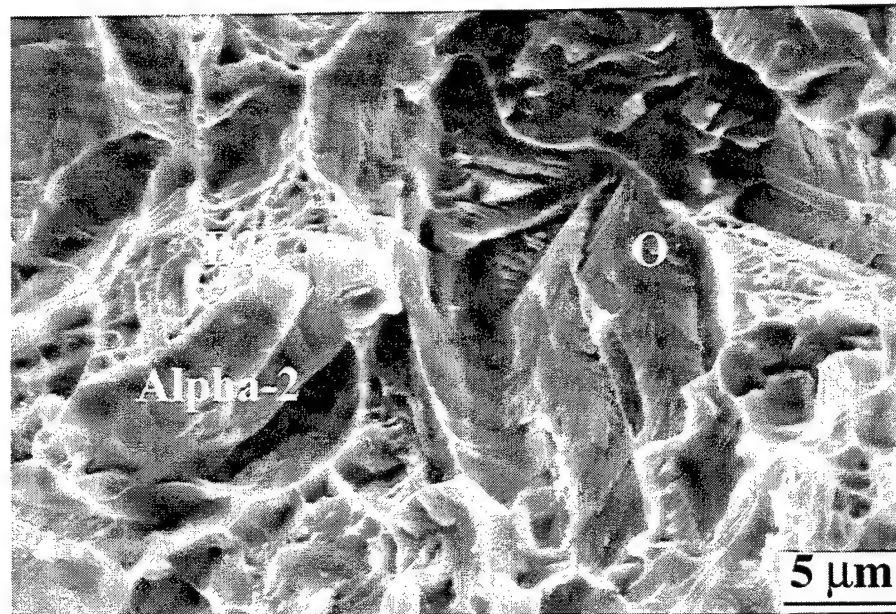


Figure 1.5 RT tensile fracture surface of a Ti-25Al-17Nb specimen showing the fracture characteristics of the constituent phases.

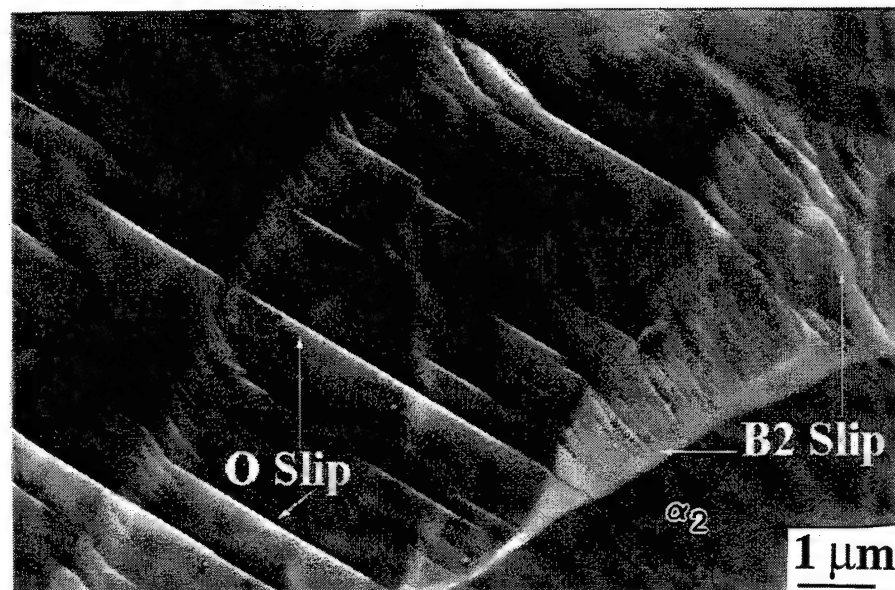


Figure 1.6 Slip compatibility between adjacent O and B2 grains for a RT deformed Ti-25Al-17Nb specimen. Note the wavy slip traces in the B2 phase and lack of slip transfer to the  $\alpha_2$  phase.

The findings of Popille and Douin (1996) contradict those of Banerjee (1995). In their studies of Ti-26Al-21Nb,  $\langle c+a \rangle$  slip was not observed at ambient temperatures and only initiated at 450°C. Only three slip systems were activated at RT, which is at variance from the von Mises criterion which states that five independent slip systems are necessary to allow for deformation accommodation at grain boundaries. In agreement, low tensile fracture strains,  $\epsilon_f < 1\%$ , were reported for the fully-O Ti<sub>2</sub>AlNb alloy (Popille-Puissochet *et al.* 1997). Though there exists discrepancies between these studies, it can be concluded that  $\langle a \rangle$  type slip is evident in the O phase at RT and  $\langle c+a \rangle$  slip is more likely to occur within O than  $\alpha_2$ . In addition, failure strains are quite low in tension for fully-O microstructures.

Other studies have confirmed that fully-O microstructures fail at low strains. In agreement with the failure to meet von Mises criterion, cracks nucleated at O/O grain boundaries (Boehlert *et al.* 1997c). Rowe (1991) reported poor RT fracture toughness, on the order of 6 MPa $\sqrt{m}$ , and elongation for a single-phase O Ti-28Al-24Nb microstructure. The associated fracture surfaces exhibited cleaved O grains. Thus similar to  $\alpha_2$ -dominated microstructures, O-dominated microstructures exhibit poor ductility, indicating the presence of the BCC phase is necessary for practical engineering use of such alloys. Both the RT strains-to-failure and toughness values of O alloys are dependent on the volume of BCC phase present. Similar to the observations on three-phase microstructures, for two-phase O+B2 microstructures the B2 phase blunts cracks formed at O/O boundaries and slip traces are transmitted between O and B2 grains (Boehlert *et al.* 1997c,d). It has been observed that O+B2 alloys containing greater than 15 volume percent B2 possess adequate RT strength and strain-to-failure, although this comes at the expense of significantly reduced creep resistance compared with those microstructures containing less B2 and more O (Boehlert *et al.* 1997c). This is in agreement with the review by Banerjee *et al.* (1993), indicating O+B2 alloys containing less than 25 Al and greater than 25 volume percent B2 show significant increases in RT

strength, strain-to-failure, and fracture toughness, with a corresponding loss in creep resistance. Such observations magnify the importance of controlling the BCC content with respect to microstructural optimization of these alloys. It was also mentioned that those nominal compositions of greater than 25 Al suffer from poor ductility and associated difficulties in processing (Banerjee *et al.* 1993). Thus controlling the Al content is also important for achieving ductility in O alloys. In addition to Al levels, interstitial oxygen contents significantly influence both ductility and processability. Wojcik *et al.* (1996) found that Ti-22Al-26Nb had poor fabricability at RT due to high levels of oxygen (1100-1500 ppm). However at 880 ppm this alloy was fabricable. Thus Al contents greater than 25at.% and oxygen contents greater than 880 ppm are unfavorable for ductility and fabricability of O+BCC alloys. Overall, the RT properties of O+BCC alloys are quite sensitive to chemistry and microstructure.

When the chemistry and microstructure are controlled, second-generation O+BCC alloys of close to a Ti<sub>2</sub>AlNb composition, which corresponds to a density of  $\rho \sim 5\text{g/cm}^3$ , exhibit higher specific tensile strengths than the lighter  $\alpha_2$ -based and first-generation O alloys. Table 1.2 lists the RT tensile properties for several first and second-generation O alloys. Rowe (1991, 1993a,b) has investigated the RT tensile and fracture toughness properties for a series of second-generation O+BCC alloys ranging in Al (21-28at.%) and Nb (20-27at.%) contents. The microstructures contained BCC volumes from 0-50%. Though Rowe has not reported the detailed characteristics of each microstructure with respect to phase volume fraction, composition, and morphology, the results suggest that those alloys containing an adequate amount of BCC are tougher at RT, yet deform more readily at elevated temperatures compared to their single-phase O counterparts. In his quaternary investigations, Rowe (1993) discovered that small additions (up to 5at.%) of vanadium (V), a beta stabilizer, on a Ti-22Al-20Nb alloy have provided RT strains-to-failure of up to 19%, see row 7 of Table 1.2. Another O+BCC alloy, Ti-22Al-27Nb, exhibited RT elongations greater than 3% and fracture toughnesses up to 27.5 MPa $\sqrt{\text{m}}$ .

In other studies of this alloy (Rowe *et al.* 1991, Chesnutt *et al.* 1993), the reported ultimate tensile strength was as high as 1415 MPa and associated strains-to-failure were near 3.6%, see row 15 of Table 1.2. Of all the near Ti<sub>2</sub>AlNb alloys investigated, the Widmanstätten O+BCC Ti-22Al-27Nb microstructure has been reported to have the best balance of tensile, creep, and fracture toughness properties (Rowe *et al.* 1991). In addition, the stability of this alloy was also good as long-term aging led to higher elongations with a small debit in strength. Other studies have also recorded attractive RT elongations, strength, and fracture toughness for alloys of nominal compositions near Ti-22Al-27Nb (Woodfield 1996, Thomas *et al.* 1996). It is for this reason that second-generation O+BCC alloys based on Ti-22Al-27Nb are being considered for aerospace applications. The beneficial properties of this alloy are depicted in the bar chart taken from Rowe (1993b) listing the creep, RT fracture toughness, and RT tensile properties for several Ti-Al-Nb alloys, see Figure 1.7. In addition, ternary alloys containing more Nb and less Al, which exhibit higher BCC-phase volumes, show increased strains-to-failure with a relatively small loss in strength, see row 19 of Table 1.2. In fact, a Ti-15Al-45Nb Nb-based alloy has shown an excellent balance of RT and elevated-temperature properties and is also drawing increased interest (Austin *et al.* 1992).

The following summarizes the important aspects discussed for the tensile behavior of O alloys. Grain boundaries are the locus of damage. It has been well established that  $\alpha_2/\alpha_2$  and O/O boundaries are preferred sites for crack nucleation, which has been explained by the limited number of slip systems in the  $\alpha_2$  and O structures and the high stress concentrations at grain boundaries. As a result, single-phase O microstructures suffer from poor RT ductility and intergranular failure is evident. Significant RT property improvements can be obtained by altering the microstructure. Heat treatment of three-phase alloys to reduce the number of  $\alpha_2/\alpha_2$  grain boundaries has been shown to increase strain-to-failure by greater than 2.5 times without loss in strength. The B2 phase is vital for achieving adequate RT ductility due to its tendency to cross-

slip, dimple, and blunt cracks. BCC volumes greater than 15% significantly increase RT strength and strain-to-failure in two-phase O+BCC alloys. Though larger BCC phase volumes have provided enhanced RT tensile properties for sub-transus microstructures, super-transus microstructures are susceptible to intergranular cracking which results in RT tensile elongations on the order of 1 percent. Alloy chemistry is also important for RT ductility. Those alloys containing greater than 25at.% Al and 880 ppm interstitial oxygen suffer from lower strains-to-failure. Higher Nb and lower Al contents provide greater strains-to-failure primarily due to increased BCC volumes. Overall, similar to three-phase O alloys, the RT tensile properties of two-phase O+B2 alloys are extremely sensitive to composition and microstructure.

Table 1.2 Orthorhombic Alloy RT Tensile Properties

Alloy Composition (reference)	Heat Treatment	0.2% YS (MPa)	UTS (MPa)	$\epsilon_f$ (%)
Ti-23Al-16Nb (Boehlert <i>et al.</i> (1997a))	1050°C/1h/WQ + 850°C/2h/FC	691	906	14.0
Ti-22Al-23Nb (Smith <i>et al.</i> (1995))	1050°C/2h + 815°C/8h/FC	836	1111	14.8
Ti-23Al-23Nb (Dary and Pollock (1996))	760°C/100h	472	638	4.0
Ti-22Al-20Nb-5V (Rowe (1993b))	815°C/24h + 760°C/100h	900	1161	18.8
Ti-22Al-24Nb (Rowe (1993b))	815°C/4h	1257	1350	3.6
Ti-22Al-25Nb (Rowe <i>et al.</i> (1991))	1000°C/1h/Ar + 815°C/2h/Ar	1245	1415	4.6
Ti-22Al-25Nb (Rowe <i>et al.</i> (1991))	1125°C/1h/BC + 815°C/2h/Ar	1134	1175	0.9
Ti-22Al-27Nb (Rowe <i>et al.</i> (1991))	815°C/1h/Ar	1294	1415	3.6
Ti-25Al-21Nb (Rowe <i>et al.</i> (1991))	1050°C/1h/Ar + 815°C/2h/Ar	847	881	0.4
Ti-15Al-45Nb (Austin <i>et al.</i> (1992))	1050/4h + 800°C/24h	865	924	15.1

WQ: water quench; FC: furnace cool; Ar: cooling performed in static argon gas; BC: brick cooled (1.5°C/sec); na: not available.

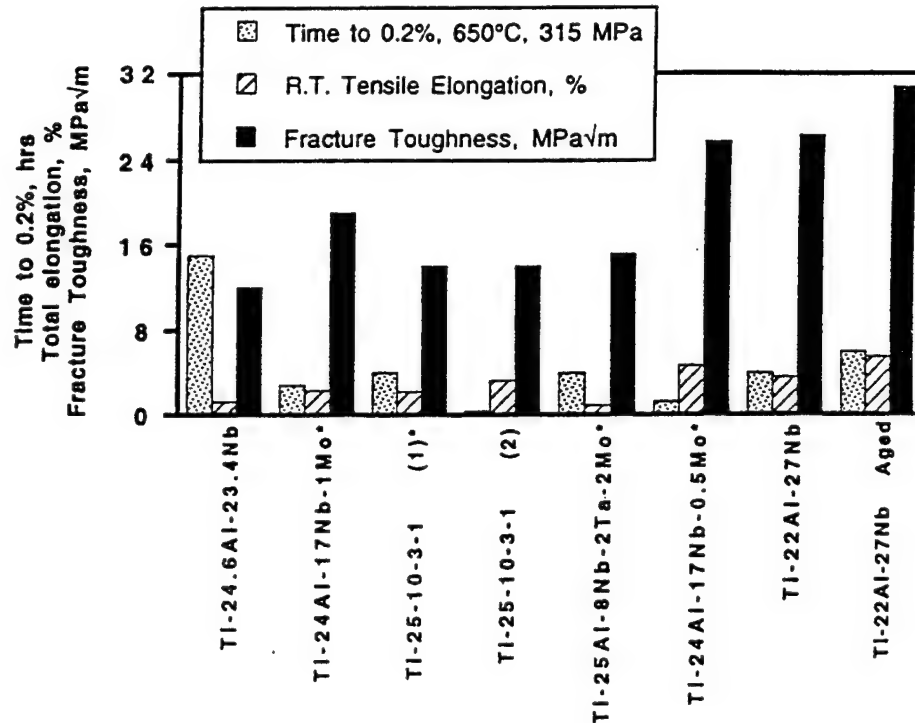


Figure 1.7 A bar chart taken from Rowe (1993b) depicting the elevated-temperature creep, RT fracture toughness, and RT tensile properties as a function of nominal alloy composition.

#### 1.4 Deficiencies in Understanding

Prior to beginning the work presented in this technical report, several deficiencies in our knowledge of the phase evolution, creep, and tensile behavior of O alloys were recognized. Some of the deficiencies pertaining to the work at hand are now mentioned.

##### 1.4.1 Phase Evolution

The ternary phase diagrams of alloys containing constant Al = 22, 25, and 27at.% with varying Ti and Nb have been determined experimentally (Muraleedharan 1995, Sagar *et al.* 1996, Miracle and Rhodes 1996). However, the temperatures of several phase boundaries remain questionable. For example no data has verified the  $\alpha_2$ +B2+O field for Nb compositions above 20at.%. By determining the range of temperatures of this three-phase field, the lower-temperature border of the  $\alpha_2$ +B2 field and the upper



border for the O+B2 field would be affixed. In addition the lower temperature O+ $\beta$  field is poorly understood. In particular, the temperature at which the composition induced disordering of the B2 phase occurs is unknown. A second deficiency, in terms of phase diagrams, is the lack of development of the pseudobinary diagram based on Ti=50at.%. Bendersky *et al.* (1991) initiated this work over 6 years ago, yet to the author's knowledge no work has been performed in this area since. The development of this diagram would be useful for determining the temperature ranges of the phase regimes associated with higher Nb-containing O+BCC alloys.

A third poorly understood issue is related to the decomposition of the B2 phase. The range of temperatures for the Widmanstätten precipitation, discontinuous precipitation, and composition invariant transformation modes has not been determined as a function of the solutionized, starting microstructure. These transformation modes significantly affect the microstructure and are therefore expected to profoundly influence the mechanical behavior of O+BCC alloys. For this reason the different transformation modes should be well-characterized for both sub-transus and super-transus solutionized microstructures. In addition, the discontinuous precipitation at B2 grain boundaries has not yet been well characterized in terms of its temperature and phase composition dependence as well as the resulting structures of the BCC phase.

#### 1.4.2 Creep Behavior

There are numerous deficiencies in our knowledge of the creep behavior of O alloys. Only some of these will be touched on here.

The BCC structure, due to its relatively open nature, is expected to be the least creep resistant of the three constituent phases. However, creep data for fully-BCC microstructures is not available. With respect to modeling, the creep data of fully-BCC microstructures could be used to represent the constituent behavior of the BCC phase. A fortuitous challenge in characterizing the BCC phase creep behavior, however, is



obtaining stable fully-BCC microstructures at projected creep temperatures. Based on the pseudobinary diagram of Bendersky *et al.* (1991), relatively high Nb and low Al contents are necessary to obtain stable fully-BCC microstructures at projected creep temperatures. It is possible that ternary alloys, containing a majority of Ti, are incapable of exhibiting fully-BCC microstructures near 650°C.

Although fully-BCC microstructures' creep data is lacking, data is available for BCC-dominated microstructures which contain a small volume of O platelets. This data has depicted the surprisingly good creep resistance of high-niobium containing alloys such as Ti-15Al-45Nb and Ti-10Al-50Nb (Austin *et al.* 1992). To date, however, investigations of such alloys have primarily been focused on oxidation resistance. Microstructure-creep relations are lacking. Careful examination of such alloys would provide useful insight into the microstructure-creep relations for O+BCC alloys containing a majority of the BCC phase. This information could also be used to aid in understanding the effect of O-phase precipitation on creep rates.

It was clear at the time this work was commenced that alloy development had preceded any definitive understanding of creep-microstructure relations in O alloys. To date the studies reporting creep parameters have been performed on a variety of O-alloy compositions and microstructures, and an accurate description of the creep mechanisms active and the stress and temperature ranges in which they are dominant is lacking. It would be useful to study the creep mechanisms of the low-to-intermediate-to-high stress regimes for one alloy composition and microstructure. In order to understand creep-microstructure relations, other microstructures could then be examined for the same alloy. The understanding gained from mechanistic studies could then be applied to understanding microstructure-creep relationships.

The number of microstructural parameters (including nominal composition, phase composition, phase volume fraction, phase morphology, and grain size) potentially affecting the creep response is large and this number is further multiplied by the several

constituent phases which may be present, making the creep-microstructure relationship quite complicated. Because the rate-controlling creep mechanisms are generally related to certain microstructural features, creep mechanistic studies are expected to aid the identification of microstructure-creep relationships. For example, Coble creep is related to the stress-directed diffusion of vacancies along grain boundaries. Thus Coble creep is a strong function of grain size. A clear understanding of the creep mechanisms could expose certain microstructural features and facilitate the understanding of microstructure-creep relationships.

Without establishing the mechanisms it is quite difficult to make a fair comparison between the O-based and  $\alpha_2$ -based alloy systems. In particular it is unfair to rank the two systems based solely on the data taken from separate studies of fully-O (Nandy *et al.* 1993) and fully- $\alpha_2$  microstructures (Mendiratta *et al.* 1988), where the testing conditions (i.e. temperature, stress, tension/compression) differed. It is noted that differences caused by tension and compression creep environments have yet to be firmly established. Some difficulties are evident with regard to determining the creep mechanisms. Difficulties arise partly from a lack of diffusion data on the O phase, in particular the activation energies of lattice and grain boundary diffusion. The creep data indicates a wide range (187-376 kJ/mol) of apparent activation energies, and knowledge of the diffusional data as well as the creep exponent in which the constant stress tests were performed would be useful for understanding the scatter in the  $Q_{app}$  data. Other difficulties include properly characterizing the transition between regimes, which generally requires carefully selected creep temperatures and applied stresses and proper characterization of the deformation.

The relative effects of microstructural instability caused by testing in the O+BCC or O fields have yet to be firmly established. Environmental effects have also not been systematically studied, especially with respect to nominal alloy content.

Lastly, microstructural evidence from deformed specimens has been lacking, including dislocation observations within the dislocation creep regime. No work has been attempted to verify the existence or non-existence of a grain boundary sliding regime. In most cases this regime has been ignored or only speculated to exist for both O and  $\alpha_2$ -based systems. A clear description of the deformation behavior would be helpful to both characterize the creep mechanisms and understand microstructure-creep relations.

#### 1.4.3 Tension Behavior

O alloys have shown excellent elevated-temperature creep resistance, especially in super-transus processed and/or heat-treated conditions (Rowe *et al.* 1991, Rowe 1991 1993 a,b, Woodfield 1996). However, these microstructures generally contain large prior B2 grains, which are difficult to refine without sub-transus working, and preferential cracking results at such grain boundaries (Rowe 1991, Gogia *et al.* 1992, Majumdar *et al.* 1994 1995, Woodfield 1996, Boehlert *et al.* 1997c). Comparing rows 11 and 13 of Table 1.2, higher elongations are exhibited by solutionizing below the B2 transus. The poor ductility of super-transus solutionized microstructures has been suggested to be a result of grain boundary precipitation of  $\alpha_2$  and/or O which induces low-energy intergranular fracture. Such microstructures are also deleterious in a fatigue environment where fatigue cracks nucleate and grow along the prior B2 grain boundaries (Luetjering *et al.* 1997). In addition, discontinuous precipitation has been discovered at prior B2 grain boundaries during aging/creep conditions, which may further deter RT ductility and toughness (Bendersky *et al.* 1991, Rowe 1991, Rowe and Larsen 1996, Rhodes 1997, Boehlert *et al.* 1997c). In terms of RT ductility, grain boundary precipitation and microstructural stability remain to be threatening issues. A better understanding of this behavior including characterization of the precipitating structures would be useful.

Ternary alloying studies have shown that oxidation resistance decreases with decreasing Al content (Austin *et al.* 1992). Although literature on post-creep ductility is scarce, this appears to be another threatening issue as intermediate temperature exposures (760°C/100h) in air have embrittled surface regions of a Ti-22Al-23Nb alloy, resulting in low strains-to-failure (Dary and Pollock 1996, Dary *et al.* 1996). In addition, edge cracking has resulted after cooling for a 900°C/500h exposed Ti-22Al-25Nb alloy (Kumpfert and Leyens, 1997). The effect of long-term aging on RT ductility and post-creep ductility are issues yet to be systematically studied.

The effect of interstitial contents on the tensile behavior has also not been systematically characterized. This is important as a wide variety of interstitial levels are present in Ti alloys depending on the purity of the starting materials and the processing techniques. It is especially challenging to control the interstitial oxygen level and maintain homogeneous materials of a relatively large scale.

It has been indicated that B2 contents greater than 15 volume percent provide good RT strength and elongation. In addition, alloys containing high Al contents are suggested to be brittle. Thus both Al content and B2 volume fraction are important microstructural parameters. The RT properties of microstructures containing high Al content and high B2 volume have yet to be reported. Investigation of such microstructures may point to which variable is more critical.

The constituent tensile properties of fully-BCC microstructures for ternary alloys, containing a majority of Ti, have not been reported. In addition, the effect of O-phase precipitation on the tensile properties of BCC-dominated microstructures, which contain low Al and high Nb contents has not been studied.

Lastly, a systematic study of microstructure-property relations for isothermal tension of O alloys has yet to be conducted and the individual influences of the  $\alpha_2$ , B2, and O phase volume fractions and morphologies have yet to be determined. In particular, the effect of phase morphology on the tensile response is also not well understood.

## CHAPTER 2

### OBJECTIVES AND APPROACH

This chapter concisely lists the objectives and describes the approach taken to accomplish the objectives. The hypothesis of this work was that it is possible to control the creep and tensile behavior of O+BCC alloys through microstructural modification.

#### 2.1 Objectives

This work was initiated due to the lack of understanding of microstructure-property relationships for O alloys. Past results indicate potential benefits, including higher RT strength and elongation and higher elevated-temperature creep resistance, of two-phase O+BCC alloys in preference to three-phase alloys which contain the  $\alpha_2$  phase. However, previous studies have not rigorously addressed the effect of phase evolution and stability on microstructure-property relationships, nor the extent and effect of grain size and phase volume and morphology on properties. In addition to the enhanced mechanical properties, two-phase O+BCC microstructures are attractive in terms of studying the effects of the microstructural features on the mechanical properties because the absence of a third phase allows easier interpretation. This work was intended to be a systematic study of O+BCC alloys which would provide a definitive understanding of the microstructure-creep and microstructure-tension relationships for O alloys. Special emphasis was placed on determining the microstructure-creep relationships as this was determined to be the primary focus of this work. The overall objectives of this work were to:

- (i) understand and characterize the phase evolution of O+BCC alloys,
- (ii) understand the effects of nominal composition, phase volume fraction, morphology, and grain size on creep and RT ductility of two-phase O+BCC alloys, and
- (iii) understand and characterize deformation mechanisms in two-phase O+BCC orthorhombic alloys.

## 2.2 Approach

To accomplish the objectives, a set of three alloy compositions within the two-phase O+BCC regime were chosen. In order to accurately distinguish phase volume fraction and morphology effects, phase composition (which can have a pronounced effect on lattice ordering, lattice parameter size, vacancy content, valence, and ultimately slip behavior) must remain constant. Thus, to eliminate phase composition as a variable, the alloys were chosen along a constant Ti tie-line and contained varying Al/Nb ratios. The tie-line chosen, Ti=50at.%, contains several alloys which have been identified as potential candidates for aerospace application. In particular, second-generation O alloys close to Ti-23Al-27Nb are being considered due to their attractive mechanical properties. The nominal compositions of the alloys chosen were Ti-25Al-25Nb, Ti-23Al-27Nb, and Ti-12Al-38Nb. Two compositions of interest, Ti-25Al-25Nb and Ti-23Al-27Nb, lie near the single-phase O and two-phase O+BCC borders at 900°C, see Figure 1.2. Phase equilibria studies (Rowe *et al.* 1993) indicate that such compositions provide a small volume fraction of B2 (< 20%) along with a dominant volume fraction of O at projected use temperatures. The Ti-25Al-25Nb alloy was chosen in order to characterize the constituent behavior of the O phase as fully-O microstructures are achievable. The Ti-23Al-27Nb alloy was chosen to characterize the behavior of O+BCC microstructures containing a small volume (<20%) of BCC phase within an O-phase matrix. The other

alloy, Ti-12Al-38Nb, lies within the single-phase BCC border at 900°C, see Figure 1.2. This alloy was chosen in order to characterize the constituent behavior of the BCC phase as fully-BCC microstructures are achievable.

The work was divided into three major components including processing, heat treatment and microstructural characterization (phase evolution), and mechanical behavior characterization (creep and RT tension behavior).

A considerable effort was placed on developing the desired processing methodology, which is described in Chapter 3. The degree of homogeneity and the flexibility of changing the post-processed microstructures are strongly dependent on the processing steps. Typically, super-transus processing favors Widmanstätten microstructures containing O-phase precipitates, which develop during the cooling cycle, within transformed B2 grains. It is difficult to obtain equiaxed primary O grains without working within the sub-transus regimes. Sub-transus processed alloys typically contain equiaxed morphologies which may then be altered through post-processing heat treatments. The disadvantages of sub-transus processing are: (i) it is difficult to obtain a high degree of homogeneity without a large amount of hot-working, and (ii) the material is harder to work primarily due to the higher flow stresses at lower temperatures. Despite the recognized difficulties with sub-transus processing, the processing temperatures were targeted below the B2-transus in order to allow flexibility in controlling resultant microstructures. In the case of the Ti-12Al-38Nb alloy, the processing conditions, which resulted in equiaxed, homogeneous microstructures for similar alloy compositions, were adopted from Austin *et al.* (1992). However, as described in the phase-evolution results section, the processing temperatures remained above the transus. In addition, one of the near Ti<sub>2</sub>AlNb alloys was intentionally processed at super-transus temperatures as described in the induction-heating procedures sub-section of Chapter 3.

Following processing, the alloys were heat treated to obtain selected microstructures, which included fully-O and fully-BCC microstructures. The intent was

to isolate the effect/influence of phase volume fraction, morphology, and grain size. In order to evaluate phase volume fraction effects, O+BCC microstructures of similar morphologies and grain sizes and different phase volume fractions were intended. In order to evaluate morphological effects, O+BCC microstructures of similar phase volume fractions and grain sizes and different morphologies were intended. In order to evaluate grain size effects, O+BCC microstructures of similar phase volumes and morphologies and different grain sizes were intended. Careful preparatory and analytical techniques, which are described in Chapter 3, were used to characterize the microstructures. Prior to undertaking this study, some important issues pertaining to the achievability of certain microstructures were recognized. The fully-BCC microstructure was not evaluated in creep because the range of creep temperatures chosen were within the O+ $\beta$  field as explained in the Ti-12Al-38Nb phase evolution sub-section of Chapter 4. This problem was highlighted in a sub-section of Chapter 1, which was devoted to the deficiencies in our knowledge of the creep behavior of O alloys. Thus only O+BCC microstructures, containing a majority of the BCC phase, were achievable at the creep temperatures chosen. In addition, one of the reported Ti-23Al-27Nb microstructures was heat-treated within the  $\alpha_2$ +B2 regime and because the  $\alpha_2$  phase transforms quite slowly at lower temperatures, as described in the phase evolution aging study sub-section of Chapter 4, metastable  $\alpha_2$  phase remained in this microstructure. Though it contained three-phases, this microstructure was included in the results because it offered a more complete description of the microstructure-property trends.

After obtaining the desired microstructures, the mechanical behavior of the alloys was characterized. The creep behavior was evaluated over a wide range of temperatures and stresses. In order to allow for diffusion controlled creep processes, the temperature range 650-760°C was chosen. This also corresponds to the uppermost range of temperatures targeted for structural applications of these alloys in both monolithic and composite forms. Based on a melting temperature ( $T_m$ ) of 1700°C (1973K), creep



temperatures between 650-760°C represent 0.47-0.52T<sub>m</sub>. Typically diffusional creep processes are not active below 0.4-0.5T<sub>m</sub>. Therefore the tests were performed in the range of temperatures where significant contributions from diffusion controlled creep are thought possible. A large applied stress range, 35-450 MPa, was chosen for the creep experiments. Based on the literature, this stress range encompasses three potential creep mechanisms. A majority of the experiments were performed within the low-to-intermediate stress range as this has been identified as the region of intended application for these alloys in both monolithic and composite forms. Selected specimens, examined within this region, were scribed with fiducial scratches in order to identify grain boundary sliding from surface observations. In an attempt to equilibrate the microstructures prior to creep experimentation, aging steps were performed within the range of creep temperatures selected. Some specimens were not aged to determine the effects of microstructural instability on creep. In addition, selected creep experiments were performed in compression to identify differences in creep behavior for tensile and compressive loadings. Although works on primary-creep mechanisms are available, a majority of the well-established theories on creep mechanisms are based on the secondary-creep regime. Due primarily to the larger knowledge base and more easily distinguishable deformation characteristics representative of the secondary-creep regime, the work was concentrated on understanding the secondary-creep mechanisms.

The tension testing was performed at a constant strain rate to eliminate strain-rate effects. In order to understand the deformation behavior in both RT tension and elevated-temperature creep, emphasis was placed on properly analyzing deformed specimens. Such techniques, described in the characterization methods section of Chapter 3, included TEM. Established models were used to aid in the understanding of microstructural effects on the tension and creep behaviors.

### 2.3 Summary

The work described in this report was an attempt to explore the phase evolution and microstructure-property relationships for near  $\text{Ti}_2\text{AlNb}$  and  $\text{Ti-12Al-38Nb}$  alloys. The primary objective of using such understanding was to develop appropriate microstructures for both monolithic alloys as well as O-based TMCs. The understanding is important for tailoring microstructures in such two-phase O+BCC alloys for obtaining a balance of matrix-influenced properties such as RT tension and high-temperature creep. The phase evolution, which plays a significant role in terms of the thermodynamic stability of the microstructure and the mechanical behavior, is discussed in detail. Emphasis is placed on microstructural transformations occurring at creep temperatures and their effect on mechanical behavior. Stress exponents, activation energies, and deformation behavior are used to understand creep mechanisms and important microstructural features. This work is also intended to describe the opportunities and limitations of using processing and heat-treatment schedules for obtaining stable microstructures that contain different phase volume fractions, morphologies, and grain sizes.

The procedures used for processing, heat treatment, experimentation, and characterization are described in detail in Chapter 3. Chapters 4 and 5 provide the experimental results and the analysis and discussion of the results, respectively. Chapter 6 summarizes this research and lists the areas of remaining uncertainty. Chapter 6 also provides assessment for the understanding that has been gained in terms of future directions of both alloy development and microstructure-property relationships.

## CHAPTER 3

### EXPERIMENTAL METHODS

This chapter deals with the experimental techniques employed in this work. It describes the procedures used for the thermomechanical processing, heat treatments, and experimental testing. It also describes how the heat-treated and tested samples were analyzed, which involved optical microscopy (OM), scanning electron microscopy (SEM), X-ray diffraction (XRD), and TEM techniques. A significant effort of this work was concentrated on processing ingot materials. Based on the limited literature available on processing of O alloys (Austin *et al.* 1992, Semiatin and Smith 1995, Woodfield 1996, Wojcik *et al.* 1996), conservative conventional thermomechanical processing techniques comprising non-isothermal forging and pack rolling were chosen. In addition, one alloy was processed using an induction heater. The processing methods section describes the processing steps used to break down the ingot structure. The material preparation and characterization method's sections describe the methods used to shape and heat treat the specimens as well as characterize the microstructure and mechanical behavior.

#### 3.1 Processing Methods

The alloys chosen for this study were grouped into two categories: near Ti<sub>2</sub>AlNb and Ti-12Al-38Nb. The target compositions of the near Ti<sub>2</sub>AlNb alloys were Ti-25Al-25Nb and Ti-23Al-27Nb. All the starting materials of this work were melted ingots, which were supplied in two sizes. The larger ingots consisted of long (175-500 mm) cylinders of approximately 75 mm diameter and the smaller ingots measured approximately 150 mm in length by 30 mm diameter. Because the shape of the smaller

ingots resembled that of a cigar, the term used to describe this casting is "cigar melt." The cigar melts were melted at the Wright Laboratory Metals and Ceramics Division of Wright-Patterson Air Force Base, Dayton, Ohio. The large near  $\text{Ti}_2\text{AlNb}$  ingots were melted at Duriron Metals Inc., Dayton, Ohio. The large Ti-12Al-38Nb ingot was melted at Pittsburgh Materials Technology Inc., Large, Pennsylvania. The techniques used to form these ingots consisted of "induction-skull" melting and/or vacuum arc remelting.

The intent of the processing study was to initially acquire three cigar melts each of  $\text{Ti}_2\text{AlNb}$  composition and systematically alter the processing parameters in order to understand processing-microstructure relations before attempting large-scale deformation on the larger castings. A summary of the initial processing work on the three cigar melts will be provided in this section, while a detailed description of the work can be found in Boehlert *et al.* (1997c).

### 3.1.1 Forging and Rolling Procedures

Three 300 gram cigar-melts were triple-melted using a Crystallox® vacuum induction melter. The heats were formulated using elemental Ti, Al, and Nb according to the stoichiometric mixture  $\text{Ti}_2\text{AlNb}$ . Following melting, the ingots were cut by a wire electron discharge machine (EDM) to a rectangular geometry, measuring 125 mm x 25 mm x 20 mm, and coated with high-temperature glass for lubrication and protection from the environment. They were then sealed in 6 mm thick stainless steel cans and unidirectionally forged according to a 2:1 ratio from 25 mm to 12.5 mm in air at a rate of 150 mm/min. Preheat treatment of the ingots included an isothermal soak at 1050°C for 15 minutes followed by a 1000°C soak for 2 minutes prior to forging. After forging, the pancakes were slowly cooled in vermiculite. The cans were weld repaired, re-evacuated and sealed at RT, then subjected to different preheat treatments prior to subsequent rolling. Rolling operations were chosen in order to input more work into the forged pancakes and further homogenize the microstructures. As a result of the rolling

operation, a significantly longer workpiece was obtained. Figure 3.1 compares the sizes of the resulting forged and forged and rolled cigar-melted ingots.

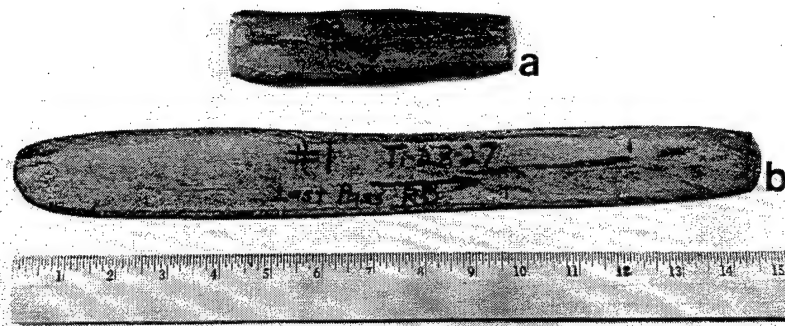


Figure 3.1 Size comparison of the (a) forged and (b) forged and rolled  $\text{Ti}_2\text{AlNb}$  cigar-melted ingots.

The rolling procedures for each  $\text{Ti}_2\text{AlNb}$  pancake (labeled A, B, and C) are given in Table 3.1. Three different heat-treatment and rolling schemes were chosen to produce a range of microstructures. The heat treatments consisted of low-temperature (A), intermediate-temperature (B), and high-temperature (C) exposures. Preheat treatment of pancake A consisted of an isothermal soak at  $815^\circ\text{C}$  for one hour followed by a  $1000^\circ\text{C}$  soak for 15 minutes prior to rolling. Preheat treatment of pancake B consisted of an isothermal soak at  $1040^\circ\text{C}$  for one hour followed by a  $1000^\circ\text{C}$  soak for 15 minutes. In an attempt to homogenize the microstructure, pancake C received a 24 hour homogenization treatment at  $1200^\circ\text{C}$ , well above the B2 transus temperature. This was followed by the same preheat treatment schedule as that of pancake B prior to rolling. Prior to finishing all the rolling passes, each of which resulted in an approximately 10% reduction in thickness, pancakes B and C were annealed at  $1060^\circ\text{C}$  for 30 minutes and then reheated at  $1000^\circ\text{C}$  for 15 minutes before continuing the remaining rolling passes. The rolling was

performed on a cold die and therefore after each pass the pancakes were reheated at 1000°C for 2-3 minutes. A qualitative assessment of the effect of the rolling preheat treatment and the intermediate annealing steps is shown in Figures 3.2, which depicts the three as-rolled sheets. Note that the greatest amount of edge cracking was exhibited by the sample which underwent the most severe rolling preheat treatment (1200°C/24h).

Table 3.1 Rolling Procedures and Parameters for the Ti<sub>2</sub>AlNb cigar-melted Ingots

<b><u>Ingot</u></b>	<b><u>A</u></b>	<b><u>B</u></b>	<b><u>C</u></b>
Preform	Forged (50%)	Forged (50%)	Forged (50%)
Can Dim,* (mm <sup>3</sup> )	140 x 60 x 12	122 x 66 x 12	150 x 66 x 12
Homogenization Treatment	-	-	1200°C/24h
Rolling-Preheat	815C/1h/1000C/0.25h	1040C/1h/1000°C/.25h	1040°C/1h/1000°C/.25h
Interpass Reheating	1000°C/2-3min	1000°C/2-3min	1000°C/2-3min
Intermediate Anneal	-	1060°C/.5h/1000°C/.25h	1060°C/.5h/1000°C/.25h
Reduction per Pass	10%	10%	10%
Roll Speed, (m <sup>2</sup> /min)	2.3	2.3	2.3
Can Dim, (mm <sup>3</sup> )	412 x 64 x 3	391x 66 x 3	419 x 74 x 3
Sheet Dim,**(mm <sup>3</sup> )	381 x 46 x 2.7	353 x 48 x 2.8	389 x 50 x 2.8

\* After forging, the cans were weld repaired, reevacuated, and sealed for use in rolling.

\*\*All rolled sheets were reheated at 1000°C for 3 minutes and then cooled slowly in vermiculite (~3°C/minute).

Figures 3.3a-c depict the as-rolled microstructures of each of the sheet materials. The largest oxygen pick-up was measured for sheet C, which is expected to be a result of the 1200°C exposure for 24 hours. Due to this severe heat treatment, the as-rolled microstructure of sheet C retained large grains, which were on the order of 500 μm, Figure 3.3c. The grain size (GS) of sheets A and B were much smaller; i.e. GS<<100μm. The as-processed sheet B microstructure was severely segregated and contained fine

particles which were highly concentrated with Al and Nb (Ti-32Al-34Nb), see white particles of Figure 3.3b. The segregation was determined to have been a result of the inhomogeneous starting ingot material. Based on the low-oxygen pick-up, the relatively high degree of homogeneity, and the fine-grained as-processed microstructure of sheet A, see Figure 3.3a, a similar rolling and forging schedule was devised for the larger ingots.

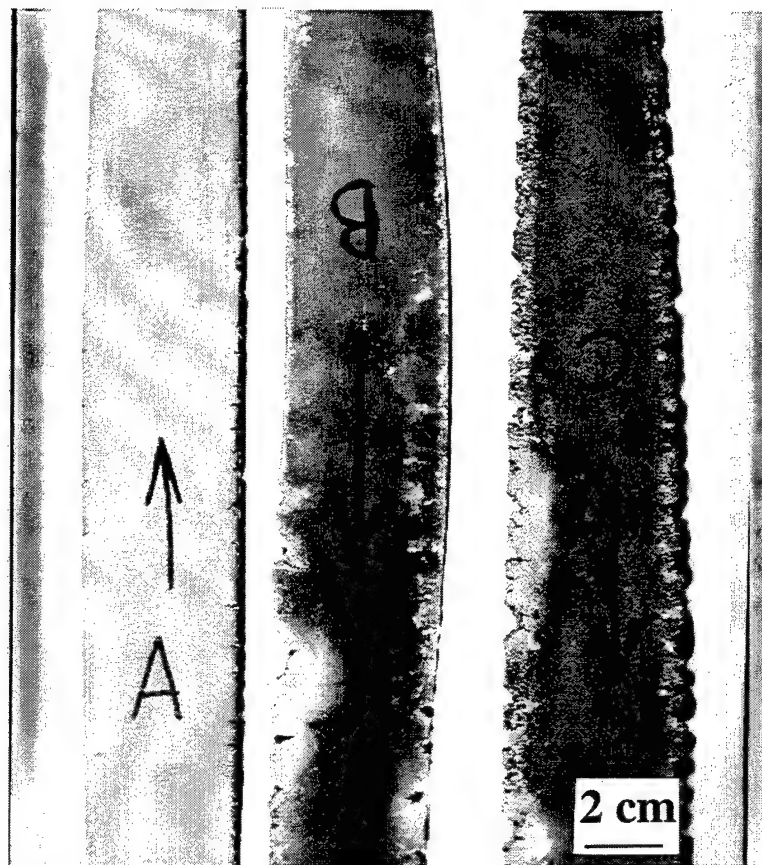


Figure 3.2 Low magnification photograph of the three as-rolled Ti<sub>2</sub>AlNb sheets.

After concluding the processing-screening study, the larger ingots were procured and prepared for processing. Forging preforms, 60 mm in diameter and 150 mm tall,

were cut from each of the larger cast ingots by EDM and coated with high-temperature glass then sealed in 6 mm thick stainless steel cans for protection from the environment. The can assemblies, made up of both the workpiece and the outer can, were unidirectionally forged (3:1 ratio) to a final height of 50 mm in air at a rate of 150 mm/min. For the near Ti<sub>2</sub>AlNb alloys, prior to forging the can assembly was heat treated at 1000°C for 15 minutes followed by a 982°C soak for 2 minutes. For the Ti-12Al-38Nb alloy, the can assembly was heat treated at 950°C for 15 minutes followed by a 932°C soak for 2 minutes. The heat treatment temperatures for the Ti-12Al-38Nb alloy were chosen based on previous processing work (Austin *et al.* 1992). The lower Al-containing ingots, Ti-23Al-27Nb and Ti-12Al-38Nb, were uniformly deformed around their centers. The post-forged can assembly for Ti-12Al-38Nb is depicted in Figures 3.4a and b. The circular cross-section of the workpiece can be clearly seen in Figure 3.4a. A bulge in the stainless steel can is present at the midpoint of the can assembly as depicted in Figure 3.4b. The highest Al-containing alloy, Ti-25Al-25Nb, did not deform uniformly and sheared at approximately a 45° angle with respect to the forging direction. Photos of the post-forged can assemblies for Ti-25Al-25Nb are depicted in Figures 3.5a and b. The circular shape of the top of the severely displaced workpiece is easily recognized in Figure 3.5a. The shearing resulted in a displacement of the stainless steel can which bulged on opposites at the top and bottom of the can assembly, see Figure 3.5b. This behavior was reproducible as an identically configured workpiece and can assembly exhibited similar behavior under the same forging conditions. However, in this case, the forging press was halted immediately after the initial shear deformation was observed. Figure 3.6 depicts the can assembly after the interrupted forging run. After forging, each pancake was cooled in vermiculite. The estimated cooling rate was 3°C per minute.



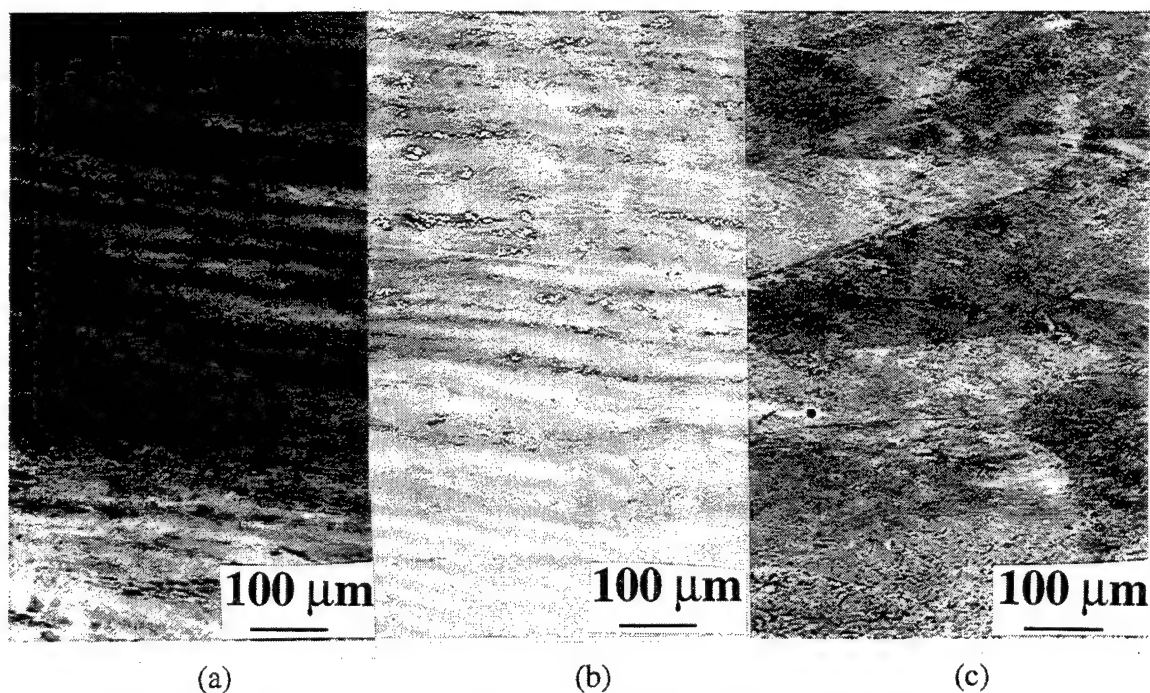


Figure 3.3 As-rolled microstructures of sheets (a) A, (b) B, and (c) C. These SEM images were taken from the thickness section and the rolling direction is horizontal.

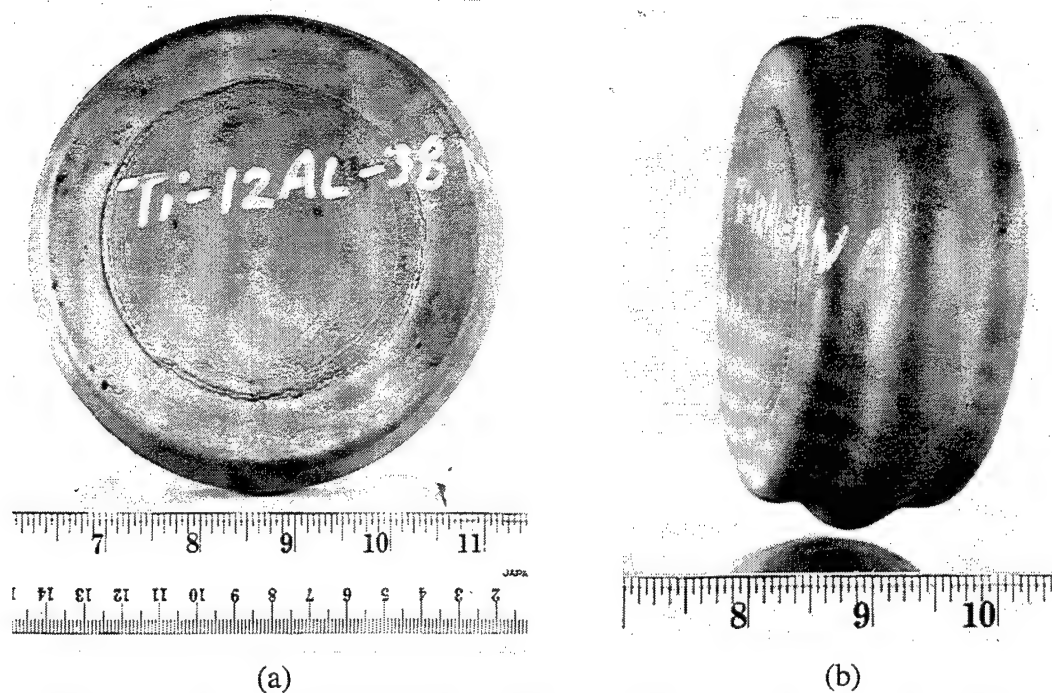
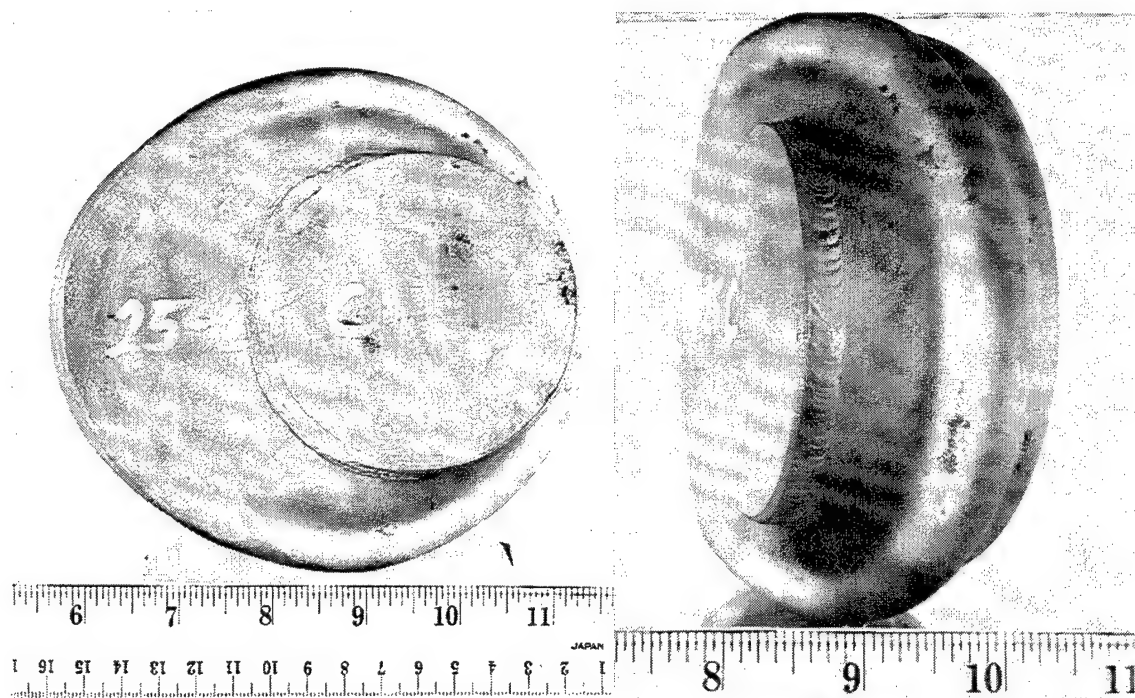


Figure 3.4 The (a) top and (b) side views of the can assembly after the first forging run for Ti-12Al-38Nb.



(a)

(b)

Figure 3.5 The (a) top and (b) side views of the can assembly after the first forging run for Ti-25Al-25Nb. Note the non-uniform deformation.

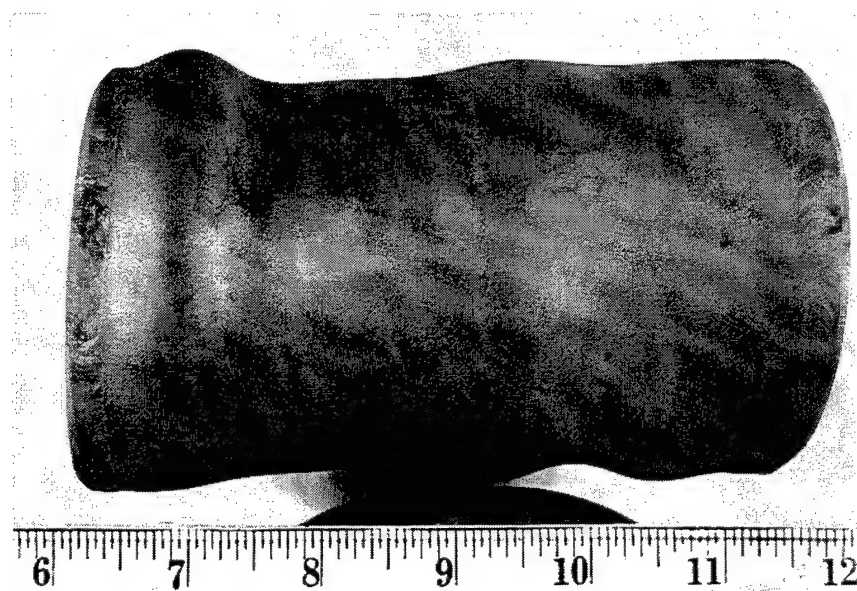
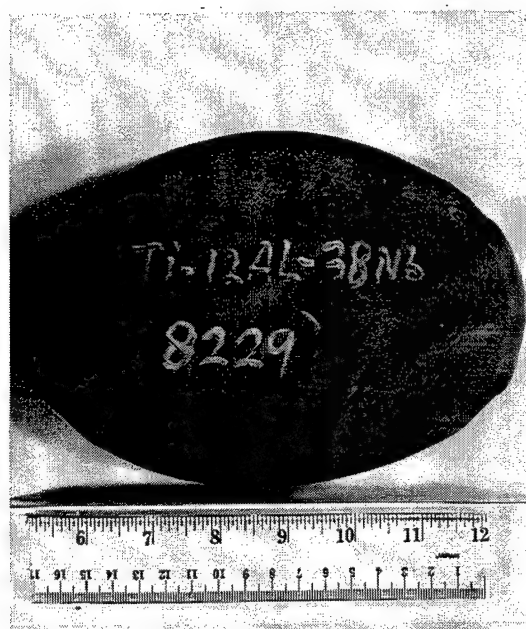


Figure 3.6 The Ti-25Al-25Nb can assembly after the interrupted forging run. Note the initiation of buckling.

After the initial forging runs, the Ti-23Al-27Nb and Ti-12Al-38Nb workpieces were removed from the can assemblies and EDM cut to a height of 75 mm. No surface cracks were observed on the workpieces after the initial forging. They were then re-canned and forged to 25 mm in a direction perpendicular to that of the original under identical forging conditions. Similar to the first forging run, the can assemblies were uniformly deformed. Figure 3.7a and b depict the extracted Ti-12Al-38Nb workpiece after the second forging run. Again the work pieces were removed and the sides of the pancakes were cut parallel to a width of approximately 75 mm. The as-cast and forged pancake microstructures for Ti-12Al-38Nb and Ti-23Al-27Nb are depicted in Figures 3.8a and b and 3.9a and b, respectively. No problems were associated with any of the forging procedures applied to these ingots and the size of the prior-B2 grain boundaries was successfully reduced.



(a)



(b)

Figure 3.7 The (a) top and (b) side views of the extracted workpiece after the second forging for Ti-12Al-38Nb.

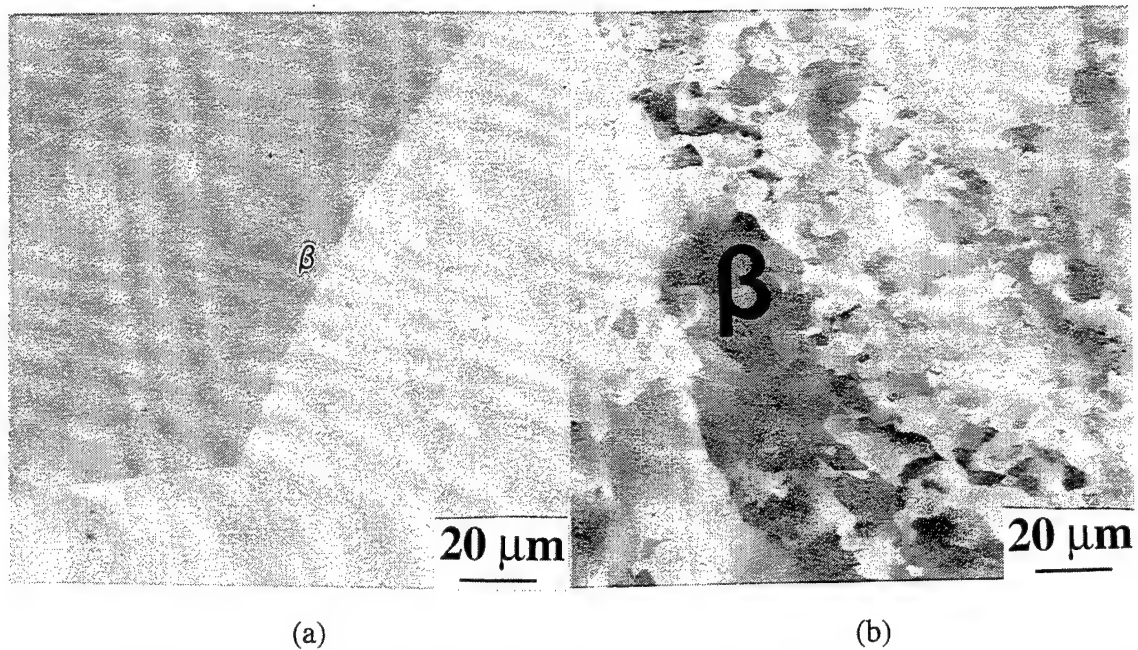


Figure 3.8 Comparison of the Ti-12Al-38Nb (a) as-cast and (b) forged microstructures. The forging direction was vertical. Note the reduction in grain size after forging.

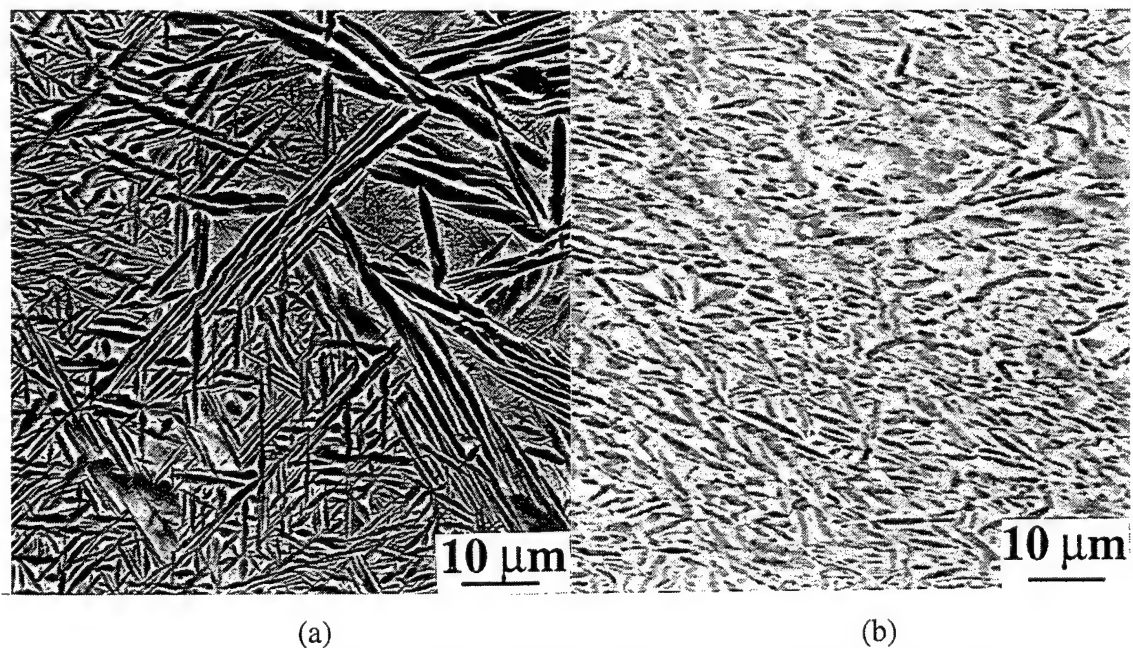


Figure 3.9 Comparison of the Ti-23Al-27Nb (a) as-cast and (b) forged microstructures. The forging direction was vertical.

The extracted Ti-25Al-25Nb workpiece after the initial forging run is depicted in Figures 3.10a-c. Along with the shearing deformation, severe cracking occurred along

the top surface of the workpiece, see Figure 3.10a. Due to the nonuniform deformation behavior, both the can assembly height and the reduction ratio were reduced prior to the second forging attempt. The slightly deformed workpiece, taken from the interrupted forging run (see Figure 3.6), was EDM cut into two pieces, which were subsequently re-canned in order to forge in the same direction as that of the first. The can assembly prior to forging was approximately 62 mm tall and the intended reduction ratio was 2:1. All other parameters, including temperature and forging speed, remained constant. The forging deformation was uniform for this run as depicted in Figures 3.11a and b. In attempt to acquire a similar amount of deformation for Ti-25Al-25Nb as that for the other alloys, the Ti-25Al-25Nb workpieces were again removed, EDM cut, and re-canned in preparation for a third forging trial. The third forging step was performed in a direction perpendicular to the first two and the reduction ratio was again 2:1. The final height of the uniformly deformed can assembly was approximately 25 mm. Similar to that of Ti-23Al-27Nb, the ingot microstructure was successfully broken down, compare Figures 3.12a and b. Therefore, the Ti-25Al-25Nb material was workable at 982°C, though both the ingot height and reduction ratios needed to be reduced from those used for the Ti-23Al-27Nb and Ti-12Al-38Nb materials. It should be noted that the applied loads for the initial forgings were greatest for Ti-25Al-25Nb and smallest for Ti-12Al-38Nb. The reason for the poorer workability of the Ti-25Al-25Nb ingot is believed to be due to the higher Al content. The poor workability of alloys containing high Al concentrations, approximately 25Al, has been reported previously (Banerjee *et al.* 1993, Wojcik *et al.* 1996).

All pancakes were cooled in vermiculite after the final forging steps. The Ti-23Al-27Nb and Ti-25Al-25Nb pancakes were re-canned and isothermally soaked at 815°C for 1 hour followed by a 982°C soak for 15 minutes prior to rolling. The unidirectional rolling steps consisted of several passes on a cold die each after a soak at 982°C for 5 minutes. For the Ti-12Al-38Nb pancake, the soak temperature was also



identical to the forging temperature, 932°C. The estimated reduction per pass was between 5-10% with a total reduction of approximately 80%. The rolling loads were recorded for each pass on a stripchart and measured between 50-70 tons depending on the reduction. Similar to the forging procedures, the largest loads and poorest workability were exhibited by Ti-25Al-25Nb as reductions of more than 5% were not achievable for this alloy. After the final pass, the sheets were reheated at the respective soaking temperatures for 3 minutes and then removed from the furnace and hung vertically for 1 minute to promote creep straightening. They were then cooled in vermiculite. Figures 3.13a and b depict the can assembly prior to rolling and the post-rolled workpiece for Ti-12Al-38Nb. Note the substantial lengthening which resulted from rolling. Figures 3.14a and b depict the can assembly prior to rolling and the post-rolled workpiece for Ti-23Al-27Nb, while Figures 3.15a and b depict the rolled can assembly and the extracted workpiece for Ti-25Al-25Nb.

Low magnification SEM images of the three as-rolled sheet microstructures are depicted in Figures 3.16a-c. It is noted that the rolling and forging steps for the near Ti<sub>2</sub>AlNb alloys were performed at 982°C, which is well below the B2 transus, while for Ti-12Al-38Nb, all the processing steps were performed at 932°C, which is above the transus. A detailed description of the phase evolution of the sheet materials, which includes the temperature ranges for the different phase regimes, is provided in the phase evolution section of Chapter 4.

### 3.1.2 Induction-Heating Procedures

One near Ti<sub>2</sub>AlNb alloy was processed above the B2 transus. The intent of the processing procedure was to produce O-phase single crystals using a technique adopted from polysynthetically twinned (PST) TiAl crystal studies (Subramanian 1997). The processing method utilized in this case was significantly different than that previously described. No forging or rolling steps were performed. Instead, two 125 mm long

cylindrical rods of 12 mm diameter were EDM cut from cigar melts, which had been hot-isostatically pressed (HIPed) at 1200°C for 4 hours at 103 MPa. One end of each of the cylindrical rods was attached to threaded rotating grips located within a sealed Crystalox® chamber. The rods were aligned directly above and below each other so that the unattached ends were close to touching. The chamber was backfilled with a partial pressure (0.02 MPa) of high-purity argon and the region between the two unattached ends was locally heated to the molten temperature using a stationary induction heater. The hot region was approximately 75 mm and the uniformly heated, molten zone was approximately 6 mm. The rotating rods were transversed at a rate of 1 mm per hour. The rotation rate was 4 revolutions per minute (rpm). Due to the slow pull rate, more than 5 days was necessary to produce a gage length of 125 mm. Due to the low-vacuum atmosphere and the high-temperature exposure, part of the sample evaporated onto the chamber walls. The evaporated material was highly concentrated with Al. Therefore, in order to compensate for the Al loss, the target composition of the original cigar melts was Ti-29Al-26Nb. The resulting composition of the 125 mm long rod was somewhat segregated and the averaged compositions provided by the chemical analysis is provided in Table 4.1. Figure 3.17 depicts the as-processed rod, which contained several evenly dispersed surface fringes. A more than 1.5 mm thick layer was removed from the outer edge prior to specimen machining in attempt to remove surface contaminants and inhomogeneities.

As will be described in Chapter 4, the rod microstructure did not consist of single crystals. Instead Widmanstatten O phase precipitated within the very large prior B2 grains and some retained B2 laths were present. Due to the sluggish nature of the B2 phase transformation and the limited range of pulling rates, efforts to obtain O single crystals were discontinued. Even though O single crystals were not produced, this material proved to be quite useful for the mechanical behavior study as will be described in Chapters 4 and 5.

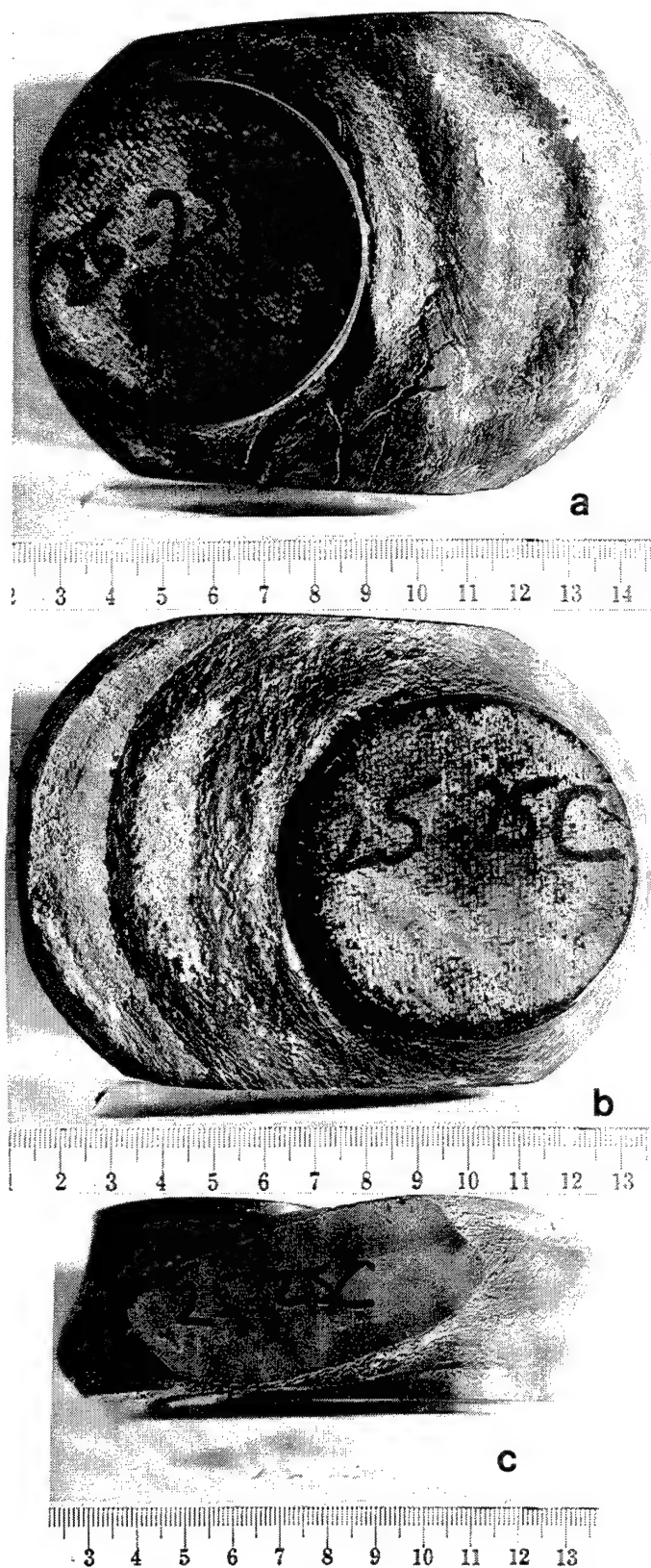


Figure 3.10 The (a) top, (b) bottom and (c) side views of the sheared Ti-25Al-25Nb workpiece after the initial forging run.





Figure 3.11 The can assemblies of the two uniformly deformed Ti-25Al-25Nb pancakes after the second forging runs.

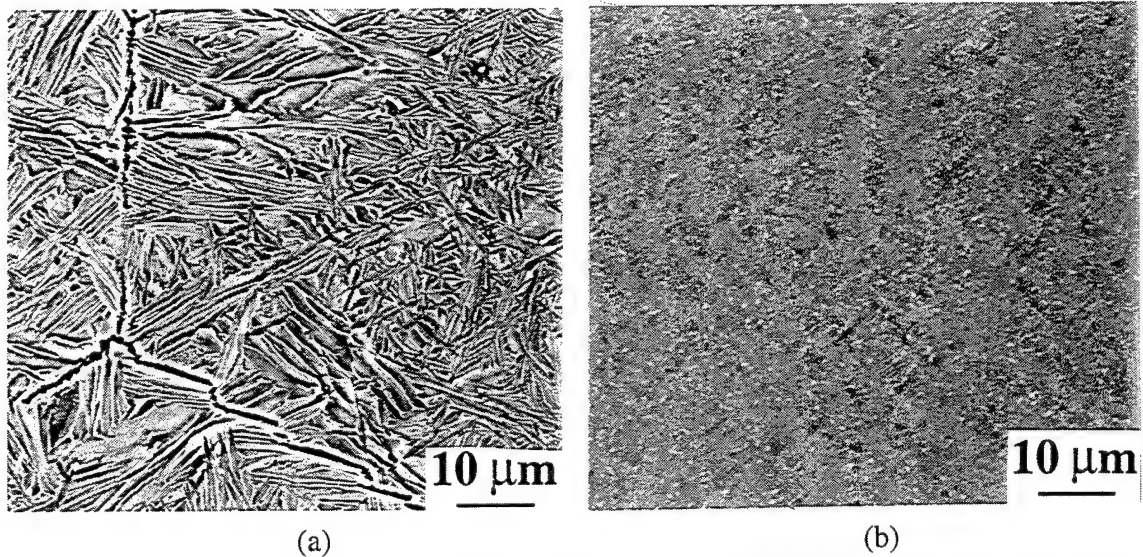


Figure 3.12 Comparison of the Ti-25Al-25Nb (a) as-cast and (b) forged microstructures. The forging direction was vertical.

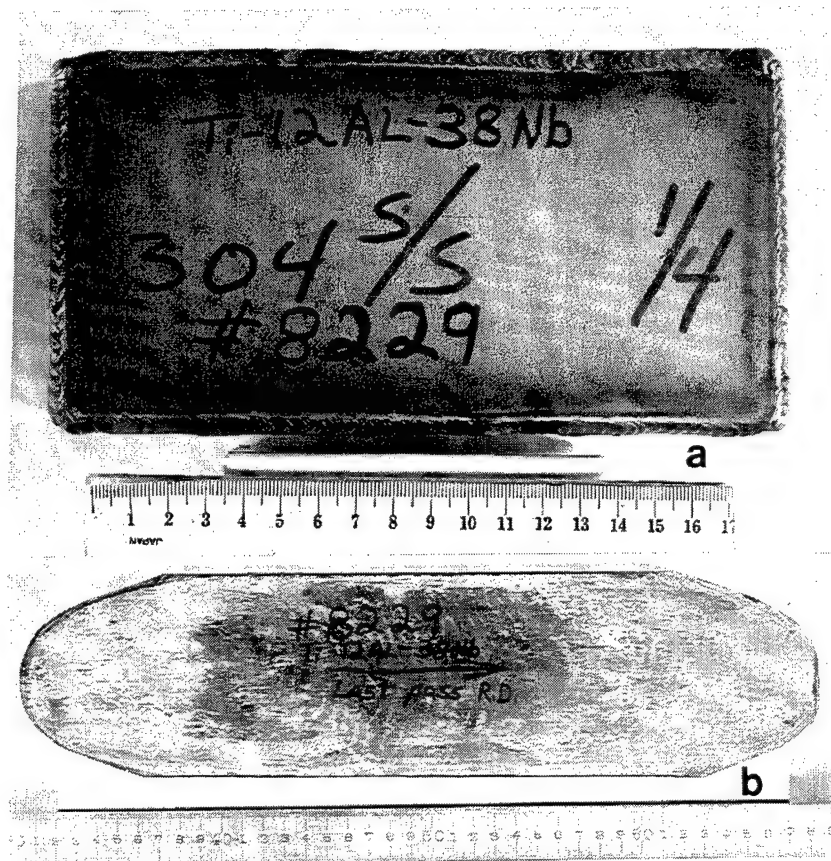


Figure 3.13 The (a) can assembly prior to rolling and the (b) extracted workpiece after rolling for Ti-12Al-38Nb.

### Material Preparation

This section will discuss the techniques adopted to machine and heat treat the materials.

Prior to machining, the sheet materials were sectioned into blanks using either an EDM or an abrasive diamond saw. The location of the sectioned blanks were mapped so that the majority of the specimens would be taken from the bulk of the sheet where most of the deformation had taken place. Figures 3.18a and b depict the locations in which the blanks were removed from the Ti-23Al-27Nb and Ti-25Al-25Nb sheets. The numbered regions represent individual specimens. Note that all specimens were machined parallel

to the rolling direction and prior to testing the machined samples were randomly selected so that any effects caused by inhomogeneities within regions of the sheets would not be compounded.

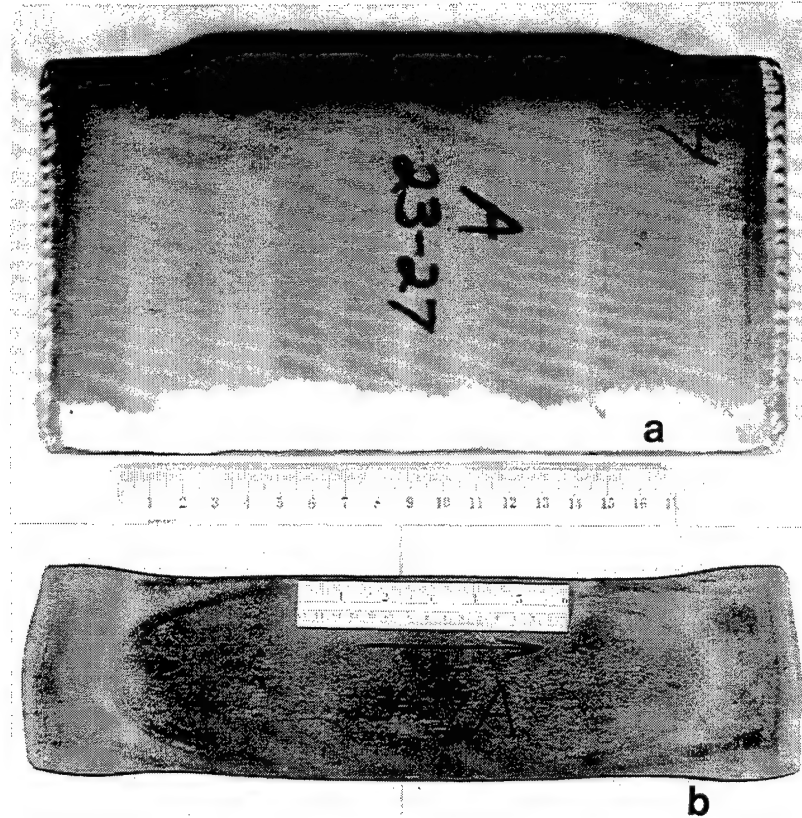


Figure 3.14 The (a) can assembly prior to rolling and the (b) extracted workpiece after rolling for Ti-23Al-27Nb.

After sectioning, the blanks were machined into cylindrical specimens containing threaded grips used for tension and tensile-creep experiments. In addition, a few cylindrical specimens were machined for compression and compression-creep experiments. A typical specimen geometry, which satisfies the American Society for Testing and Materials (ASTM) Standard for Creep Testing (E139), is illustrated in Figure 3.19. Note that the coarse thread diameter in the grip section was greater than  $7/4$  that of the gage diameter. The Ti-12Al-38Nb and Ti-23Al-27Nb blanks were machined at Dynapoint Tool Inc., West Carrolton, Ohio, using a silicon carbide tool. The threaded

ends were centered and the specimen was turned on a lathe. No difficulties were associated with machining these alloys. On the other hand, several silicon carbide tools were broken in attempting to turn the initial Ti-25Al-25Nb blanks. Thus, similar to the processing observations, Ti-25Al-25Nb was the most difficult to machine and an alternative machining method was employed. Instead, the rectangular blanks were electron discharge machined into cylinders and machined using a low-stress grinding technique by Bitec Production Machining, Dayton, Ohio. A similar surface finish was provided for these specimens as that for Ti-23Al-27Nb and Ti-12Al-38Nb.



Figure 3.15 The post-rolled (a) can assembly and (b) extracted workpiece for Ti-25Al-25Nb.

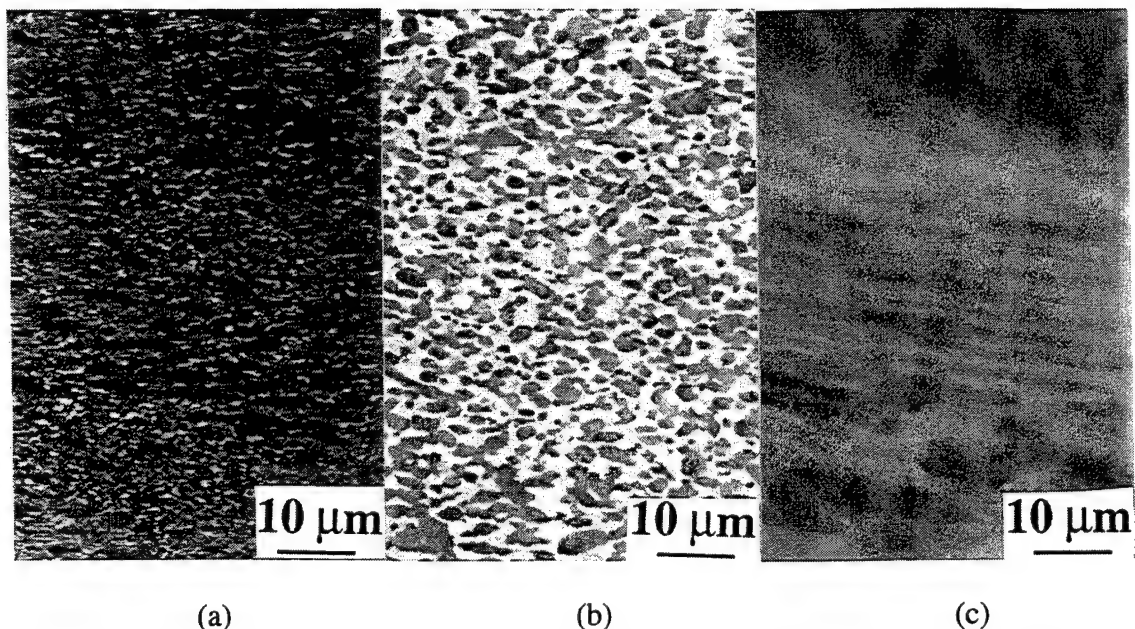


Figure 3.16 As-rolled microstructures of the (a) Ti-25Al-25Nb, (b) Ti-23Al-27Nb, and (c) Ti-12Al-38Nb sheets. These SEM images were taken from the thickness section and the rolling direction is horizontal.

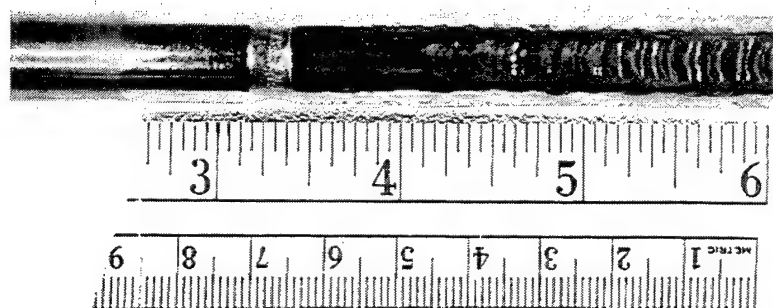


Figure 3.17 The as-fabricated near  $\text{Ti}_2\text{AlNb}$  rod which was induction heated for five days using a Crystallox machine specially designed for producing single crystals.

The materials not sectioned into blanks were used for the heat-treatment and phase-evolution studies. Both the machined specimens as well as the excess materials

were heat treated in the following manner. They were wrapped in a tantalum foil and encapsulated in quartz tubes backfilled with a partial pressure of high-purity argon gas. The capsules were subjected to solution treatments within open-air muffle furnaces followed by water quenching (WQ) or control cooling (CC) to RT. The capsules were then either broken and the samples removed, or they were reheated at a lower temperature followed by water quenching for the aging and microstructural-stability studies. The targeted heat-treatment temperatures were maintained within  $\pm 5^{\circ}\text{C}$ . To guide selection of suitable solutionizing temperatures for appropriately obtaining different phases as well as changing phase volume fractions, an estimate of the phase boundaries was obtained by solutionizing samples at temperatures ranging between  $875^{\circ}\text{C}$  and  $1200^{\circ}\text{C}$  followed by water quenching. To guide the understanding of microstructural stability, aging treatments of between 0.25-670 hours at temperatures below  $875^{\circ}\text{C}$  were performed on selected solutionized samples. Although emphasis was not placed on understanding cooling-rate effects, a few samples were control-cooled to RT to understand the phase evolution in such cases. In addition, in order to assess the effect of microstructural instability on the creep behavior, companion coupons were heat treated at  $650^{\circ}\text{C}$  for between 44-300 hours, and those microstructures were compared with crept specimens. A detailed description of the heat-treatment and phase-evolution results can be found in the Chapter 4.

### 3.3 Characterization Methods

This section will discuss the experimental equipment and procedures used to characterize the materials' behavior.

#### 3.3.1 Testing

Creep Experiments. The tensile creep test equipment employed for this study was specially designed at Wright Laboratory Materials and Manufacturing Directorate in



University of Dayton Research Institute (UDRI), Dayton, Ohio to perform elevated-temperature testing of metals and metal and ceramic matrix composites. The test apparatus were made up of three major components: test frame, temperature control unit, and personal computer (PC). The testing utilized all three components.

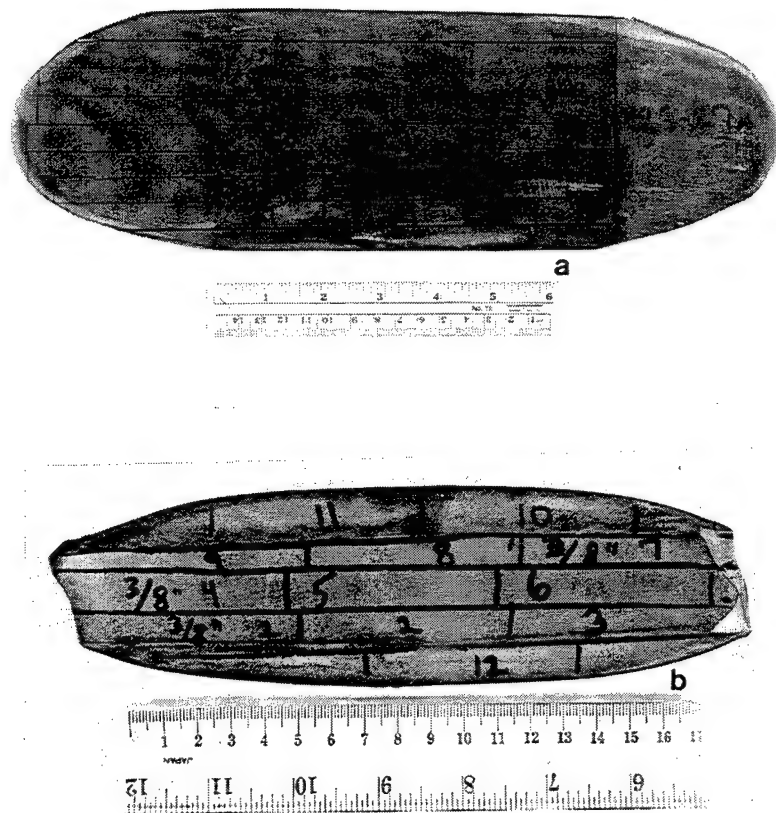


Figure 3.18 Specimen mapping for the (a) Ti-23Al-27Nb and (b) Ti-25Al-25Nb sheets. Sections were cut along the bold lines and the numbered regions represent the blanks from which specimens were machined.

A majority of the constant-load tensile-creep experiments were performed on a vertical load frame with a 20:1 lever-arm ratio in air between 650°C-760° and 35-450

MPa. A 10 kilonewton (kN) load cell was attached to the load train to measure the magnitude of the load. Although the experiments were constant load, in most cases the reduction in cross-sectional area was not sufficient to significantly alter the stress, therefore the stresses were assumed to be constant. In the cases which involved a high amount of strain, the stresses were recalculated according to the estimated reduction in cross-sectional area.

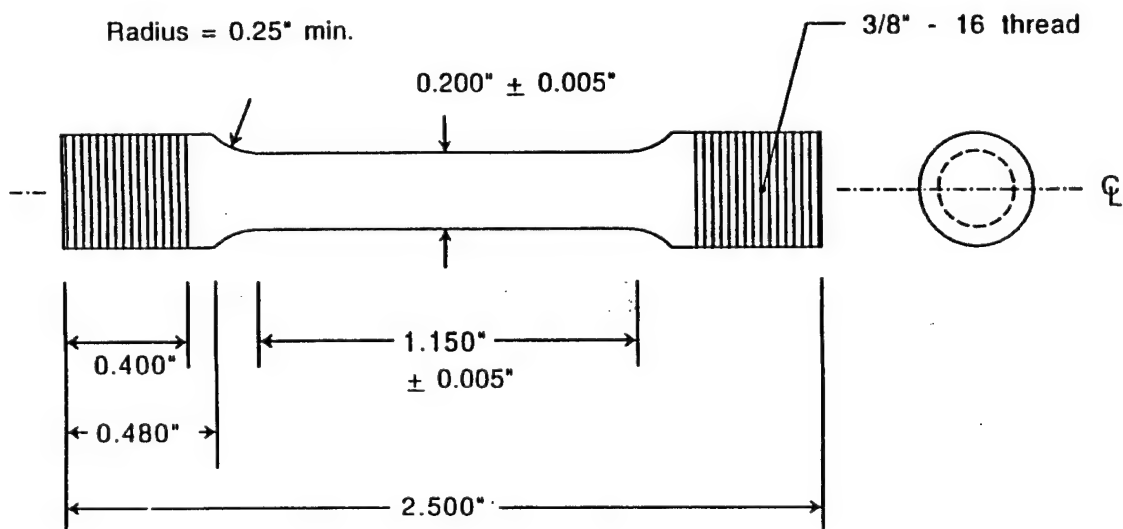


Figure 3.19 A typical specimen geometry, containing a cylindrical gage section, used for the tension and tensile-creep experiments.

Thermal control of the test sample was provided by an insulated furnace, which surrounded the specimen and grips. The furnace was designed for closed-loop feedback control of one area, approximately 25 mm, of a particular specimen. Specimen temperatures were monitored by attachment of two chromel-alumel type K thermocouples directly to the specimen's reduced section. Targeted temperatures were maintained within  $\pm 5^\circ\text{C}$ . Threaded superalloy pull-rods were used to affix the grips to



the load train. The primary function of the gripping system was to secure the specimen without inducing bending moments during the loading process. Cooling was not an important issue as a majority of the load train was located well outside the furnace. The extension was measured by two parallel linear variable differential transformers (LVDTs) attached to the extensometer, which were mounted onto the specimen at opposite ends of the gage length. Periodically throughout the test, an IBM PC monitored load, LVDT displacement, and temperature values from the load cell, extensometer, and thermocouples, respectively. After the test, strain data was reduced from the LVDT displacements using a seven-point incremental method.

In order to identify deformation behavior from surface observations, finely-polished rectangular specimens were tested using a second machine containing a horizontal test frame equipped with a Mechanical Testing Systems (MTS) servohydraulic load actuator. The following description will summarize the salient features of this apparatus, while a more complete description is provided by Hartman and Russ (1989). A photo of the testing apparatus can be found in Boehlert (1993).

A 25 kN force was achievable through the mechanical assembly, consisting of a load control unit equipped with a load cell. Hydraulic friction grips were used to affix the specimen. To help minimize bending, the grips incorporated precisely machined outer surfaces which were used to obtain transverse alignment to better than 0.025 mm and angular alignment to better than 0.0002 radians (Hartman and Russ, 1989). The grip assemblies were actively cooled due to the high temperature involved in the creep test. This was accomplished by pumping a water/anti-freeze mixture through cooling channels drilled in the grips and then passing the coolant through a heat exchanger. Thermal control of the test specimen was provided by radiant energy heat lamps controlled by Barber Colmans process control equipment. The lamps were designed for closed-loop feedback control of four zones of a particular specimen. Major components of the thermal-control system included two banks of four quartz lamps and a water/anti-freeze

cooling system for the lamp bodies. Heating was applied using the two banks of quartz lamps, symmetrically located approximately 10 mm away from the specimen's faces. A 12.7 mm MTS high-temperature extensometer with alumina silica ceramic rods, fitted with 5 mm conic points, was employed to measure specimen strain. The strain data stored in the data files were calculated from the displacement measured by the extensometer.

The core of the computer automated test equipment was an IBM PC equipped with a National Instruments interface board and software specially designed to perform both creep and thermomechanical fatigue (TMF) testing. The software and component architecture were designed by George Hartman of UDRI. The user enters test parameters including specimen thickness and width, hold temperature, waveform, hold times, hold stress, etc. through a series of interactive menus. The program then sends tailored messages to set up the temperature and load profiles. Throughout the test, the PC monitored load, displacement, and temperature values from the load cell, extensometer, and thermocouples, respectively.

The typical rectangular specimen geometry used on this testing apparatus, 100 mm x 4 mm x 2 mm, was EDM cut from the sheets prior to heat treatment. After the heat treatment, approximately 25  $\mu\text{m}$  was ground, through use of sequentially finer grits of silicon carbide (SiC) paper, from the exposed surfaces to remove EDM heated layers and contamination. A better than 1  $\mu\text{m}$  grit fine polish was performed on one face of the specimens. Selected specimens were marked with shallow fiducial scratches imposed during the polishing procedure in order to qualitatively assess the deformation behavior. As described in the section devoted to the creep deformation behavior of near  $\text{Ti}_2\text{AlNb}$  alloys (Chapter 4), these specimens aided in the identification of creep deformation mechanisms and, in particular, grain boundary sliding. To ensure integrity of the polished faces, the fiducially-marked specimens were tested in vacuum. These specimens were tested within an Oxygon® vacuum chamber, which surrounded the heated area and

most of the load train. At the creep temperature, the typical atmosphere was  $9 \times 10^{-7}$  torr. Although the data from these experiments were compared with those taken from experiments performed in air, this study was not intended to establish environmental effects on the creep behavior. The main purpose for performing the limited amount of vacuum tests was to secure the integrity of the polished and fiducially-marked specimens. Some of the polished specimens, which were not fiducially marked, were tested in air. Although a discolored oxidation layer formed on the surface, sufficient integrity of the polished face remained so that quality characterization of the surface deformation was provided by back-scatter detector (BSD) SEM images.

One cylindrical creep specimen was loaded in compression to determine the effect of tensile versus compressive loading conditions. The data from this specimen was compared with that for an identically heat-treated specimen which was tested in tension under identical creep conditions. The compression creep experiment was performed on an Applied Test System, Inc. (ATS) vertical load frame equipped with a LVDT attached to the compression platens. The specimen, which was 9 mm in height and 5 mm in diameter, was enclosed in a sealed chamber in which a 0.01 MPa partial pressure of flowing argon gas was pumped. Load, strain, and displacement data were periodically collected throughout the test.

All creep specimens were loaded parallel to the rolling direction. The creep experiments were conducted such that the specimens were soaked at the creep temperature for at least 30 minutes prior to applying load in order to minimize the thermal stresses. In most cases, after the creep had proceeded well into the secondary regime, either the load or temperature was changed or the creep tests were discontinued. No specimens were unloaded prior to reaching the secondary regime. The tested specimens were cooled under load to minimize recovery of the deformed structures. Some specimens were taken to failure which was defined as the sample breaking into two pieces.

Tensile Experiments. The two elevated temperature tensile experiments were performed on a vertical MTS load frame in air at 650°C. The load frame was equipped with a 50 kN load cell and superalloy pull-rods which were attached to the grips used for the threaded round-bar geometry, see Figure 3.19. A 12.7 mm MTS high-temperature extensometer with alumina silica ceramic rods, fitted with 5 mm conic points, was employed to measure specimen strain. Because one of the specimens broke prematurely in the grip section, an elevated temperature compression test was performed on the same alloy in order to more accurately determine the flow properties. The compression specimen geometry was 10 mm in height by 6 mm in diameter. This experiment was performed in vacuum ( $10^{-5}$  torr) on a Brew Instron 4500 test machine. For both the tension and compression experiments, the strain rate was  $10^{-4}$ /s. The specimens were soaked for 30 minutes at temperature before applying load. Displacement, strain, and load data were recorded periodically throughout the tests.

A majority of the RT tensile specimens were machined to a "dog-bone" geometry. Those specimens not machined into a round bar geometry, see Figure 3.19, were EDM cut so that the gage section was 17 mm long by 3 mm wide. The specimens were ground through sequentially finer grits of SiC paper to remove surface contaminates and EDM affected layers. Similar to the rectangular creep specimens, selected tensile specimens were finely polished to a better than  $1\text{ }\mu\text{m}$  finish prior to testing in order to evaluate the mechanisms of slip and damage from surface observations. Testing was performed at RT on an Instron 8500 servo-hydraulic mechanical testing machine, equipped with a 10 kN load cell, at a constant strain rate of  $10^{-4}$ /s. Strain was measured using a mounted 12.7 mm gage length Instron extensometer. The load, strain, and displacement data were recorded periodically throughout the experiments using a Macintosh PC and Strawberry Tree® data acquisition software.

All tensile test specimens were loaded parallel to the rolling direction. A majority of the specimens were taken to failure which was defined as the sample separating into two pieces.

### 3.3.2 Metallography

Because the focus of this work was to understand microstructure-property relationships, it was important to characterize the microstructures in terms of the phases present and the structure of the phases. In order to identify significant microstructural features, it was also important to quantify the microstructures. The microstructural features which were considered the most relevant to the mechanical behavior were phase volume fraction, composition, morphology, and grain size. Because phase volume fraction, composition, and grain size are capable of being quantified, the relevant parameters were measured accordingly and related to the mechanical behavior. Although the volume fraction of different morphologies will be discussed briefly, morphology was typically considered to be a microstructural feature more characterized than quantified in this work.

Careful metallurgical practices were employed to characterize the microstructures and mechanical deformation. In order to evaluate the microstructures involved in the phase-evolution studies, the as-processed and heat-treated samples were sectioned using a diamond blade and mounted in Konductomet®. The section orientations consisted of thickness sections cut perpendicular to the rolling plane, which were oriented either parallel, termed longitudinal, or perpendicular, termed transverse, to the rolling direction. The third orientation consisted of the rolling plane, termed face, of the sheets. Surface preparation of mounted samples involved wet grinding on 240, 320, 400, and 600 grit SiC papers and polishing using 15, 6, and 3 micrometer diamond paste followed by Buehler Mastermet colloidal 0.06  $\mu\text{m}$  silica suspensions. The mounted samples were evaluated using a Leica 360 FE SEM, and a Japan Electron Optics Ltd. (JEOL) 733 electron

microprobe. The Leica 360 FE SEM was also used to evaluate the deformation behavior of tested specimens. The deformed surfaces of specimens polished prior to testing as well as the fractured surfaces provided insight to the damage evolution. In addition, tested specimens, which were sectioned, mounted, and polished, aided in distinguishing differences between the bulk and surface deformations.

Several samples taken from each material were analyzed for the constituent elements. The amounts of nitrogen and oxygen were quantified using a Leco Corporation Model TC-136 Oxygen/Nitrogen Analyzer. This instrument was calibrated using standard materials traceable to the National Institute of Standards and Technology (NIST). Typical analytical precision data for this instrument with standard homogeneous titanium samples are: oxygen  $(0.191 \pm 0.007)\%$  (w/w) at 0.191% and nitrogen  $(0.015 \pm 0.003)\%$  (w/w) at 0.015%. Most of the Ti, Al, Nb, and Fe contents were analyzed by means of solution X-ray fluorescence spectrometry and the data were obtained using a Kerex Corporation Model 770 Delta Analyst. In some cases absorption spectrometry techniques were used to analyze Ti, Al, and Fe. X-ray diffraction (XRD) studies were performed using a Rigaku Rotoflex RU-200 series (RU-200BH) rotating anode X-ray generator, run at 150 mA and 40 kV. The samples analyzed were sectioned and polished to a 600  $\mu\text{m}$  grit finish. The data was reduced according to Cohen's Analysis to confirm the presence of the different phases. Differential thermal analysis (DTA), typically employing a 15°C/minute cooling and heating rate, was performed using a Du Pont High Temperature DTA system on sections of the as-processed material to estimate the B2 transus temperature.

Before describing how the microstructures were characterized and quantified, a description of how the foils used in the TEM study were fabricated is now included. Thin parallel sections, approximately 375  $\mu\text{m}$  thick, were cut using a diamond blade. Typically for the deformed specimens, the sections were cut perpendicular to the loading direction. Each section was then mounted on a 25 mm diameter aluminum grinding stub

using a heat-sensitive mounting medium. Next, the section was mechanically polished to a thickness of approximately 125  $\mu\text{m}$  using 600 grit SiC paper. The cores were then removed from the sections using a coring tool and a diamond paste abrasive. The 3 mm cores were mechanically dimpled. The dimpling procedure consisted of mounting the core to a steel stub, again using a heat-sensitive mounting medium, and polishing using a cloth wheel and an abrasive suspension. Dimpling was considered to be complete when the minimum thickness, measured at the apex of the dimple, was approximately 20  $\mu\text{m}$ . After dimpling, samples were placed in an ion-mill at approximately  $10^{-4}$  torr. Using a 1 mA current and oriented at a  $14.5^\circ$  inclination angle with respect to the sample, a 6 kV ion source bombarded the sample until perforation was achieved, which typically required between 6 and 36 hours depending on the thickness of the sample. After the sample was perforated, a final milling step at 4 kV, 1 mA, and a  $13^\circ$  inclination angle was performed for 1 hour. The resulting TEM foils, used for phase identification and deformation characterization, were evaluated using both a JEOL JEM-2000FX and a Philips 200 CM field emission electron microscope at 200 kV.

Characterization of the microstructures was performed primarily through phase identification using TEM and X-ray techniques. Grains were identified by the characteristic electron diffraction patterns of their respective structures. Selected area diffraction patterns (SADPs), obtained through tilting experiments using a double-tilt holder, were employed to identify the phases of grains larger than 3  $\mu\text{m}$ . This technique provided the basis for determining the temperature ranges of the  $\alpha_2$ +B2,  $\alpha_2$ +B2+O, and B2+O fields, as the grains resulting from solutionizing in these regions were larger than 3  $\mu\text{m}$ . The SADPs were indexed according to the lattice parameters listed in Table 3.2. The lattice parameters of the respective phases were also determined from Cohen's Analysis of the X-ray diffraction results. XRD was useful in determining the order of the BCC structure above the transus. Although XRD was used on sub-transus heat-treated samples, several of the  $\alpha_2$  and O peaks overlapped and were difficult to clearly separate.

This was also true for some O and B2 peaks. In addition, due to the lower phase volume fraction present in some microstructures, the resulting peak intensities were too low to resolve accurately. A third disadvantage was that this technique did not reliably distinguish between the ordered and disordered structures of the BCC phases for subtransus samples as the super-lattice peaks of the B2 phase were of low intensity. For these reasons, TEM was deemed more reliable and used more frequently than XRD in this work. CBED and microdiffraction techniques were employed to distinguish between the structure of the fine grains ( $GS < 3 \mu m$ ) which precipitated during the lower temperature aging treatments. The CBED and microdiffraction patterns were differentiated by the size of the condenser aperture used. For condenser apertures larger than  $200 \mu m$ , the patterns were considered to be CBED patterns, while microdiffraction patterns utilized smaller condenser apertures and therefore contained finer diffracting spots.

Table 3.2 The Lattice Parameters of the Different Phases

Structure	a (nm)	b (nm)	c (nm)
$\alpha_2$	5.78	5.78	4.63
B2	3.23	3.23	3.23
O	6.33	9.70	4.80

Quantifying the microstructures was primarily performed using SEM techniques. Phase volume fractions were determined quantitatively using NIH image analysis software on digitized, high-contrast BSD images taken from the Leica 360 FE SEM. In the BSD images the BCC phase was the lightest, the  $\alpha_2$  phase was the darkest, and the O phase was of intermediate contrast. The image contrast served to distinguish between the phases. This was determined to be a reliable method because identified grains within TEM foils were consistently distinguished by their contrast when viewed in the SEM with BSD mode. Density slices of different contrast levels were used to fill the digitized



images. Once the contrast level associated with a given phase was deemed satisfactory, the area fraction of pixels containing this contrast was calculated and represented as the area fraction of the respective phase. The average of all the values was then related to the volume fraction of the phase as measurements were made on several images taken from the three sheet orientations. The measurement error, estimated to be  $\pm 5\%$ , was a function of the resolution of the relatively low magnification (500-3000 times) images and the capabilities of the software.

Phase compositions were measured by microprobe analysis of several different regions of the samples. The activation volume for the microprobe at 15 kV was approximately  $2 \mu\text{m}^3$ . A measurement error of  $\pm 1\%$  should be taken into consideration for the reported mean values.

The spatial grain size (GS) measurements were obtained using the mean line-intercept method. This method consists of counting the number of grain boundary intercepts lying along straight lines drawn across SEM images. The images were of relatively low magnification, ranging between 100-3000 times, in order to provide a large enough area to reduce any local inhomogeneities. The length of the marked lines were divided by the number of intercepts counted and this number was multiplied by a factor (1.74) used to compensate for equiaxed grain shapes (Langdon 1982). The sizes of the non-equiaxed grains were not measured. All measurements were then averaged before reporting the grain sizes. It is important to note that the grain boundary intercepts were counted independent of phase. Therefore, the reported values represented all the phases present in a given microstructure.

## CHAPTER 4

### RESULTS

This chapter provides a description of the results on the phase-evolution, creep, and tensile behavior of O+BCC phase alloys and is therefore divided into three sections. Special emphasis is placed on the creep behavior as this topic was identified as the main focus of this work.

#### 4.1 Phase Evolution

As listed in Chapter 2, one of the objectives of this work was to understand and characterize the phase evolution of O+BCC orthorhombic alloys. A considerable amount of work has been performed in this area since the discovery of the O phase and several of the findings have been related to conventional titanium metallurgy. The approach of this work was to process the alloys at a temperature below the B2 transus and perform subsequent heat treatments to identify the temperature ranges of the phase fields. In addition, lower-temperature aging treatments were used to characterize the transformation behavior of the phases. Several researchers have chosen to process O alloys at temperatures above the B2 transus. In general, such procedures result in more homogeneously distributed microstructures as typically diffusivities are increased with temperature and single-phase B2 grains of similar composition evolve quite rapidly. However, the B2 grain growth is also quite rapid above the B2 transus and it is difficult to obtain fine-grained microstructures devoid of prior B2 grain boundaries without performing hot work below the transus. In addition, super-transus processed alloys do not possess primary O or  $\alpha_2$  grains as secondary phases generally evolve from a parent

B2 grain. Although the sub-transus processed alloys of this work did contain some segregated regions and chemical banding, the wide range of microstructures obtained from the subsequent heat treatments provided for a thorough understanding of the microstructural evolution and also provided excellent flexibility in the control of microstructural parameters for the microstructure-property study as will be described in the creep and tensile behavior results' sections. For this reason a majority of the description of the phase-evolution behavior will be devoted to the sub-transus processed sheet materials and a smaller portion will involve the super-transus processed material. This section is divided into two parts based on the materials whose compositions are near  $\text{Ti}_2\text{AlNb}$  and Ti-12Al-38Nb.

#### 4.1.1 Near $\text{Ti}_2\text{AlNb}$ Alloys

The average chemical compositions of the near  $\text{Ti}_2\text{AlNb}$  alloys are given in Table 4.1. Three of the four alloys were targeted for a stoichiometric  $\text{Ti}_2\text{AlNb}$  composition. However, as can be seen in Table 4.1, the measured compositions differed; in particular the Nb contents, which ranged between 23-27at.%. The Al contents were close to the targeted 25at.%. Henceforth these alloys will be referred to by their measured compositions; Ti-25Al-24Nb, Ti-25Al-23Nb, and Ti-25Al-27Nb. For Ti-23Al-27Nb, the Ti, Al, and Nb contents indicate good adherence to the target composition. The interstitial contents, and in particular oxygen, of the Ti-25Al-23Nb and Ti-23Al-27Nb alloys were significantly higher than those of Ti-25Al-24Nb and Ti-25Al-27Nb. This was determined to be a result of the high interstitial contents in the procured ingots<sup>1</sup>. The low-oxygen alloys were processed from the smaller ingots, which were melted from the same batch of starting materials. The high-oxygen materials were processed from another batch of starting materials. Although the starting materials have not been traced to their respective manufacturers, it is believed that the purity of these materials was

---

<sup>1</sup> The Ti-25Al-23Nb and Ti-23Al-27Nb ingots were procured from Duriron, Inc., Dayton, OH, and the Ti-25Al-24Nb and Ti-25Al-27Nb ingots were melted at Wright Laboratory, Dayton, OH.

responsible for the differences in interstitial contents. In particular, it is felt that the smaller ingots made use of low-oxygen sponge. Studies based on materials processed from small ingots melted at the same location also reported low-oxygen interstitial levels (Szaruga *et al.* 1992). The interstitial levels of each alloy was measured after each processing step and none of the processing or heat-treatment steps significantly increased the interstitial contents. The interstitial oxygen levels had a profound influence on the temperature ranges of the high-temperature phase fields and the RT tensile properties. The influence on the former will be described in the following paragraph and the influence on the latter will be described in the tensile behavior result's section.

Table 4.1 Chemical Analysis of the near Ti<sub>2</sub>AlNb Alloys

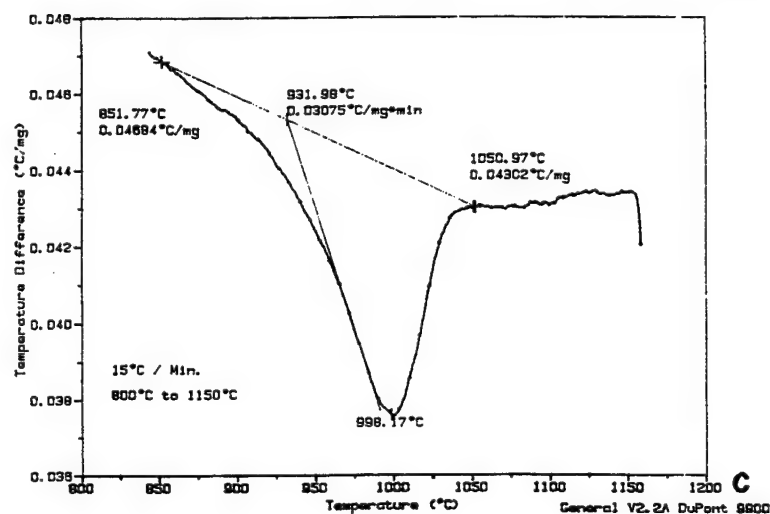
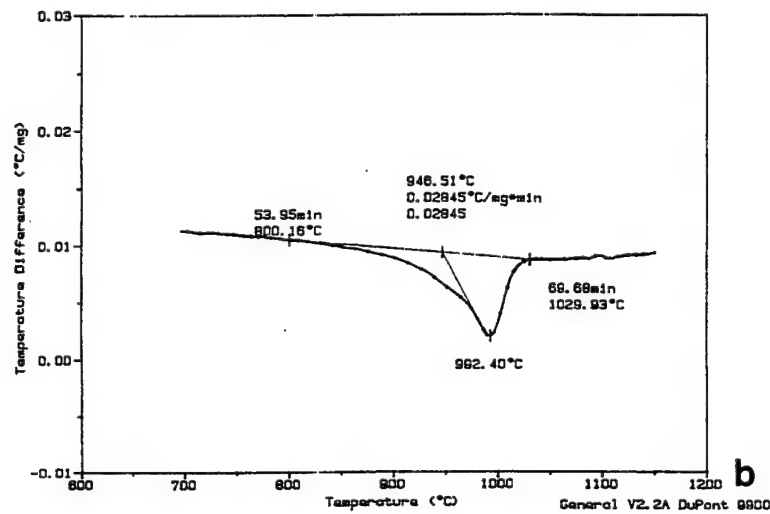
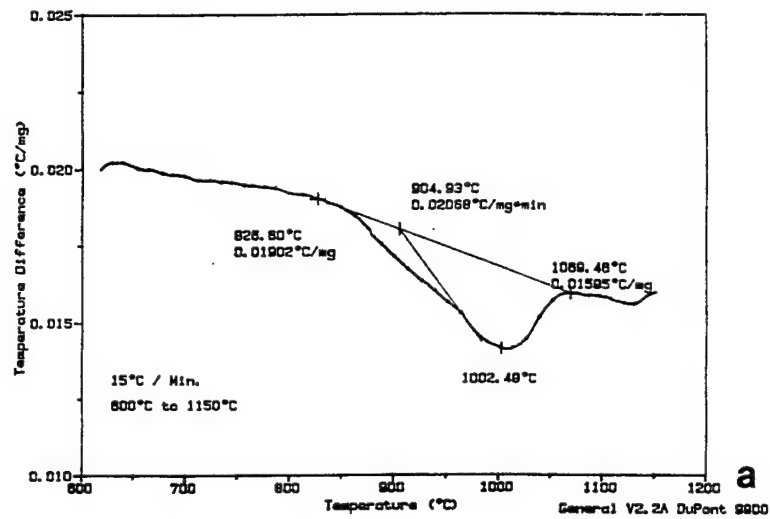
Material	atomic percent			weight parts per million		
	Ti	Al	Nb	N	Fe	O
Ti-23Al-27Nb*	Bal	23.2	27.2	200	1100	1160
Ti-25Al-24Nb*	Bal	25.4	24.2	110	350	280
Ti-25Al-23Nb*	Bal	24.7	23.3	150	290	930
Ti-25Al-27Nb**	Bal	25.0	26.6	120	325	290

\* Sub-transus forged and rolled. \*\* Super-transus processed.

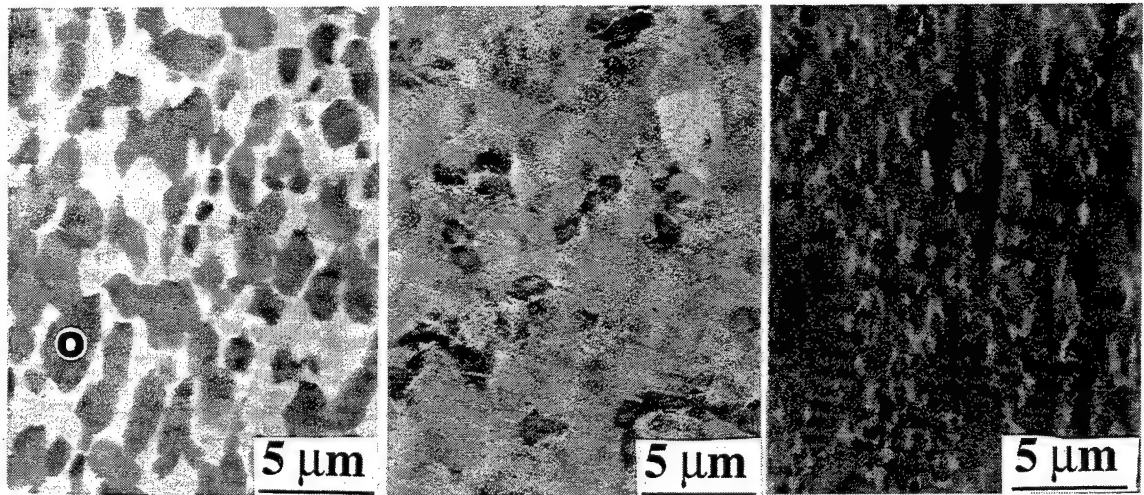
The B2 transus was sensitive to interstitial oxygen content. DTA results, Figures 4.1a-c, indicated the B2 transus to be 1070°C for Ti-23Al-27Nb, 1030°C for Ti-25Al-24Nb, and between 1051-1064°C for Ti-25Al-23Nb, which were in good agreement with the metallographic and XRD observations. The trend shows that the transus temperature increases with lower Al and higher oxygen concentrations, while no consistent trend exists for Nb concentration. Assuming the transus is insensitive to Al and Nb concentrations near Ti<sub>2</sub>AlNb (Bendersky *et al.* 1991), increasing oxygen increments of 220 weight ppm increase the transus roughly 10°C, which is close to that observed for Ti-22Al-23Nb (Rhodes *et al.* 1993) and Ti-25Al-10Nb-3V-1Mo (Szaruga *et al.* 1992). This is also similar to the work of Van Thyne and Kessler (1954), who found that the addition

of 10 Al to pure Ti increased the oxygen sensitivity so that the effect of oxygen on the transus temperature is increased approximately 5°C per 100 ppm oxygen. Thus similar to other studies, oxygen had a profound effect on the B2 transus temperature.

The as-rolled sheet microstructures, depicted in Figures 3.16a and b and Figure 3.3a (lower magnification) and Figures 4.2a-c (higher magnification), contained elongated B2 and O and/or  $\alpha_2$  grains, approximately 4  $\mu\text{m}$  in size, with fine O-phase precipitates within the B2 grains. This precipitation occurred during the gradual cool to RT. Table 4.2 describes the microstructures obtained after different heat treatments for Ti-23Al-27Nb. The average spatial grain size (GS) was calculated using a factor of 1.74 times  $d$ , the planar grain size determined by the mean line-intercept method (Langdon, 1982). The planar grain size was measured for the equiaxed grains associated with the solution-treated microstructures. It is important to note that the GS values listed in Table 4.2 did not represent only one phase, but these values represent the average equiaxed grain size of the entire microstructure and included all the equiaxed-grain-shaped phases present. The sizes of the lath-type phases, occurring in the extremely fine regions, obtained within the equiaxed prior B2 grains after aging treatments, were not measured. The structures of these phases will be described in more detail later in the aging-study section. In general, the grain size increased with increasing solution-treatment temperature, see Table 4.2. The exception to this trend is the 1000°C solution-treated microstructure, which contained a smaller average grain size than that of the 900°C and 950°C solution-treated microstructures, compare rows 3, 4, and 6 of Table 4.2. The reason for this result is that the 1000°C solution-treatment resulted in a three-phase microstructure containing extremely fine  $\alpha_2$  grains. All other solution-treated microstructures represented in Table 4.2 contained only two phases and none of the phases present were as fine as the  $\alpha_2$  phase within the three-phase microstructure. Note that the 1000°C solution-treated, three-phase microstructure was not evaluated in the mechanical behavior study.



Figures 4.1 DTA plot of temperature difference versus temperature for the heating curves of (a) Ti-23Al-27Nb, (b) Ti-25Al-24Nb and (c) Ti-25Al-23Nb. The heating rate was 15°C/minute.



(a) (b) (c)  
Figure 4.2 As-rolled (a) Ti-23Al-27Nb, (b) Ti-25Al-24Nb, and (c) Ti-25Al-23Nb microstructures. The rolling direction is vertical.

Table 4.2 The Measured Average Grain Sizes, Phase Volume Percents and Compositions for the Ti-23Al-27Nb Heat-Treated Microstructures

Heat Treatment	$\alpha_2$			BCC			O			GS $\mu\text{m}$
	Al	Nb	V <sub>p</sub>	Al	Nb	V <sub>p</sub>	Al	Nb	V <sub>p</sub>	
875°C/100h/WQ			0%	15.1	36.5	27%	24.8	24.2	73%	3.8
875°C/40h/WQ/650°C/336h/WQ			0%	na	na	14%	na	na	86%	3.8
900°C/45h/WQ			0%	<b>17.0</b>	<b>33.8</b>	<b>63%</b>	24.4	24.7	37%	5.8
950°C/45h/WQ			0%	<b>20.1</b>	<b>30.7</b>	<b>52%</b>	25.2	23.6	48%	6.6
950°C/45h/WQ/650°C/373h/WQ			0%	na	na	16%	na	na	84%	6.6
1000°C/45h/WQ	25.6	16.1	3%	<b>18.8</b>	<b>31.7</b>	<b>43%</b>	25.0	24.5	54%	5.0
1000°C/45h/WQ/650°C/304h/WQ	25.3	15.8	3%	na	na	16%	na	na	81%	5.0
1025°C/200h/WQ	25.6	15.5	12%	<b>22.1</b>	<b>28.5</b>	<b>88%</b>			0%	8.7
1025°C/45h/WQ/650°C/450h/WQ	25.6	15.4	12%	na	na	14%	na	na	74%	8.7
1090°C/0.5h/WQ			0%	<b>22.0</b>	<b>27.3</b>	<b>100%</b>			0%	177.0
1090°C/0.5h/WQ/650°C/112h/WQ			0%	na	na	<b>20%</b>	na	na	80%	177.0

WQ: water quenched; bold data represents the ordered BCC, B2, structure; na: not available

Phase volume percent (V<sub>p</sub>) and chemical composition are also indicated for each microstructure. Measurement errors of  $\pm 5\%$  and  $\pm 1\%$  apply for the reported values of phase volume percent and composition, respectively. Note the wide variation in V<sub>p</sub>s with heat treatment. In general, the chemistry of the O phase was close to the stoichiometric Ti<sub>2</sub>AlNb composition. The chemistry of the  $\alpha_2$  phase was a relatively constant Ti-25Al-16Nb. The BCC phase composition, which was enriched in Nb, changed depending on

its volume percent. Solution treatment temperatures higher than 875°C favored the B2 phase (bold data); however, the B2 phase disordered below 750°C, in agreement with previous work (Bendersky *et al.* 1991). The structure of the BCC phase between 750-875°C was not determined.

Similar to Table 4.2, Table 4.3 lists the measured microstructural parameters for the Ti-25Al-24Nb, Ti-25Al-23Nb, and Ti-25Al-27Nb alloys. The phase compositions and grain sizes followed similar trends as that of Ti-23Al-27Nb. GS tended to increase with increasing heat-treatment and/or processing temperature. Note the extremely large GS for the super-transus processed Ti-25Al-27Nb alloy, see the last row of Table 4.3. The composition of the B2 phase increased in Al and decreased in Nb for higher-temperature solution treatments. The B2 Vp increased with solutionizing temperature as well. Comparing alloys, the BCC phase volume depended on alloy composition. For a given temperature in the O+B2 phase field, lower B2 volumes were exhibited by those alloys containing greater Al concentration. This was depicted for the 875°C heat treatments where Ti-25Al-24Nb exhibited a fully-O microstructure, while Ti-25Al-23Nb and Ti-23Al-27Nb contained approximately 10 and 27% BCC phase, respectively (compare rows 3 and 10 of Table 4.3 and row 1 of Table 4.2). Thus the BCC phase composition and volume are dependent on temperature.

**Solution-Treatment Study.** In order to identify the temperatures defining the different phase fields, the as-rolled sheets were solution treated at different temperatures followed by water quenching. Selected Ti-23Al-27Nb heat-treated microstructures, which were solutionized in different phase fields, are illustrated in Figures 4.3a-d. In these BSD images, the light, gray, and dark regions correspond to the B2, O, and  $\alpha_2$  phases, respectively. As mentioned, solution treatments of 875°C and above produced equiaxed microstructures containing the B2 phase along with the O and/or  $\alpha_2$  phases. As previously mentioned, the solution-treatment temperatures generally resulted in larger average grain sizes (see rows 1,3,4,6,8,10 of Table 4.2). This average grain size



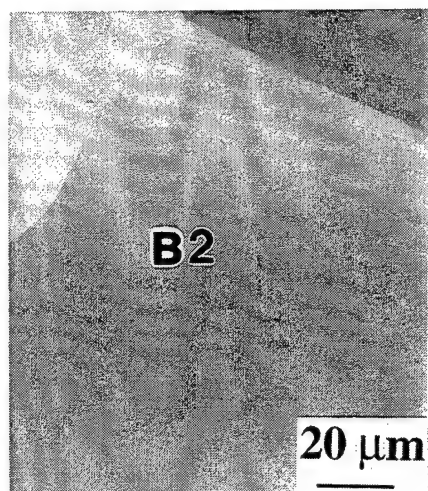
difference, which is primarily an effect of the increasing B2 grain size with temperature, plays an important role in determining mechanical properties as described in the creep behavior sections of Chapters 4 and 5. In addition to grain size, phase volume fraction and morphology, which could be controlled through heat-treatment, were important for the microstructure-property examinations. Thus, heat treatments were used to control microstructures. For example, in order to evaluate phase-volume effects, microstructures of similar phase composition, morphology, and grain size and different phase volume percents were produced through different heat treatments, see row 1 of Table 4.2 and row 9 of Table 4.3.

Table 4.3 The Measured Average Grain Sizes, Phase Volume Percents and Compositions for the Ti-25Al-24Nb, Ti-25Al-23Nb, and Ti-25Al-27Nb Microstructures

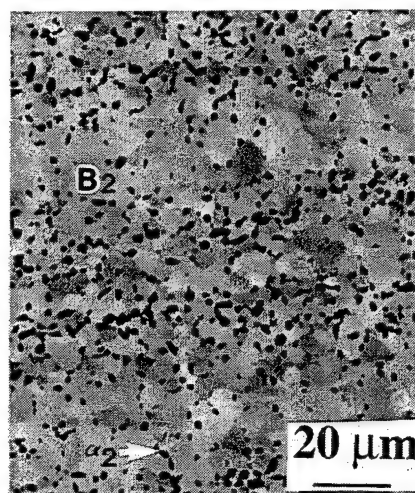
Alloy and Heat Treatment	$\alpha_2$			BCC			O			GS $\mu\text{m}$
	Al	Nb	Vp	Al	Nb	Vp	Al	Nb	Vp	
<b>Ti-25Al-24Nb</b>										
as-rolled (sub-transus)			*	na	na	63%	na	na	37%	4.5
875°C/100h/WQ			0%			0%	25.3	25.5	100%	17.1
875°C/100h/WQ/900°C/8h/WQ			0%	<b>19.8</b>	<b>29.5</b>	<b>18%</b>	24.9	24.7	82%	17.1
930°C/100h/WQ			0%	<b>17.2</b>	<b>32.6</b>	<b>5%</b>	24.9	24.8	95%	10.1
975°C/100h/WQ			0%	<b>21.9</b>	<b>28.4</b>	<b>21%</b>	25.4	24.5	79%	10.4
<b>Ti-25Al-23Nb</b>										
650°C/166h/WQ			0%	na	na	5%	24.8	24.9	95%	3.8
875°C/100h/CC			0%	15.9	31.8	10%	24.5	22.9	90%	na
910°C/8h/WQ			0%	na	na	<b>6%</b>	na	na	94%	8.4
910°C/8h/WQ/650°C/218h/WQ			0%	na	na	4%	na	na	96%	8.4
950°C/45h/WQ			0%	20.8	27.5	<b>25%</b>	25.2	22.7	75%	na
950°C/45h/WQ/650°C/223h/WQ			0%	na	na	5%	25.2	22.6	95%	na
1010°C/8h/WQ	25.7	15.2	6%	<b>23.8</b>	<b>24.8</b>	<b>94%</b>			0%	na
<b>Ti-25Al-27Nb</b>										
as-processed (super-transus)			0%	na	na	4%	na	na	96%	1305.0

WQ: water quenched; CC: control cooled at 28°C/minute to RT; na: not available; \*: a small volume of  $\alpha_2$  phase may have been present; bold data represents the ordered BCC, B2, structure.

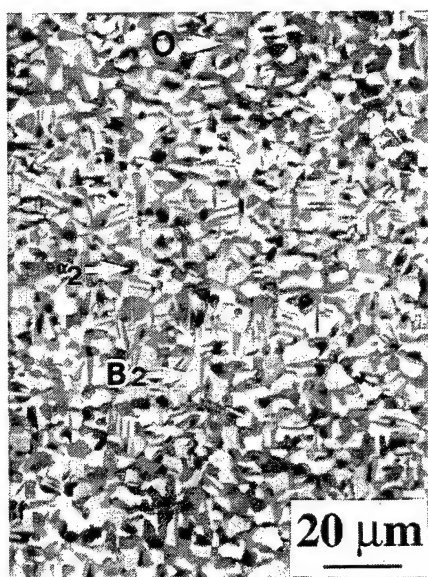
Solution treatments above the B2 transus resulted in large-grained fully-B2 microstructures, Figure 4.3a. XRD data which displayed three main peaks and the super-lattice (210) peak, see Figure 4.4, confirmed the presence of the ordered B2 phase.



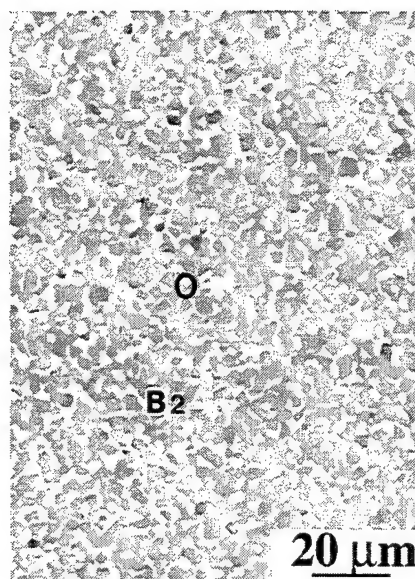
(a)



(b)



(c)



(d)

Figure 4.3 Microstructures of Ti-23Al-27Nb solution treated and water quenched samples. Solution-treatment temperatures were (a) 1090°C, (b) 1025°C, (c) 1000°C, and (d) 900°C.

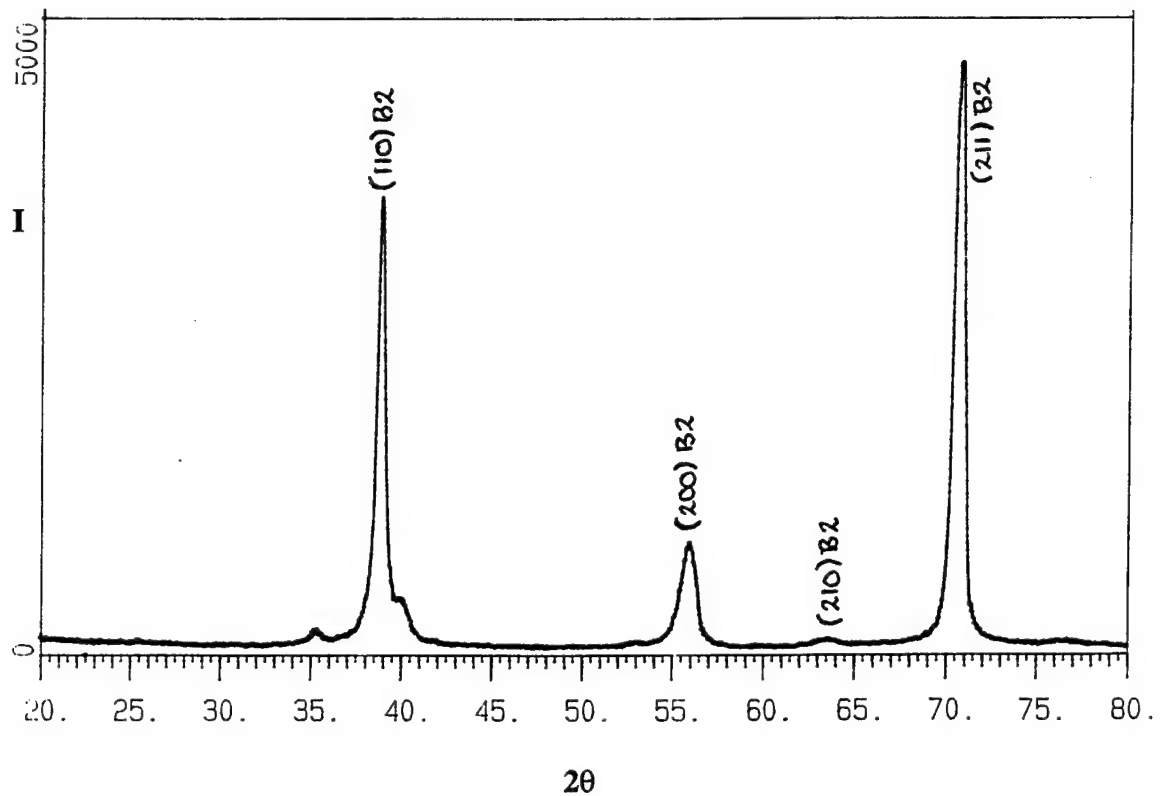


Figure 4.4 XRD plot of Intensity versus  $2\theta$  for a Ti-25Al-24Nb heat-treated (1090°C/0.5h/WQ) fully-B2 microstructure.

Solution treatments between 1000°C and the B2 transus resulted in  $\alpha_2$ +B2 microstructures. As described earlier, the transus temperatures were higher for those alloys containing greater interstitial oxygen. Thus, in agreement with observations of increased  $\alpha_2$  stability with increased interstitial oxygen level (Rhodes *et al.* 1993, Boehlert *et al.* 1997a, Takag and Ouchi 1997), larger interstitial oxygen contents resulted in a greater  $\alpha_2$ +B2 temperature range. A 1025°C treatment exhibited a majority of B2 phase, approximately 88% by volume, with the remainder as  $\alpha_2$ , Figure 4.3b. The OR between adjacent  $\alpha_2$  and B2 grains was:  $[11\bar{2}0]\alpha_2//[1\bar{1}1]B2$ ;  $(0001)\alpha_2/(011)B2$ , which is the well known Burgers OR (Burgers 1934). A SADP depicting this relationship is given in Figure 4.5a. Work by Sagar *et al.* (1996) has shown that at 975°C, the  $\alpha_2$  phase

undergoes dynamic recrystallization which destroys the Burgers OR. Assuming no  $\alpha_2$ /B2 OR exists in the as-rolled microstructure, the current OR was restored through the sub-transus 1025°C solution treatment, where both the  $\alpha_2$  and B2 phase volumes increased at the expense of the O-phase volume. Previously, ORs were found in microstructures where the  $\alpha_2$  phase grew from a single-phase B2 microstructure (Saqib *et al.* 1995). In the current study the microstructure evolved from the as-rolled microstructure. Thus, the  $\alpha_2$  phase evolves from the B2 phase even in equiaxed sub-transus microstructures.

Just below the two-phase  $\alpha_2$ +B2 phase field lies a three-phase  $\alpha_2$ +B2+O field. The relatively narrow temperature range for this field was 975-1000°C. A typical three-phase  $\alpha_2$ +B2+O microstructure is depicted in Figure 4.3c, where the B2 phase was continuous. Because the O phase formed preferentially as a ring around the  $\alpha_2$  phase, some  $\alpha_2$  phase is expected to have been present in the as-rolled microstructure. This microstructure is similar to three-phase microstructures in other O alloys (Muraleedharan *et al.* 1992a, Gogia *et al.* 1992, Majumdar *et al.* 1994 1995, Smith *et al.* 1995, Boehlert *et al.* 1997a), except the 'rim-O' phase is much thicker for the current case. The  $\alpha_2$  content was only 3% (see row 6 of Table 4.2), indicating that a large volume of the  $\alpha_2$  phase may not be achievable in this region.

The O+B2 field ranged between 875-975°C. Solution treatments in this field resulted in equiaxed O+B2 microstructures without any  $\alpha_2$  and lower temperatures corresponded to greater O volumes, see rows 1, 3, and 4 of Table 4.2 and rows 3,5,6 and 10,11,13 of Table 4.3. Figure 4.3d depicts a 900°C heat-treated microstructure which contained approximately 63% O by volume, see row 3 of Table 4.2. The OR found between the O and B2 grains is common (Muraleedharan *et al.* 1992b),  $[\bar{1}11]_{B2} // [1\bar{1}0]_O$ ;  $(110)_{B2} // (001)_O$ , see Figure 4.5b. For the microstructures of Figures 4.3b-d, the B2 phase was verified by super-lattice reflections in the  $[001]$  B2 SADP, see Figure 4.5c.

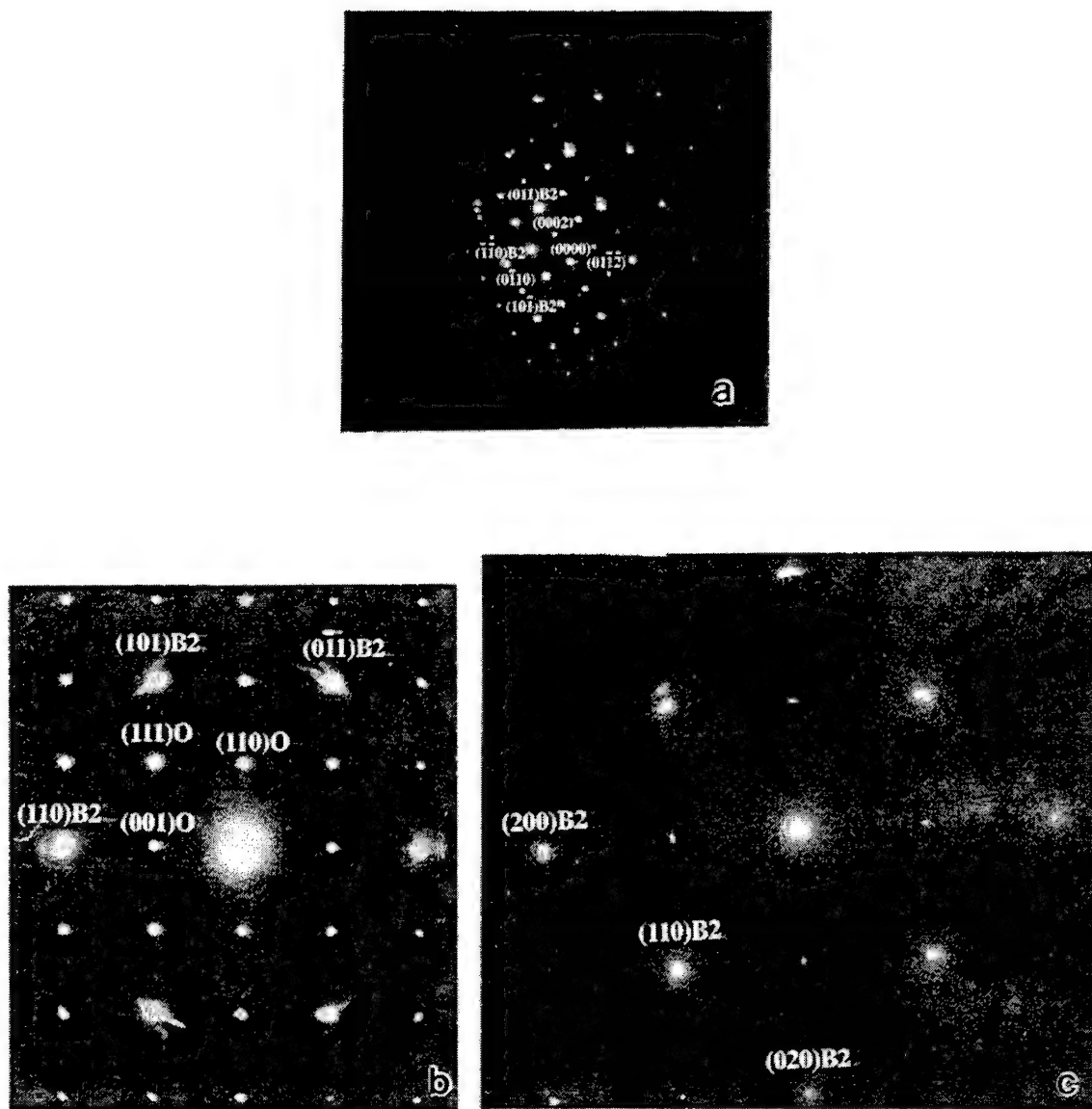


Figure 4.5 SADPs taken from neighboring (a)  $\alpha_2$ +B2 and (b) O+B2 grains for 1025°C/40h/WQ and 900°C/45h/WQ solution treatments, respectively, of Ti-23Al-27Nb. The ORs are:  $[11\bar{2}0]\alpha_2//[1\bar{1}1]B2$ ;  $(0001)\alpha_2//(011)B2$ ,  $[\bar{1}11]B2//[1\bar{1}0]O$  and  $(110)B2//(001)O$ . (c) Verification of the ordered B2 structure in a 900°C solution-treated sample depicting super-lattice reflections from a  $[001]$  zone axis.

In addition to the determination of the temperature boundaries for the respective phase fields, three important observations regarding the phase evolution of  $\text{Ti}_2\text{AlNb}$  alloys were obtained from the solution-treatment study. The first observation is that samples subjected to super-transus solution treatments, which were either control cooled (CC) to RT or water quenched (WQ) and then aged in the O+B2 region, were devoid of equiaxed phases and retained large prior B2 grains containing fine precipitates of O and  $\alpha_2$ , see Figures 4.6a and b. The fine  $\alpha_2$  precipitates formed at prior B2 grain boundaries during the controlled cooling, see Figure 4.6a. Thus, fine equiaxed grains are only obtainable when hot work is performed below the transus. For samples solutionized in the  $\alpha_2$ +B2 region which were then heated in the O+B2 region, the microstructures maintained the  $\alpha_2$  phase and contained Widmanstätten O within the prior B2 grains. In addition the 'rim-O' phase was observed around  $\alpha_2$  similar to that of the samples solution treated within the three-phase field. Figures 4.7a and b compare the microstructures of samples solutionized in the  $\alpha_2$ +B2 region; one of which was then heated in the O+B2 region. Combining these observations, the O phase tends to grow from the B2 phase in a lenticular fashion for samples solutionized in the higher-temperature B2 and  $\alpha_2$ +B2 fields. However, processing near the O+B2 field followed by solutionizing within the O+B2 field results in equiaxed O+B2 microstructures, see Figure 4.3d. For equiaxed O+B2 microstructures, the B2 decomposes lenticularly below a certain transition temperature as described in the aging-study section.

The second observation is that solution treatments near 875°C provided an interesting contrast in microstructures for near  $\text{Ti}_2\text{AlNb}$  alloys. The phase morphology, associated with O phase growth, transitions near 875°C. Above 875°C, equiaxed primary B2 grains coarsen while equiaxed primary O grains shrink. Below 875°C, Widmanstätten O and BCC phases evolve as is described in the aging-study section. In addition, 875°C solution treatments depict the effect of nominal composition on microstructure where those alloys which contained higher Al exhibited higher volumes of

primary equiaxed O phase, see Figures 4.8a-c. In fact, a fully-O microstructure, depicted in Figure 4.8a, was obtained for the Ti-25Al-24Nb alloy, while the other two alloys, which contained less Al, exhibited some equiaxed B2 grains. The lowest Al-containing alloy, Ti-23Al-27Nb, exhibited the greatest B2 volume, see Figure 4.8c. Due to phase stability issues and the slower diffusion kinetics for phase transformation at lower temperatures, which is described in the aging-study section, solution treatments near 875°C may be the most practical method of obtaining stable fully-O microstructures for sub-transus processed Ti<sub>2</sub>AlNb.

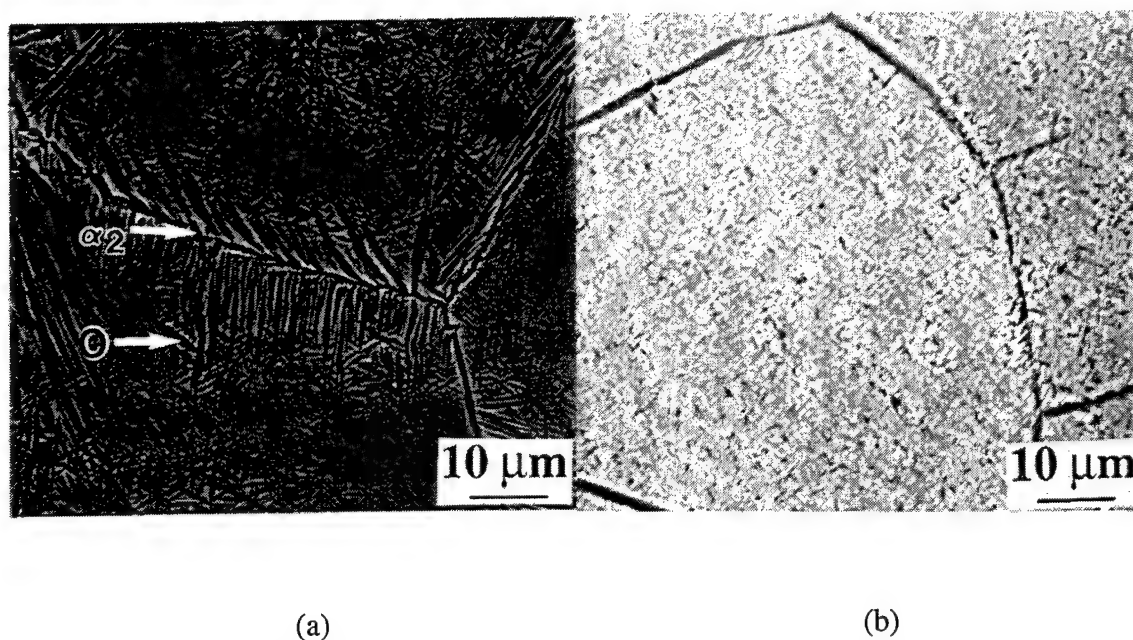


Figure 4.6 Super-transus heat-treated Ti-23Al-27Nb microstructures: (a) 1150°C/0.5h/CC at 15°C/min. to RT and (b) 1090°C/0.5h/WQ/900°C/8h/WQ; containing large prior B2 grains with O and  $\alpha_2$  precipitates.

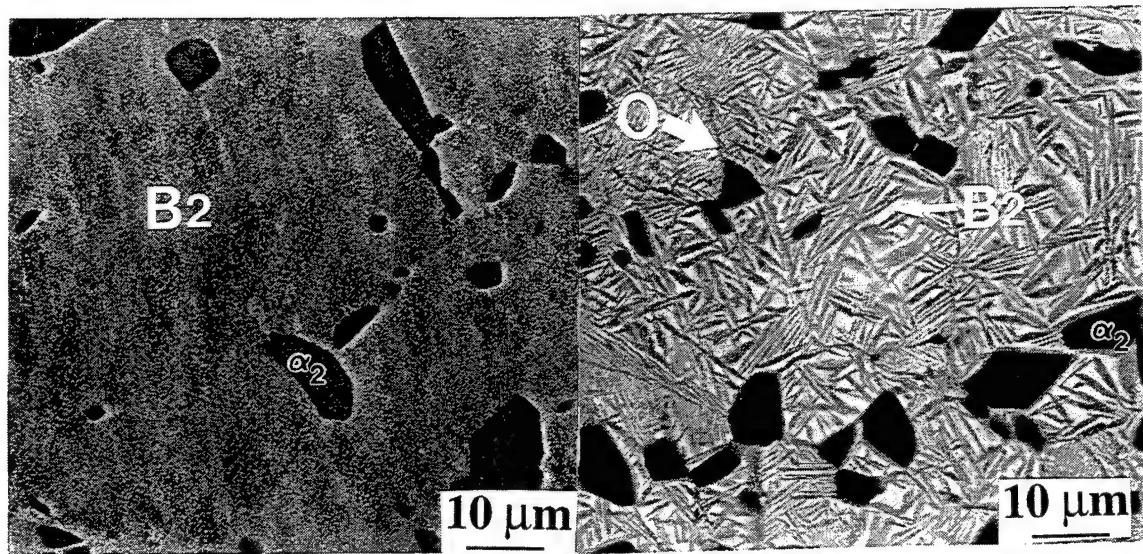
The third observation regarding phase evolution is that a fully-lenticular O+B2 microstructure was exhibited when the fully-O microstructure (see Figure 4.8a) was re-

solutionized in the O+B2 region followed by water quenching, see Figure 4.9a. In this case, the B2 phase was expected to have nucleated at grain boundaries and then grew in a lenticular fashion within the equiaxed O grains. This is markedly different from the B2 growth in the as-rolled microstructures where the pre-existing B2 phase coarsened in an equiaxed morphology. Thus similar to O-phase precipitation in super-transus fully-B2 microstructures, see Figures 4.6a and b, Widmanstätten precipitation of the B2 phase occurred within fully-O microstructures. It is noted that this may not be an equilibrium condition as the B2 phase volume for this heat treatment (900°C) was greater than that at 930°C, compare rows 4 and 5 of Table 4.3. It is also noted that slowly heating the fully-O microstructure from 875°C to 900°C resulted in an equiaxed O+B2 microstructure. Thus the quenching treatment prior to re-solutionizing appeared to favor the lenticular nucleation and growth of the B2 phase. This observation is useful from a microstructure-property point-of-view as the morphology of O+B2 microstructures may be significantly altered while the phase volume percents and compositions may be held relatively constant. Figures 4.9a and b depict O+B2 microstructures containing similar phase volume percents and different morphologies. Because fully-O microstructures were not obtained for Ti-23Al-27Nb and Ti-25Al-23Nb, sub-transus heat-treated fully-lenticular O+B2 microstructures were also not obtained. Therefore microstructure is sensitive to both alloy composition and heat treatment. Overall, through the proper selection of alloy composition and thermomechanical processing steps (including heat treatments), a range of microstructures including fully-O and fine-grained, fully-lenticular O+B2 microstructures are capable for near Ti<sub>2</sub>AlNb alloys.

Aging Study. In order to investigate microstructural stability, aging treatments were performed on selected solutionized and water quenched samples. Figure 4.10a depicts a Ti-23Al-27Nb baseline O+B2 microstructure solutionized at 950°C for 45 hours. Figures 4.10b-d illustrate the microstructures obtained after aging treatments between 650-850°C for 13 hours followed by water quenching. Each microstructure exhibited Widmanstätten



precipitates of the O phase within the B2 grains. The size and volume of the precipitates depended on aging temperature. The largest precipitate size occurred at 850°C and the finest size was exhibited at 650°C. The primary O grains remained relatively unchanged. This is an important aspect for the design of microstructures because the ratio of the primary O phase volumes to the precipitated O phase volumes will differ depending on the initial solution treatment. In addition, the primary O and prior B2 grain sizes were unaffected by aging as the precipitation only occurred within the B2 grains. Aged microstructures which were re-solution treated above and below 875°C reconfirmed the morphological transition; those microstructures re-solutionized below 875°C remained lenticular while those re-solutionized above 875°C contained only equiaxed grains. Thus, Widmanstatten precipitation starts between 850-875°C for sub-transus, two-phase O+B2 near Ti<sub>2</sub>AlNb alloy microstructures.



(a) (b)

Figure 4.7 Comparison of the Ti-23Al-27Nb (a)  $\alpha_2$ +B2 solution-treated (HT:1025°C/200h/WQ) microstructure with (b) that for the solution-treated microstructure after subsequent heating within the O+B2 field (HT:1025°C/200h/WQ/925°C/2h/WQ). Note the  $\alpha_2$  phase remained and Widmanstatten O precipitated in (b).

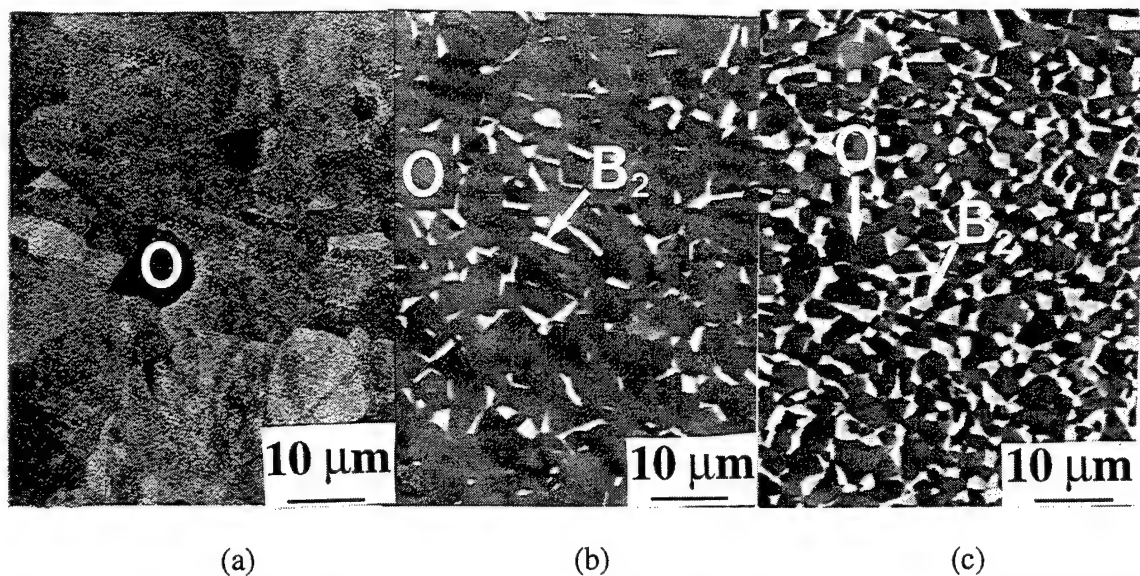


Figure 4.8 Near  $\text{Ti}_2\text{AlNb}$  microstructures which have been solution treated at  $875^\circ\text{C}$ : (a) Ti-25Al-24Nb, (b) Ti-25Al-23Nb, and (c) Ti-23Al-27Nb. These images show the effect of alloy composition, in particular Al content, on O phase volumes.

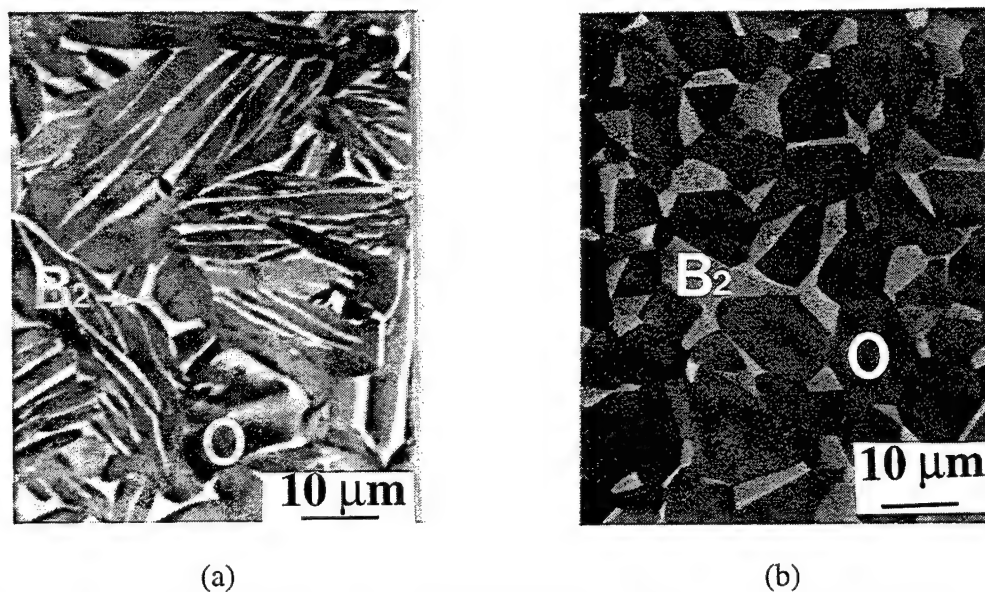


Figure 4.9 Ti-25Al-24Nb heat-treated sheet microstructures: (a)  $875^\circ\text{C}/100\text{h}/\text{WQ}/900^\circ\text{C}/8\text{h}/\text{WQ}$  and (b)  $975^\circ\text{C}/100\text{h}/\text{WQ}$ . These microstructures depict the effect of heat treatment on morphology.

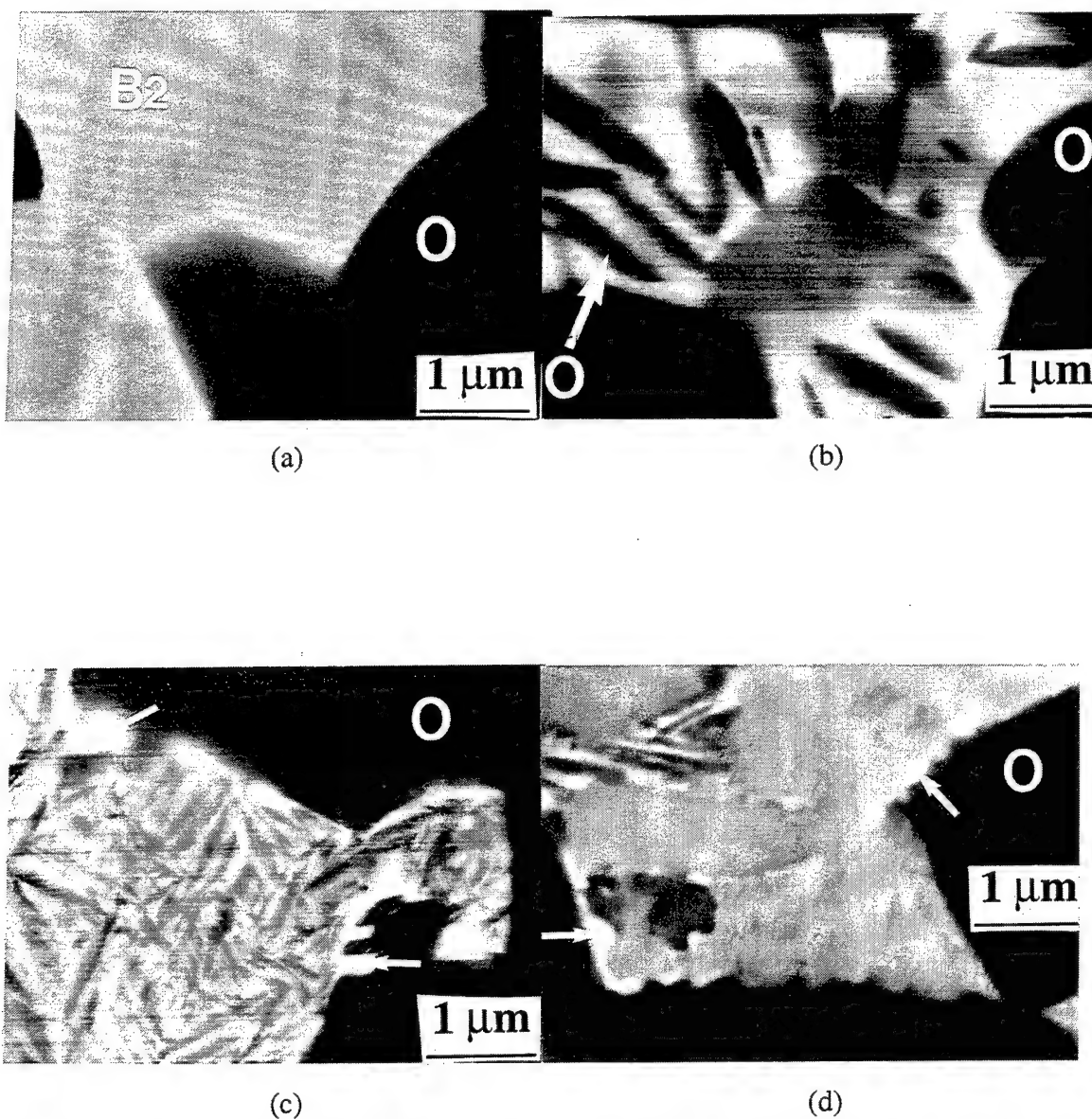


Figure 4.10 Effect of aging temperature on microstructure. Comparison of a Ti-23Al-27Nb solution-treated (a) (950°C/45h/WQ) microstructure with solution-treated and aged microstructures. The specimens were aged at (b) 850°C, (c) 750°C, and (d) 650°C for 13 hours followed by water quenching. The arrows indicated in (c) and (d) represent the initiation of discontinuous precipitation.

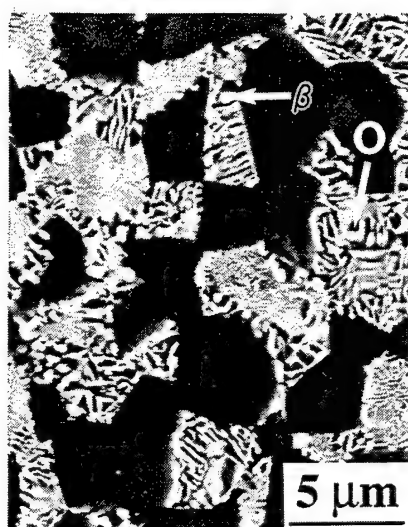
The microstructures obtained on aging at 650°C and 750°C depicted a small volume of discontinuous precipitation initiating at O/B2 interfaces, indicated by arrows in Figures 4.10c and d. This phenomenon, which resembled the initial stages of cellular reaction (Tu 1972), was investigated in detail using long-term aging treatments. Figures 4.11a-d depict the microstructural changes occurring after aging at 650°C for 24, 48, 96 and 304 hours. For long aging times, the discontinuous precipitation products coarsened and advanced into B2 grains. The migration of the discontinuous transformation interface resulted in the consumption of the fine, uniformly distributed Widmanstatten precipitates. After 304 hours, some of the fine precipitates remained, indicative that the discontinuous precipitation was incomplete. This is evident in the 1025°C  $\alpha_2$ +B2 solution-treated (Figure 4.12a) case where after 610 hours at 650°C, see Figure 4.12b, a large volume of the discontinuous precipitation was present yet some of the finer precipitation remained. The discontinuous precipitation was characterized by both O-phase precipitation and disordering of the B2 phase as CBED patterns, Figures 4.13a and b, taken from the frontal regions, identified the alternating platelets as O and  $\beta$ . High magnification dark field images of these regions are depicted in Figures 4.14a and b and the corresponding OR between the platelets,  $[01\bar{1}]\beta//[00\bar{1}]O$ ,  $(\bar{2}11)\beta//(110)O$ , is depicted in Figure 4.14c. Misfit dislocations were observed within the discontinuously precipitated regions and formed preferentially at O/ $\beta$  interfaces, Figure 4.15. This transformation behavior occurred independent of slight changes in nominal composition for near Ti<sub>2</sub>AlNb alloys. The 650°C aged microstructures of solution-treated Ti-25Al-24Nb and Ti-25Al-23Nb samples are depicted in Figures 4.16a and b. Interestingly, the Ti-25Al-24Nb fully-O microstructure (see Figure 4.8a) remained fully O after aging at 650°C, while the O+B2 microstructures did not transform to fully-O microstructures, see Figure 4.16a. Thus the transformation kinetics at 650°C are expected to be quite slow.



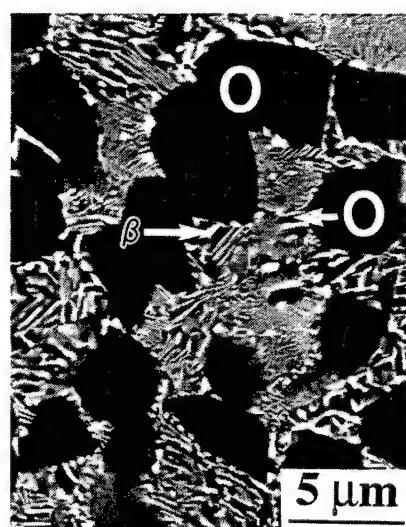
(a)



(b)



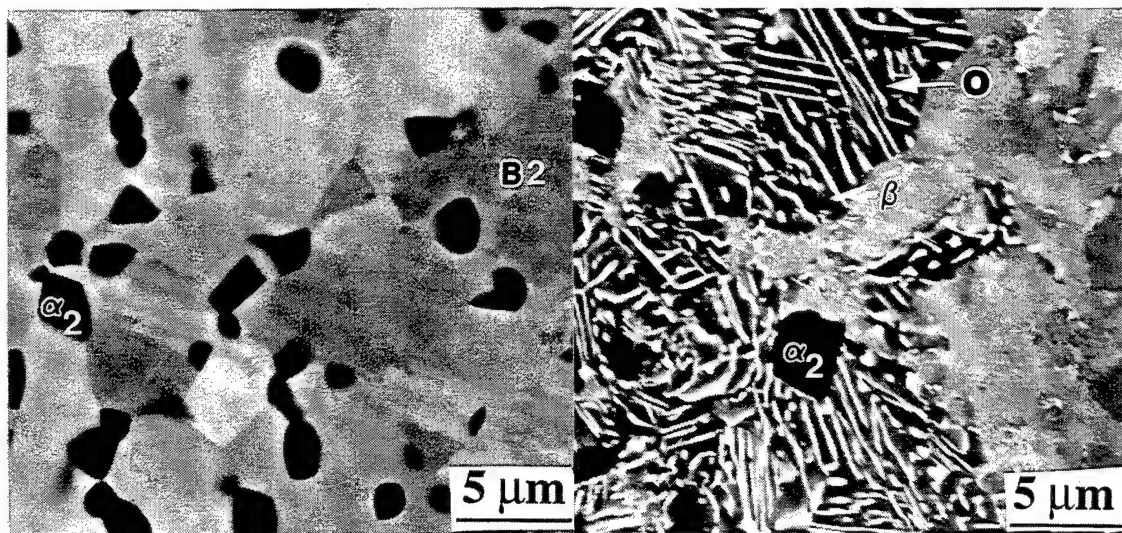
(c)



(d)

Figure 4.11 Effect of aging time on microstructure. These Ti-23Al-27Nb specimens were solution-treated at 950°C and then aged at 650°C for (a) 24 hours, (b) 48 hours, (c) 100 hours, and (d) 304 hours followed by water quenching.

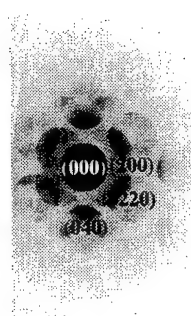




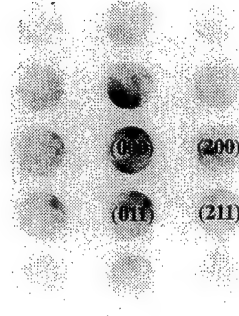
(a)

(b)

Figure 4.12 Ti-23Al-27Nb microstructures obtained by (a) solution treatment at 1025°C/45h/WQ and (b) solution treatment at 1025°C/45h/WQ plus aging at 650°C/610h/WQ. The majority of the B2 phase has undergone discontinuous precipitation.



(a)



(b)

Figure 4.13 CBED patterns taken from the discontinuous precipitating region for a Ti-23Al-27Nb 950°C/45h/WQ/650°C/373h/WQ heat-treated sample. The patterns are identified as (a)  $[00\bar{1}]O$  and (b)  $[01\bar{1}]\beta$ .

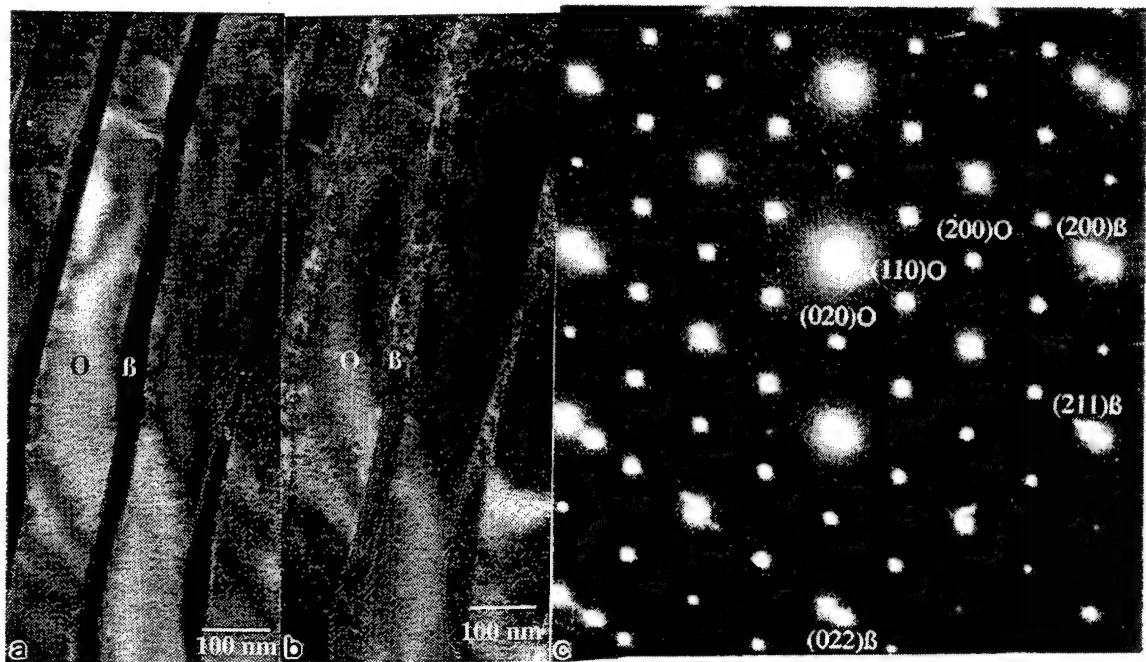


Figure 4.14 Dark field images of the (a) O phase and (b) O+β phase platelets corresponding to the CBED patterns of Figure 4.13. (c) SADP taken from the same region depicting the corresponding OR:  $[01\bar{1}]\beta//[00\bar{1}]O$ ,  $(211)\beta//(110)O$ .

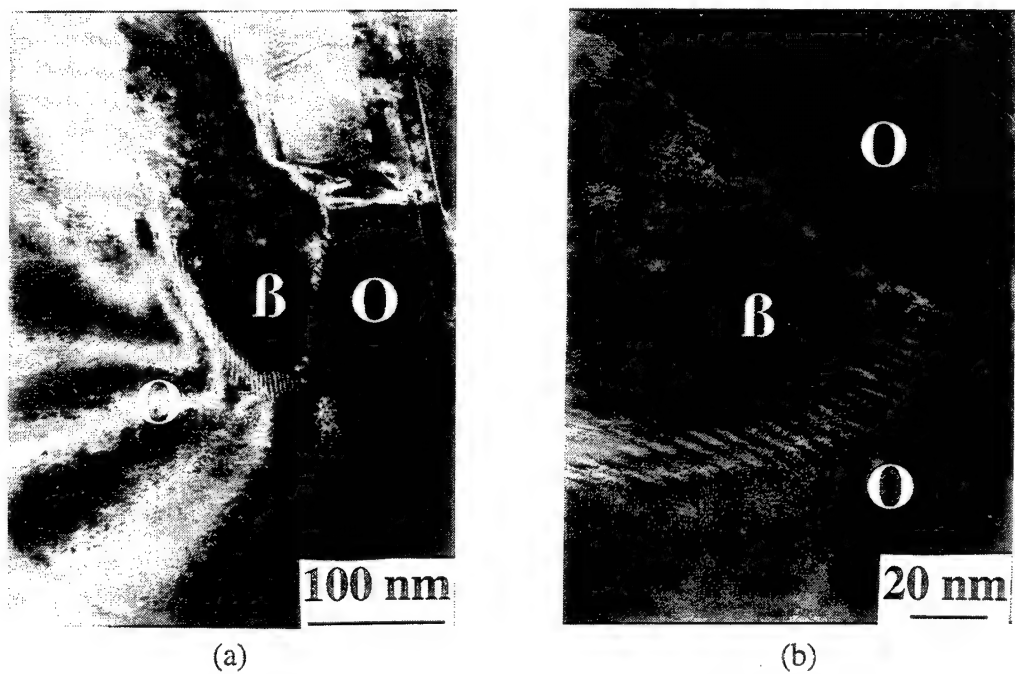


Figure 4.15 (a) Lower and (b) higher magnification bright field images of transformation misfit dislocations at O/β interfaces for a Ti-23Al-27Nb 950°C/45h/WQ/650°C/66h/WQ heat-treated sample.

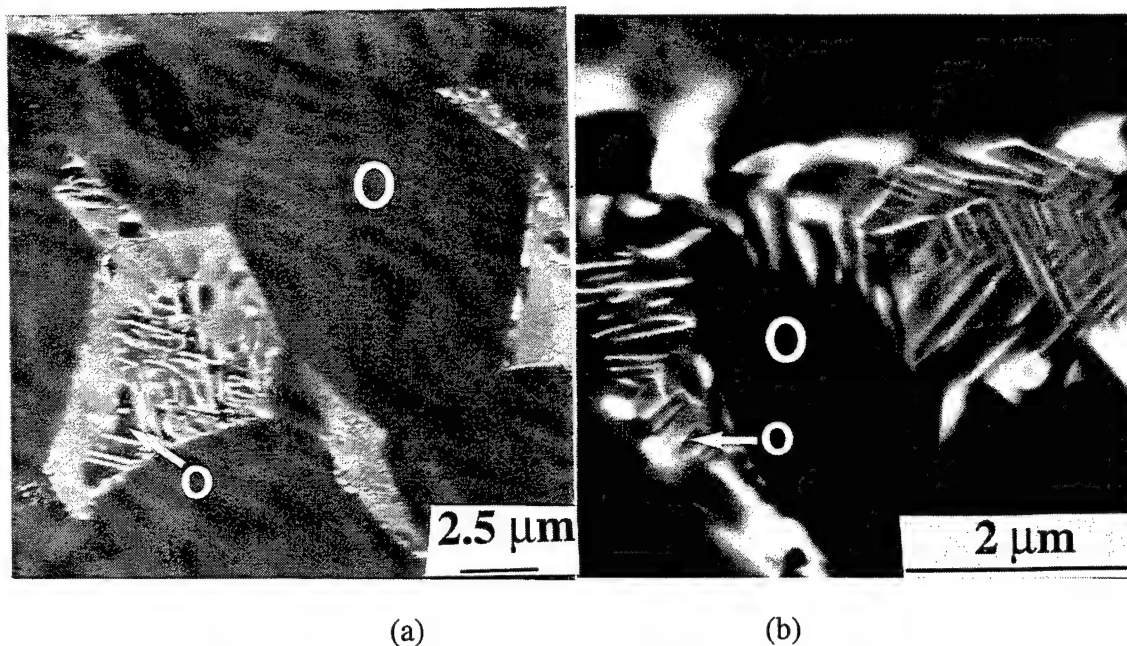


Figure 4.16 Solution treated and aged microstructures for (a) Ti-25Al-24Nb (975°C/100h/WQ/650°C/300h/WQ) and (b) Ti-25Al-23Nb (950°C/45h/WQ/650°C/304h/WQ). The microstructures exhibited discontinuous precipitation at prior B2 grain boundaries.

The  $\beta$  phase was not solely associated with the discontinuously precipitated regions. It was also found within the fine, homogeneously-precipitated regions. Interestingly, in some cases the ordered B2 phase was also retained in regions surrounding the fine-precipitated O phase. Figure 4.17 depicts transformed B2 grains containing both  $\beta$  and B2 in the uniformly precipitated regions. The discontinuous precipitation was exhibited in very small volumes for those microstructures solution treated below 950°C prior to aging. In those cases the majority of precipitation occurred homogeneously throughout the bulk. This is depicted for a 875°C solutionized then aged Ti-23Al-27Nb sample in Figure 4.18. A comparison of the amounts of discontinuous precipitation present for samples solutionized at different temperatures can also be made using Figures 4.11d and 4.43b, which represent the aged microstructures of samples solutionized at 950°C and 910°C, respectively.



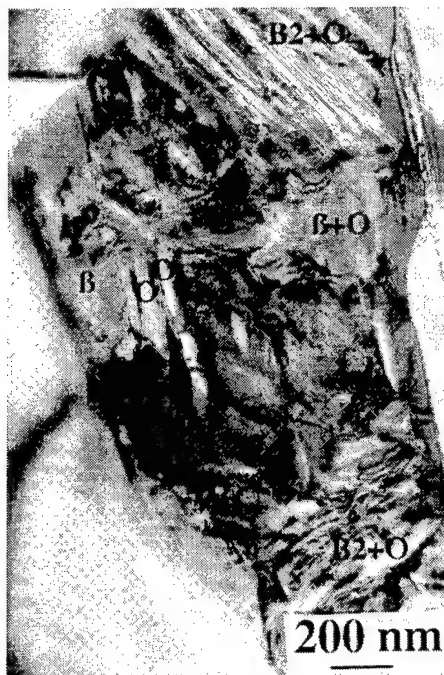


Figure 4.17 A transformed B2 region containing the  $\beta$ , B2, and O phases for a Ti-23Al-27Nb 875°C/40h/WQ/650°C/320h/WQ heat-treated sample.

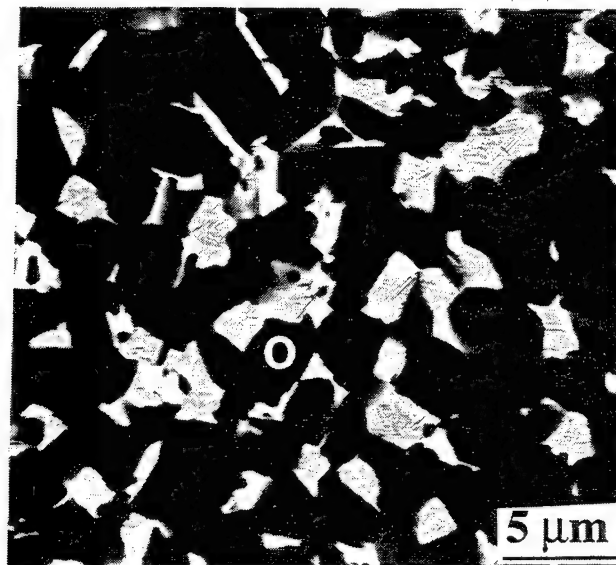


Figure 4.18 SEM micrograph of a transformed B2 region containing only small volumes of discontinuous precipitation for a Ti-23Al-27Nb 875°C/40h/WQ/650°C/288h/WQ heat-treated sample.

The following summarizes the microstructural observations from the aging study performed on sub-transus solutionized samples. The O phase precipitated

homogeneously within B2 grains for all solution-treated samples which were aged below 875°C. Discontinuous precipitation, characterized as alternating O+ $\beta$  platelets at O/B2 or  $\alpha_2$ /B2 grain boundaries, was exhibited for solution-treated and quenched samples which were aged at  $T \leq 750^\circ\text{C}$ . Samples solutionized at higher temperatures and aged at lower temperatures exhibited greater volumes of discontinuous precipitation. The prior B2 regions not associated with the discontinuous precipitation contained Widmanstätten O precipitates with surrounding  $\beta$  and/or retained B2 phases. After aging at 650°C for long times, Ti-25Al-24Nb fully-O microstructures remained fully-O and O+BCC microstructures remained O+BCC, indicating the transformation kinetics are quite slow at this temperature. Temperature dictates the BCC phase composition and the discontinuous precipitation appears to be driven by the compositional gradient within the BCC phases as described in phase evolution discussion section of Chapter 5.

Although the fully-B2 super-transus solution-treated then aged microstructures also exhibited grain-boundary precipitation, the precipitation behavior was not identical to that of the sub-transus solutionized then aged microstructures. Figures 4.19a-c depict the Ti-23Al-27Nb super-transus solutionized baseline microstructure of Figure 4.3a after aging times of 2, 9, and 100 hours, respectively, at 650°C. Identical heat treatments were performed for Ti-25Al-23Nb and the corresponding SEM images are illustrated in Figures 4.20a-d, where Figure 4.20a depicts the super-transus solutionized and quenched microstructure and Figures 4.20b-d represent the 2, 9, and 100 hour aged conditions. Although the 2 hour aged Ti-23Al-27Nb microstructure did not appear to be much different than the unaged microstructure, compare Figures 4.3a and 4.19a, XRD results indicated that significant transformation took place. In fact, after only 15 minutes at 650°C, the XRD peaks had shifted. Figures 4.21a-c compare XRD plots of intensity versus  $2\theta$  for the as-solutionized Ti-23Al-27Nb sample as well as the 15 minute and 2 hour aged samples. The  $2\theta$  values of the peaks for the aged samples were different than those of the B2 peaks for the solutionized and unaged sample, indicative that a

transformation had occurred. For the aged samples, several new peaks were observed at  $2\theta$  values expected for the O phase. These peaks are labeled in Figures 4.21b and c. It is noted that some of the calculated  $2\theta$  values for both O and B2 peaks are quite close, making it difficult to distinguish between the phases using the measured  $2\theta$  peak values. For example, (211)B2 and (223)O peaks are expected for  $2\theta$  values between  $70.5$ - $70.9^\circ$ . Other  $2\theta$  peak values, however, such as that for the (042)O ( $2\theta \sim 55.0^\circ$ ), (041)O ( $2\theta \sim 42.3^\circ$ ), and (262)O ( $2\theta \sim 66.2^\circ$ ) peaks, are only associated with the O phase and therefore make it easier to distinguish between the phases. These XRD results do not confirm that complete transformation from B2 to O had occurred, however they do indicate that within 15 minutes the O phase transformed within B2. For this reason the microstructures which were aged for at least 15 minutes were considered to be composed of transformed B2 grains.

Metallography revealed that for short aging times ( $t \leq 9\text{h}$ ), aligned platelets coarsened at B2/B2 boundaries, see Figures 4.19a,b and 4.20b,c. A higher magnification image of the platelets is depicted in Figure 4.22. Each group of aligned platelets can be considered as a colony. With increased aging time, the interface of the colony and the transformed-B2 grain migrated toward the interior of the grain similar to that for the sub-transus solutionized and aged microstructures. Unlike the sub-transus solutionized and aged microstructures, the platelets behind the migrating interface divided into separate cells containing distinct boundaries. These cells coarsened with time and formed an elliptical shape so that for longer aging times the microstructure could be described as colonies containing several equiaxed-shaped cells. Eventually the separate colonies impinged upon each other and after 100 hours the colonies consumed nearly all of the prior B2 grains, see Figures 4.19c and 4.20d. The growth of the colonies appeared to be more rapid for Ti-25Al-23Nb than Ti-23Al-27Nb. Although, the compositional dependence on the kinetics of the colony growth are not well known at present, this is the first observation to suggest such a dependence.

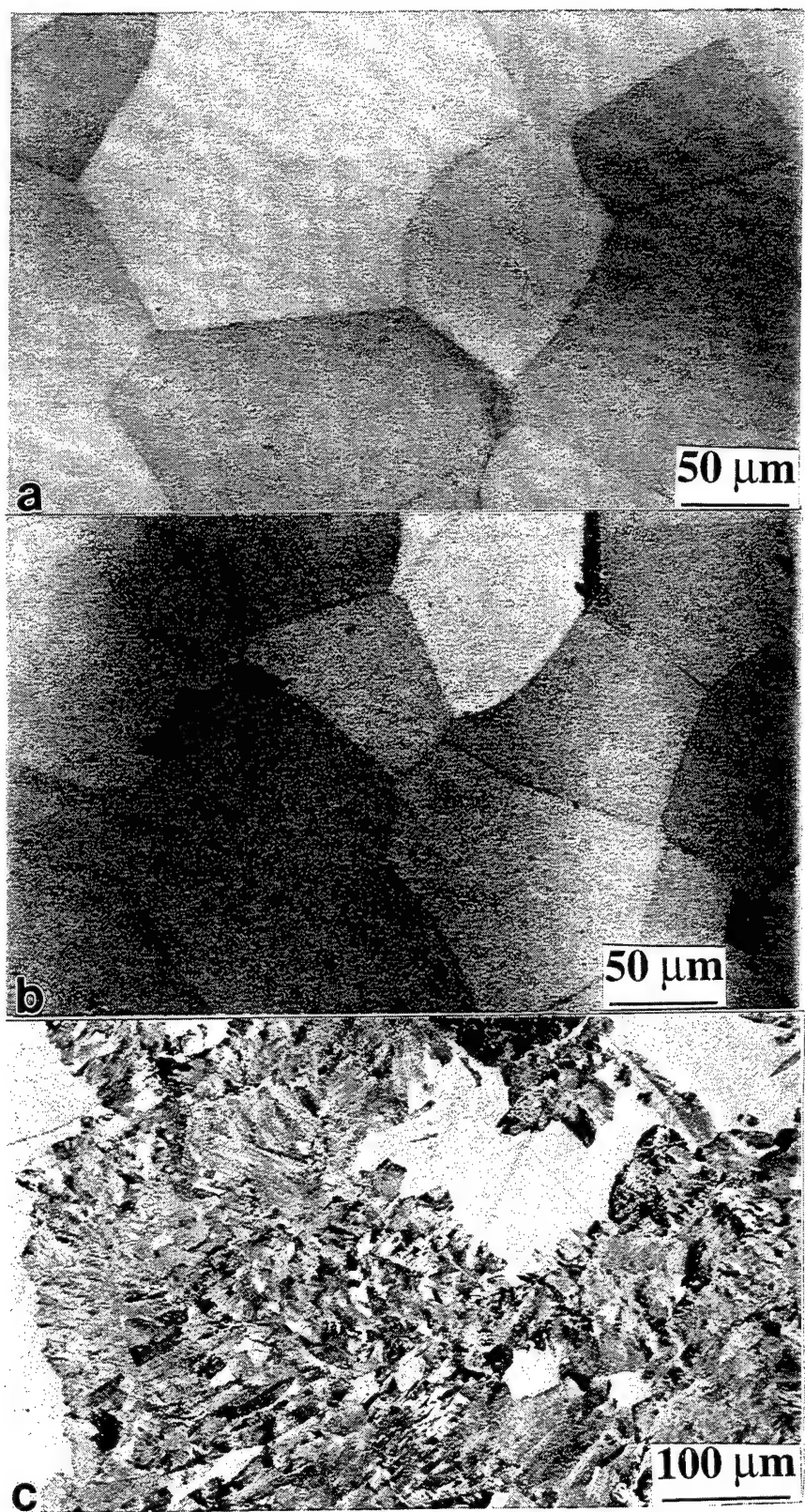


Figure 4.19 Ti-23Al-27Nb super-transus solution-treated samples ( $1090^{\circ}\text{C}/0.5\text{h}/\text{WQ}$ ) which were aged at  $650^{\circ}\text{C}$  for (a) 2, (b) 9 and (c) 100 hours, followed by water quenching. Precipitates coarsened at (transformed-B2)/(transformed-B2) boundaries.

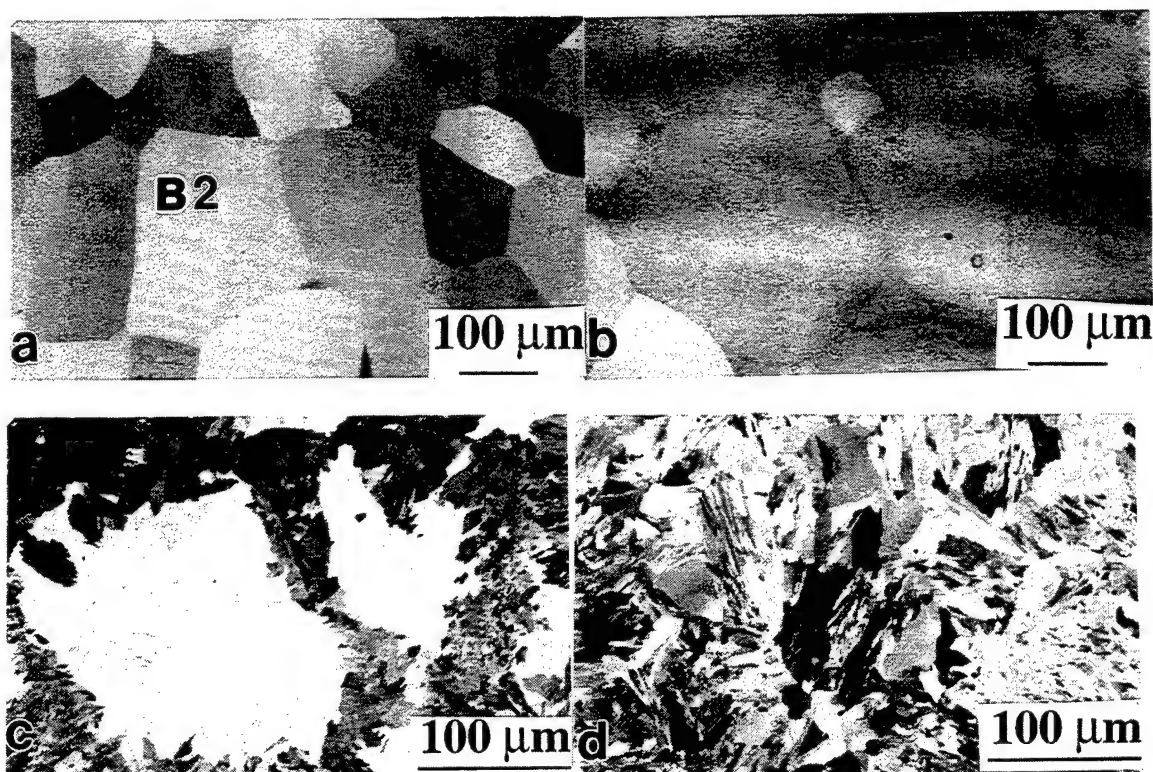


Figure 4.20 Microstructures of a Ti-25Al-23Nb (a) super-transus solution-treated sample (1090°C/0.5h/WQ) which had been aged at 650°C for (b) 2, (c) 9 and (d) 100 hours, followed by water quenching. Precipitates coarsened at (transformed-B2)/(transformed-B2) boundaries.

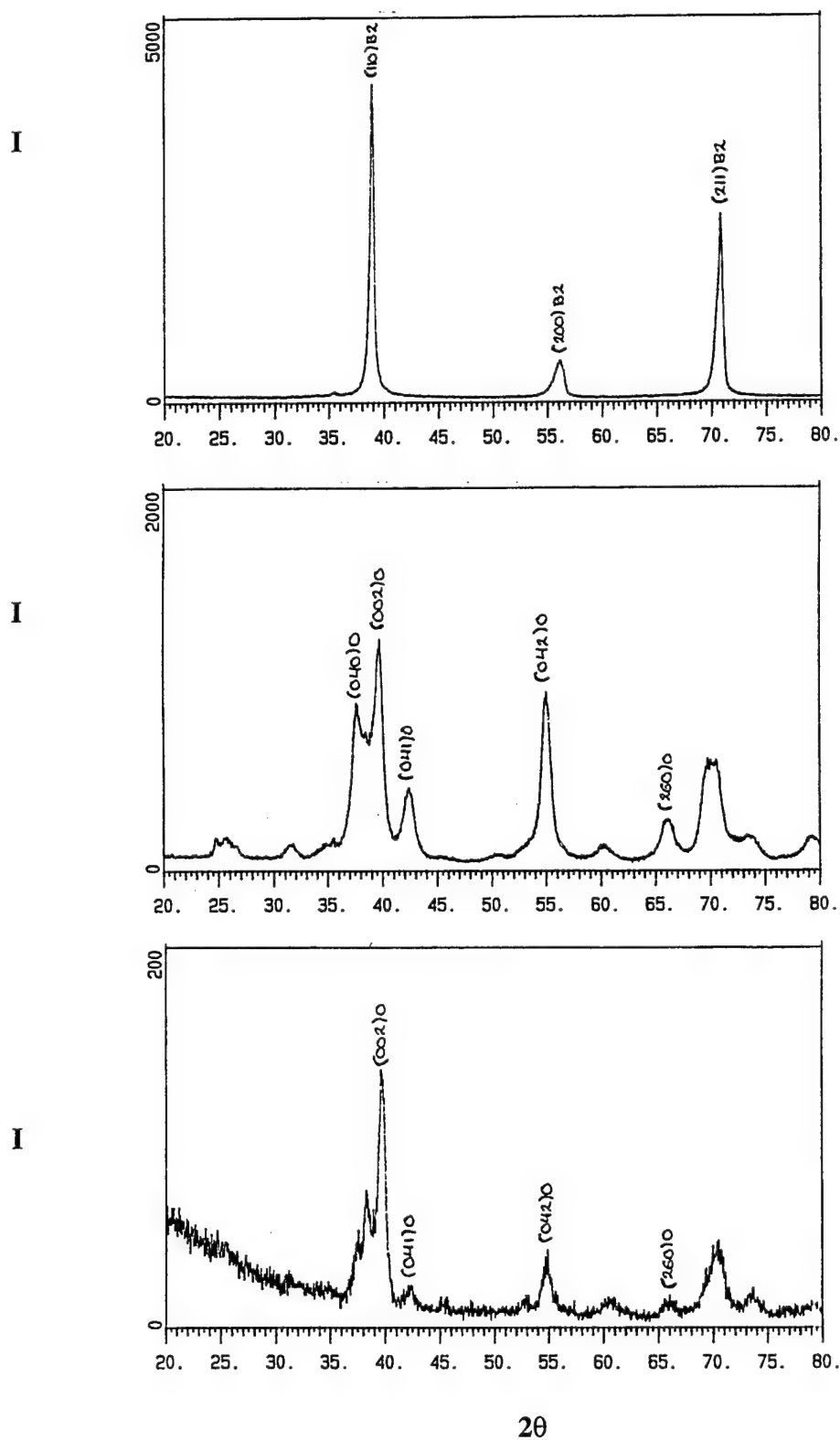


Figure 4.21 XRD plot of Intensity versus  $2\theta$  for a Ti-23Al-27Nb (a) super-transus solution-treated sample (1090°C/0.5h/WQ) which had been aged at 650°C for (b) 0.25 and (c) 2 hours, followed by water quenching.



Figure 4.22 A high-magnification BSD SEM image of the aligned grain-boundary precipitates for a heat-treated (1090°C/0.5h/WQ/650°C/9h/WQ) Ti-23Al-27Nb sample.

In addition to colony growth, extremely fine B2 platelets reprecipitated within the transformed-B2 grains. For longer aging times ( $t > 2$  hours), the B2 platelets were observed within both the colony structures as well as the bulk, see Figure 4.20c and d. A higher magnification BSD image illustrates the B2 platelets within separate cells of a colony, Figure 4.23. Microdiffraction patterns of such regions identify the B2 and O structures, Figures 4.24a and b. Thus the separate cells consisted of a matrix of O phase with fine B2 platelets. The OR between the phases was identical to that of the equiaxed sub-transus solutionized microstructures, see Figure 4.24c. As seen in Figure 4.23, the B2 platelets were preferentially oriented in one direction within a given O cell indicating that one B2 variant was dominant. The strong directionality of the B2 platelets enabled easy identification of cell boundaries. In addition, prior-B2 grain boundaries, which appeared to have been destroyed in the low magnification images of Figures 4.19c and 4.20d, could also be identified through high magnification SEM imaging, see Figure 4.23, and they contained thicker interface regions than the cell boundaries. At some O/O cell boundaries, discontinuous precipitation resulted in a coarser platelet size, see Figures 4.23 and 4.25, similar to that of the sub-transus solutionized then aged microstructures.



However, in this case the discontinuous precipitation did not migrate far and was not a dominant feature. In addition, the prior B2 grain boundaries contained small particles which were expected to be enriched with Nb due to their contrast, see white particles along prior B2 grain boundaries in Figure 4.23. This suggested that chemical partitioning occurred during the transformation.

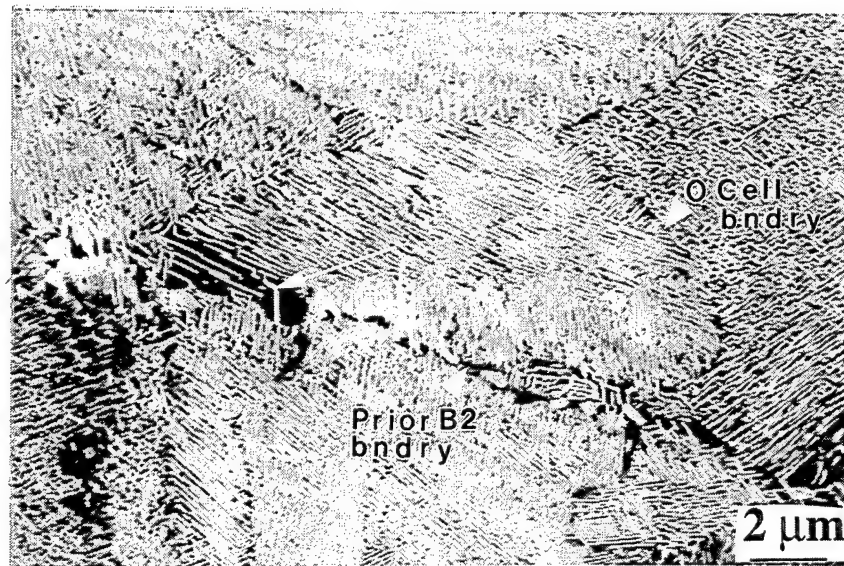


Figure 4.23 High magnification BSD image of a 1090°C solutionized Ti-23Al-27Nb sample which was aged at 650°C for 681 hours. Discontinuous precipitation is identified by the unlabeled arrows.

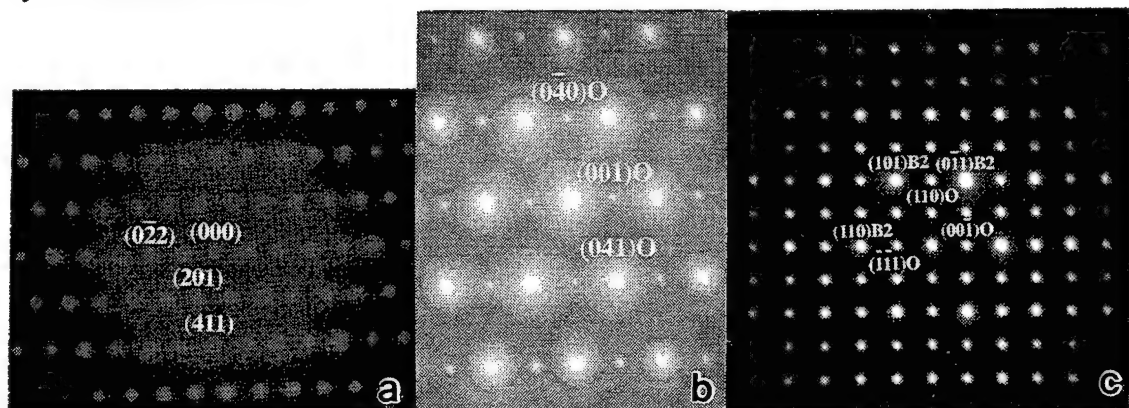


Figure 4.24 Microdiffraction patterns identifying the (a)  $[\bar{1}22]$ B2 and (b)  $[100]$ O structures within precipitated regions of a 1090°C solutionized Ti-23Al-27Nb sample which was aged at 650°C for 681 hours. The OR between the phases ( $[\bar{1}11]$ B2// $[1\bar{1}0]$ O and  $(110)$ B2// $(001)$ O) is depicted in (c).





Figure 4.25 Microstructure of a 1090°C solutionized Ti-23Al-27Nb sample which was aged at 650°C for 681 hours depicting discontinuous precipitation resulting in coarser platelets at O/O boundaries.

The following summarizes the microstructural observations from the aging study performed on super-transus solutionized samples. B2-to-O transformation occurred within 15 minutes at 650°C. O-phase colonies precipitated discontinuously at grain boundaries and the boundary of such precipitates migrated within the grain. For longer aging times the discontinuous precipitation consumed the entire transformed-B2 grain. B2 platelets re-precipitated within both the O colonies and the bulk within 9 hours at 650°C.

Re-solutionizing the super-transus then aged samples in the O+B2 regime resulted in larger volumes of B2 laths. This is indicated for Ti-23Al-27Nb and Ti-25Al-23Nb samples in Figures 4.26a and b. Comparing the super-transus solutionized sample which was then heated at 900°C, see Figure 4.6b, with a super-transus sample that was aged at 650°C then 900°C, see Figure 4.26a, similar microstructures resulted indicating that the 900°C condition can be restored after lower temperature-aging exposures.

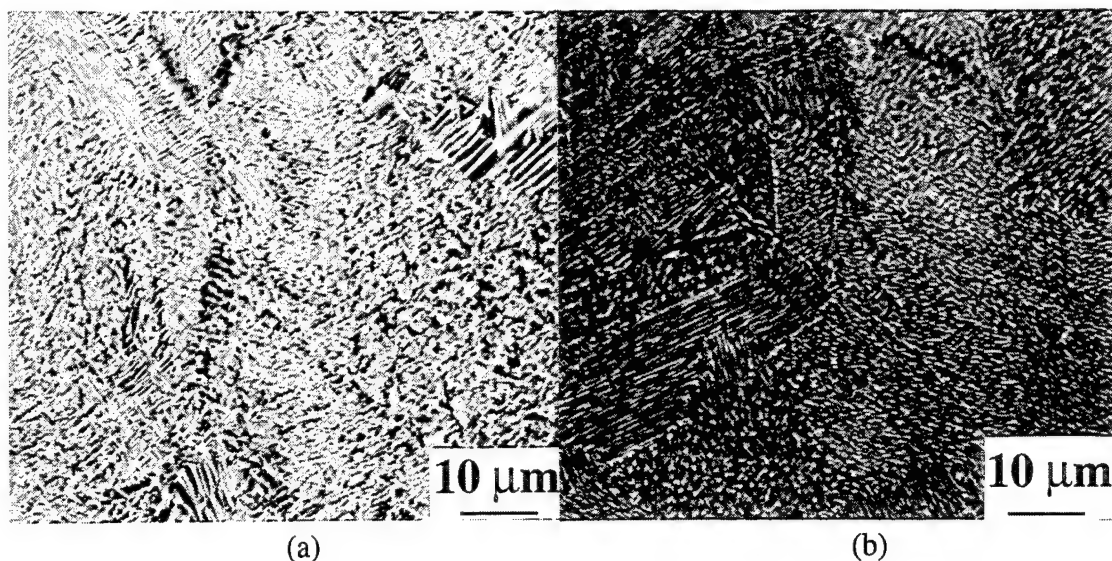


Figure 4.26 Heat-treated microstructures of (a) Ti-23Al-27Nb (HT:1090°C/1h/WQ/650°C/9h/WQ/900°C/8h/WQ) and (b) Ti-25Al-23Nb (HT:1090°C/1h/WQ/650°C/2h/WQ/900°C/8h/WQ).

Three important observations regarding the phase evolution of near  $\text{Ti}_2\text{AlNb}$  alloys were obtained from the aging study performed on both the super-transus and sub-transus solutionized samples. The first observation was that below a certain temperature Widmanstatten precipitation occurred. Widmanstatten precipitation of the O phase occurred below 875°C for the sub-transus samples solutionized within the O+B2 regime. Above 875°C, Widmanstatten precipitation was not evident and equiaxed B2 grains coarsened. For super-transus fully-B2 and sub-transus  $\alpha_2$ +B2 microstructures, Widmanstatten precipitation occurred at a much higher temperature ( $T > 900^\circ\text{C}$ ) indicating that either the grain size or the coherency of the B2/B2 boundaries played a role. Initial results suggest the Widmanstatten-start temperature is increased with increasing B2 grain size as the Ti-23Al-27Nb fine-grained ( $\text{GS}=3.8\ \mu\text{m}$ ) 875°C solutionized microstructure remained equiaxed when aged at 850°C while the larger-grained ( $6.6\ \mu\text{m}$ ) 950°C microstructure exhibited Widmanstatten O at 850°C. A similar trend has also been observed for other two-phase metals (Aaronson *et al.* 1990).

The second observation is that lower aging temperatures induced grain boundary precipitation and grain-boundary precipitate coarsening. For the sub-transus

microstructures, discontinuous precipitation of O and  $\beta$  platelets occurred at O/B2 and  $\alpha_2$ /B2 boundaries for  $T \leq 750^\circ\text{C}$ . For super-transus solutionized microstructures aged at  $650^\circ\text{C}$ , coarsening of O cells occurred preferentially at transformed-B2 boundaries. In both cases the interface of the coarsening grain boundary precipitates migrated within the grain for longer aging times. Combining the first two observations, for aging steps between  $750$ - $875^\circ\text{C}$ , Widmanstätten precipitation was favored, while aging below  $750^\circ\text{C}$  favored discontinuously coarsened precipitation which consumed the transformed B2 grains.

The third observation concerns the phase stability of  $\text{Ti}_2\text{AlNb}$  alloys. Because the discontinuous precipitation of the sub-transus solutionized and aged microstructures consisted of O+ $\beta$  platelets, the O+ $\beta$  phase field is expected to encompass the  $650$ - $750^\circ\text{C}$  temperature range. The boundary between the O+B2 and O+ $\beta$  fields is expected to lie between  $875^\circ\text{C}$  and  $750^\circ\text{C}$  for near  $\text{Ti}_2\text{AlNb}$  alloys. However, the ability to obtain O+ $\beta$  microstructures depends upon the volume and composition of the pre-aged B2 phase as the super-transus solutionized then aged microstructures maintained the ordered B2 structure after over 670 hours at  $650^\circ\text{C}$ . The diffusion kinetics of the  $\alpha_2$  phase appeared to be even more sluggish than that for the B2 phase as negligible volumes of the  $\alpha_2$  phase had transformed after 450 hours at  $650^\circ\text{C}$ , compare rows 6-9 of Table 4.2 and Figures 4.12a and b.

Super-transus Processed Near  $\text{Ti}_2\text{AlNb}$  Alloy. The phase evolution for the super-transus processed Ti-25Al-27Nb alloy was not studied in as great a detail as for the sub-transus processed near  $\text{Ti}_2\text{AlNb}$  alloys. The as-processed material, which was produced through highly localized heating at the molten temperature and then cooled very slowly using a Crystalox® machine (see the induction-heating procedures section of Chapter 3 for a description of the procedure), exhibited extremely large prior B2 grains containing preferentially oriented O laths, see Figure 4.27. The last row of Table 4.3 lists the grain size and approximate phase volume percents for the as-processed microstructure. This

microstructure is similar to that of the Ti-23Al-27Nb super-transus solutionized then control cooled sample, see Figure 4.6a, however the prior-B2 grain size and the volume of O laths were larger for Ti-25Al-27Nb. The larger prior-B2 grain size is expected to be a result of the higher-temperature exposure. The larger volume of O laths is expected to be a result of the higher Al content, which stabilizes the O phase, see Figures 4.8a-c. Electron Back Scattering Patterns (EBSP) revealed large regions of texturing of the O phase which is expected to be a result of the OR in which the O phase precipitated within the large parent B2 grains. A  $\{001\}$  pole figure (Figure 4.28a), taken from a section cut perpendicular to the longitudinal rod direction, indicated that the O phase was textured. The texturing was close to  $(\bar{1}31)O$  as indicated by comparison with the stereographic projection of O on (001), see Figure 4.28b. As mentioned above, the O laths were also non-randomly oriented, indicative that dominant O variants existed. In order to investigate microstructural stability, this alloy was aged at 650°C for more than 600 hours. The ordered B2 structure was retained as indicated by the  $[011]B2$  SADP, Figure 4.29. Thus, similar to the other near  $Ti_2AlNb$  alloys, super-transus microstructures tended to retain the ordered B2 phase even after long aging times at low temperatures.

#### 4.1.2 Ti-12Al-38Nb

The measured composition of the Ti-12Al-38Nb sheet material, provided in Table 4.4, was close to Ti-13Al-39Nb. The interstitial oxygen level was intermediate to the low-oxygen and high-oxygen near  $Ti_2AlNb$  alloys, see Table 4.1. Note that this ingot, procured from a different manufacturer, was melted from a different batch of starting materials than those of the near  $Ti_2AlNb$  alloys. The as-rolled sheet, depicted in Figures 3.16c (lower magnification) and 4.30a (higher magnification), consisted of 33  $\mu m$   $\beta$  grains which were elongated in the rolling direction. The disordered  $\beta$  phase was identified by the  $[011]\beta$  SADP, see Figure 4.30b. No ordered B2 or  $\alpha_2$  grains were

evident. Although no O phase was detected by TEM analysis of foils taken from the as-rolled sheet,  $\beta$  zone axis SADPs contained anomalies which sometimes indicate a fine second phase is present. DTA using 3°C/minute heating and cooling rates also did not indicate any phase transformations occurring between 600-1000°C, see Figure 4.31. However aging treatments between 650-800°C confirmed the precipitation of fine O platelets within the  $\beta$  grains. Thus, the cooling rates employed in the DTA analysis were rapid enough to suppress a significant volume of O-phase precipitates, as verified by the lack of O precipitates found in the DTA sample. Figures 4.32a-c depict the microstructures of samples aged at 650°C for 24 hours followed by heating at 850°C, 800°C, and 750°C, respectively. Based on the disappearing-phase method, the  $\beta \rightarrow \beta + O$  transus was close to 800°C as a small volume of O platelets was observed for the 800°C condition, while more O phase was observed at 750°C and no O phase was observed at 850°C.



Figure 4.27 A bright field TEM image of the as-processed Ti-25Al-27Nb microstructure containing O and B2 laths; the longitudinal rod direction is horizontal.

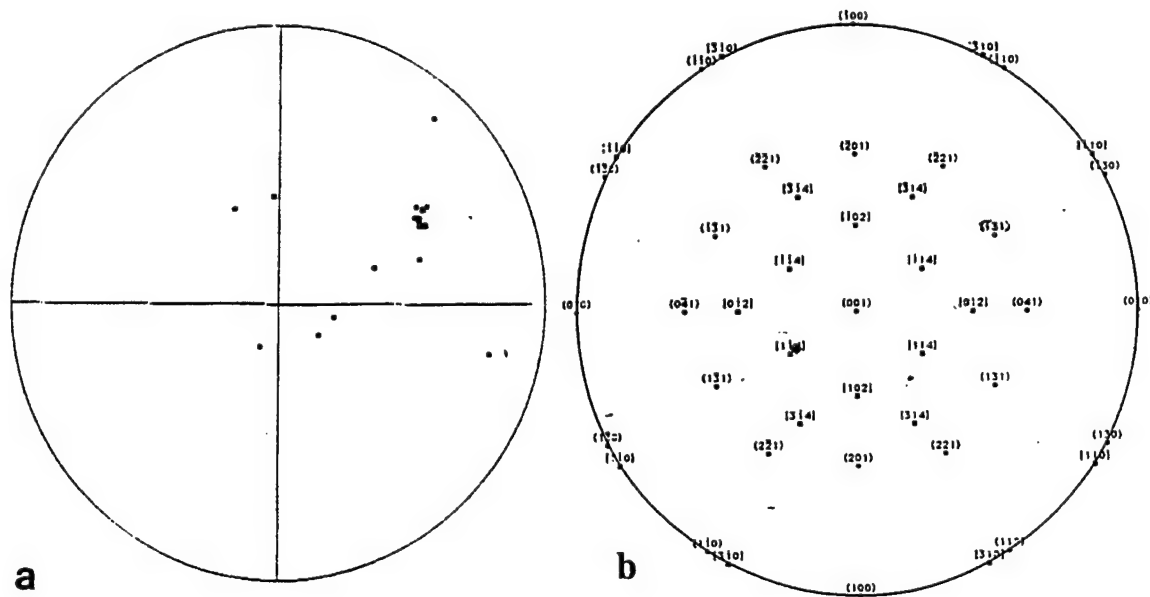


Figure 4.28 The (a) {001} pole figure of the as-processed Ti-25Al-27Nb microstructure taken from a section perpendicular to the longitudinal rod direction. A (b) stereographic projection of O on (001) taken from Banerjee (1995). These figures indicate that the O phase was textured close to  $(\bar{1}31)O$ .

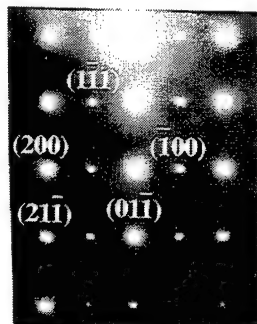


Figure 4.29 SADP taken for the  $[011]B2$  zone axis for a Ti-25Al-27Nb sample aged at  $650^{\circ}C$  for 670 hours.

Table 4.4 Chemical Analysis of the As-Rolled Ti-12Al-38Nb Sheet Material

Material	atomic percent			weight parts per million		
	Ti	Al	Nb	N	Fe	O
Ti-12Al-38Nb	Bal	13.2	39.2	70	255	575

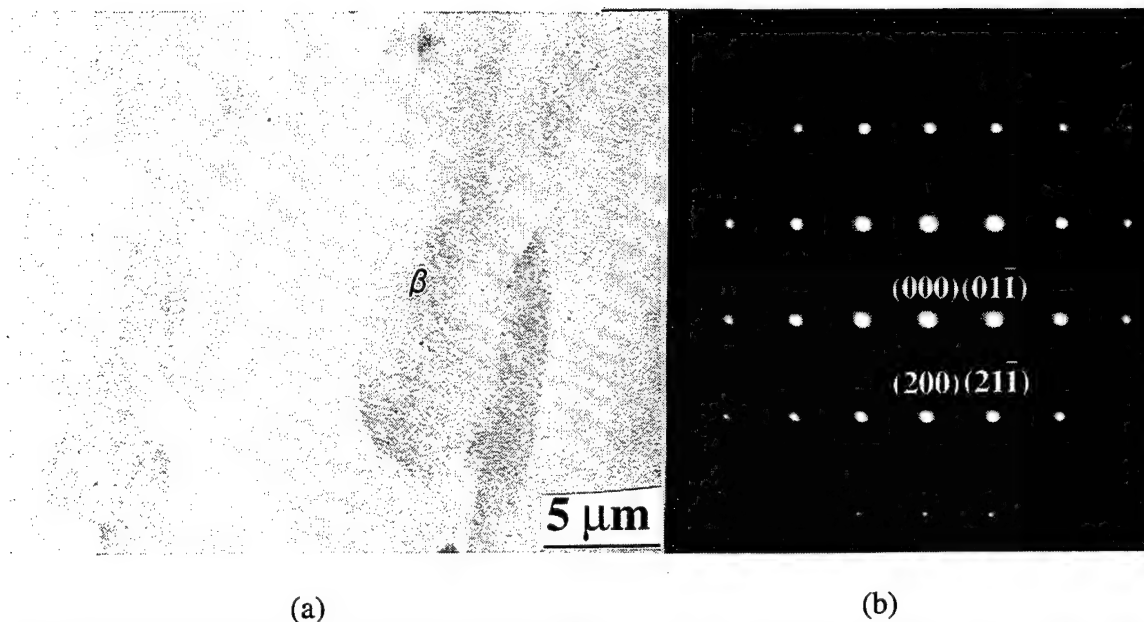


Figure 4.30 The (a) as-rolled Ti-12Al-38Nb microstructure; the rolling direction was vertical. The (b) SADP of the  $[011]$   $\beta$  zone axis for as-rolled Ti-12Al-38Nb.

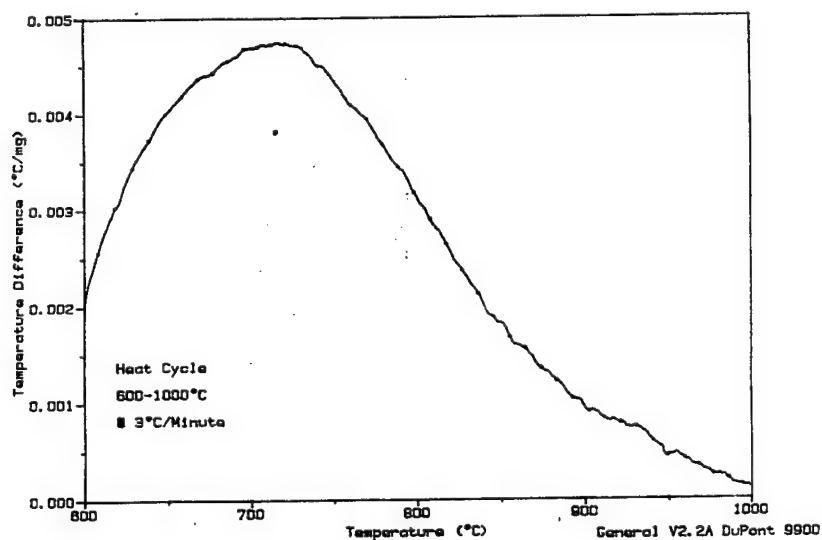


Figure 4.31 DTA plot of temperature difference versus temperature for the heating curve of the as-rolled Ti-12Al-38Nb sheet. The heating rate was 3°C/minute between 600-1000°C.

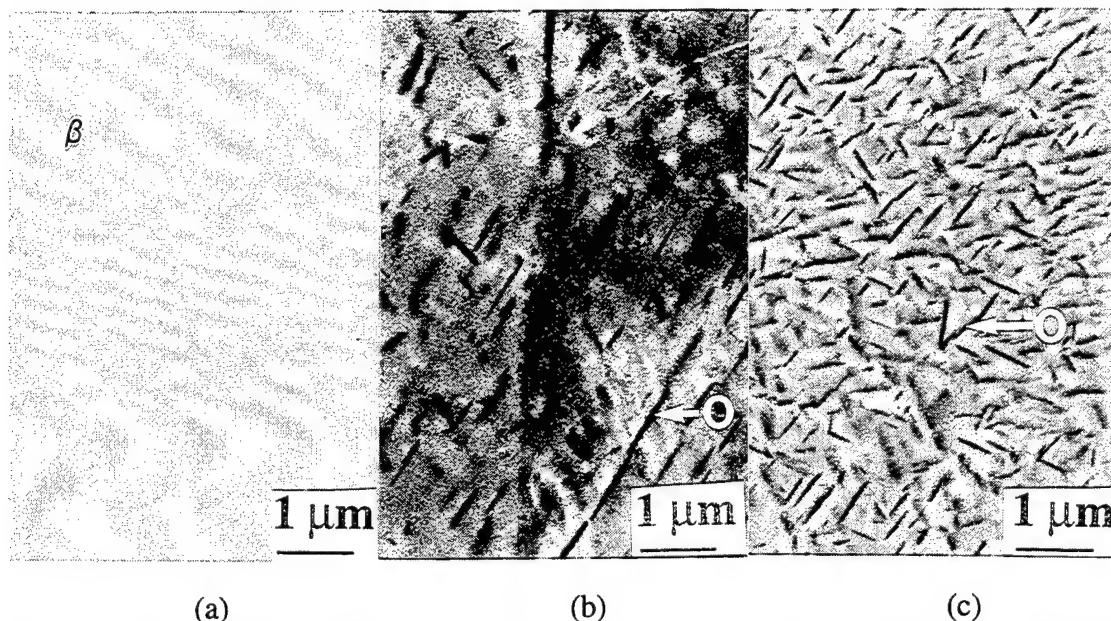


Figure 4.32 Ti-12Al-38Nb microstructures of samples aged at 650°C for 24 hours followed by heating at (a) 850°C, (b) 800°, and (c) 750°C for 5 hours followed by water quenching. The  $\beta \rightarrow \beta + O$  transus was close to 800°C.

Identical to that of the near  $Ti_2AlNb$  alloy studies, 650°C aging treatments were performed in order to investigate microstructural stability for Ti-12Al-38Nb. The O phase volume percent increased with aging time. Figures 4.33a-d depict the as-rolled microstructure after aging for 24, 50, 100, and 304 hours. Judging from the relatively constant 30 volume percent of O phase, the microstructures appeared to be stable after 50 hours, which was chosen as the minimum aging time for specimens used in the creep study. Therefore, less time was necessary to equilibrate Ti-12Al-38Nb microstructures at 650°C compared with the near  $Ti_2AlNb$  microstructures. The O phase, identified in the  $[00\bar{1}]O$  microdiffraction pattern (Figure 4.34a), grew with two or three main variants, judging from the common directions of the platelets. The disordered  $\beta$  structure was retained in samples aged between 650-760°C as evidenced from the  $[011] \beta$  microdiffraction pattern, Figure 4.34b. The OR between O and  $\beta$ , depicted in Figure



4.34c, was identical to the O/BCC OR of the near  $\text{Ti}_2\text{AlNb}$  alloys. Similar to that for the near  $\text{Ti}_2\text{AlNb}$  alloys, the aging transformation resulted in dislocations which formed at O/ $\beta$  interfaces, see Figures 4.35a and b.

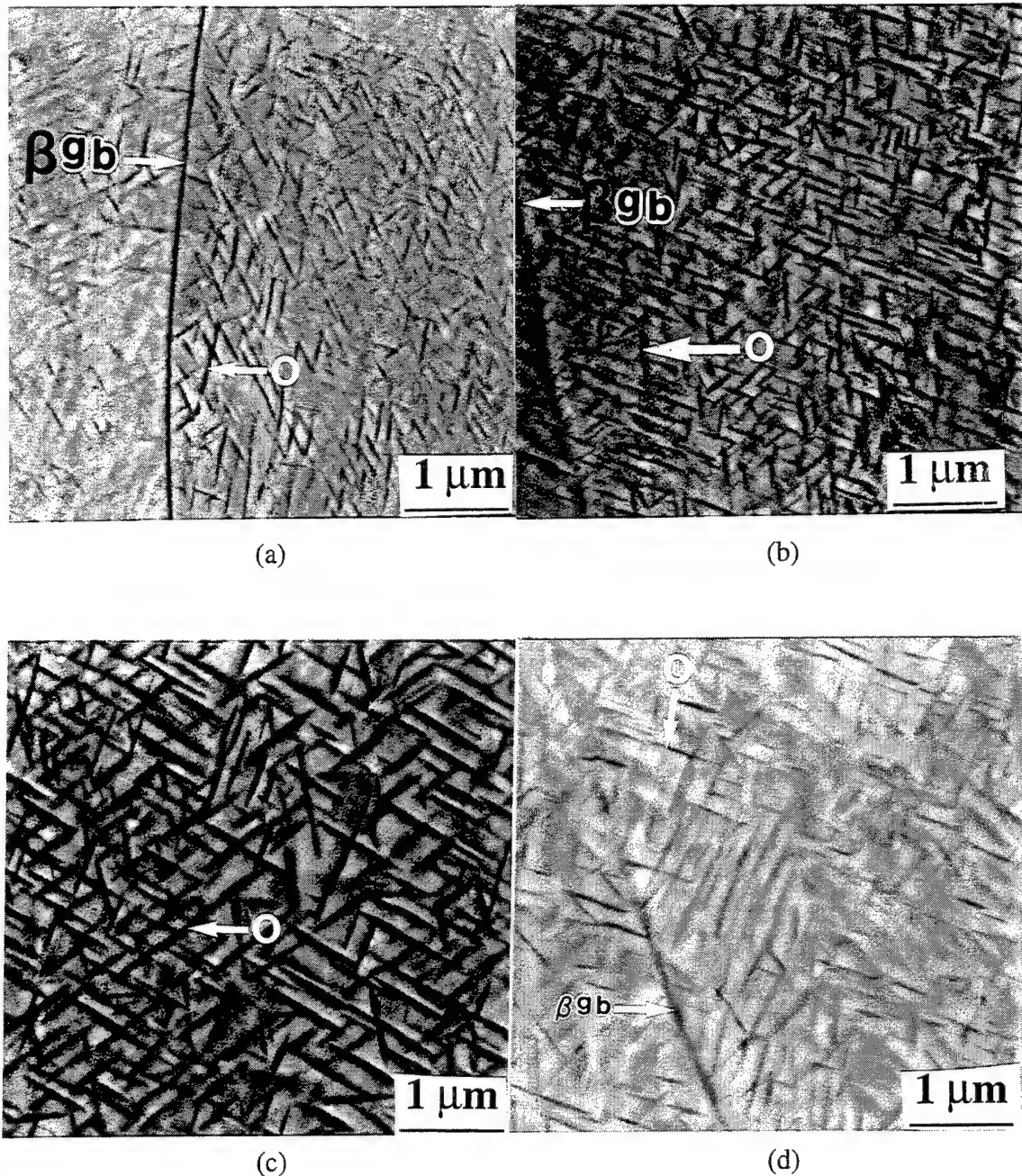


Figure 4.33 Effect of aging time on microstructure. These images depict the as-rolled Ti-12Al-38Nb microstructure after aging at 650°C for (a) 24 hours, (b) 50 hours, (c) 100 hours, and (d) 304 hours, followed by water quenching.

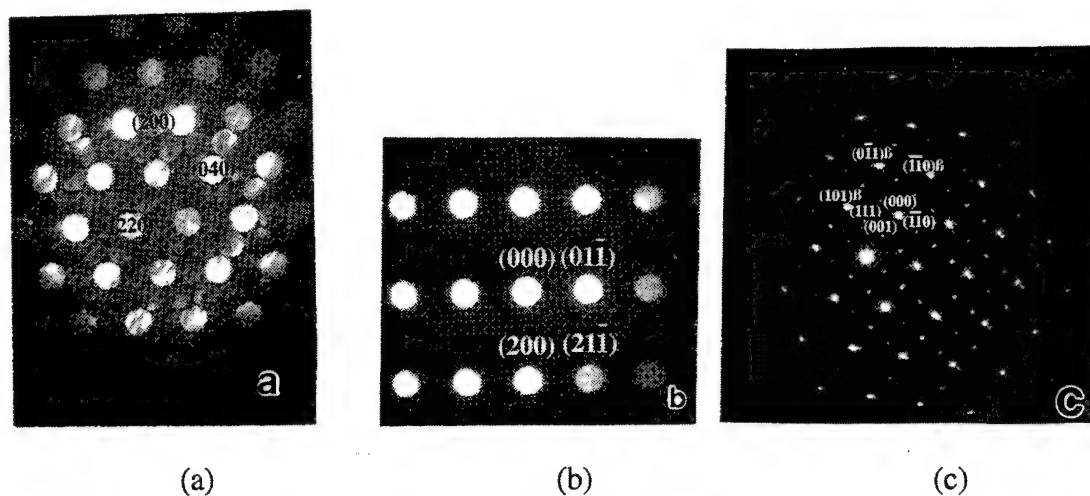


Figure 4.34 Microdiffraction patterns of the O and  $\beta$  structures for a heat-treated ( $650^{\circ}\text{C}/435\text{h}/\text{WQ}$ ) Ti-12Al-38Nb sample illustrating the (a)  $[00\bar{1}]$ O zone axis and the (b)  $[011]$   $\beta$  zone axis. (c) SADP of the O/ $\beta$  OR:  $[\bar{1}11]\beta_2//[\bar{1}10]\text{O}$ ;  $(110)\beta_2//(001)\text{O}$ .

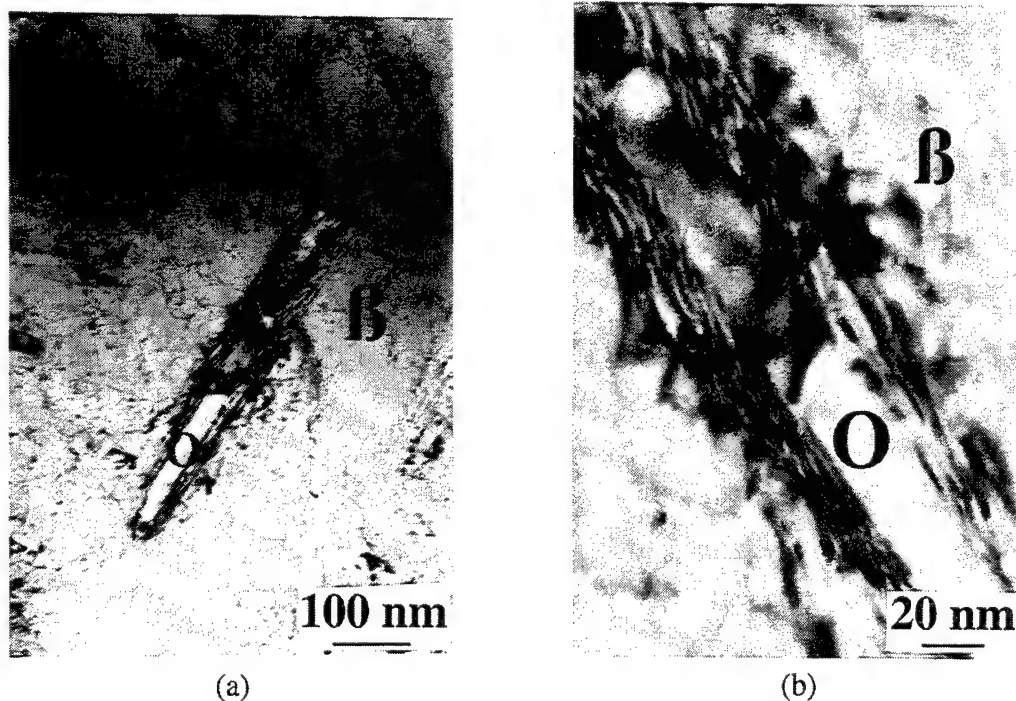


Figure 4.35 (a) Lower and (b) higher magnification bright-field TEM images of transformation misfit dislocations at O/ $\beta$  interfaces for a Ti-12Al-38Nb  $650^{\circ}\text{C}/411\text{h}/\text{WQ}$  heat-treated sample.

A unique aspect of the phase evolution of this alloy was that the  $\beta$  grain size could be significantly varied without altering other microstructural features such as the phase volume percents, compositions, and morphology. This proved to be quite useful for the microstructure-property study as described in creep and tensile behavior results' sections. Figures 4.36a-c depict the increasing  $\beta$  grain sizes for samples isothermally solutionized at increasing temperatures; 900°C, 950°C, and 1200°C. The corresponding grain sizes are listed in Table 4.5, which summarizes the as-rolled and heat-treated Ti-12Al-38Nb microstructures. Under isothermal heat-treatment conditions, normal grain growth for single-phase materials is well described by the following empirical equation (Hu and Rath 1970, Seetharaman and Semiatin 1997):

$$GS^n - GS_0^n = k t \quad (4.1)$$

where  $n$  is the grain growth exponent,  $GS$  is the heat-treated  $\beta$  grain size,  $GS_0$  is the pre-heat treated grain size and in this case the  $\beta$  grain size of the as-rolled sheet, and  $t$  is the annealing time. The variable  $k$  is estimated by the Arrhenius equation:

$$k = k_0 \exp(-Q_{app}/RT) \quad (4.2)$$

where  $k_0$  is a kinetic constant,  $Q_{app}$  is the activation energy for grain growth,  $R$  is the gas constant, and  $T$  is absolute temperature. For most single-phase materials, the value of  $n$  ranges between 2-10 due to the drag force exerted by solute atoms on grain boundaries (Higgins *et al.* 1992). Taking  $n=3$ , the corresponding values of  $k$  are represented on the  $\ln k$  versus  $(1/T)$  plot depicted in Figure 4.37. Because the three data points do not lie along a common straight line, it appears that there is a bimodal distribution of the activation energies. For grain growth below 950°C,  $Q_{app}$  is approximately 258 kJ/mol, which is close to that predicted from the diffusion coefficients of the binary Ti-Nb system presented by Sherman (1963). The calculated  $Q_{app}$  for Ti-39Nb was approximately 252 kJ/mol. Thus it appears that 13Al does not significantly effect the diffusion rates below

950°C. For grain growth above 950°C, the measured  $Q_{app}$  was approximately 96 kJ/mol which is much smaller than that expected. In particular this is unexpected because typically grain growth is correlated with lattice self-diffusion. Anomalies have been observed for  $\beta$  grain growth which results in lower values of  $Q_{app}$ s close to the transus temperatures (Sherman 1963), however a transus is not expected near 1200°C and this observation remains unexplained.

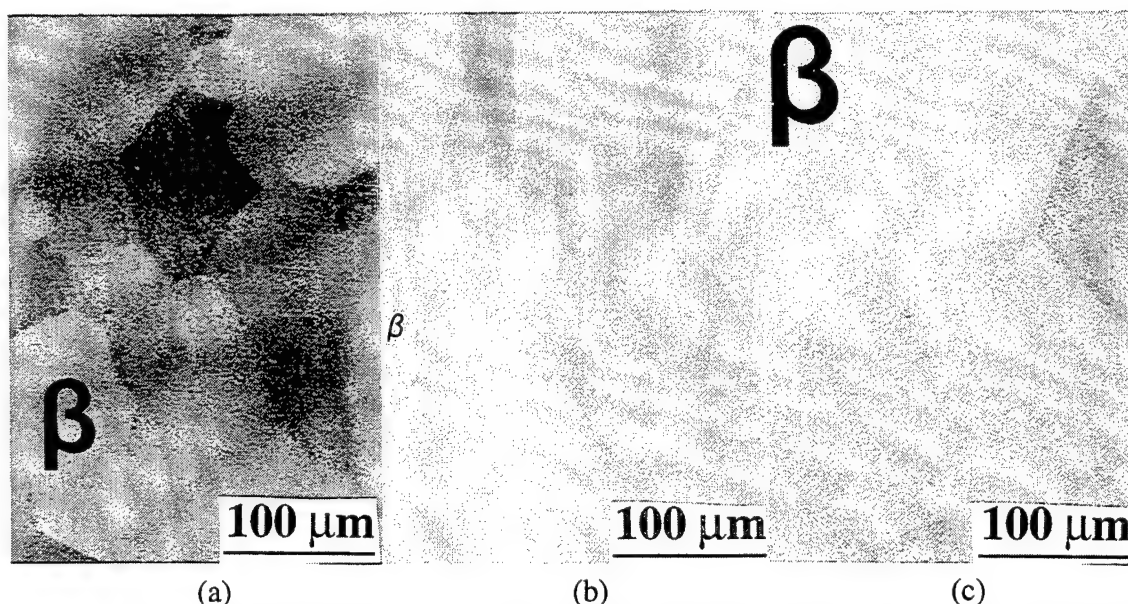
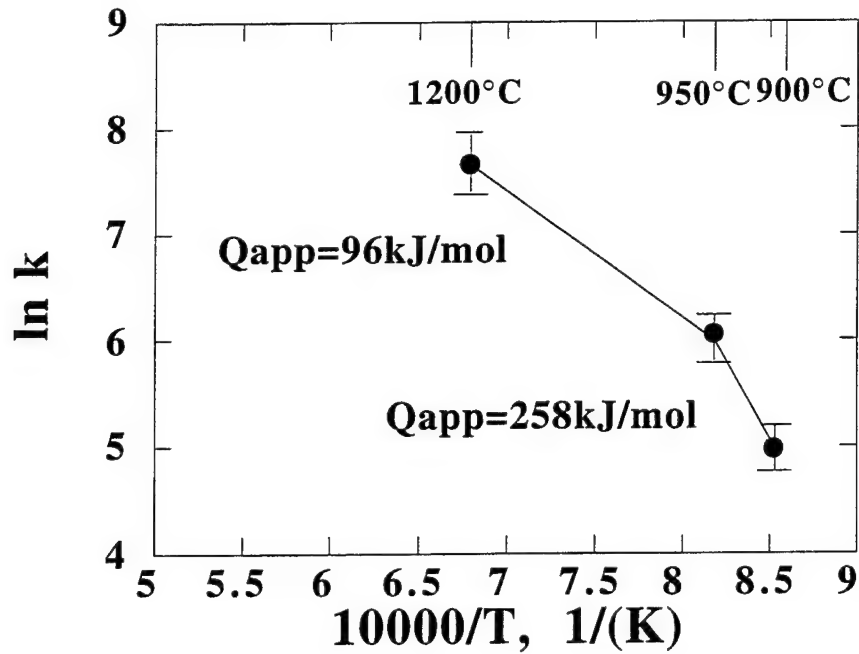


Figure 4.36 Microstructures of Ti-12Al-38Nb solution treated and water quenched samples. Solution-treatment temperatures were (a) 900°C, (b) 950°C, and (c) 1200°C. These images depict the effect of solution-treatment temperature on  $\beta$  grain size.

Table 4.5 Ti-12Al-38Nb Heat Treatments and Measured Average Grain Sizes and Phase Volume Percents and Compositions

Heat Treatment	$\beta$			$\alpha$			$\beta$ GS ( $\mu\text{m}$ )
	Al	Nb	Vp	Al	Nb	Vp	
650°C/55h/WQ	na	na	72%	na	na	28%	33.2
900°C/5h/WQ	12.4	40.7	100%			0%	138.2
900°C/5h/WQ/650°C/60h/WQ	na	na	71%	na	na	29%	138.2
950°C/5h/WQ	na	na	100%			0%	197.5
950°C/5h/WQ/650°C/62h/WQ	na	na	69%	na	na	31%	197.5
1200°C/5h/WQ	na	na	100%			0%	336.9
1200°C/5h/WQ/650/60h/WQ	na	na	68%	na	na	32%	336.9

WQ: water quenched; na: not available.



(a) (b)  
Figure 4.37 A plot of  $\ln k$  vs  $(1/T)$ , based on equations 4.1 and 4.2, depicting the  $\beta$  grain growth for heat-treated Ti-12Al-38Nb.

After the grain sizes were determined for the respective super-transus solutionizing temperatures, samples were again aged at 650°C. Similar to that for the as-rolled material, a stable volume of approximately 30% O platelets precipitated within 50 hours. Interestingly, the O phase first precipitated at the large  $\beta$  grain boundaries. This is depicted for a sample which was water quenched prior to reaching 5 hours at 650°C, see Figure 4.38. Thus diffusion appeared to be faster across the high angle grain boundaries than within the bulk. It is also noted that a small volume of grain-boundary precipitates was observed at some  $\beta/\beta$  boundaries for solution treated then aged samples, see Figure 4.39. Similar to the discontinuous precipitation of the near Ti<sub>2</sub>AlNb alloys, the precipitates were identified by alternating light and dark bands. However, the precipitates were never noticed more than 2  $\mu\text{m}$  away from the grain boundaries, and they appeared to have been related to the chemical banding in the as-rolled material as has been similarly observed in other studies (Rowe 1993a, Rowe and Larsen 1996).



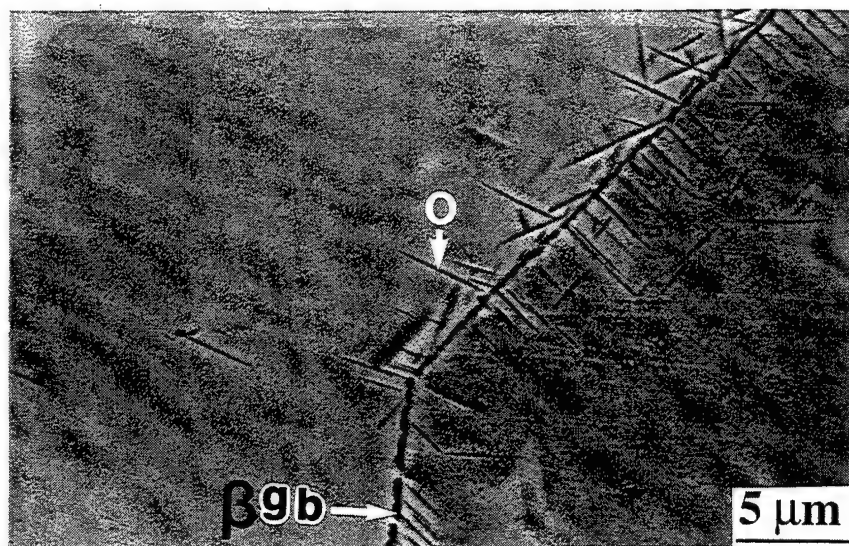


Figure 4.38 SEM image of a 900°C solutionized Ti-12Al-38Nb sample which was aged at 650°C for less than 5 hours. The O phase precipitated initially at the  $\beta$  grain boundaries.

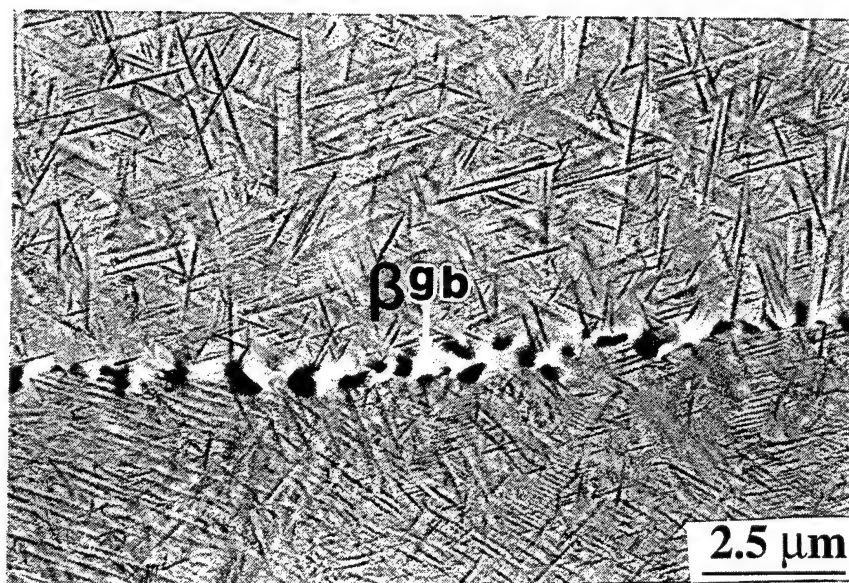


Figure 4.39 Grain boundary precipitates for a heat-treated (900°C/5h/WQ/650°C/62h/WQ) Ti-12Al-38Nb sample.

## 4.2 Creep Behavior

The creep strain-life behavior of near Ti<sub>2</sub>AlNb and Ti-12Al-38Nb alloys resembled that for most pure metals and alloys (Hertzberg 1976, Evans and Wilshire 1985). A plot of creep strain<sup>2</sup> versus time illustrates the three classic creep stages, Figure 4.40. Although the creep rates appeared to approach a steady state within the secondary creep stage, the structure of the deforming samples was not constant, as is described in the creep deformation behavior sub-section. Therefore, the lowest measured creep rate was represented as the minimum creep rate ( $\dot{\epsilon}_{\min}$ ) and not the steady-state creep rate. This is an important result as steady-state creep rates may not be applicable for many O-alloy microstructures. The transition from the primary to secondary stages was determined by the 'onset method' (Mishra and Banerjee 1994). The primary transient time ( $t_p$ ) and primary creep strain ( $\epsilon_p$ ) along with the tangent used to obtain these values are indicated in Figure 4.40. Normal primary creep transients were observed, indicative of recovery-controlled creep.

Although some work has been performed on primary creep mechanisms (Malakondaiah and Rao 1981, Malakondaiah *et al.* 1988, Mishra and Banerjee 1994 1995, Hayes 1996), a majority of the well established theories on creep mechanisms have been based on the secondary creep regime (Nix and Ilschner 1980, Evans and Wilshire 1985). Because special emphasis was placed on determining microstructure-creep relations for O alloys in the low-to-intermediate stress range, the work was concentrated on understanding the secondary-creep mechanisms, which are easier to characterize due to the larger knowledge base, and applying this understanding to develop microstructure-creep relations.

---

<sup>2</sup> Creep strain was measured after the initial loading at temperature was completed.

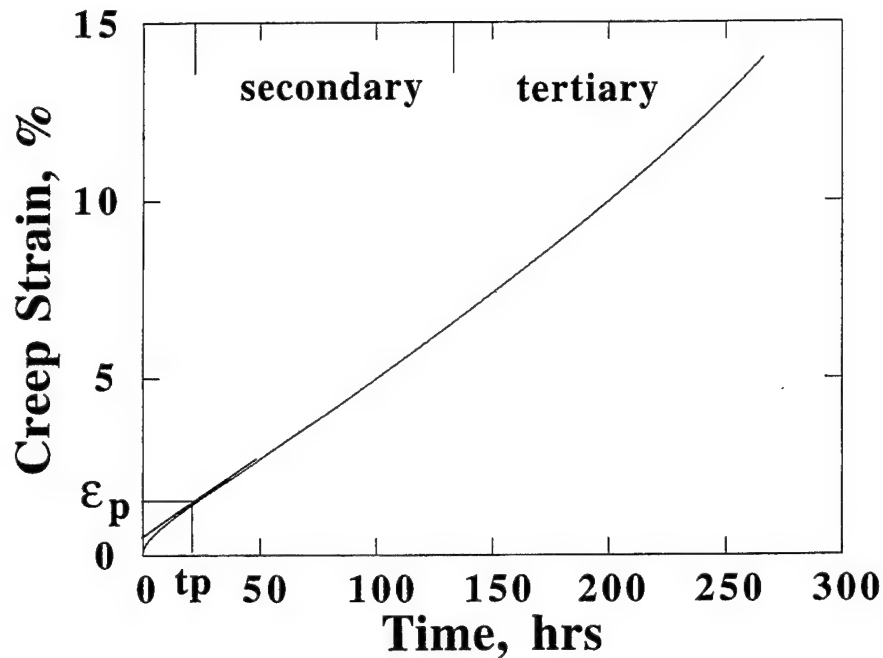


Figure 4.40 Creep strain versus time plot for the as-rolled Ti-25Al-24Nb sheet material depicting the three stages of creep. The tangential line used in the 'onset method' to determine  $\epsilon_p$  and  $t_p$  is indicated.

#### Near $\text{Ti}_2\text{AlNb}$ Alloys

The near  $\text{Ti}_2\text{AlNb}$  microstructures investigated in the creep behavior study could be grouped into three categories based on their solution-treatment temperatures. The categories included super-transus B2, sub-transus  $\alpha_2+\text{B2}$ , and sub-transus  $\text{O}+\text{B2}$  microstructures which were aged in the  $\text{O}+\beta$  region at  $650^\circ\text{C}$ . As described in the previous sections, the aging treatment induced the precipitation of O and BCC platelets within equiaxed prior B2 grains. Henceforth, these microstructures will be referred to by their solution-treatment temperature. In addition, selected specimens were solution-treated in the  $\text{O}+\text{B2}$  region, without aging, to examine the effect of microstructural instability on creep behavior. This section will be separated into topics pertaining to the aging and tension/compression effects, mechanical properties, and deformation behavior of the chosen microstructures.



Aging and Tension/Compression Effects. Figure 4.41 compares creep strain versus time curves for aged and unaged Ti-23Al-27Nb specimens which underwent identical O+B2 (950°C) solution-treatments. The microstructures of the aged and unaged specimens are depicted in Figures 4.11d and Figure 4.10a, respectively. Aging resulted in lower creep strains, where the solution-treated and unaged condition exhibited higher primary strains, primary creep rates, and minimum creep rates than the solution-treated and aged condition. The most significant effect occurred within the primary creep regime as within the first few hours after loading the strains of the unaged specimens had doubled compared to that of the aged specimen, see Figure 4.41. The differences in minimum creep rates between aged and unaged specimens were within a factor of 1.3. The solution-treated only samples were unloaded after 44 and 66 hours of creep to identify the effect of load on instability. There was no significant difference, in terms of phase volumes or sizes, from heat-treated samples which were aged for similar exposure times without load. Figures 4.42a and b compare an unaged specimen which was crept at 650°C/172 MPa for 66 hours and a heat-treated sample which was aged at 650°C for 50 hours. Creep strain rate versus time data indicate that strain rates reached a constant value within 10 hours of applying load. Thus, the samples were unloaded well after the transient creep regime and within the secondary regime. As seen in the aging studies, the volume of discontinuous precipitates increased during creep deformation.

An identical study was performed on aged and unaged Ti-25Al-23Nb specimens which were solutionized at a lower temperature (910°C) in the O+B2 phase field. The 910°C microstructure contained less B2 phase volume than the 950°C microstructure, as previously described in the phase evolution solution-treatment study sub-section. The pre-creep microstructures of these specimens are illustrated in Figures 4.43a and b. Note that less cellular precipitation of O+ $\beta$  platelets was exhibited in the aged microstructures of the 910°C solutionized case compared to the 950°C solutionized case, compare Figure 4.43b with Figure 4.11d. Figure 4.44 compares the creep strain versus time curves for the

aged and unaged 910°C solutionized microstructures of Figures 4.43a and b. Similar to Figure 4.41, this plot shows that aging decreased the primary strain and primary creep rate.

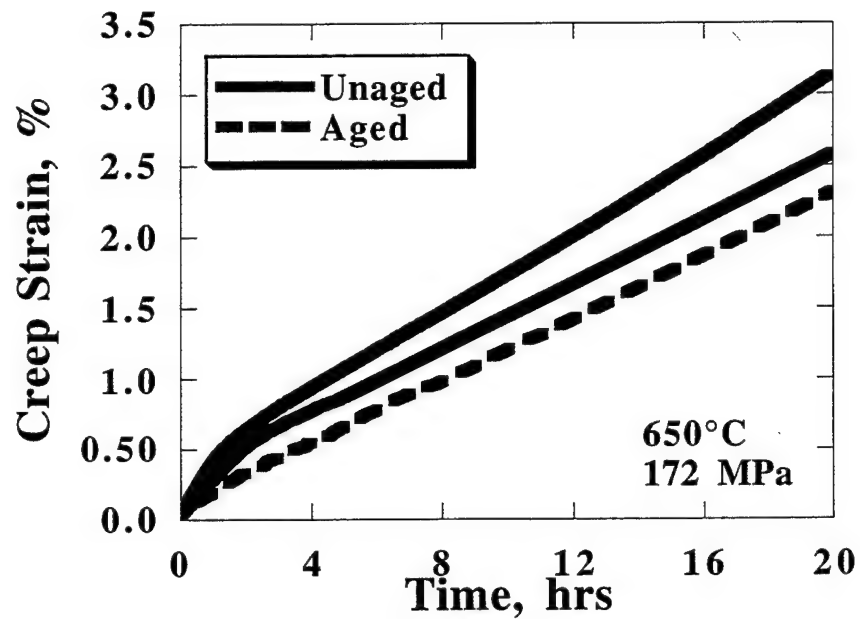


Figure 4.41 Creep strain vs time curves for solution treated (950/45/WQ) and solution treated and aged (950°C/45h/WQ/650°C/304h/WQ) Ti-23Al-27Nb specimens.

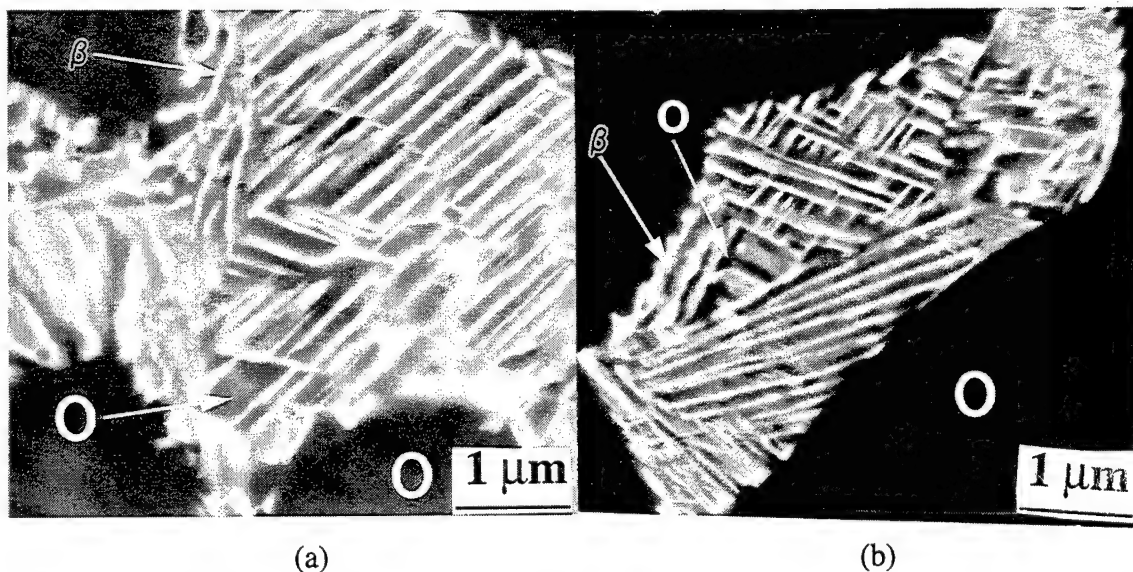


Figure 4.42 Ti-23Al-27Nb samples which were solution-treated at 950°C. One sample (a) was crept at 650°C/172 MPa for 66 hours and the other (b) was heat treated at 650°C for 50 hours.

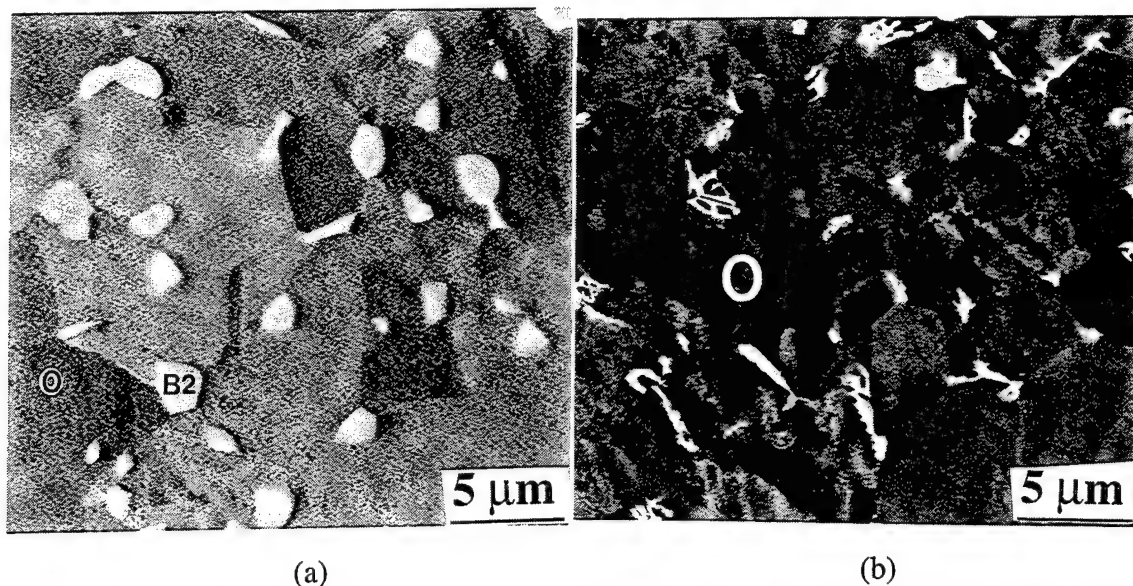


Figure 4.43 Comparison of a Ti-25Al-23Nb solution-treated (a) (910°C/8h/WQ) microstructure with a solution-treated and aged (b) (910°C/8h/WQ/650/218h/WQ) microstructure.

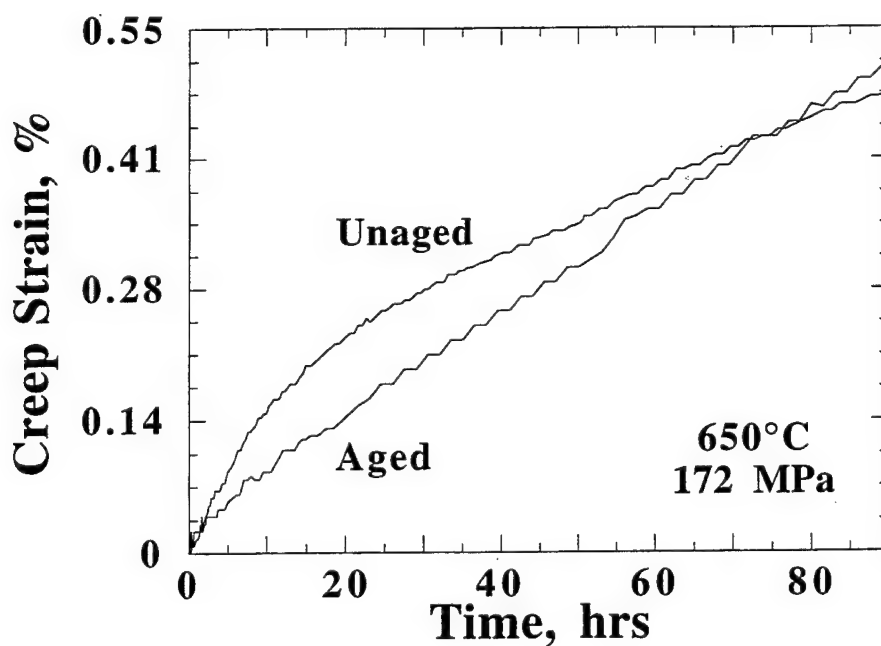


Figure 4.44 Creep strain vs time curves for solution treated (910°C/8h/WQ) and solution treated and aged (910°C/8h/WQ/650°C/218h/WQ) Ti-25Al-23Nb specimens.

Figure 4.45 compares creep strain versus time curves for Ti-23Al-27Nb specimens with identical microstructures. One specimen was tested in tension while the other specimen was tested in compression. The creep temperature was 650°C, and the applied stress was 172 MPa. The tensile and compressive creep strains were nearly identical. In addition, nearly identical secondary creep rates were obtained in both tension and compression for an applied stress of 250 MPa. Therefore, in terms of the creep properties, the difference between tension and compression loadings was determined to be insignificant. Except for the two loading conditions mentioned, no other compression creep experiments were performed.

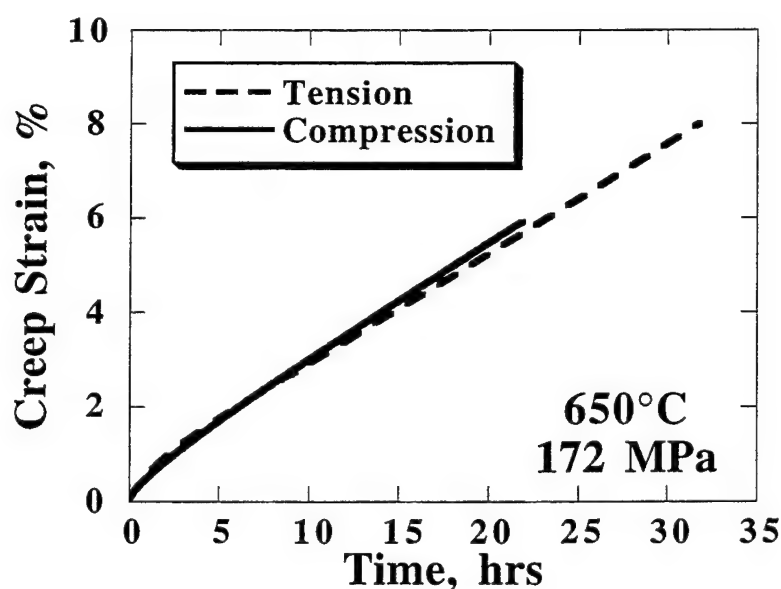


Figure 4.45 Creep strain vs time curves for tension and compression loadings of Ti-23Al-27Nb specimens which were solutionized at 875°C and then aged at 650°C. The creep conditions were 650°C/172 MPa.

Mechanical Properties. Table 4.6 lists the  $\epsilon_p$ ,  $t_p$ , and  $\dot{\epsilon}_{min}$  for the heat-treated Ti-23Al-27Nb specimens tested in creep. Also included in Table 4.6 are the average spatial grain sizes (GS), measured from the solutionized microstructures, and the creep testing conditions. The results indicate that for a given test condition higher-temperature solution treatments, which correspond to larger grain sizes, offer greater creep resistance. For example, a greater than two times decrease in primary creep strain and minimum

creep rate was observed for samples solutionized at 950°C compared with 875°C. The best creep resistance was found for the super-transus microstructure, which contained a prior B2 grain size of approximately 177  $\mu\text{m}$ . The relationship between grain size and creep rate depends on the dominant creep mechanism. In order to understand the significance of grain size and other microstructural parameters on creep, the temperature and stress ranges for the active creep mechanisms were estimated based on well-established creep theories.

In order to calculate the secondary-stage creep parameters ( $n$  and  $Q_{\text{app}}$ ) for a given microstructure, the creep test matrix included experiments in which temperatures were held constant and stresses were varied or stresses were held constant and temperatures were varied. This was accomplished by testing different specimens which were identically heat treated or by changing the load or temperature after the specimen had reached the secondary stage. Examples of step-loading experiments and temperature-change experiments are depicted in Figures 4.46a and b. This type of testing was acceptable because the amount of post-heat treatment deformation did not significantly effect the minimum creep rates. In general, strain rates increased more rapidly for small increments in temperature compared with small increments in stress.

The creep parameters were calculated from the power-law creep equation for minimum creep rate:

$$\dot{\epsilon}_{\text{min}} = A \sigma^n \exp(-Q_{\text{app}}/RT) \quad (4.3)$$

where  $A$  is a constant,  $\sigma$  is the applied stress,  $R$  is the gas constant, and  $T$  is the absolute temperature. The  $\sigma$  term has also been represented by the applied stress normalized by the elastic modulus. However, the moduli, measured during the initial loading to the maximum applied stress, of the near  $\text{Ti}_2\text{AlNb}$  microstructures did not vary significantly between 650-760°C and were approximately 120 GPa. Therefore, the applied stress

normalized by the modulus was not employed in this equation. The creep exponent values were calculated from a power-law curve fit between  $\log \dot{\epsilon}_{\min}$  and  $\log \sigma$ . The activation energies were calculated from a linear curve fit between  $\ln \dot{\epsilon}_{\min}$  and  $T^{-1}$ .

Table 4.6 Creep Properties for Heat-Treated Ti-23Al-27Nb Microstructures

Heat Treatment	$\sigma$ /Temp (MPa/ $^{\circ}$ C)	$\epsilon_p$ (%)	$t_p$ (h)	$\dot{\epsilon}_{\min}$ (1/s)	GS*** $\mu\text{m}$
875 $^{\circ}$ C/45h/WQ/650 $^{\circ}$ C/304h/WQ*	352/650	0.72	0.30	3.31E-06	3.8
875 $^{\circ}$ C/45h/WQ/650 $^{\circ}$ C/304h/WQ	250/650	na	na	1.50E-06	3.8
875 $^{\circ}$ C/24h/WQ/650 $^{\circ}$ C/218h/WQ**	249/650	na	na	1.13E-06	3.8
875 $^{\circ}$ C/45h/WQ/650 $^{\circ}$ C/304h/WQ	172/650	1.40	3.7	6.71E-07	3.8
875 $^{\circ}$ C/24h/WQ/650 $^{\circ}$ C/218h/WQ**	172/650	2.00	6.2	6.88E-07	3.8
875 $^{\circ}$ C/45h/WQ/650 $^{\circ}$ C/200h/WQ*	172/654	1.43	4.7	5.20E-07	3.8
875 $^{\circ}$ C/45h/WQ/650 $^{\circ}$ C/304h/WQ	100/650	na	na	3.00E-07	3.8
875 $^{\circ}$ C/45h/WQ/650 $^{\circ}$ C/304h/WQ	50/655	3.12	57.2	8.51E-08	3.8
875 $^{\circ}$ C/45h/WQ/650 $^{\circ}$ C/304h/WQ	50/709	na	na	3.15E-07	3.8
875 $^{\circ}$ C/45h/WQ/650 $^{\circ}$ C/304h/WQ	50/760	1.90	1.6	2.86E-06	3.8
950 $^{\circ}$ C/45h/WQ	172/650	0.79	4.3	2.94E-07	6.6
950 $^{\circ}$ C/45h/WQ	171/651	0.77	2.8	3.80E-07	6.6
950 $^{\circ}$ C/45h/WQ/650 $^{\circ}$ C/304h/WQ	172/650	0.68	5.1	2.90E-07	6.6
1025 $^{\circ}$ C/45h/WQ/650 $^{\circ}$ C/288h/WQ	172/650	0.69	10.8	9.93E-08	8.7
1025 $^{\circ}$ C/45h/WQ/650 $^{\circ}$ C/288h/WQ	100/650	1.30	67.0	3.61E-08	8.7
1025 $^{\circ}$ C/45h/WQ/650 $^{\circ}$ C/288h/WQ	50/650	0.79	172.0	8.83E-09	8.7
1025 $^{\circ}$ C/45h/WQ/650 $^{\circ}$ C/288h/WQ	50/707	na	na	5.27E-08	8.7
1025 $^{\circ}$ C/45h/WQ/650 $^{\circ}$ C/288h/WQ	50/764	0.80	4.0	3.96E-07	8.7
1090 $^{\circ}$ C/0.5h/WQ/650 $^{\circ}$ C/112h/WQ	442/650	na	na	4.90E-08	177.0
1090 $^{\circ}$ C/0.5h/WQ/650 $^{\circ}$ C/112h/WQ	394/650	na	na	3.17E-08	177.0
1090 $^{\circ}$ C/0.5h/WQ/650 $^{\circ}$ C/112h/WQ	360/650	na	na	2.32E-08	177.0
1090 $^{\circ}$ C/0.5h/WQ/650 $^{\circ}$ C/112h/WQ	318/650	na	na	1.43E-08	177.0
1090 $^{\circ}$ C/0.5h/WQ/650 $^{\circ}$ C/112h/WQ	246/650	na	na	9.58E-09	177.0
1090 $^{\circ}$ C/0.5h/WQ/650 $^{\circ}$ C/112h/WQ	172/650	na	na	4.27E-09	177.0
1090 $^{\circ}$ C/0.5h/WQ/650 $^{\circ}$ C/112h/WQ	97/650	na	na	2.71E-09	177.0
1090 $^{\circ}$ C/0.5h/WQ/650 $^{\circ}$ C/112h/WQ	50/650	0.13	115.0	1.00E-09	177.0
1090 $^{\circ}$ C/0.5h/WQ/650 $^{\circ}$ C/112h/WQ	50/705	0.14	113.8	1.32E-09	177.0
1090 $^{\circ}$ C/0.5h/WQ/650 $^{\circ}$ C/112h/WQ	50/730	na	na	2.10E-09	177.0
1090 $^{\circ}$ C/0.5h/WQ/650 $^{\circ}$ C/112h/WQ	50/760	na	na	4.03E-09	177.0
1090 $^{\circ}$ C/0.5h/WQ/650 $^{\circ}$ C/112h/WQ	100/760	na	na	1.83E-08	177.0
1090 $^{\circ}$ C/0.5h/WQ/650 $^{\circ}$ C/112h/WQ	75/760	na	na	9.49E-09	177.0
1090 $^{\circ}$ C/0.5h/WQ/650 $^{\circ}$ C/112h/WQ	36/760	na	na	1.47E-09	177.0

WQ: water quenched; na: not available; \*\*\*: GS represents the average equiaxed grain size of the corresponding heat-treated microstructures before they were aged at 650 $^{\circ}$ C; \*: tested in vacuum ( $9 \times 10^{-7}$  torr); \*\*: tested in compression with 0.01 MPa partial pressure of flowing argon.

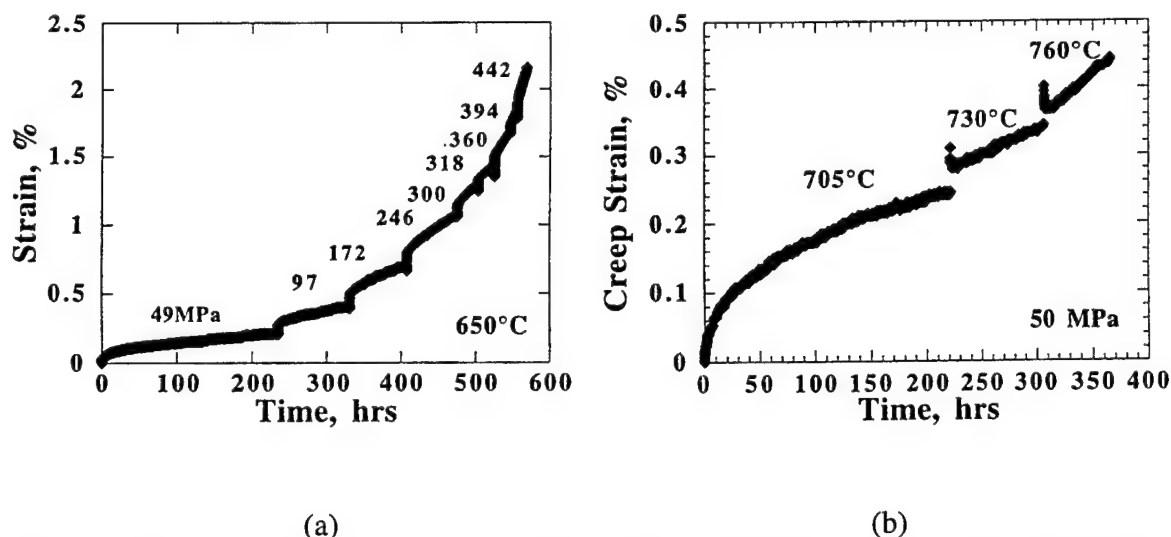


Figure 4.46 Examples of the creep strain versus life behavior for single-specimen experiments, which were (a) incrementally loaded from 50 to 442 MPa in steps while the temperature remained constant (650°C), or (b) the temperature was increased from 705°C to 760°C in steps while the load was held constant (i.e. stress = 50 MPa). Note that the load or temperature was changed only after the secondary stage was reached. An identical heat treatment (1090°C/0.5h/WQ/650°C/112h/WQ) was performed on each specimen prior to testing.

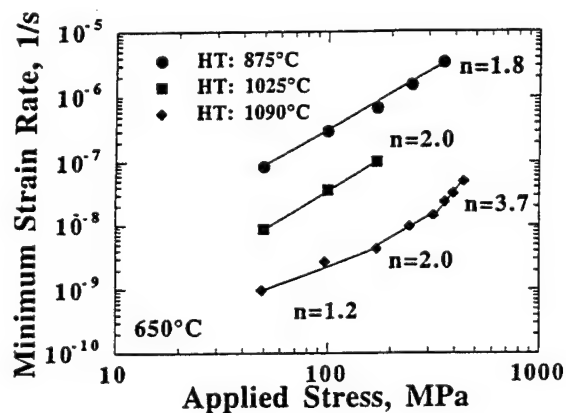
Table 4.7 lists the calculated creep parameters for the heat-treated microstructures based on the data listed in Table 4.6. Figures 4.47a and b show plots of  $\log \dot{\epsilon}_{\min}$  versus  $\log \sigma$  at  $T=650^\circ\text{C}$  and  $\ln \dot{\epsilon}_{\min}$  versus  $(1/T)$  for  $\sigma=50$  MPa, respectively. The strain rate dependence on stress for the super-transus solutionized then aged specimens, see Figure 4.47a, exhibited the classic transition in creep exponents noticed for pure metals and alloys (Evans and Wilshire 1985). Each creep-exponent transition typically corresponds to a change in deformation mechanism. The creep exponents of the sub-transus  $\alpha_2+B2$  and  $O+B2$  microstructures were constant over the stress range examined which suggests that a single mechanism was dominant. For applied stresses between 172-352 MPa, all

the microstructures exhibited a creep exponent close to two, indicating the same creep mechanism may be dominant for this applied stress range. The strain rate dependence on temperature also exhibited the classic behavior of metals and alloys, where the slope, taken from the linear relationship between  $\ln \dot{\epsilon}_{\min}$  and  $T^{-1}$ , yielded  $Q_{app}$ .

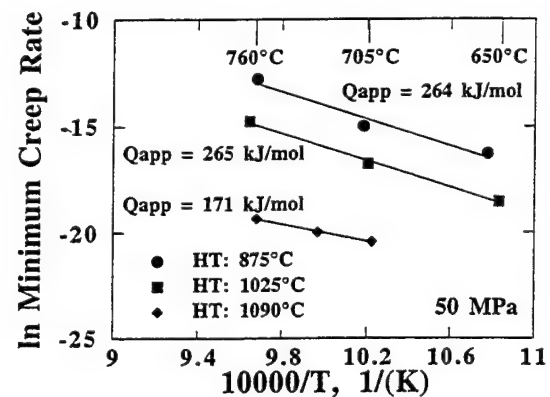
Table 4.7 Measured Creep Exponents and Apparent Activation Energies for Heat-Treated Ti-23Al-27Nb Microstructures

Heat Treatment	$\sigma/T$ (MPa/ $^{\circ}\text{C}$ )	n	$\sigma/T$ (MPa/ $^{\circ}\text{C}$ )	$Q_{app}$ (kJ/mol)
875°C/45h/WQ/650°C/304h/WQ	50-352/650	1.8	50/655-760	264
1025°C/45h/WQ/650°C/288h/WQ	50-172/650	2.0	50/650-764	265
1090°C/0.5h/WQ/650°C/112h/WQ	50-172/650	1.2	50/650-705	38
1090°C/0.5h/WQ/650°C/112h/WQ	172-318/650	2.0		
1090°C/0.5h/WQ/650°C/112h/WQ	318-450/650	3.7		
1090°C/0.5h/WQ/650°C/112h/WQ	35-100/760	2.0	50/705-760	171

WQ: water quenched.



(a)



(b)

Figure 4.47 Creep plots for three Ti-23Al-27Nb microstructures, represented by their solution-treatment temperatures; (a) stress dependence of  $\dot{\epsilon}_{\min}$  at  $T=650^{\circ}\text{C}$  and (b) temperature dependence of  $\dot{\epsilon}_{\min}$  for  $\sigma = 50 \text{ MPa}$ .



The creep exponent was dependent not only on stress but also temperature. This is depicted in Figures 4.48a and b which shows the low-stress creep behavior of the super-transus microstructure at 650°C and 760°C. At 760°C  $n=2.4$ , while at 650°C  $n=1.2$  (see Figure 4.48a). Stress exponents close to unity have been related to Harper-Dorn (H-D) (Ruano *et al.* 1988), Nabarro-Herring (N-H) (Herring 1950) or Coble (C) (Coble 1963) creep mechanisms, while stress exponents close to two have been related to grain boundary sliding. Thus, based solely on the creep exponent, grain boundary sliding may be contributing more significantly at 760°C than 650°C. The temperature increase also corresponded to an increase in  $Q_{app}$ , which is depicted in the Arrhenius plot showing the temperature dependence of  $\dot{\epsilon}_{min}$ , Figure 4.48b. The data corresponding to  $\sigma=50$  MPa could be represented by the two straight lines having different slopes. Above 705°C, the straight line had a larger slope and, from a least-square calculation, a  $Q_{app}$  energy of approximately 171 kJ/mol was obtained. Below 705°C, the straight line had a smaller slope yielding a  $Q_{app}$  equal to approximately 38 kJ/mol. Because both of these values are significantly lower than that expected for lattice self-diffusion in O alloys, the H-D and N-H mechanisms, which are based on lattice self-diffusion, are not expected to be significantly contributing. The trend indicates that the  $Q_{app}$  is higher at 760°C than 650°C for  $\sigma=50$  MPa. Observations of  $Q_{app}$  increasing with temperature have also been recorded for pure  $\alpha$ -Ti (Malakondaiah and Rao 1981),  $\alpha_2$  (Mendiratta and Lipsitt 1980) and  $\alpha+\beta$  (Miller *et al.* 1987) alloys. Miller *et al.* (1987) suggested that at higher temperatures with higher activation energies, self-diffusion might overtake the effects of oxygen diffusion thereby leading to a transition in slope. The measured activation energies from that study were similar ( $Q_{app}$  was equal to 53 kJ/mol and 143 kJ/mol in the lower temperature and higher temperature regions, respectively.) to those of the current study. Malakondaiah and Rao (1981) noted that the transition from Coble to N-H regimes was responsible for the increase in  $Q_{app}$  with temperature above 700°C. However, a more significant jump in  $Q_{app}$ , from 104 to 273 kJ/mol was observed in their

studies compared with the smaller jump in the current work. Nevertheless, volume diffusion may be contributing along with grain boundary diffusion to increase the apparent activation energy with increasing temperature, and oxygen diffusion may be significantly contributing at the lowest temperature (650°C). This result indicates that within potential transition regions, as indicated in this case by the changed  $n$  and  $Q_{app}$  values, more than one mechanism may be contributing significantly. Therefore, in order to avoid extraneous effects which complicate the analysis, care should be taken to characterize  $Q_{app}$ s where one mechanism is dominant.

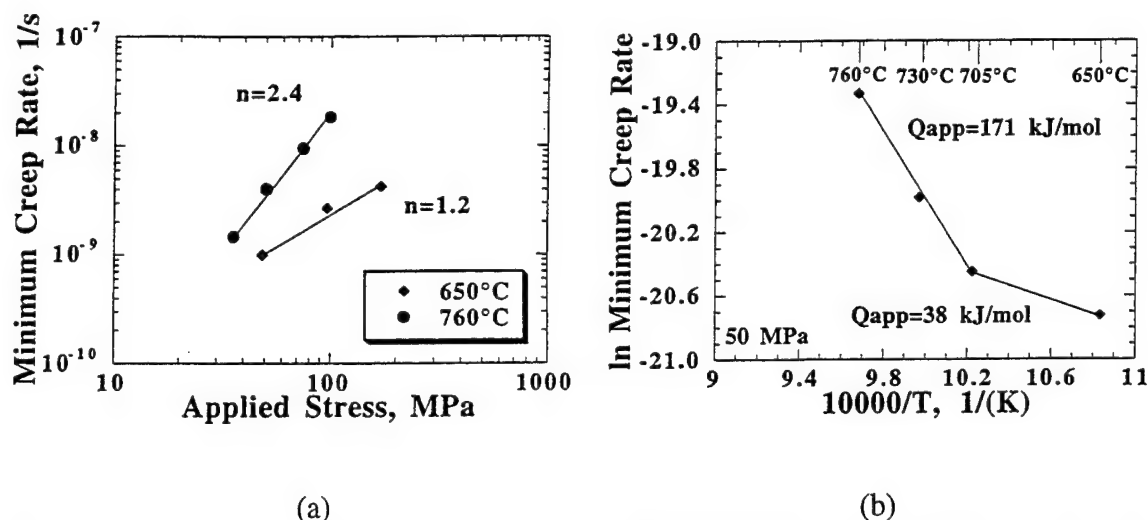


Figure 4.48 Creep plots for the super-transus Ti-23Al-27Nb microstructure. (a) Log  $\dot{\epsilon}_{min}$  vs log  $\sigma$  curves at 650°C and 760°C. (b) Arrhenius plot of  $\ln \dot{\epsilon}_{min}$  vs  $10^4/T$  for an applied stress of 50 MPa, where the 650-705°C data exhibited a lower  $Q_{app}$  than the 705-760°C data.

The  $Q_{app}$  obtained for the super-transus microstructures at  $\sigma=50$  MPa was 0.65 times those of the sub-transus microstructures ( $Q_{app} \sim 265$  kJ/mol), compare row 6 with rows 1 and 2 of Table 4.7. Although the stress exponents were not evaluated for the sub-transus microstructures at temperatures between 705-760°C, in each case, the strain rate

data used to calculate  $Q_{app}$  was well-represented by a straight line, see Figure 4.47b, which is expected when one mechanism is dominant. The creep exponent for these microstructures between 50-352 MPa was close to two. Therefore, grain boundary sliding was suggested to be the dominant mechanism and based on the significantly higher  $Q_{app}$ s, the activation energy for lattice self-diffusion was expected to be closer to 265 kJ/mol than 171 kJ/mol. These observations indicate that the stress range of the creep mechanisms are dependent on microstructure. The  $Q_{app}$  values were similar to those obtained for sub-transus Ti-24Al-11Nb microstructures ( $Q_{app}=260$  kJ/mol), which were considered to be close to that of lattice self-diffusion (Mishra and Banerjee 1990). In addition, the strain rates of the sub-transus Ti-24Al-11Nb microstructures were comparable to those of Ti-23Al-27Nb, and in both cases lower strain rates were observed for larger average grain sizes. This indicates that similar dominant mechanisms may be active for both alloys at low-to-intermediate stress levels, and grain size appears to be an important microstructural feature.

The sub-transus heat-treated microstructures' primary creep data also suggested a grain boundary mechanism. Using the power-law equation for transient time (Malakondaiah *et al.* 1988, Hayes 1996):

$$t_p = k (\sigma)^{-n} \exp(-Q_{app}/RT) \quad (4.4)$$

where  $k$  is a pre-exponential rate constant and the rest of the parameters are defined in equation 4.3. The stress exponent was 1.8 and 2.6 for the 1025°C and 875° solutionized microstructures, which suggested a grain boundary mechanism was dominant (Mishra and Banerjee 1995).

For the stress range 172-318 MPa, the creep exponent,  $n=2.0$ , of the super-transus microstructure suggested grain boundary sliding was dominant as well. For stresses greater than 318 MPa, the creep exponent transitioned to approximately 3.7, see Figure

4.47a and row 5 of Table 4.7. Dislocation climb is suggested to be the rate-controlling process when  $n > 3.5$  (Weertman 1968, Evans and Wilshire 1985). No  $Q_{app}$  values were obtained for the super-transus microstructure for stresses between 172-442 MPa.

Table 4.8 lists  $\epsilon_p$ ,  $t_p$ ,  $\dot{\epsilon}_{min}$ , GS, and the testing conditions for the Ti-25Al-27Nb, Ti-25Al-23Nb, and Ti-25Al-24Nb creep specimens. Table 4.9 lists the corresponding creep parameters obtained for Ti-25Al-27Nb and Ti-25Al-23Nb. The super-transus processed Ti-25Al-27Nb microstructure exhibited a similar transition in creep exponents as that of the super-transus Ti-23Al-27Nb microstructure, though the creep rates for a constant applied stress were lower for the larger-grained Ti-25Al-27Nb. For applied stresses between 172-317 MPa, the stress exponent was close to two, while above 317 MPa  $n$  tended toward 5.1, see rows 2 and 3 of Table 4.9. The  $Q_{app}$ , calculated at constant  $\sigma=394$  MPa, was 346 kJ/mol, which is close to that found for a fully-O alloy at a similar applied stress level (Nandy *et al.* 1993). This  $Q_{app}$  was approximately twice that of the super-transus Ti-23Al-27Nb microstructure at  $\sigma=50$  MPa.

To evaluate the effect of phase volumes on  $Q_{app}$ , Ti-25Al-23Nb microstructures containing 95% O phase volume percent were examined under identical conditions ( $\sigma=50$  MPa, 650-760°C) as Ti-23Al-27Nb microstructures, which contained 86% O phase volume percent. In order to obtain microstructures which contained similar grain sizes and morphologies, Ti-25Al-23Nb was heat treated at 650°C while Ti-23Al-27Nb was solutionized at 875°C then aged at 650°C (compare the microstructural parameters from row 2 of Table 4.2 and row 9 of Table 4.3). The creep rates of the Ti-25Al-23Nb microstructure are listed in rows 12-14 of Table 4.8, and the creep rates of the Ti-23Al-27Nb microstructure are listed in rows 8-10 of Table 4.6. The apparent activation energy for Ti-25Al-23Nb ( $Q_{app}=311$  kJ/mol) was higher than that for Ti-23Al-27Nb ( $Q_{app}=264$  kJ/mol), see Figure 4.49. However, the minimum creep rates at 50 MPa/760°C were nearly identical for both microstructures, while the lower temperature strain rates criss-crossed (i.e. The Ti-23Al-27Nb strain rate was lower at 705°C and higher at 650°C than

Ti-25Al-23Nb). Thus, the difference in  $Q_{app}$  is primarily a result of the different minimum creep rates at 705°C and 650°C. These observations indicate that for two-phase O+BCC microstructures of near Ti<sub>2</sub>AlNb alloys, slight changes in O phase volume, which result from slight changes in nominal composition, have a slight effect on strain rate for low applied stresses.

Table 4.8 Creep Properties for Heat-Treated Ti-25Al-27Nb, Ti-25Al-23Nb and Ti-25Al-24Nb Microstructures

Heat Treatment	$\sigma$ /Temp (MPa/°C)	$\epsilon_p$ (%)	$t_p$ (h)	$\dot{\epsilon}_{min}$ (1/s)	GS* $\mu m$
<b>Ti-25Al-27Nb</b>					
as-processed	394/760	na	na	2.16E-07	1305.0
as-processed	394/705	na	na	1.66E-08	1305.0
as-processed	394/650	na	na	2.03E-09	1305.0
as-processed	317/650	na	na	6.82E-10	1305.0
as-processed	249/650	na	na	3.55E-10	1305.0
as-processed	172/650	0.05	46.0	1.69E-10	1305.0
<b>Ti-25Al-23Nb</b>					
910°C/8h/WQ	50/650	0.45	77.0	6.49E-09	8.4
910°C/8h/WQ/650°C/218h/WQ	50/650	0.34	56.0	8.49E-09	8.4
650°C/116h/WQ	48/650	0.44	18.2	4.11E-08	4.0
650°C/116h/WQ	48/705	0.43	1.6	5.97E-07	4.0
650°C/116h/WQ	49/760	na	na	3.02E-06	4.0
<b>Ti-25Al-24Nb</b>					
as-rolled	172/650	1.40	19.8	1.29E-07	4.5
930°C/100h/WQ	172/650	0.60	59.4	1.74E-08	10.1
975°C/100h/WQ	172/650	0.71	56.9	1.70E-08	10.4
875°C/100h/WQ	172/650	0.40	60.2	8.62E-09	17.1

WQ: water quenched; na: not available; \*: GS represents the average equiaxed grain size of the corresponding heat-treated microstructures before they were aged and/or creep tested.

The creep parameter data, obtained in the experimental study of the near Ti<sub>2</sub>AlNb alloys, suggest three separate creep mechanisms are active. For stresses less than 100 MPa, the lowest  $n$  and  $Q_{app}$  values were obtained. For the super-transus Ti-23Al-27Nb microstructure, the  $n$  values were close to unity and the  $Q_{app}$  was expected to resemble that for grain-boundary diffusion, which suggests a Coble creep mechanism exists. For

applied stresses between 100-352 MPa, a grain boundary sliding mechanism was suggested. This is supported by  $n$  values close to two and  $Q_{app}$ s significantly greater than those within the Coble creep regime. For stresses greater than 352 MPa, dislocation climb was suggested as the  $n$  values were greater than 3.5 and the  $Q_{app}$ s were approximately twice that obtained within the Coble creep regime. The  $Q_{app}$  for lattice self-diffusion is expected to be close to 346 kJ/mol, while the apparent activation energy for grain boundary diffusion is expected to lie close to 171 kJ/mol. The stress range for the Coble and grain boundary sliding mechanisms appeared to be dependent on microstructure as the sub-transus near Ti<sub>2</sub>AlNb microstructures did not exhibit Coble creep characteristics at  $\sigma=50$  MPa. Based on the creep mechanisms and the microstructure-creep rate trends, a strong grain size dependence is suggested within the low-to-intermediate applied stress range.

Table 4.9 Measured Creep Exponents and Apparent Activation Energies for Heat-Treated Ti-25Al-23Nb and Ti-25Al-27Nb Microstructures

Heat Treatment	$\sigma$ /Temp (MPa/°C)	$n$	$\sigma$ /Temp (MPa/°C)	$Q_{app}$ (kJ/mol)
<b>Ti-25Al-27Nb</b>				
as-processed	172-317/650	2.3	394/650-760	346
as-processed	317-394/650	5.1		
<b>Ti-25Al-23Nb</b>				
650°C/116h/WQ			50/650-760	311

WQ: water quenched;

The strong grain size-creep rate trend was also observed for the Ti-25Al-24Nb microstructures, which were examined for one testing condition; 650°C/172 MPa. Based on the creep parameter data, this condition lies within the grain boundary sliding regime. The Ti-25Al-24Nb specimens were not aged, and the O phase precipitated within the B<sub>2</sub> grains during the experiments. However, as seen in the aging-effects sub-section, similar minimum creep rates were achieved for both aged and unaged specimens. Therefore

similar secondary-creep mechanisms are expected for aged and unaged specimens. The data show that  $\dot{\epsilon}_{\min}$  decreased with increasing grain size, see rows 17-20 of Table 4.8. This is depicted in the creep strain versus time plots, Figure 4.50a. Although minimum creep rates also tended to decrease with increasing O-phase volume, this trend was not strictly obeyed as the microstructure containing 79% O phase had a similar minimum creep rate as the microstructure containing 95% O phase. Each microstructure contained a similar grain size, compare rows 18 and 19 of Table 4.8. The morphology was not altered; each microstructure contained equiaxed O+B2 grains. Combining the data of the Ti-23Al-27Nb and Ti-25Al-27Nb alloys with that of the Ti-25Al-24Nb alloy at 650°C/172 MPa, greater creep resistance was exhibited by those microstructures containing larger grain sizes. A plot of  $\log \dot{\epsilon}_{\min}$  versus  $\log \sigma$  depicting the GS- $\dot{\epsilon}_{\min}$  correlation is given in Figure 4.51. No consistent trend was exhibited with respect to phase volume fraction. In fact, contrary to previous observations of creep resistance increasing with O phase volume and decreasing with  $\alpha_2$  phase volume, the sub-transus  $\alpha_2$ -containing microstructure exhibited greater creep resistance than some O+BCC microstructures. That is, the three-phase Ti-23Al-27Nb microstructure, containing approximately 10%  $\alpha_2$ , exhibited greater creep resistance than O+BCC microstructures containing a higher O-phase volume, compare 1025°C data with 950°C and 875°C data of Table 4.6. The average GS of the  $\alpha_2$ -containing microstructure was larger than that of the O+BCC microstructures. Thus phase volume fraction does not appear to be as significant as grain size within the grain boundary sliding regime.

The super-transus microstructures exhibited better creep resistance than the sub-transus equiaxed microstructures. Thus large-grained, transformed-B2 microstructures favor creep resistance. Transformed-BCC microstructures containing different grain sizes were not examined for near Ti<sub>2</sub>AlNb alloys and will be compared in the section which describes the creep behavior of Ti-12Al-38Nb.

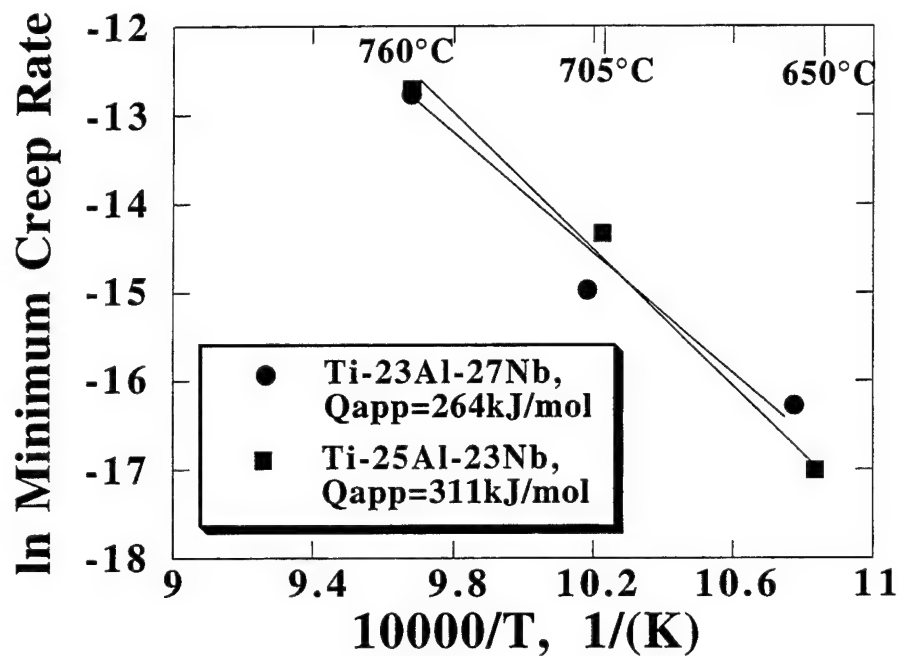


Figure 4.49  $\ln(\dot{\epsilon}_{\min})$  vs  $(1/T)$  for similar Ti-23Al-27Nb and Ti-25Al-23Nb microstructures at  $\sigma = 50$  MPa. The heat treatments used to obtain the similar microstructures were  $875^{\circ}\text{C}/45\text{h}/\text{WQ}/650^{\circ}\text{C}/304\text{h}/\text{WQ}$  for Ti-23Al-27Nb and  $650^{\circ}\text{C}/116\text{h}/\text{WQ}$  for Ti-25Al-23Nb.

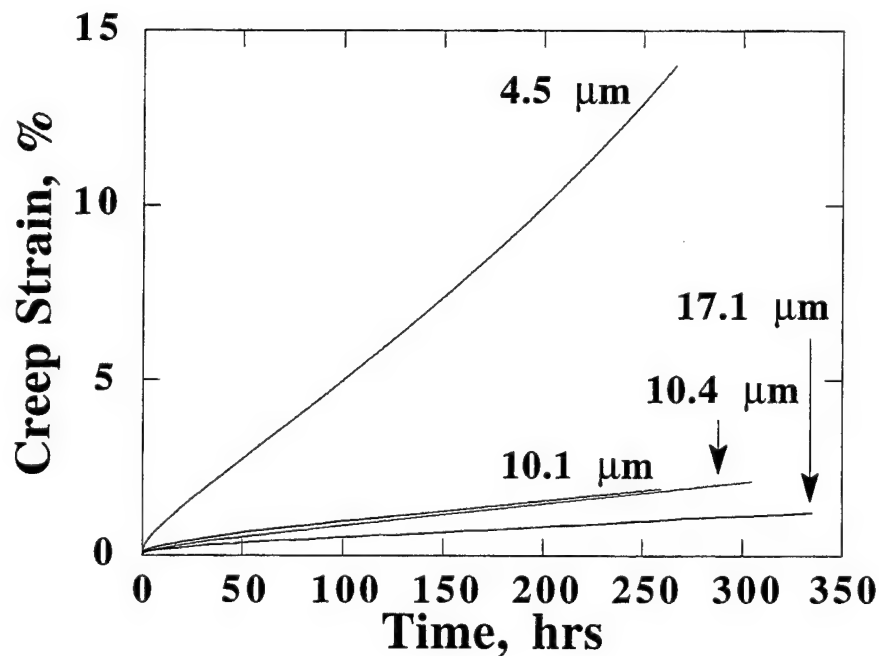


Figure 4.50 Creep strain versus time plot for Ti-25Al-24Nb specimens at  $650^{\circ}\text{C}/172$  MPa. The average GS of the specimens are depicted next to each curve.



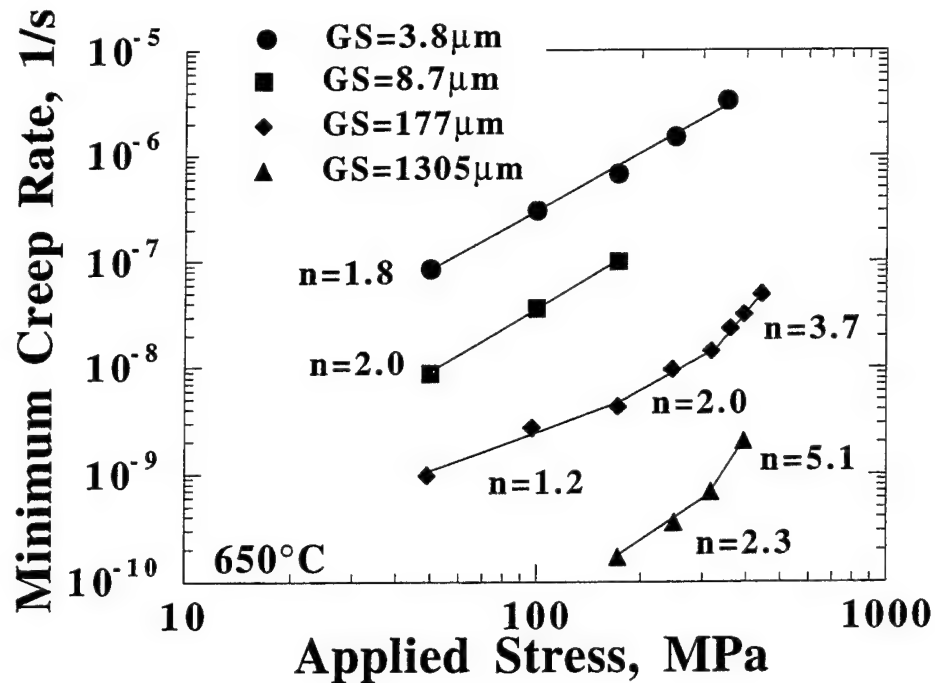


Figure 4.51  $\log \dot{\epsilon}_{\min}$  vs  $\log \sigma$  for Ti-23Al-27Nb and Ti-25Al-27Nb microstructures, which are represented by their grain sizes.

Deformation Behavior. In order to understand the deformation behavior, the polished surfaces of selected specimens were marked with shallow fiducial scratches located both parallel and perpendicular to the loading axis. Microstructural evidence of the fiducially-marked specimens indicated that grain boundary sliding contributed to creep strains. Surface grain boundary offsets were observed at (equiaxed O)-(equiaxed O) and (equiaxed O)-(prior B2) boundaries for a sub-transus Ti-23Al-27Nb specimen which was unloaded after 4 and 9.8% creep strain, compare Figures 4.52a-c. A majority of the sliding was observed at boundaries oriented at 45 degrees to the stress axis. As summarized by Langdon (1972), boundary sliding in the bulk is roughly equivalent to sliding at the surface for low total strains in specimens having cut surfaces. Although the percentage of strain attributed to sliding can be calculated from properly placed fiduciary markings (Langdon 1972, Evans and Wilshire 1985), such calculations are not reported in this work for two reasons. First, the extremely fine O and prior B2 grain sizes of the sub-

transus microstructures made it impractical to accurately measure offset distances with the low magnification imaging necessary for representing global strains. Second, the fiduciary line thicknesses were large with respect to the grain sizes and therefore large measuring errors are associated. Very fine grids would be required to accurately measure the grain and sliding strains. Although the main purpose of the fiduciary markings was to qualitatively access the deformation behavior using surface observations, local measurements revealed that sliding strains were as high as 6% for the specimen deformed to 9.8% creep. Such a location is depicted in Figure 4.53. This measurement was based on the displacement offsets at (equiaxed-O)/(equiaxed-O) and (equiaxed-O)/(prior-B2) boundaries divided by the O-phase grain diameter. Thus high local strains were provided by grain boundary sliding.

Grain boundary sliding was accompanied by cracking. Throughout the specimens cracking was found along the grain boundaries, especially at O/O boundaries. The extent of cracking was dependent on creep strain. A larger extent of cracking was observed for those specimens which achieved greater strains, compare Figures 4.54a and b. In addition, the cracking at the surface appeared to be more extensive than that within the bulk. This is depicted in BSD photomicrographs comparing the bulk and surface deformation for a specimen which exhibited 9.8% creep strain, see Figures 4.54a and 4.55, respectively. This may be related to the topography at the free surface, which had a higher surface roughness than that of the flatter, polished bulk section. Thus the surface observations were important for understanding the sliding behavior, yet they appear to exaggerate the extent of cracking compared to that within the bulk. The cracking behavior of the specimens crept in tension and compression were similar. This is depicted in BSD photomicrographs comparing the bulk deformation for specimens which exhibited 9.8% creep strain in tension, Figure 5.54a, and compression, Figure 4.56. Unlike that of the tension specimen, the grain boundary cracks observed in the compression sample were located on boundaries parallel to the loading direction, see

Figure 4.56. Because the cavities developed within the secondary stage, the microstructures were not constant and steady-state creep was not achieved. After reaching a minimum, the secondary creep rates were observed to accelerate with increasing creep strain. Wedge cracks typically formed at triple point locations, see Figure 4.52b. In tensile creep, the first evidence of cracks was observed on those O/O boundaries located perpendicular to the loading axis, see Figure 4.52b. In addition these boundaries opened up the largest cracks as seen for the higher strains, see Figure 4.52c. This type of cracking is expected within the grain boundary sliding regime as such boundaries are incapable of sliding (Gandhi and Raj 1981). The amount of strain attributed to the grain boundary cavitation was estimated from bulk observations. Several lines were drawn across SEM images, representing surface and sub-surface polished sections, both perpendicular and parallel to the stress axis. The length of the cavity openings was measured and divided by the length of the respective lines. The averaged strain values from the cavity-opening measurements represented a minority of the creep strains achieved. Therefore, grain boundary cracking could not be the rate-controlling mechanism.

The deformation observations suggest that grain boundary sliding was controlling the creep rate. The grain boundary sliding and grain boundary cavitation processes are not considered to be independent, and they appear to be contributing to the majority of the creep strain. The total creep strain can be represented by (Evans and Wilshire 1985):

$$\epsilon_{\text{tot}} = \epsilon_{\text{gbs}} + \epsilon_{\text{g}} \quad (4.5)$$

where  $\epsilon_{\text{tot}}$  is the measured creep strain,  $\epsilon_{\text{gbs}}$  is the strain attributed to grain boundary sliding, and  $\epsilon_{\text{g}}$  is the strain contribution from within the grains. If a majority of the creep strain is attributed to grain boundary sliding, the strain contribution within the grains is expected to be minor.

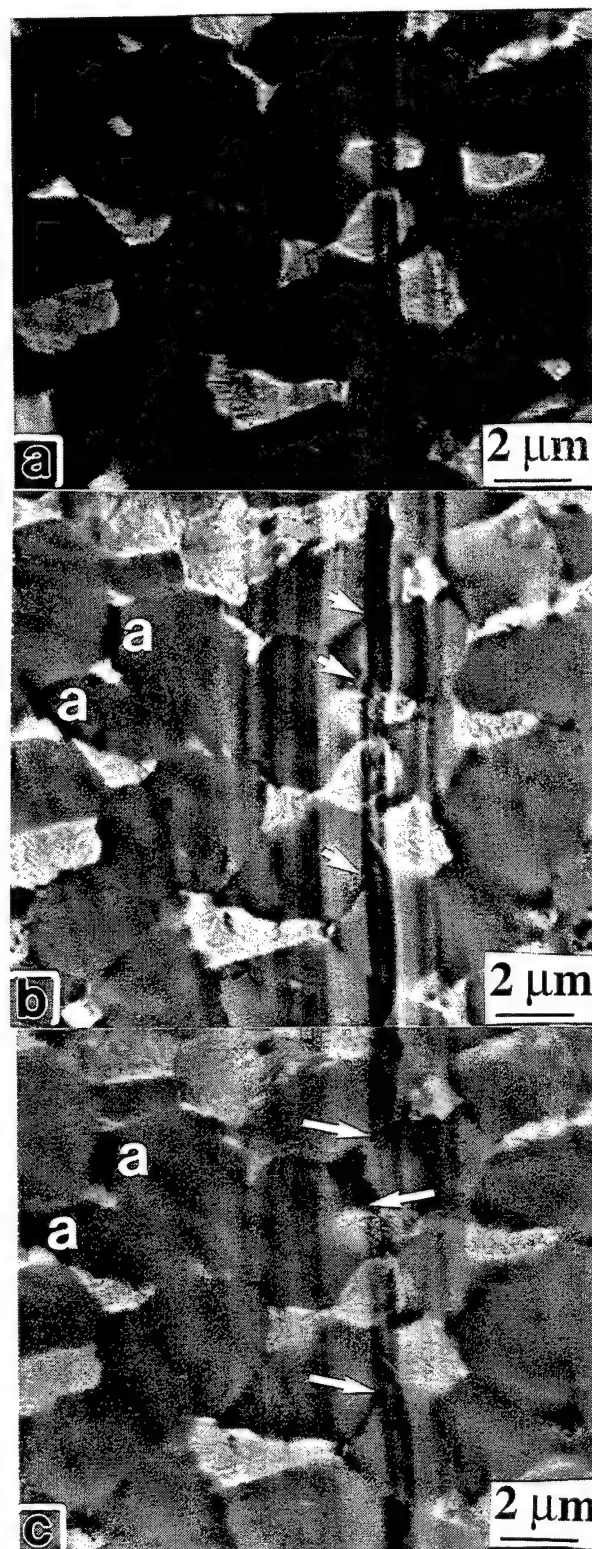


Figure 4.52. A Ti-23Al-27Nb 875°C heat-treated sample containing fiducial marks; (a) prior to creep and after (b) 4% creep, and (c) 9.8% creep at 650°C/172 MPa. Arrows indicate displacement offsets at grain boundaries. Cracks nucleated at O/O boundaries, marked 'a' in (b) and (c), aligned normal to the loading axis (horizontal).

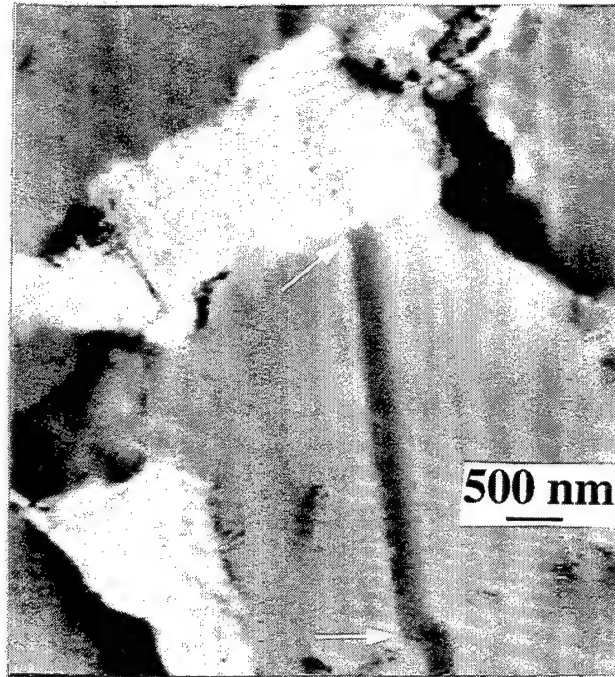


Figure 4.53 SEM image of local grain boundary offsets (indicated by arrows) for the 875°C heat-treated Ti-23Al-27Nb specimen depicted in Figure 4.52c, which deformed to 9.8% creep.

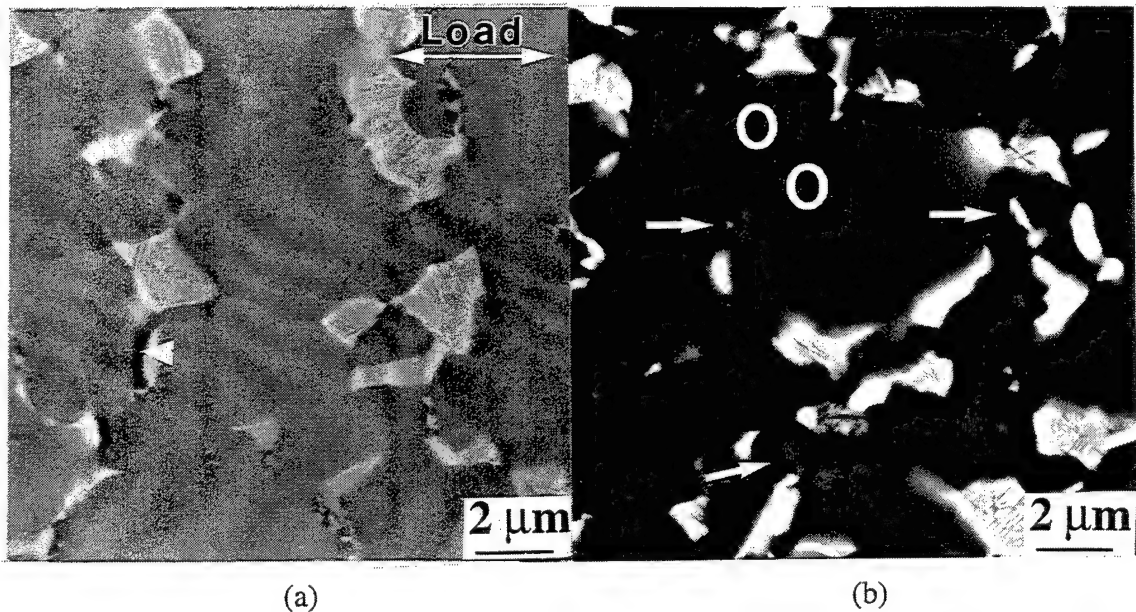


Figure 4.54. The deformed, sub-surface microstructures of Ti-23Al-27Nb 875°C/45h/WQ/650°C/304h/WQ heat-treated tension specimens which were unloaded within the secondary creep regime. Grain boundary cracking is indicated by the arrows. The respective loading conditions and creep strains were (a) 650°C/172 MPa; 9.8% and (b) 650°C/100 MPa; >20%.

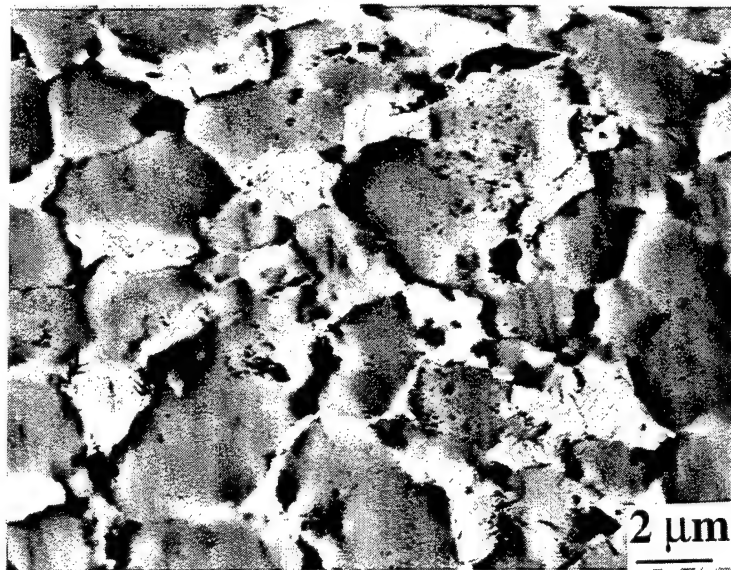


Figure 4.55 Severe grain boundary cracking at the surface for a Ti-23Al-27Nb 875°C/45h/WQ/650°C/304h/WQ heat-treated specimen which exhibited 9.8% creep strain before unloading within the secondary creep stage. The loading condition was 650°C/172 MPa.

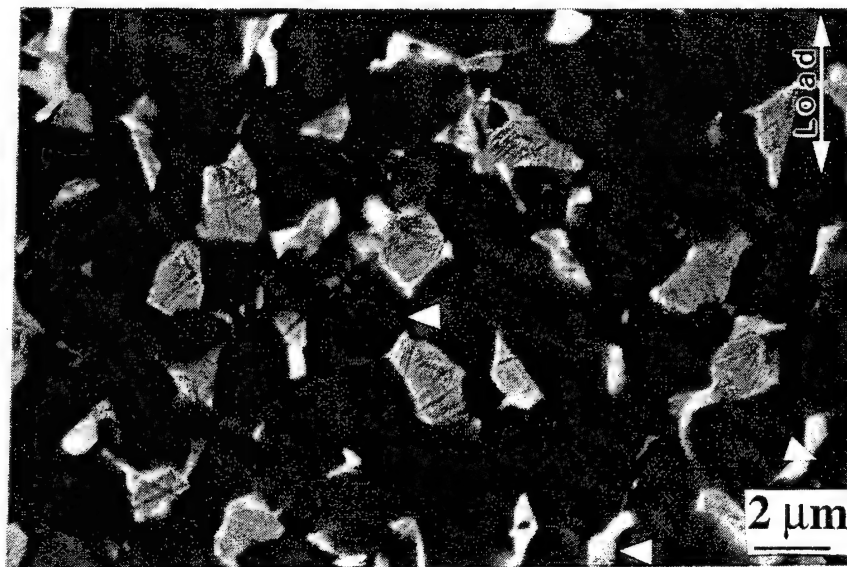


Figure 4.56 The deformed, sub-surface microstructure of the Ti-23Al-27Nb 875°C/24h/WQ/650°C/218h/WQ heat-treated compression specimen which exhibited 9.8% creep. The specimen was unloaded in the secondary creep regime after being incrementally loaded from 172-250 MPa at 650°C.



The grain boundary cracking occurred independent of environment. In a vacuum environment, surface grain boundary cracks were observed after specimens reached 4% creep, see Figure 4.52b, whereas in air, surface grain boundary cracking developed within 2.1% creep, see Figures 4.57a and b. These observations were made for sub-transus microstructures tested under identical creep stresses and temperatures. It is noted that the vacuum creep specimen was not unloaded prior to reaching 4% creep. In each case O/O boundaries were preferred sites for cracking and in many cases the B2 phase blunted such cracks, see Figure 4.57a. The susceptibility of O/O grain boundary cracking was evidenced even at near-surface locations, where the environment was expected to play a dominant role. This is depicted in the secondary electron and BSD images of the same location, Figures 4.58a and b, respectively, where a surface crack was retarded inside a transformed B2 grain and continued along primary O grain boundaries. Except for near-surface locations of air-tested specimens, few cracks penetrated grains deeply.

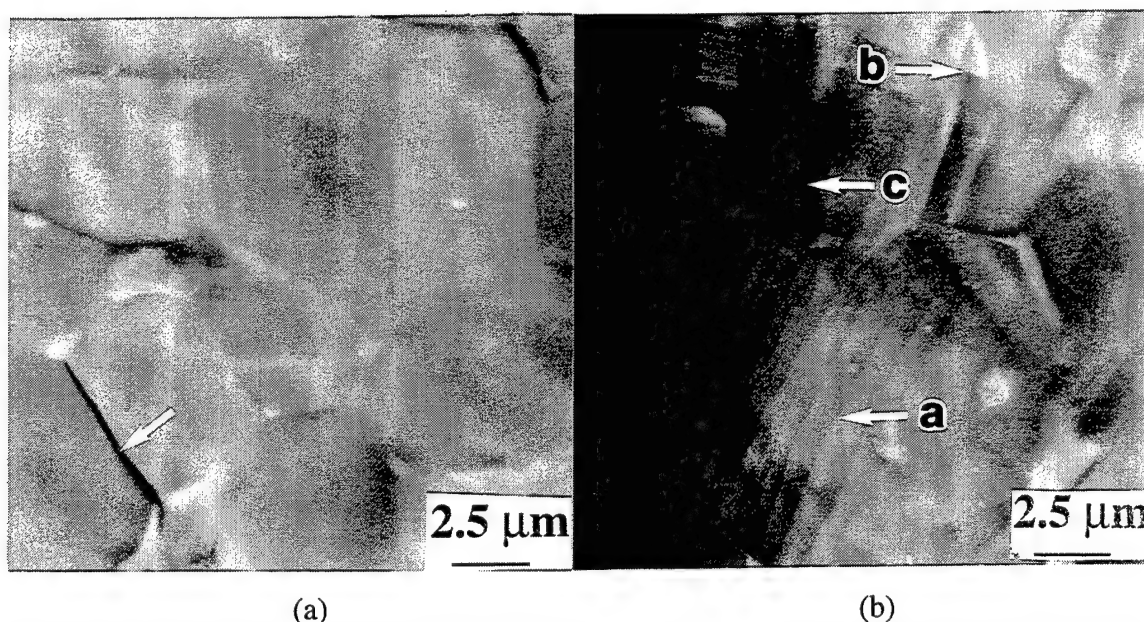


Figure 4.57 Elevated temperature creep cracking and slip for a heat treated (930°C/100h/WQ) Ti-25Al-25Nb specimen crept to 2.1% at 650°C/172 MPa. (a) O/O grain boundary cracks were blunted by B2. (b) Planar slip in the O phase (arrow a), slip transmittability between O and B2 grains (arrow b), and surface cracks (arrow c) were evident next to the specimen's edge.

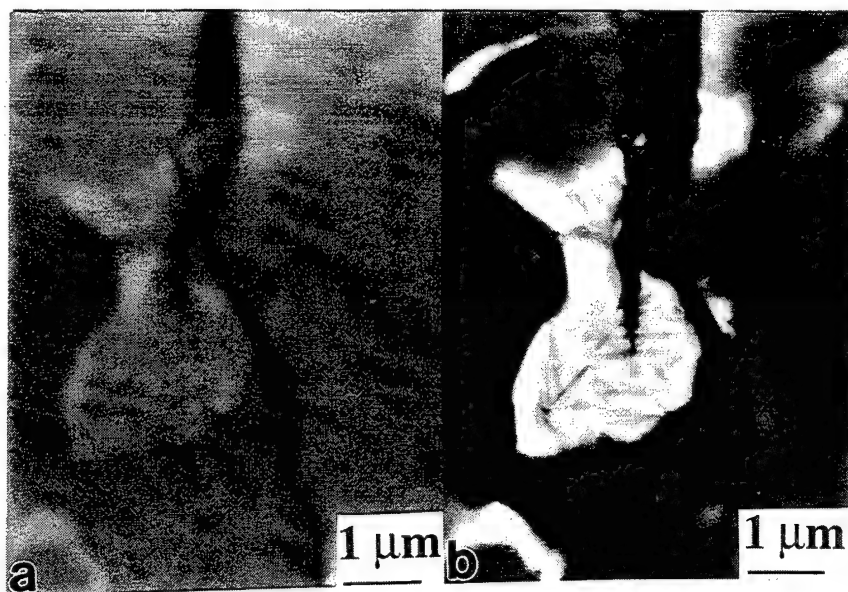


Figure 4.58 SEM (a) secondary electron and (b) BSD images of the same location illustrating a surface crack which was retarded inside a transformed B2 grain and continued along primary O grain boundaries for a sub-transus Ti-23Al-27Nb specimen tested at 650°C/100 MPa.

The surface cracks which grew transgranularly and perpendicular to the stress axis were only observed for the specimens tested in air. In such cases the environment was suspected to have influenced the crack growth as oxide scales were observed along the crack surfaces. The oxide scale thickness, however, was much less than the crack depth. It appeared therefore that the surface cracks grew by local oxidation and cracking ahead of the crack tip. The severe surface cracking, up to 500  $\mu\text{m}$ , was expected to be responsible for the higher secondary creep rate of the air-tested specimen compared with the vacuum-tested specimen, compare rows 4 and 6 of Table 4.6. Figures 4.59a and b depict the surface cracking exhibited by a sub-transus specimen strained to over 20% at 650°C/100 MPa. The duration of the creep test in this case was 283 hours. The surface cracks widened behind the crack tip, see Figure 4.59b.



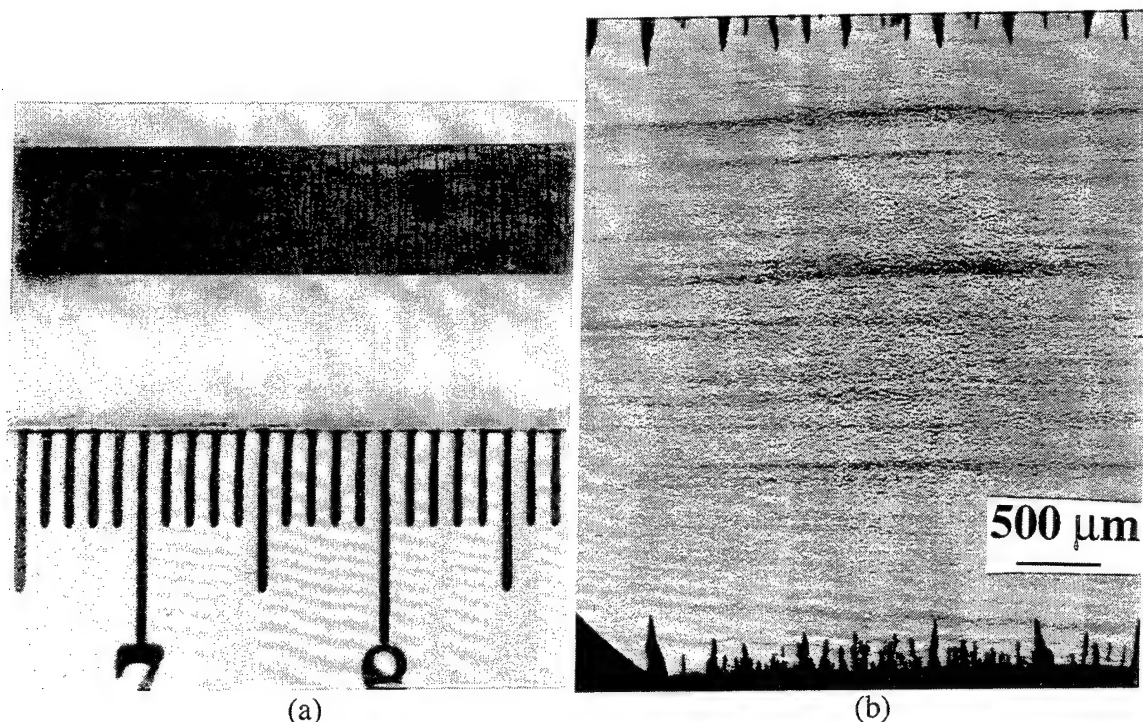


Figure 4.59 The (a) surface and (b) cross-sectional views of the environmentally-assisted surface cracking for a 875°C/45h/WQ/650°C/304h/WQ Ti-23Al-27Nb specimen, which exhibited over 20% creep strain at 650°C/100 MPa. The specimen was unloaded after 283 hours.

Surface observations revealed that slip was planar within O grains and slip transmittability was evident between O and B2, see Figure 4.57b. However for applied stresses less than 352 MPa, few slip traces were exhibited even for samples strained to more than 9%, see Figure 4.52c. This is in agreement with the low strain contributions expected within the grains. TEM investigations revealed relatively little evidence of deformation for specimens crept below 352 MPa. A typical post-creep microstructure, depicting the dislocation activity, for sub-transus solutionized specimens is represented in Figures 4.60a-c. Some dislocations lied in pile-up configurations at (equiaxed O)-(equiaxed O) grain boundaries as shown in Figure 4.60c. Other dislocations formed preferentially at O/ $\beta$  interfaces, Figure 4.60a, within transformed B2 regions. However these were also found in the grip regions of the long-term aged samples, see Figure 4.15, and therefore they probably resulted from transformation stresses. A large number of equiaxed O grains were examined for specimens which were unloaded in the secondary

creep regime after exhibiting at least 6% creep strain. Few grains exhibited a significant number of dislocations, see Figure 4.60b. After comparing the microstructures of gage regions and grip sections, it was concluded that the dislocation activity within the equiaxed O grains could not be responsible for the creep strains measured.

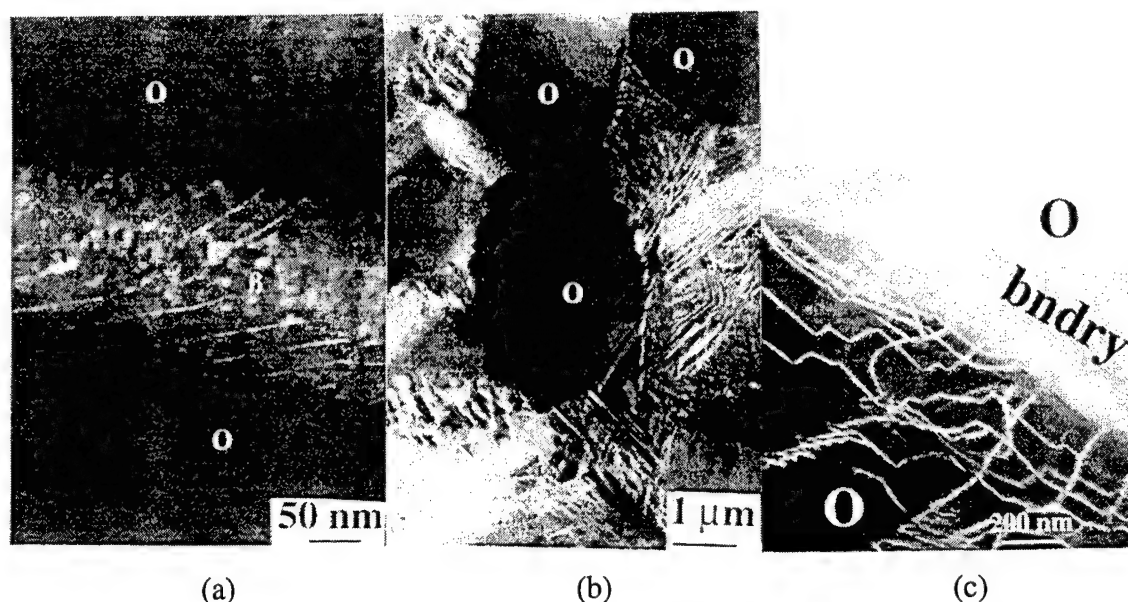


Figure 4.60 The post-creep microstructure of a 950°C/45h/WQ heat-treated Ti-23Al-27Nb specimen which exhibited more than 6% creep strain at 650°C/100 MPa. Dislocations formed preferentially at (a) O/B interfaces although this was also observed in heat-treated samples which were not creep deformed. A limited number of dislocations were observed within equiaxed O grains, see (b) and (c). In some cases the dislocations piled up at a (equiaxed O)-(equiaxed O) interfaces, see (c).

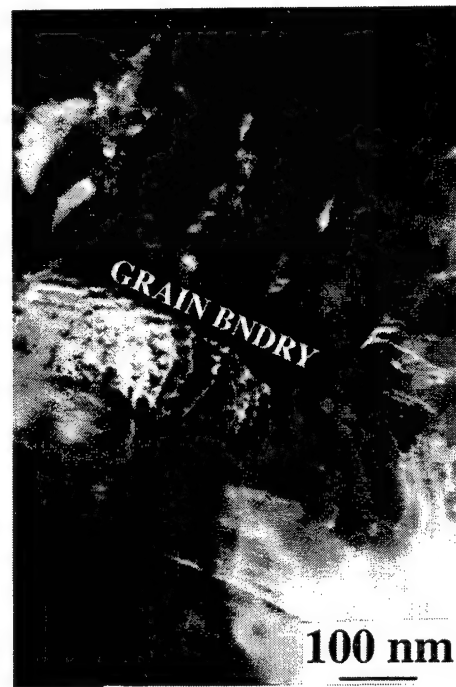
Analysis of deformed samples tested within the dislocation creep regime showed larger dislocation densities than the deformed microstructures of the grain boundary sliding and Coble creep regimes. The dislocations within the O phase congregated as slip bands for the super-transus Ti-25Al-27Nb microstructure, see Figure 4.61. In addition, a greater density of dislocations was found within B2 platelets, which appeared to be saturated, Figure 4.62a. In some cases, however, dislocations were observed to pile-up near grain boundaries, see Figure 4.62b.



Figure 4.61 The deformed Ti-25Al-27Nb as-processed microstructure tested at 394 MPa/760°C. Dislocations formed within O grains in slip bands.



(a)



(b)

Figure 4.62 Bright-field TEM images of a post-crept Ti-23Al-27Nb super-transus microstructure containing (a) B2 platelets which are saturated with dislocations and (b) piled-up dislocations near a grain boundary for a specimen crept at 650°C/442 MPa.

Combining the deformation observations with the creep parameter data, there are strong indications that grain boundary sliding and dislocation climb are the active creep mechanisms. Low dislocation densities within grains were observed within the low-to-intermediate ( $\sigma < 352$  MPa) stress regime. Grain boundary offsets indicated that a majority of the creep strain accumulated through slid grains and cavitation within this regime. Sliding appeared to be accommodated by grain boundary cracking, and stationary boundaries, located 90 degrees to the stress axis, opened the largest cracks in tensile creep. A higher dislocation density was observed for samples crept within the high stress ( $\sigma > 352$  MPa) regime, which is considered to be dominated by dislocation climb.

#### 4.2.2 Ti-12Al-38Nb

As mentioned in the phase-evolution results section, an attractive aspect, in terms of determining microstructure-property relationships, of the phase evolution of Ti-12Al-38Nb was that the grain size can be controlled without significantly affecting other microstructural features such as phase volume percents and morphologies. Because such a strong grain size dependence was observed for the near Ti<sub>2</sub>AlNb alloys, this correlation served as the focus of the microstructure-creep relation study for Ti-12Al-38Nb.

Grain Size Effects. Prior to creep examination, specimens were solutionized above the  $\beta$  transus to obtain equiaxed microstructures containing average  $\beta$  grain sizes of 138 and 337  $\mu\text{m}$ . The specimens were then aged at 650°C to equilibrate approximately 30 volume percent of O platelets, uniformly dispersed within the  $\beta$  matrix. The data from these specimens were compared with that for the as-rolled material, containing a 33  $\mu\text{m}$   $\beta$  grain size, which was also aged at 650°C. The creep stress and temperatures ranged from 50-172 MPa and 650°C-705°C, respectively. Table 4.10 lists the testing conditions,  $\epsilon_p$ ,  $t_p$ ,  $\dot{\epsilon}_{\text{min}}$ , and GS for each of the heat-treated specimens tested. Similar to the relationship observed for the near Ti<sub>2</sub>AlNb alloys, minimum creep rates decreased with increasing

grain size from 33 to 138  $\mu\text{m}$ . However, for the 138 and 337 $\mu\text{m}$  grain size microstructures, the minimum creep rates were similar and therefore the prior  $\beta$  grain size was not controlling the minimum creep rates. Figure 4.63 is a creep strain versus time plot for each of the Ti-12Al-38Nb microstructures examined at 650°C/50 MPa. This plot shows that the greatest primary creep resistance was exhibited by the 900°C heat-treated microstructure, which contained a 138  $\mu\text{m}$   $\beta$  grain size. An intermediate primary creep resistance was exhibited by the largest  $\beta$ -grained (GS=337  $\mu\text{m}$ ) microstructure.

Table 4.10 Creep Properties for Heat-Treated Ti-12Al-38Nb Microstructures

Heat Treatment	$\sigma/T$ (MPa/°C)	$\epsilon_p$ (%)	$t_p$ (h)	$\dot{\epsilon}_{\min}$ (1/s)	GS* ( $\mu\text{m}$ )
650°C/55h/WQ	172/650	na	na	5.41E-08	33.2
650°C/55h/WQ	100/650	na	na	7.97E-09	33.2
650°C/55h/WQ	50/650	0.31	118.0	2.65E-09	33.2
650°C/55h/WQ	50/705	0.66	116.0	8.85E-09	33.2
900°C/5h/WQ/650°C/62h/WQ	173/650	na	na	3.58E-08	138.2
900°C/5h/WQ/650°C/62h/WQ	150/650	na	na	2.02E-08	138.2
900°C/5h/WQ/650°C/62h/WQ	125/650	na	na	7.27E-09	138.2
900°C/5h/WQ/650°C/62h/WQ*	125/650	1.17	90.0	6.98E-09	138.2
900°C/5h/WQ/650°C/62h/WQ*	135/650	na	na	7.69E-09	138.2
900°C/5h/WQ/650°C/62h/WQ	100/650	na	na	3.88E-09	138.2
900°C/5h/WQ/650°C/62h/WQ	50/650	0.16	112.7	1.23E-09	138.2
900°C/5h/WQ/650°C/62h/WQ	50/675	na	na	1.66E-09	138.2
900°C/5h/WQ/650°C/62h/WQ	50/705	0.48	124.0	4.39E-09	138.2
1200°C/5h/WQ/650°C/53h/WQ	123/650	na	na	7.15E-09	336.9
1200°C/5h/WQ/650°C/53h/WQ	101/650	na	na	5.23E-09	336.9
1200°C/5h/WQ/650°C/53h/WQ	76/650	na	na	2.28E-09	336.9
1200°C/5h/WQ/650°C/53h/WQ	50/650	0.25	190.5	1.26E-09	336.9
1200°C/5h/WQ/650°C/53h/WQ	50/675	0.93	162.0	1.93E-09	336.9
1200°C/5h/WQ/650°C/53h/WQ	50/705	na	na	3.20E-09	336.9
1200°C/5h/WQ/650°C/53h/WQ	150/705	na	na	1.93E-07	336.9
1200°C/5h/WQ/650°C/53h/WQ	136/705	na	na	8.29E-08	336.9
1200°C/5h/WQ/650°C/53h/WQ	123/705	na	na	4.66E-08	336.9
1200°C/5h/WQ/650°C/53h/WQ	123/675	na	na	1.73E-08	336.9

WQ: water quenched; na: not available; \*: tested in vacuum ( $9 \times 10^{-7}$  torr); \*: GS represents the average equiaxed grain size of the corresponding heat-treated microstructures before they were aged at 650°C.

Mechanical Properties. Similar to the near Ti<sub>2</sub>AlNb alloys, the creep parameter data for Ti-12Al-38Nb suggested three separate creep mechanisms exist. Table 4.11

summarizes the creep parameter data, while Figures 4.64a and b show plots of the stress and temperature dependence on  $\dot{\epsilon}_{\min}$ , respectively. At the lowest applied stress,  $\sigma=50$  MPa, Coble creep behavior was exhibited as  $n$  was between 1-2 and  $Q_{app}$  was between 127-178 kJ/mol, see rows 1, 3, and 5 of Table 4.11. The activation energies within the Coble creep regime were similar for both Ti-12Al-38Nb and near Ti<sub>2</sub>AlNb microstructures. This suggests that the activation energy for grain boundary diffusion is relatively insensitive to phase volume and grain size for O+BCC alloys.

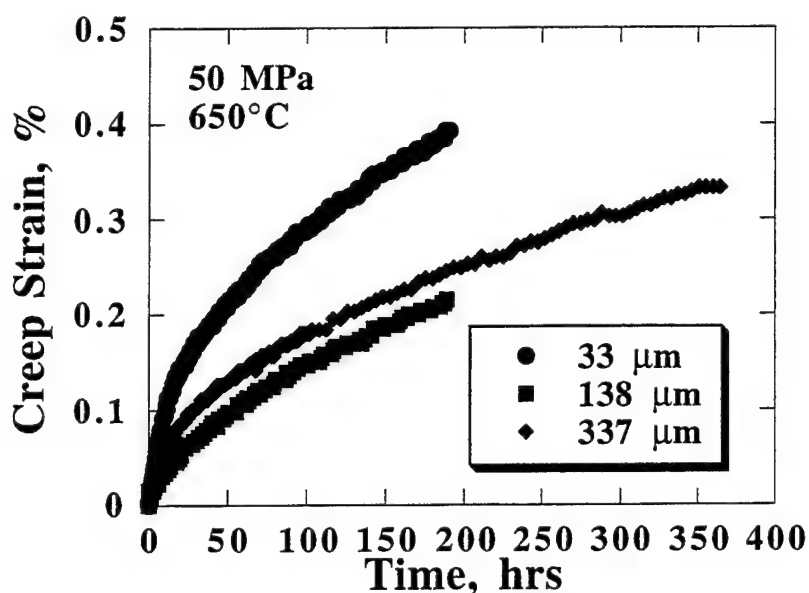


Figure 4.63 Creep strain versus time plots for the three Ti-12Al-38Nb heat-treated microstructures, represented by their average prior  $\beta$  grain size, tested at 650°C/50 MPa.

Table 4.11 Measured Creep Exponents and Apparent Activation Energies for Heat-Treated Ti-12Al-38Nb Microstructures

Heat Treatment	$\sigma$ /Temp (MPa/°C)	$n$	$\sigma$ /Temp (MPa/°C)	$Q_{app}$ (kJ/mol)
650°C/55h/WQ	50-100/650	1.6	50/650-705	178
650°C/55h/WQ	100-172/650	3.5		
900°C/5h/WQ/650°C/62h/WQ	50-135/650	1.9	50/650-705	175
900°C/5h/WQ/650°C/62h/WQ	135-172/650	6.1		
1200°C/5h/WQ/650°C/53h/WQ	50-123/650	2.0	50/650-705	127
1200°C/5h/WQ/650°C/53h/WQ	123-150/705	7.2	123/650-705	256

WQ: water quenched.

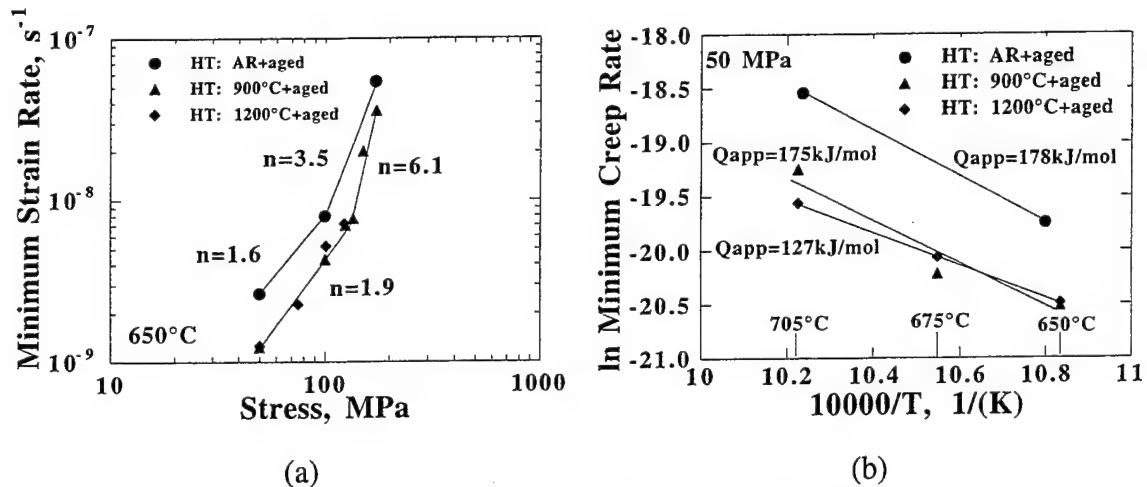


Figure 4.64 Creep plots for three heat-treated Ti-12Al-38Nb microstructures. (a) Log  $\dot{\epsilon}_{min}$  vs log  $\sigma$  curves at  $T = 650^\circ\text{C}$ , where the data indicates a transition in creep exponent at 135 MPa. (b) Temperature dependence of  $\dot{\epsilon}_{min}$  for  $\sigma = 50$  MPa.

Between 75-135 MPa, the creep exponent was close to two, see rows 3 and 5 of Table 4.11 and Figure 4.64a. The  $Q_{app}$  was 256 kJ/mol at  $\sigma = 123$  MPa, see row 6 of table 4.11. Thus, nearly identical values of  $n$  and  $Q_{app}$  were exhibited by Ti-12Al-38Nb and near  $\text{Ti}_2\text{AlNb}$  alloys at intermediate applied stresses. These creep parameters suggest grain boundary sliding to be the dominant creep mechanism.

For stresses greater than 135 MPa, the creep exponents were greater than or equal to 3.5, see rows 2, 4 and 6 of Table 4.11. Thus, the creep exponent transitioned to high values at lower stresses compared with the near  $\text{Ti}_2\text{AlNb}$  alloys. For comparison purposes, the stress at which the grain boundary sliding-to-dislocation climb transition occurred was greater than 318 MPa for the near  $\text{Ti}_2\text{AlNb}$  microstructures. This result indicates that the strain rates increased more rapidly with increasing stress for Ti-12Al-38Nb. This also indicates that the creep mechanisms' stress ranges are dependent on nominal alloy composition.

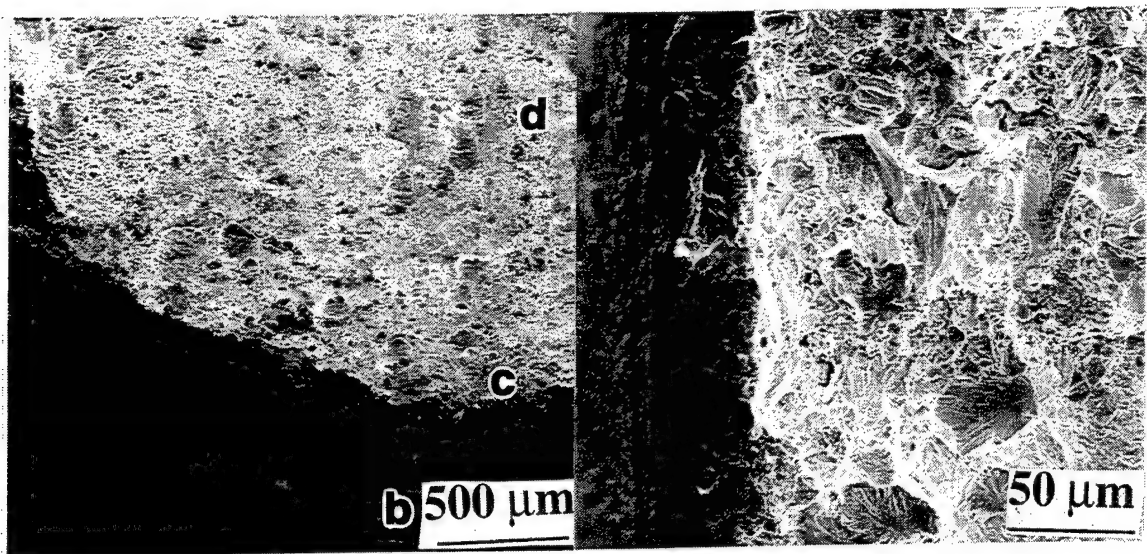
**Deformation Behavior.** Fracture surface observations indicated that Ti-12Al-38Nb was more sensitive to the environment than near  $\text{Ti}_2\text{AlNb}$  alloys. A larger environmental affected zone surrounded the fracture surfaces of Ti-12Al-38Nb specimens compared



with near  $\text{Ti}_2\text{AlNb}$  specimens. This was true even for specimens which were exposed under lower stresses for less time. Figures 4.65a and b compare fracture surfaces of a super-transus Ti-23Al-27Nb specimen, which was step-loaded from 50-442 MPa, with a Ti-12Al-38Nb specimen, which was step-loaded from 50-172 MPa. The Ti-23Al-27Nb failed after reaching 2% creep in 600 hours, while the Ti-12Al-38Nb specimen failed after reaching 3% creep in 350 hours. Although the Ti-12Al-38Nb specimen exhibited good creep resistance, its relatively poor environmental resistance was expected to have facilitated its failure. The larger environmentally affected zone led to a greater reduction in load-bearing cross-sectional area, thereby leading to its premature failure. The embrittled surface regions of the Ti-12Al-38Nb specimen revealed a featureless fracture, see Figure 4.66a, while the interior surfaces failed in a ductile manner exhibiting dimples, see Figure 4.66c. The regions intermediate to the surface and the interior exhibited a combination of the brittle and ductile features, see Figure 4.66b. Thus, this material was expected to have maintained a high level of toughness at temperature, however, its poor oxidation resistance was believed to have led to rapid crack growth rates thereby reaching its toughness at a low stress level. Larger surface cracks were also observed for Ti-12Al-38Nb specimens compared with the near  $\text{Ti}_2\text{AlNb}$  alloys. These observations indicate that nominal composition is quite important for the environmental resistances of O+BCC alloys. In particular, the low Al content was expected to be responsible for the poorer environmental resistance.

Even after 8% creep strain very few creep dislocations were observed for the 33  $\mu\text{m}$   $\beta$  grain size microstructure tested at  $\sigma = 50$  MPa and  $T = 650^\circ\text{C}$ . Figure 4.67 depicts a TEM image taken from the gage section of this specimen. This observation is in agreement with a Coble creep mechanism.

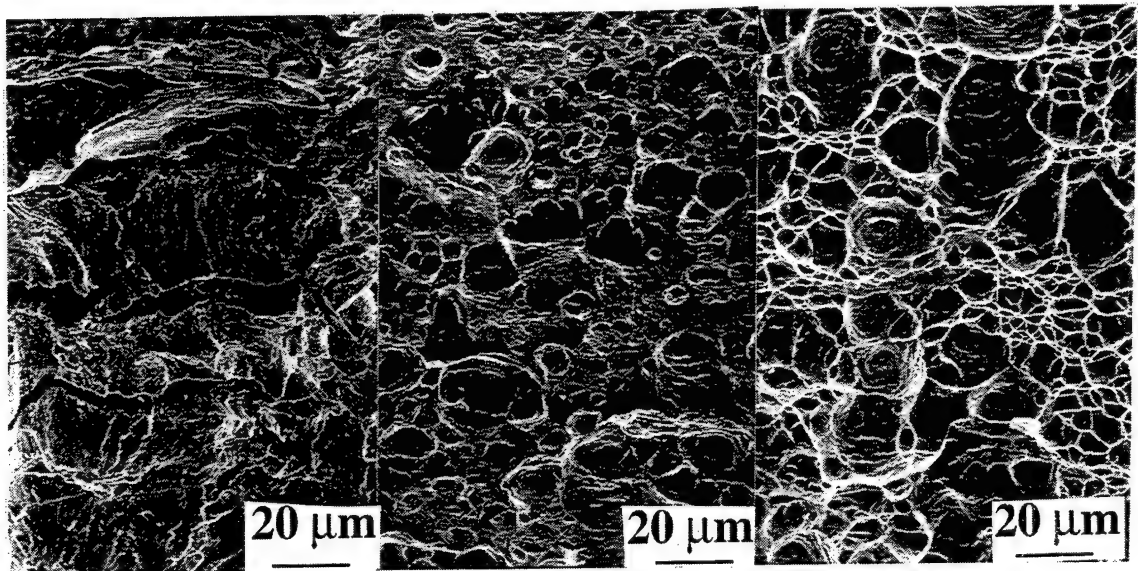




(a)

(b)

4.65 Creep fracture surface of step-loaded (a) Ti-12Al-38Nb (HT:650°C/55h/WQ) and (b) Ti-23Al-27Nb (HT:1090°C/0.5h/WQ/650°C/112h/WQ) specimens crept at 650°C. The Ti-12Al-38Nb failed at 172 MPa after 350 hours and 3% strain, while the Ti-23Al-27Nb specimen failed at 442 MPa after 600 hours and 2% strain. Note the environmental affected zone was much larger for the Ti-12Al-38Nb specimen.



(a)

(b)

(c)

4.66 Higher magnification SEM images of the Ti-12Al-38Nb creep fracture surface depicted in Figure 4.65a. These photos were taken from the regions marked (a) b, (b) c, and (c) d.

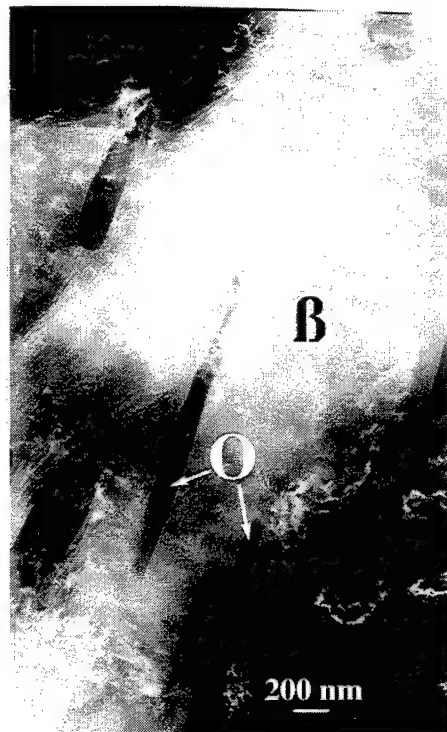


Figure 4.67. TEM image of a post-crept Ti-12Al-38Nb 650°C heat-treated microstructure which failed after reaching 8% creep at  $\sigma=50$  MPa.

### Summary

Comparing the creep data for the near Ti<sub>2</sub>AlNb and Ti-12Al-38Nb microstructures evaluated, microstructure-creep relationship trends are evident. Although the O-phase volume percent was considerably less for Ti-12Al-38Nb, its creep resistance compared favorably with the near Ti<sub>2</sub>AlNb alloys. Based on previous creep data, especially the superior creep resistance observed for a fully-O alloy (Nandy *et al.* 1993), this was an unexpected result as O-dominated microstructures were thought to be superior to both the  $\alpha_2$  and BCC-dominated microstructures. However, taking a closer look at the active creep mechanisms and the general microstructure-creep relationships within a respective regime, microstructural features other than phase volume percent appeared to be more influential to the creep behavior. For a given creep condition, the inverse

relationship between minimum creep rate and average equiaxed grain size was obeyed for grain sizes up to  $177\mu\text{m}$ . This is depicted in the  $\log \dot{\epsilon}_{\text{min}}$  versus  $\log \sigma$  plot of Figure 4.68. Thus, at first glance, grain size appears to be more influential than phase volumes for O+BCC alloys. However, above  $177\mu\text{m}$  the relationship between grain size and minimum creep rate for the solutionized microstructures breaks down. The  $337\mu\text{m}$   $\beta$  grain size microstructure exhibited similar secondary creep rates as the  $138\mu\text{m}$  grain size microstructure. This result is discussed in the creep behavior section of Chapter 5. In addition, the creep exponent transitioned to  $n \geq 3.5$  at a lower stress for Ti-12Al-38Nb compared with the near Ti<sub>2</sub>AlNb alloys, see Figure 4.68 and Tables 4.7 and 4.11. This is also discussed in the creep behavior section of Chapter 5. The observations made in the creep results sections emphasize the importance of understanding and characterizing creep mechanisms, and in particular the stress and temperature ranges of each mechanism, prior to understanding microstructure-creep relationships.

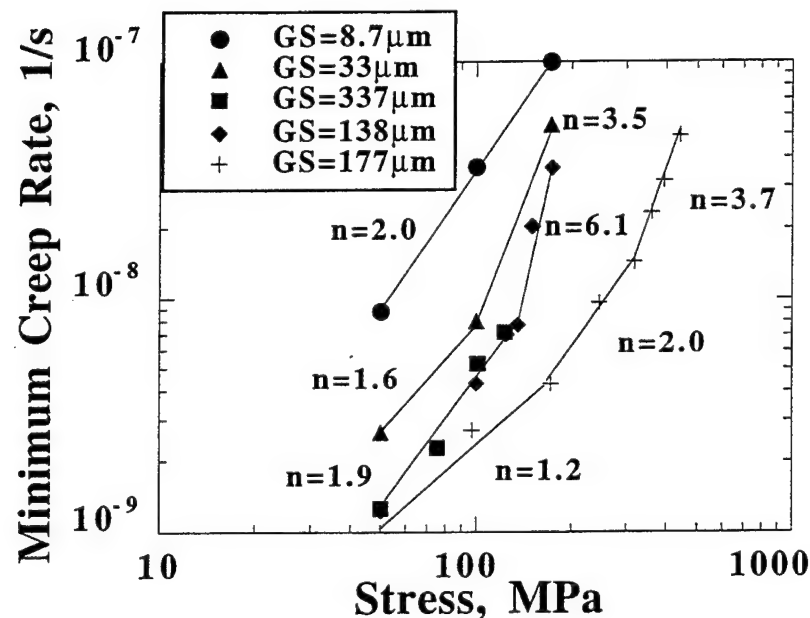


Figure 4.68  $\log \dot{\epsilon}_{\text{min}}$  vs  $\log \sigma$  curves at  $650^\circ\text{C}$  for selected near Ti<sub>2</sub>AlNb and Ti-12Al-38Nb microstructures, represented by the average equiaxed grain size of the corresponding solution treatments.

### 4.3 Tension Behavior

The tensile behavior results section is split into two parts dealing with elevated-temperature tensile properties and RT tensile behavior. The elevated-temperature tensile testing work was focused on determining the flow properties of selected creep microstructures. The objectives of the RT tensile testing study was to understand microstructure-tension relationships. Therefore, the experiments involved a much broader range of microstructures, and a more in-depth characterization of the deformation behavior was performed. The description of the RT tensile behavior is divided into sub-sections dealing with constituent phase properties, second-phase strengthening, and deformation behavior as well as interstitial oxygen, aging, grain size, and morphology effects. Unlike the phase evolution and creep behavior results sections, the near Ti<sub>2</sub>AlNb and Ti-12Al-38Nb alloys will be not be discussed in separate sub-sections.

#### 4.3.1 Elevated-Temperature Properties

In order to help explain the creep behavior trends and understand the effect of temperature on yield strength, selected Ti-23Al-27Nb and Ti-12Al-38Nb microstructures were tested in elevated-temperature tension experiments. In particular this data was intended to provide insight as to why the creep exponents exhibited such a strong dependence on alloy composition and stress. It was felt that higher elevated-temperature flow stresses would be linked with higher transition stresses between the grain boundary sliding and dislocation climb regimes. Higher ratios of applied stress to flow stress have been associated with the dislocation climb regime (Doner and Conrad 1975, Ruano *et al.* 1988). The super-transus solutionized then aged microstructures selected for this examination represented those which exhibited different applied stress values for the transition between creep exponents close to two and those greater than or equal to 3.5.

The 650°C tensile properties, including 0.2% yield strength (YS), ultimate strength (UTS), elongation-to-failure ( $\epsilon_f$ ), and modulus (E), for the selected microstructures are listed in Table 4.12. In each case the results represent only one test performed. The results indicate that the elevated-temperature YS was dependent on composition. The super-transus Ti-23Al-27Nb specimen failed within the grip section at the first thread, most likely due to the high stress concentration, prior to exhibiting plastic deformation within the gage section. The stress within the gage section was 388 MPa at failure. Therefore, a value greater than 388 MPa is expected for both the YS and UTS. The sub-transus Ti-23Al-27Nb compression specimen achieved a YS equal to 675 MPa and a UTS equal to 862 MPa, see row 3 of Table 4.12. Thus, the YS for Ti-23Al-27Nb is higher than that for Ti-12Al-38Nb, which exhibited a YS of 391 MPa, see last row of Table 4.12. A similar 650°C yield strength has been reported for an orthorhombic Ti-25Al-17Nb alloy (YS~400 MPa), while lower yield strengths have been obtained by the  $\alpha_2$ -based Ti-24Al-11Nb and the metastable  $\beta$  alloy, Timetal®21S (Boehlert *et al.* 1997b). Thus O+BCC alloys maintain higher elevated-temperature yield strengths than  $\alpha_2$  and  $\beta$ -based systems. Ti-23Al-27Nb exhibited exceptionally high-elevated temperature strength. The Ti-12Al-38Nb specimen necked outside the extensometer's gage length, therefore the estimated strain-to-failure was much greater than that recorded by the extensometer ( $\epsilon=11\%$ ). In fact, the sample completely unloaded prior to failure and the specimen diameter was significantly reduced, indicative that the local strain was quite high. A cup-and-cone fracture occurred.

Combining the elevated temperature flow properties with the creep behavior of the two alloys, the transition stress between the grain boundary sliding and dislocation climb creep regimes increased with flow stress. This result is in agreement with the hypothesis.

Table 4.12 The Heat Treatments and 650°C Tensile/Compression Properties for Selected near Ti<sub>2</sub>AlNb and Ti-12Al-38Nb Microstructures

Alloy and Heat Treatment	0.2% YS MPa	UTS MPa	ε <sub>f</sub> %	E GPa
<b>Ti-23Al-27Nb</b> 1090°C/0.5h/WQ/650°C/112h/WQ 875°C/24h/WQ/650°C/218h/WQ*	>388** 675	>388** 862	0.4 na	104 na
<b>Ti-12Al-38Nb</b> 900°C/5h/WQ/650°C/62h/WQ	391	441	>11.1	68

WQ: water quenched; na: not available; \*: compression tested; \*\*: The 0.2% proportional limit method could not be used due to the low strain-to-failure achieved. Therefore the maximum stress within the gage section, which underestimates both the YS and UTS, provides a conservative estimate.

#### 4.3.2 RT Tension Behavior

Constituent Phase Properties. The RT tensile properties, including 0.2% yield strength (YS), ultimate strength (UTS), elongation-to-failure (ε<sub>f</sub>), and modulus (E), for selected microstructures are listed in Table 4.13. In most cases the results represent the average of at least two tests. The volume percents and chemistry of the O and BCC phases are also listed in Table 4.13. Elastic modulus data on O alloys has suggested that the O phase is more compliant than the α<sub>2</sub> and BCC phases (Akkurt *et al.* 1991). The current data contradict this, and the BCC structures were the most compliant, while the O phase was the least compliant. The elastic moduli of the BCC phases were dependent on composition. The elastic modulus of the fully-β Ti-12Al-38Nb microstructure was 84 GPa, while E was 96 and 109 GPa for the fully-B2 Ti-23Al-27Nb and Ti-25Al-24Nb microstructures, respectively (see rows 28, 4 and 21 of Table 4.13). Thus higher Al and lower Nb contents favor ordering of the BCC structure and result in higher moduli. The modulus of the fully-O Ti-25Al-24Nb microstructure was 137 GPa, see row 20 of Table 4.13. In general, the microstructural trends exhibited for E could be represented by the isostrain equation:

$$E = E_O v_O + E_{BCC} (1 - v_O) \quad (4.7)$$

where  $E_O$  and  $E_{BCC}$  are the elastic moduli of the O and BCC phases, respectively, and  $v_O$  is the volume fraction of the O phase. The moduli decreased with temperature. In particular, moduli taken from the 650°C tensile experiments, see Table 4.12, were approximately 20% lower than those measured at RT.

Table 4.13 The Heat Treatments and RT Tensile Properties for Selected near Ti<sub>2</sub>AlNb and Ti-12Al-38Nb Microstructures

Alloy and Heat Treatment	YS	UTS	$\epsilon_f$	E	O			BCC		
	MPa	MPa	%	GPa	Al	Nb	Vp	Al	Nb	Vp
<b>Ti-23Al-27Nb**</b>										
950°C/24h/WQ	572	572	0.5	126	25.2	22.8	45%	<b>20.8</b>	<b>29.9</b>	<b>55%</b>
950°C/24h/WQ/650°C/50h/WQ	481	481	0.4	130	25.2	22.8	84%	na	na	16%
1090°C/0.5h/WQ	365	365	0.4	96			0%	<b>22.0</b>	<b>27.3</b>	<b>100%</b>
1090°C/0.5h/WQ/650°C/100h/WQ	699	699	0.5	130	na	na	80%	na	na	<b>20%</b>
<b>Ti-23Al-27Nb*</b>										
950°C/52h/WQ	838	838	0.8	109	25.5	23.5	35%	21.5	28.1	<b>65%</b>
950°C/52h/WQ/650°C/306h/WQ	518	518	0.3	145	25.5	23.3	80%	na	na	20%
<b>Ti-25Al-23Nb**</b>										
950°C/45h/WQ	765	765	0.6	127	25.2	22.7	75%	<b>20.8</b>	<b>27.5</b>	<b>25%</b>
950°C/45h/q/650°C/223h/WQ	742	742	0.5	137	25.2	22.6	95%	na	na	5%
<b>Ti-25Al-24Nb*</b>										
as-rolled	1125	1237	5.0	126	25.7	23.5	37%	<b>24.7</b>	<b>25.8</b>	<b>63%</b>
975°C/100h/WQ	798	832	4.3	127	25.4	24.5	79%	<b>21.9</b>	<b>28.4</b>	<b>21%</b>
930°C/100h/WQ	696	696	0.7	130	24.9	24.8	95%	17.2	32.6	<b>5%</b>
875°C/100h/WQ/900°C/8h/WQ	657	657	0.6	135	24.9	24.7	82%	19.8	29.5	<b>18%</b>
875°C/100h/WQ	694	704	1.0	137	25.3	25.5	100%			0%
1040°C/0.5h/WQ	672	672	0.6	106			0%	<b>25.0</b>	<b>25.9</b>	<b>100%</b>
<b>Ti-25Al-27Nb*</b>										
as-processed	849	872	1.5	73	na	na	96%	na	na	<b>4%</b>
<b>Ti-12Al-38Nb*</b>										
650°C/55h/WQ	809	869	12.3	89			28%			72%
900°C/5h/WQ	553	566	>27	84			0%	12.4	40.7	100%
900°C/5h/WQ/650°C/5h/WQ	563	563	>16	93	na	na	5%	na	na	95%
900°C/5h/WQ/650°C/59h/WQ	665	726	13.6	86	na	na	29%			71%
1200°C/5h/WQ/650°C/62h/WQ	1005	1019	2.0	89	na	na	32%			68%

\*: interstitial oxygen content < 600 ppm; \*\*: interstitial oxygen content > 900 ppm;  
WQ: water quenched; bold data represents the ordered B2 structure; na: not available

Along with the elastic modulus, the strength and ductility of the BCC phase was strongly dependent on composition. The intermetallic B2-phase (based on  $\text{Ti}_2\text{AlNb}$ ) microstructures, produced through super-transus heat treatment of Ti-25Al-24Nb, were brittle ( $\epsilon_f < 1\%$ ) and exhibited strengths up to 672 MPa, see row 21 of Table 4.13. On the other hand, the disordered  $\beta$  microstructures, produced through super-transus heat treatment of Ti-12Al-38Nb, were extremely ductile ( $\epsilon_f > 27\%$ ) and exhibited strengths of 553 MPa, see row 28 of Table 4.13. Thus BCC phase composition is an important microstructural feature and high Al and low Nb contents, which favor the ordered B2 structure, favor higher RT tensile strengths yet much poorer elongation. The fully-B2 Ti-23Al-27Nb microstructure also exhibited poor RT elongation. However, due to the much higher interstitial oxygen content of the Ti-23Al-27Nb sheet material, the heat-treated microstructures of this alloy were not compared with the lower-oxygen Ti-25Al-24Nb and Ti-12Al-38Nb microstructures. Instead the higher-oxygen Ti-23Al-27Nb and Ti-25Al-23Nb alloys are discussed in the interstitial oxygen and aging effects sub-section.

Similar to fully-B2 microstructures, intermetallic O-phase (based on  $\text{Ti}_2\text{AlNb}$ ) microstructures were brittle. Ti-25Al-24Nb fully-O microstructures, produced by heat treatment at 875°C, exhibited elongations-to-failure of approximately 1% and yield strengths up to 694 MPa, see row 20 of Table 4.13. Figures 4.69a and b depict the tensile behavior for the fully-B2, fully- $\beta$ , and fully-O microstructures. Similar yield strengths were exhibited by the  $\text{Ti}_2\text{AlNb}$  fully-B2 and fully-O microstructures while the lowest strength and highest elongation was exhibited by the Ti-12Al-38Nb fully- $\beta$  microstructure. The fully-B2 and fully-O microstructures failed prior to achieving 1% elongation, whereas the fully- $\beta$  microstructure did not fail after over 27% elongation.

Second-Phase Strengthening. The tensile behavior of the fully- $\beta$  microstructure resembled that of elastic, perfectly-plastic materials as little work-hardening was exhibited, see Figure 4.69b. In fact, consistently a load drop occurred just after yielding. However, the microstructures containing O precipitates did not exhibit this behavior and



significant strengthening occurred when O volumes greater than 5% were present. This is depicted in Figure 4.69a and b as the stress-strain curves of O+BCC microstructures, containing approximately 30% (Figure 4.69b) and 40% (Figure 4.69a) O phase, for Ti-12Al-38Nb and Ti-25Al-24Nb, respectively, are included. These results show the strengthening effect of minority O volumes on BCC matrix microstructures. This strengthening occurred without inhibiting ductility as the elongations-to-failure were at least 5%. In fact, the Ti-25Al-24Nb O+B2 microstructure containing 37% equiaxed O phase exhibited the highest yield strength,  $YS=1125$  MPa, and its  $\epsilon_f$  (5%) was higher than that of the fully-B2 microstructure. Thus both the ductility and strength of O+B2 microstructures were higher than those of its constituent phases. This result may be partly attributed to the OR between the O and B2 structures which allows slip transfer between grains thereby reducing detrimental stress concentration effects. This is shown in the deformation behavior sub-section. O+B2 microstructures containing a majority of the equiaxed O phase also resulted in higher strengths and elongations than the fully-O and fully-B2 microstructures. This was observed for the O+B2 microstructure containing 21% B2 which exhibited 4.3% elongation and a yield strength of nearly 800 MPa, see row 17 of Table 4.13. Note that in this case the B2 composition was lower in Al and higher in Nb compared with that of the fully-B2 Ti<sub>2</sub>AlNb microstructure. Therefore, along with the beneficial OR, this microstructure was expected to have taken advantage of the increased ductility within the B2 phase due to its decreased Al and increased Nb contents. For O+B2 microstructures containing more than 79% O, the brittle characteristics of the O phase dominated and poor ductility resulted. This was depicted for a O+B2 microstructure, which contained 95% equiaxed O phase and exhibited similar properties as that of the fully-O microstructure, see row 18 of Table 4.13.

Two types of strengthening behaviors were exhibited. The first type occurred for the O+ $\beta$  Ti-12Al-38Nb alloy. Strengthening of the  $\beta$  matrix occurred with the addition of O-phase platelets, and a corresponding decrease in  $\epsilon_f$  was observed. Greater decreases in

$\epsilon_f$  were observed with higher O volumes, compare rows 29 and 30 of Table 4.13. In order to better understand the strengthening behavior, the data from the 28% O-platelet microstructure (see row 27 of Table 4.13) was incorporated into existing models based on reinforcements within ductile-phase matrices (Evans *et al.* 1991, Bao *et al.* 1991, Davis and Allison 1995). Assuming the O phase acts as rigid needles, and taking into account their volume fraction and random orientation within the  $\beta$  grains, the finite element model developed by Bao *et al.* (1991) predicts the yield strength for this two-phase microstructure to be approximately 1.5 times larger than that of the single-phase  $\beta$  microstructure. This is in excellent agreement with the experimental results (compare rows 27 and 28 of Table 4.13). Thus, it appears that the O phase acts as a reinforcement similar to that of composite materials. This is important for the design of microstructures intended for tensile-driven properties as the geometry and volume of the reinforcing O phase may be varied for obtaining optimal strengths in ductile, continuous- $\beta$  matrices.

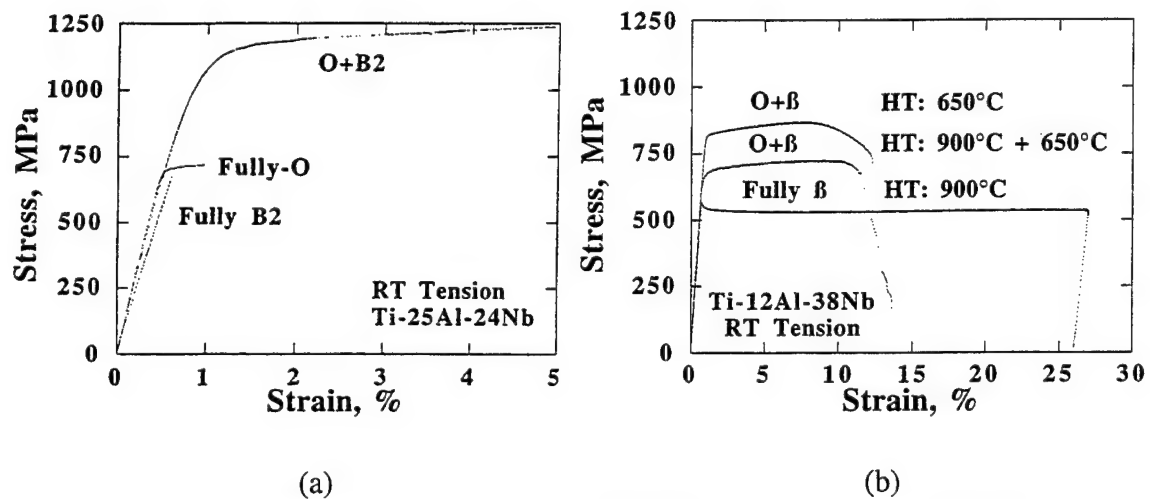


Figure 4.69 Stress vs strain plot for selected (a) Ti-25Al-24Nb and (b) Ti-12Al-38Nb specimens, including those heat treated to obtain fully-O, fully-B2 and fully- $\beta$  microstructures. Also depicted are curves for O+BCC microstructures, represented by the volume and morphology of the O phase, which show the strengthening effect of the O phase within the BCC matrix.

The second type of strengthening occurred for the O+B2 Ti-25Al-24Nb microstructures. In these cases, the single-phase O microstructure was toughened by the addition of the second phase, B2, and both higher strengths and elongations were obtained. The B2 phase inhibited the brittle fracture characteristics of the single-phase microstructures by preventing grain boundary cracking while allowing slip transmittability between the phases. This is further discussed in the next section which will focus on the deformation and fracture characteristics of the two phases.

Deformation Behavior. Fracture surfaces of the fully-B2, fully- $\beta$ , and fully-O specimens depict the ductile and brittle fracture characteristics of each of the constituent phases. The fully-O and fully-B2 microstructures revealed intergranular fracture and cleaved grains, see Figures 4.70a and 4.71a and b, while ductile dimples were evident throughout the fully- $\beta$  microstructure, Figure 4.70b. In addition, the fully- $\beta$  specimens exhibited a cup-and-cone type fracture representative of ductile metals (Hertzberg 1976). All specimens, even those which fractured at low strains, showed evidence of slip. Planar slip traces were identified in the O phase, while the  $\beta$  phase exhibited wavy slip. The surface slip trace behavior of the fully- $\beta$  microstructure is depicted in Figures 4.72a and b. Slip compatibility was evident in the fully- $\beta$  microstructure as slip traces were readily transmitted across grain boundaries and interconnected within grains. The latter observation resulted in the checkered appearance of Figure 4.72b. Thus cross-slip is expected for fully- $\beta$  microstructures. Slip transmission between O grains was not evident in the fully-O microstructure and a significant amount of cross-slip was not expected. Due to the slip incompatibility between O grains, cracks developed at O/O boundaries which resulted in low failure strains. Very little cracking was evident in the fully- $\beta$  specimen, which was unloaded after obtaining more than 27% strain. Observations of surface deformation were not available for the fully-B2 microstructures, however, Banerjee (1994) has reported inhomogeneous slip occurs in such cases.

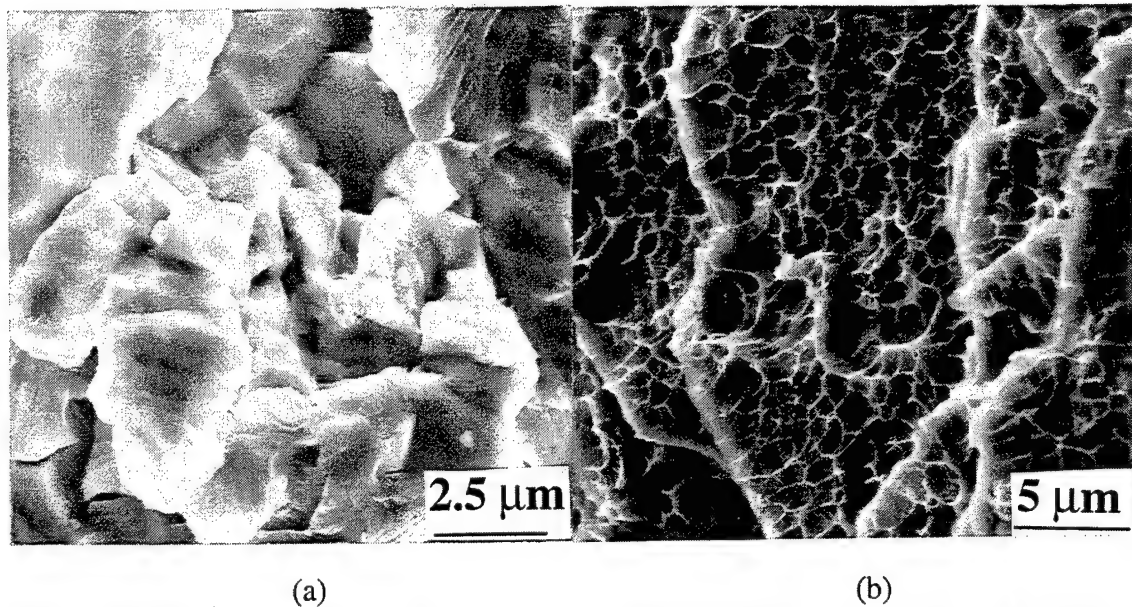


Figure 4.70 Fracture surfaces of the heat-treated (a) fully-O Ti-25Al-24Nb and (b) fully- $\beta$  Ti-12Al-38Nb microstructures.

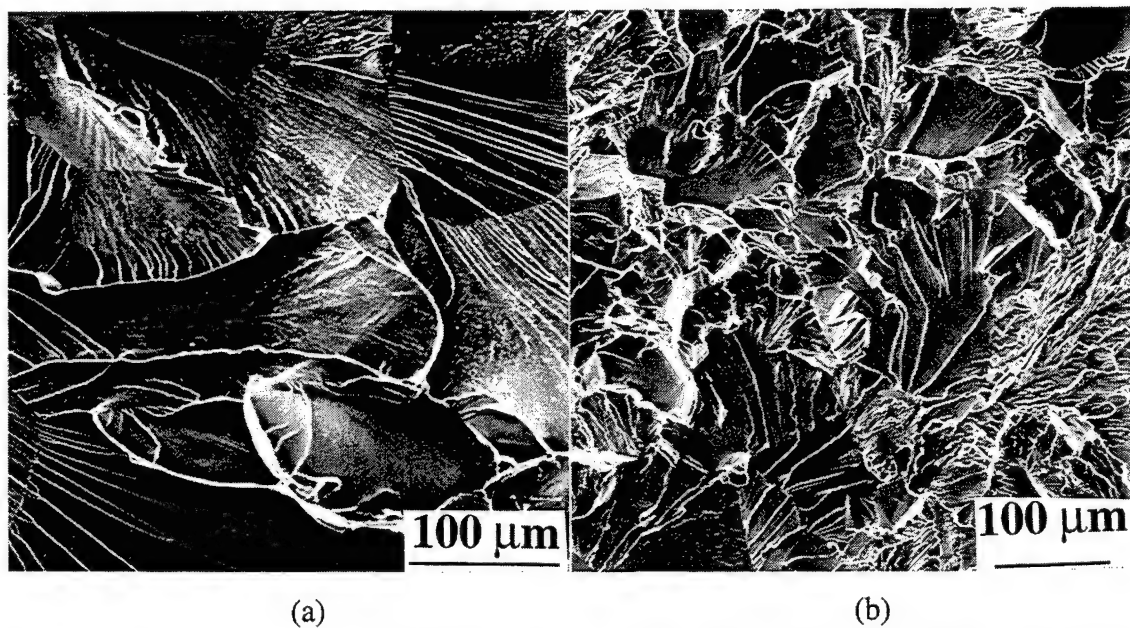


Figure 4.71 Fracture surfaces of the heat-treated fully-B2 (a) Ti-25Al-24Nb and (b) Ti-23Al-27Nb microstructures.

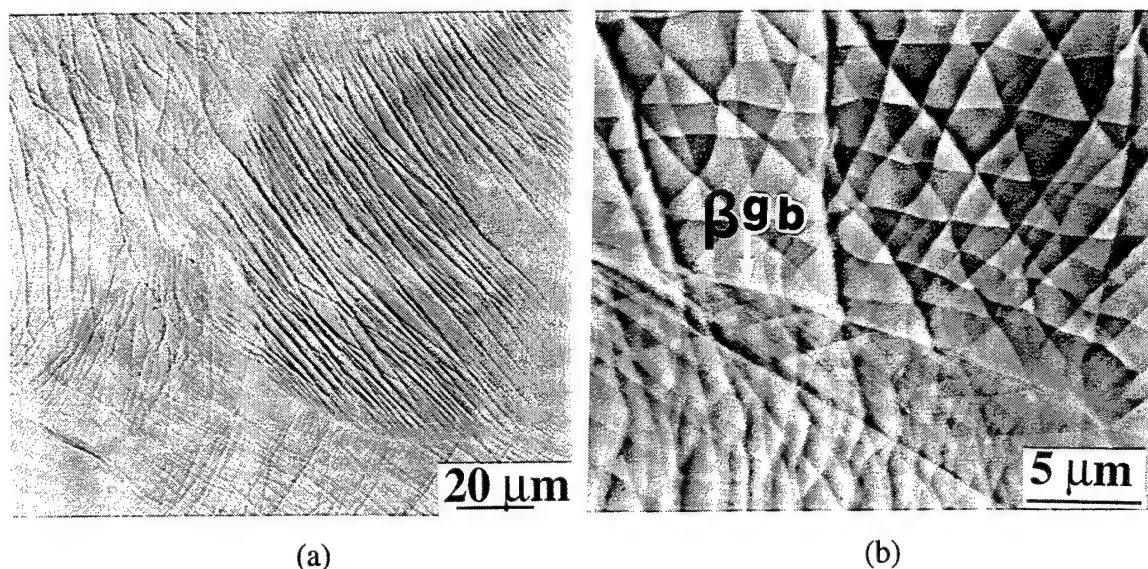


Figure 4.72 (a) Lower and (b) higher magnification SEM images illustrating the slip behavior of the fully- $\beta$  Ti-12Al-38Nb microstructure, obtained from surface observations. The photo in (b) indicates slip traces were interconnected within grains.

The two-phase O+B2 microstructures exhibited a combination of the fracture characteristics; both cleaved and faceted O grains and dimples within B2 regions, see Figure 4.73. For O-dominated microstructures, O/O cracking developed, while for microstructures which contained a sufficient volume of B2 phase, slip compatibility between O and B2 grains was observed and less O/O cracks were noticed due to the lower number of O/O adjacencies. Figure 4.74 depicts the slip and fracture characteristics of an O+B2 Ti-25Al-24Nb microstructure which exhibited greater than 4% elongation. Though O-phase slip traces were linear, there were indications of them being deflected within a grain, indicative of a cross-slip or kink mechanism. In addition, slip interaction was observed between adjacent O and B2 grains, where slip traces in the O phase were often transmitted to the B2 phase. This is anticipated to reduce stress build-up in the O grains and hence delay potential cracking. Slip was wavy within the B2 phase, see Figure 4.74. This is consistent with the observations of cross-slip within other B2 compounds, such as NiAl (Miracle 1993). Thus wavy slip and ductile dimpling were

exhibited for the B2 phase in O+B2 microstructures and not in the fully-B2 microstructures. Most often cracks nucleated at boundaries between adjacent O grains. This was expected to have resulted in the poor ductilities of O-dominated microstructures. However, when the B2 phase blunted such cracks, as depicted in Figure 4.74, good ductility was exhibited. For O+ $\beta$  Ti-12Al-38Nb microstructures, slip was also compatible between the O platelets and the  $\beta$  matrix. Figure 4.75 illustrates surface slip traces for a sample which achieved over 12% strain. The wavy  $\beta$  slip traces readily transgressed the small O-phase platelets and no cracks were observed in this specimen behind the fracture surface.

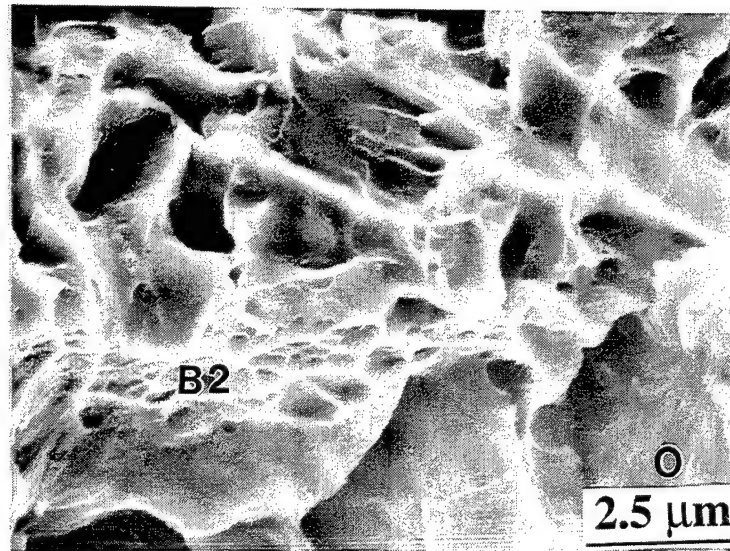


Figure 4.73 The fracture surface of the as-rolled Ti-25Al-24Nb microstructure which exhibited cleaved and faceted fracture in O grains and dimples in B2 regions.

Interstitial Oxygen and Aging Effects. For the higher-oxygen containing Ti-23Al-27Nb and Ti-25Al-23Nb alloys, sub-transus solution-treated microstructures exhibited slightly greater strength and elongation compared with sub-transus solution-treated then 650°C aged microstructures, compare rows 2,3 and 12,13 of Table 4.13. On the other hand, the super-transus fully-B2 microstructure had lower YS and  $\epsilon_f$  than the super-transus solutionized then 650°C aged microstructure, compare rows 4 and 5 of Table



4.13. However, the RT elongations for these alloys, independent of heat treatment, were poor ( $\epsilon_f < 1\%$ ). This data is in contrast to the data of Ti-25Al-24Nb, see rows 16 and 17 of Table 4.13. The data of Ti-25Al-24Nb show that when a sufficient amount of BCC phase is present, good strengths ( $>800$  MPa) and elongations ( $>4\%$ ) are exhibited. The interstitial content for this alloy, which is more than three times lower than that of the higher-oxygen Ti-23Al-27Nb and Ti-25Al-23Nb alloys, was expected to have played a dominant role.

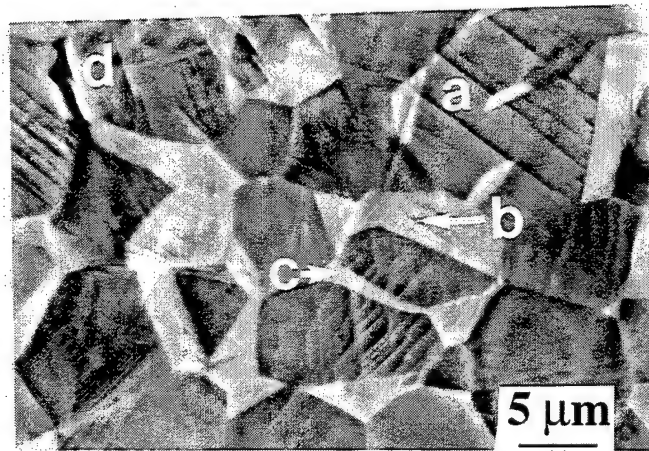


Figure 4.74 A RT tensile deformed O+B2 Ti-25Al-24Nb microstructure which was heat treated at 975°C/100h/WQ. Planar slip is illustrated in the O phase (a) and wavy slip is seen the B2 phase (b). Slip compatibility of the two phases is also illustrated (c). O/O grain boundary cracks were blunted by B2 grains (d).

In order to examine the effect of interstitial oxygen content on RT tensile behavior, an additional Ti-23Al-27Nb sheet was processed from a low-oxygen containing ingot. This ingot was forged and rolled at identical temperatures as the higher-oxygen containing sheets and the tensile results were compared for identical post-processing heat treatments. The higher-oxygen Ti-23Al-27Nb sheet contained 1160 ppm oxygen, while the lower-oxygen sheet contained 550 ppm oxygen. The chemical analysis of the two as-processed sheet materials are compared in Table 4.14. For similar heat treatments the

results show that only a very small improvement in strength was exhibited by the microstructures containing 550 ppm oxygen, compare rows 2,3 with 8,9 of Table 4.13. Although a larger increase in strain was exhibited for the solutionized and unaged sample compared with the solutionized and aged sample, the lower-oxygen alloy microstructures also exhibited elongations less than 1%. Thus even for B2 volumes near 50% and oxygen contents as low as 550 ppm, the Ti-23Al-27Nb microstructures were brittle. In terms of structural applications, this is not a desirable result. Overall, however, the current data shows that when a sufficient amount of B2 phase and oxygen contents less than 550 ppm are present, adequate RT elongations result.

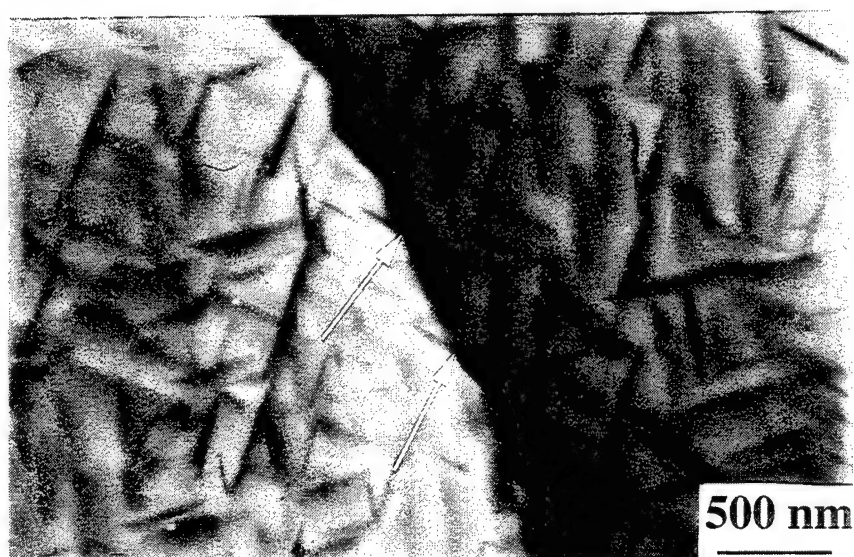


Figure 4.75 The deformation behavior for a heat treated (900°C/5h/WQ/650°C/55h/WQ) Ti-12Al-38Nb microstructure which was strained to more than 12% at RT. Wavy  $\beta$  slip traces readily transgressed O-phase platelets, indicated by the arrows.

Table 4.14 Chemical Analysis of the Lower-Oxygen and Higher-Oxygen Ti-23Al-27Nb Sheet Materials

Material	atomic percent			weight parts per million		
	Ti	Al	Nb	N	Fe	O
Ti-23Al-27Nb**	Bal	23.2	27.2	200	1100	1160
Ti-23Al-27Nb*	Bal	23.1	26.7	120	880	550

\*: lower-oxygen; \*\*: higher-oxygen.



Grain Size and Morphology Effects.  $\beta$  grain size significantly effected the RT tensile properties. This was determined by examination of Ti-12Al-38Nb microstructures which contained the same O-phase volume percent and morphology and different grain sizes. Rows 27, 30, and 31 of Table 4.13, compare the RT tensile properties of such microstructures. For larger grain sizes between 33-138 $\mu$ m, the elongation to failure remained relatively constant (12-14%) while the yield strength decreased from 809 to 665 MPa. A greater effect on properties was found for increasing grain sizes above 138 $\mu$ m. The microstructure which contained a 337  $\mu$ m  $\beta$  grain size exhibited the highest strength, YS~1005 MPa, and the lowest elongation,  $\epsilon_f$ ~2%, of all the Ti-12Al-38Nb microstructures investigated. It also exhibited an intergranular fracture. This indicates that the advantages of obtaining lower Al and higher Nb in the  $\beta$  phase is negated for grain sizes greater than 138  $\mu$ m. As mentioned previously, Banerjee (1994) has reported that inhomogeneous slip occurs within  $\beta$  grains for large grain sizes. Combining the RT tensile and elevated-temperature creep results, the largest  $\beta$ -grained microstructure provided worse primary creep resistance and lower elongation-to-failure than the intermediate  $\beta$  grain size microstructure. Similar minimum creep rates were exhibited by both microstructures. This indicates that there is no advantage in obtaining very large-grained  $\beta$  microstructures for intermediate temperature applications driven by the tensile and creep behavior.

The largest prior-B2 grain size near Ti<sub>2</sub>AlNb alloy microstructure, which was composed almost entirely of O-phase laths, see Figure 4.27, also exhibited high strength and poor ductility, see row 24 of Table 4.13. Interestingly, however, one specimen exhibited more than 5% elongation without failing. The surface of this sample exhibited Luder bands, depicted in the low-magnification optical photographs of Figures 4.76a and b, across the gage section. In addition the stress-strain behavior exhibited a corresponding load drop at yield. The specimen thickness, which was on the order of the prior-B2 grain size (1.3 mm), as well as the texturing of this material are expected to have

played a role. Although the O phase has been reported to lack a sufficient number of slip systems at RT (Popille and Douin 1996, Popille-Puissochet *et al.* 1997), high elongations-to-failure may not be uncommon in this case. Within a respective prior-B2 grain the O phase grew in preferred orientations, see Figure 4.27, indicative that a dominant variant existed. In addition, from the EBSD results, see Figure 4.28a, even larger regions were determined to be textured. Thereby within large zones, the O phase was textured. The material may thus act more or less as if it were formed of rather large grains, some large enough to consume the entire thickness of the sample. Under these conditions, specimens where slip bands happen not to intersect grain boundaries may exhibit increased ductility in tension. Because this behavior was not exhibited by three other specimens tested, the data for this sample was not included in Table 4.13. Nonetheless, this result shows that localized slip may lead to large scale deformation of O phase microstructures, even for those containing large Al concentrations and large prior B2 grains. TEM foils taken from regions outside the localized slip region but within the specimen gage length indicated that dislocations saturated the B2 phase, see Figure 4.77. This indicates that the B2 phase deformed much more readily than the O phase. Some dislocations did transgress boundaries into the O phase yet a lower density of dislocations was noticed within the O phase.

In order to evaluate morphology effects on RT tension, microstructures containing similar B2 phase volumes, roughly 20%, and different morphologies were evaluated. As mentioned previously, the equiaxed O+B2 microstructure exhibited excellent strength and adequate elongation. The fully-lenticular O+B2 microstructure exhibited lower strength, 657 MPa, and poor ductility,  $\epsilon_f=0.6\%$  (see row 19 of Table 4.13). In this case the fracture was localized and cracks transgressed B2 laths, see Figure 4.78. This behavior was similar to the O+B2 microstructure which contained only 5% B2. Thus, in effect, the lath morphology acted to reduce the effectiveness of the B2 volume by not dispersing the slip and blunting cracks. This result further enforces the importance of

maintaining sufficient B2 volumes and sizes for obtaining ductility in near  $\text{Ti}_2\text{AlNb}$  alloys.

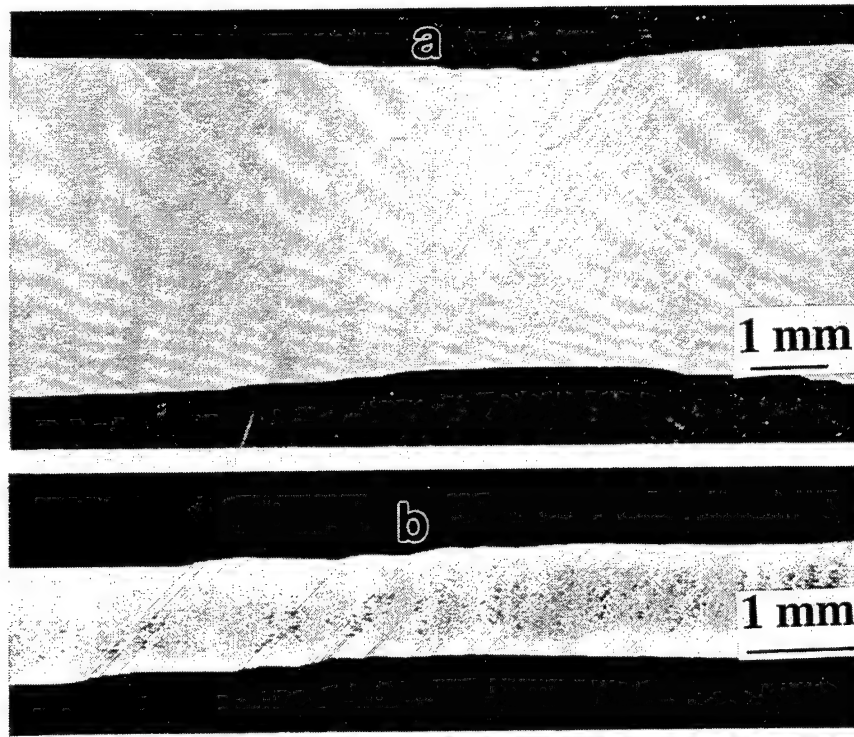


Figure 4.76 A RT deformed Ti-25Al-27Nb specimen exhibiting concentrated (Luder) deformation bands along its (a) face and (b) edges.

### Summary

The following summarizes the important aspects of the tensile behavior study of O+BCC alloys. The BCC phase RT properties were strongly dependent on composition. Higher Al and lower Nb led to increased strength and decreased ductility. Compositions close to the intermetallic B2,  $\text{Ti}_2\text{AlNb}$ , exhibited intergranular fracture and elongations-to-failure of less than 1%. Ti-12Al-38Nb compositions exhibited ductile dimpling, cup-and-cone type fractures and achieved elongations greater than 27%. The B2 microstructures' yield strengths were over 100 MPa higher than that of the  $\beta$  microstructures. Fully-O microstructures, based on the intermetallic composition

Ti<sub>2</sub>AlNb, were brittle and exhibited elongations of 1% and strengths of 700 MPa. The RT properties of O+BCC microstructures depended on phase volume percent and morphology. O-phase dominated microstructures exhibited grain boundary cracking. Poor ductilities resulted when only small B2 volumes (<20%) were present. Although the B2 phase in such microstructures contained lower Al and higher Nb, which favor ductility, the ductile characteristics of the B2 phase, including wavy slip, ductile dimples, and crack blunting, were not enough to compensate for the O/O cracking within the O matrix. When a sufficient volume of B2 was present, higher elongation ( $\epsilon_f > 4\%$ ) and strength ( $800 \text{ MPa} < \text{YS} < 1125 \text{ MPa}$ ) resulted as the number of O/O adjacencies decreased, and slip compatibility, which reduced grain boundary cracking, was exhibited by adjacent O and B2 grains. Fully-lenticular O+B2 microstructures, containing 20% B2 phase, exhibited poor ductility. Thereby, lenticular microstructures reduce the effectiveness of the B2 phase. In addition, large-grained BCC microstructures suffered from poor ductilities. This may be related to the inhomogeneous slip tendencies of the BCC phase.

The highest elongations were exhibited by  $\beta$ -dominated microstructures which contained a minority of O phase. However with decreasing O phase volumes, strength decreased as was observed for the fully- $\beta$  and 95%  $\beta$  microstructures (YS~550 MPa). In addition, the YS of the O+ $\beta$  alloy, Ti-12Al-38Nb, significantly decreased with temperature. The 650°C YS was approximately 0.6 times that at RT, compare row 6 of Table 4.12 with row 30 of Table 4.13. Although the optimal O+BCC microstructure for tensile-driven properties is believed not to have been found in this investigation, it is expected to contain between 20-60% equiaxed B2 phase and achieve strengths greater than 1125 MPa, while maintaining adequate RT elongation ( $\epsilon_f > 4\%$ ).

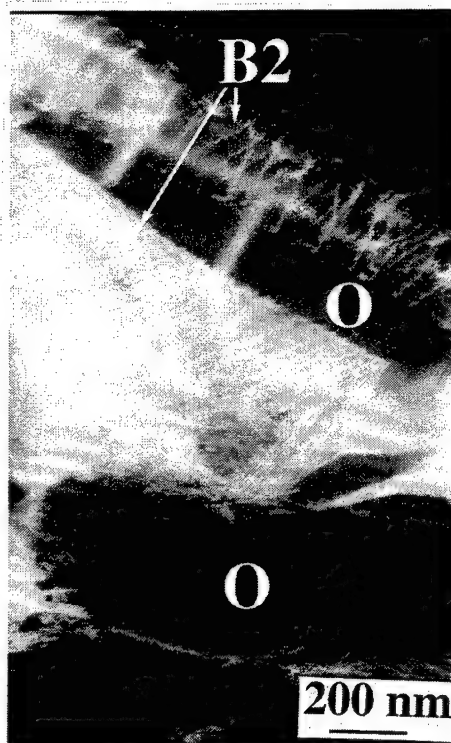


Figure 4.77 A RT deformed Ti-25Al-27Nb specimen exhibiting a greater dislocation build-up within the B2 phase compared with the O phase.

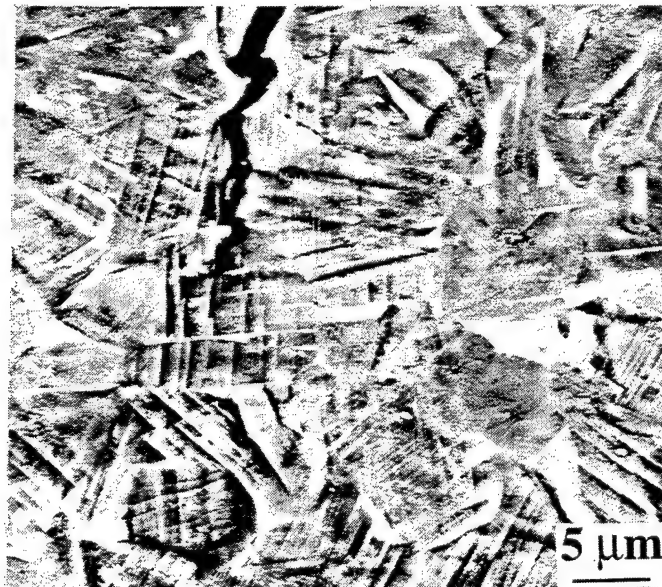


Figure 4.78 A RT deformed fully-lenticular O+B2 microstructure which exhibited a localized fracture where cracks transgressed B2 laths.

## CHAPTER 5

### ANALYSIS AND DISCUSSION

Similar to Chapter 4 this Chapter will be separated into three main sections which discuss the phase evolution, creep behavior, and tensile behavior results. Dissimilar to Chapter 4, for the most part, the discussion of the near Ti<sub>2</sub>AlNb and Ti-12Al-38Nb alloys will be combined as similar themes evolve for these O+BCC alloys.

#### 5.1 Phase Evolution

##### 5.1.1 Equilibria

The compositions of the  $\alpha_2$ , B2, and O phases (see Tables 4.2 and 4.3) for the near Ti<sub>2</sub>AlNb alloys are in agreement with compositional data from O alloys of similar nominal compositions (Rhodes 1997). However, the Nb content of the  $\alpha_2$  phase (Ti-25Al-16Nb) was significantly higher than that found in a Ti-25Al-17Nb alloy;  $\alpha_2$  ≈ Ti-25Al-11Nb (Majumdar *et al.* 1994 1995, Boehlert *et al.* 1997a). Thus for alloys containing higher nominal Nb contents, the Nb solubility in  $\alpha_2$  increases and Nb is expected to have substituted at Ti sites more frequently. This agrees with previously developed phase diagrams depicting the  $\alpha_2$ +B2 and  $\alpha_2$ +B2+O fields extending with increased Nb concentrations (Muraleedharan 1995, Muraleedharan 1995b, Sagar *et al.* 1996, Rhodes 1997). This is an important observation as such a large jump in Nb is expected to influence the mechanical behavior of the  $\alpha_2$  phase.

To more easily visualize the phase regions of near Ti<sub>2</sub>AlNb alloys, the Ti-22Al isopleth, first developed by Miracle *et al.* (1996) and later modified by Boehlert *et al.*

(1997e), has been provided in Figure 5.1. The current data for Ti-23Al-27Nb are overlaid. The B2 transus is approximately 1070°C. The  $\alpha_2$ +B2 phase field ranges between 1000-1070°C. The narrow three-phase  $\alpha_2$ +B2+O field ranges between 975-1000°C. Although this phase diagram and others (Muraleedharan 1995, Muraleedharan 1995b, Sagar *et al.* 1996) have included the three-phase field for nominal Nb contents up to 35at.%, to the author's knowledge, this is the first work to verify the existence of this regime for alloys containing more than 20Nb. The extremely narrow temperature range and low  $\alpha_2$ -phase volume present, see row 6 of Table 4.2, makes experimental verification difficult. The O+B2 phase field ranges between 750-975°C. The O+ $\beta$  phase field exists below 750°C. The B2-to- $\beta$  disordering is assumed to be a second-order transformation, whereby an O+B2+ $\beta$  field is not considered. Although microstructures containing each of the O+B2+ $\beta$  phases have been discovered at 650°C, see Figure 4.17, this is expected to be due to the slow diffusion kinetics of lower-temperature transformation and not an equilibrium condition. For temperatures below 650°C, the phase equilibria suggest that fully-O microstructures are stable. However, no experimental verification has been provided. The verification of this regime is expected to be even more difficult than that for the three-phase  $\alpha_2$ +B2+O regime as the transformation kinetics at low temperatures are slow. For example, aging within the O+ $\beta$  regime at 650°C for over 28 days failed to result in completely stable microstructures. Higher nominal Al contents significantly increase the temperature of the single-phase O field (Muraleedharan 1995, Muraleedharan 1995b). This was verified by the fully-O microstructure, which was produced through an 875°C heat-treatment of Ti-25Al-24Nb. However, the processing and heat-treatment schedules have a significant influence on the phase equilibria. This is depicted for the Ti-25Al-27Nb alloy, which exhibited an O+B2 microstructure after super-transus processing and slow-cooling followed by aging at 650°C for 28 days. In addition, O+B2 solution treatments followed by long-term aging treatments below 875°C resulted in O+BCC microstructures for Ti-25Al-24Nb. Thus the

phase evolution and the temperature ranges of the different phase regimes for near  $\text{Ti}_2\text{AlNb}$  alloys is strongly dependent on alloy composition and the processing and heat-treatment schedules.

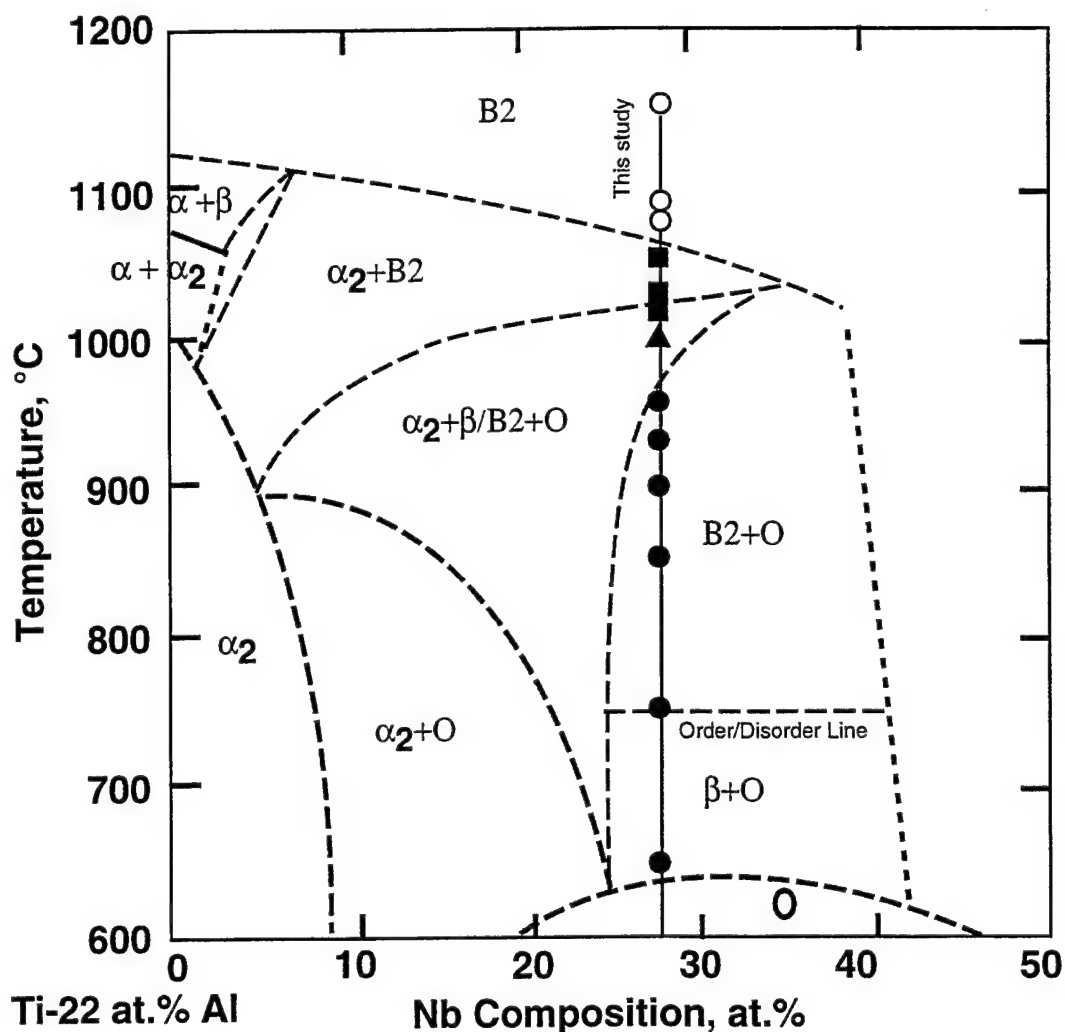


Figure 5.1 The Ti-22Al isopleth with the current data overlaid for a Nb composition of 27at.%.

As observed in the aging study, the lower-temperature microstructures do not always consist of only the O and BCC phases. Once the  $\alpha_2$  phase is formed, through solutionizing within the  $\alpha_2$ +B2 or  $\alpha_2$ +B2+O fields or super-transus solutionizing followed by slow-cooling, it is quite stable and does not fully transform after long-aging



times at lower temperatures, see Figures 4.7 and 4.12. The diffusion kinetics for  $\alpha_2$  are sluggish at low temperatures as negligible decreases in  $\alpha_2$  phase volume percents were observed, see Table 4.2. The 'rim-O' phase, which forms at the periphery of  $\alpha_2$  (see Figures 4.3c and 4.7b), is considered to be partially responsible for this as it appears to act as a diffusion barrier between the relatively low-Nb containing  $\alpha_2$  and high-Nb containing BCC phases. On the other hand, the  $\alpha_2$  phase is easy to remove by super-transus solutionizing, where single-phase B2 microstructures are quickly equilibrated. In such cases the O phase readily transforms to B2, and therefore it does not interfere with  $\alpha_2$  transformation. Thus, due to the slower diffusion kinetics at lower temperatures as well as the formation of the 'rim-O' phase, the  $\alpha_2$  is very stable and difficult to remove without super-transus solutionizing. This is an important point to consider for the phase evolution of near Ti<sub>2</sub>AlNb alloys as the  $\alpha_2$  phase is not an equilibrium phase below 975°C.

Small changes in Al content (between 23-25at.%) did not significantly change the temperature ranges of the  $\alpha_2$ +B2,  $\alpha_2$ +B2+O and O+B2 phase regions for near Ti<sub>2</sub>AlNb alloys as can be seen by comparing the Ti-22Al isopleth (Figure 5.1) with the Ti-25Al-xNb vertical section (Figure 1.3). The current Ti-25Al-23Nb data lies within the projected boundaries of the respective phase regimes of the Ti-25Al-xNb vertical section. Interstitial oxygen content, however, does have a significant influence on the phase boundaries especially the B2 transus and  $\alpha_2$ +B2 field. As mentioned in the phase-evolution results section, the B2 transus was between 21-34°C lower for Ti-25Al-24Nb than for Ti-25Al-23Nb, though the Ti, Al, Nb contents were quite similar, see Table 4.1. Greater oxygen contents tend to stabilize the  $\alpha_2$  phase (Rhodes *et al.* 1993, Boehlert *et al.* 1997a), and in this case higher interstitial oxygen levels increased the temperature range for the  $\alpha_2$ +B2 field and subsequently caused the B2 transus to rise for Ti-25Al-23Nb (930 ppm oxygen) with respect to that for Ti-25Al-24Nb (280 ppm oxygen). Thus interstitial oxygen levels must be considered whenever phase equilibria studies are

involved for ternary titanium alloys. It is noted that the phase diagram in Figure 1.3 was developed for compounds containing roughly 800 ppm oxygen.

Although the transus between the O+B2 and O+ $\beta$  fields is indicated in Figures 5.1 and 1.3, few published works are available documenting this transition for near Ti<sub>2</sub>AlNb alloys (Bendersky *et al.* 1991, Rhodes 1997). In addition, the practical significance of the order/disorder temperature is not well understood. As has been conclusively shown here, the ability of obtaining equilibrium low-to-intermediate temperature microstructures depends largely on the processing and heat-treatment schedules. In agreement with the current observations, it has been shown that the  $\alpha_2$  phase, formed by sub-transus heat treatment, is extremely stable and resilient to transformation at lower temperatures (Muraleedharan *et al.* 1992a 1995a, Gogia *et al.* 1992). Though both the  $\alpha_2$  and B2 phases are not considered to be equilibrium phases at 650°C, they often are present after long-term aging treatments. As mentioned above, the kinetics of  $\alpha_2$  transformation is extremely slow and the formation of the 'rim-O' phase is expected to act as a diffusion barrier to deter further transformation. On the other hand, the decomposition of the B2 phase, though slow, is relatively rapid compared with  $\alpha_2$ .

The B2 phase transformed to O+BCC mixtures through three main routes. In each case the B2 phase volume decreased and its composition tended toward higher Nb and lower Al contents. Thus the composition tended more toward the disordered  $\beta$  structure. In terms of the fine equiaxed-grained sub-transus microstructures, for decreasing temperatures between 875-975°C, the equiaxed B2-phase grains shrunk at O/B2 grain boundaries and smaller B2 grain sizes resulted. Correspondingly, the size and volume of the O-phase grains increased. Below 875°C, Widmanstätten O precipitated within B2, see Figure 4.10. The O+ $\beta$  equilibrium may be somewhat responsible for this morphological change, as it has been suggested that the nature of the precipitate shape is obtained through the minimization of elastic energy where the  $\beta$  phase preferentially forms as platelets (Bendersky *et al.* 1991). For the lower aging temperatures,

discontinuous precipitation of O and  $\beta$  occurred at O/B2 and  $\alpha_2$ /B2 boundaries. The highest temperature in which the discontinuous precipitation occurred was 750°C. Thus the O+B2/O+ $\beta$  transus is expected to lie close to 750°C for near Ti<sub>2</sub>AlNb compositions. This temperature is also within the range expected for disordering from the work of Bendersky *et al.* (1991). The diffusion kinetics of the B2 phase at lower temperatures make it impractical to precisely pinpoint this transition as the BCC phase is slowly being depleted in Al and enriched in Nb during the transformation reactions and this eventually leads to disordering. This is what was expected to have occurred for the 650°C aged sample depicted in Figure 4.17, where both the B2 and  $\beta$  structures were found within a transforming prior B2 grain. As mentioned previously, although the B2 to  $\beta$  transition is expected to be a second order transformation, in this case the incomplete transformation was expected to be caused by the slow diffusion kinetics. Although the compositions of the very fine BCC phases were not measured, the transition from B2 to  $\beta$  is expected to occur between Ti-17Al-34Nb and Ti-12Al-41Nb compositions as the former composition was measured for the equiaxed B2 phase at 900°C, see row 3 of Table 4.2, and the latter was measured in the fully- $\beta$  Ti-12Al-38Nb microstructure, see Table 4.5. This estimated transition composition is within the range of compositions measured for the B2 phase (Ti-20Al-36Nb) and the  $\beta$  phase (Ti-12Al-38Nb) for Ti-20Al-36Nb and Ti-25Al-18Nb alloys, respectively (Rhodes 1997).

### 5.1.2 Cellular Precipitation

Along with the order/disorder transition, the nature of the B2 transformation was related to BCC-phase chemistries. The grain boundary discontinuous precipitation, observed for sub-transus solutionized microstructures which were aged at 750°C and below, is defined as cellular precipitation according to the reaction:



where B2 is the super-saturated phase,  $\beta$  is of similar structure but with a lower thermodynamic excess of solute (Al), and O is the equilibrium precipitate. Similar transformations have been observed in several metallic alloy systems (Tu 1972, Melton and Edington 1974, Gupta 1975, Martin and Doherty 1976, Krishnamurthy and Gupta 1977, Porter and Easterling 1981) including the Ti-Cu, Ti-Ag, and Ti-Al systems (Williams 1973, Denquin and Naka 1996). For example, cellular reaction of  $\alpha+\beta$  at prior  $\beta$  grain boundaries consumes the tempered martensite mixture of  $\alpha+\alpha''$  in Ti-Cu. In the active Ti-Cu eutectoid system coarse lamellar  $\alpha+\text{Ti}_2\text{Cu}$  consumes the finer  $\alpha+\text{Ti}_2\text{Cu}$  matrix where it has been suggested that the cellular reaction is the result of incomplete chemical segregation during the rapid eutectoid reaction and the coarser lamellar structure within cellular regions tends to reduce the surface energy. Cellular reaction also occurs in  $\alpha+\beta$  Ti-Ag systems where  $\alpha+\text{Ti}_3\text{Ag}$  cellular product forms at massive  $\alpha$  boundaries in Ti-17wt.% Ag. Thus it appears to be easier for such systems to lower their total free energy by cellular transformation rather than by the coarsening of individual precipitates within the bulk. For the current case, cellular reaction was evidently related to the coherency of the O/B2 and  $\alpha_2/\text{B2}$  phases as well as the composition of the B2 phase. The two factors which had the greatest effect on cellular precipitation were the solutionizing and aging temperatures, where higher solutionizing temperatures and lower aging temperatures were more conducive to this type of reaction. This may be explained in terms of BCC-phase chemistry and composition induced disordering (Kestner-Weycamp *et al.* 1989).

Upon aging below 875°C, the O phase precipitates uniformly within B2 grains, and the chemistry of the O phase typically adheres to its  $\text{Ti}_2\text{AlNb}$  stoichiometry. As the volume fraction of O phase increases, the B2 phase volume fraction decreases and the B2 composition loses Al and gains Nb. As mentioned previously, at some point the B2 structure disorders due this chemistry difference. The B2 phase is thus considered to be super-saturated with respect to  $\beta$ . The degree of this super-saturation depends on the

composition gradient between the BCC structures which is a function of the solutionizing and aging temperatures. As the composition gradient between the B2 phase and the  $\beta$  phase narrows, such as through lower-temperature solutionizing and higher-temperature aging or through slow-cooling treatments, the degree of super-saturation lessens. In this case only small chemistry changes are necessary for the transition of B2 to  $\beta$ , which may be accommodated by diffusion within the bulk of the B2 region. However, at higher solutionizing and lower aging temperatures, the degree of super-saturation of B2 with respect to  $\beta$  is increased, whereby a more severe compositional gradient exists. In agreement, large composition differences have been discovered between the B2 and  $\beta$  phases for Ti-22Al-27Nb samples heat treated between 650-1038°C (Rhodes 1997). The B2 composition at 1038°C was Ti-21Al-27Nb, while the  $\beta$  composition at 650°C was Ti-10Al-46Nb. When large composition gradients exist, the driving force for cellular precipitation is great and subsequent diffusion along grain boundaries tends to be the kinetically favorable route (Tu 1972, Martin and Doherty 1976, Porter and Easterling 1981). Thus the thermal activation processes which favor cellular precipitation are enhanced by higher solution-treatment temperatures and lower aging temperatures which lead to larger BCC phase compositional gradients.

This reasoning is consistent with the discontinuous precipitation exhibited for the heat-treated microstructures of similar alloys (Rowe 1991, Bendersky *et al.* 1991, Gogia *et al.* 1992, Muraleedharan *et al.* 1992a, Banerjee *et al.* 1993, Rowe and Larsen 1996, Rhodes 1997). To the author's knowledge, these are the only works to characterize such a cellular precipitation phenomenon for O+BCC alloys. Although this instability at 650°C is similar to that observed by Rowe (1993a) and Rowe and Larsen (1996), the cellular precipitation of the current work was not stress enhanced and its migrating front was observed to move well within the grain bulk. It was not limited to segregated bands nor associated with the fully-O microstructure as was found for Ti-26Al-25Nb and Ti-25Al-22Nb alloys (Rowe 1993a). The instability observed by Rowe and Larsen (1996)

appeared to be more closely associated with that found in the Ti-12Al-38Nb solutionized and aged microstructure, see Figure 4.39, which formed as a result of segregated banding at  $\beta/\beta$  grain boundaries and was never located far from this boundary. In addition, due to the load dependence, the instability observed by Rowe (1993a) was more closely related to stress-assisted discontinuous precipitation found in  $\beta$  heat treated  $\alpha_2+\beta$  (Rowe and Giliotti 1990, Rowe and Hall 1991) and  $O+\alpha_2$  (Rowe *et al.* 1991) alloys. Load did not change the nature of the cellular precipitation in the current work, see Figure 4.42.

From the aging studies of the sub-transus processed and  $O+B2$  solutionized  $Ti_2AlNb$  alloys, the range of temperatures which favor Widmanstatten  $O$  precipitation lie between 750-875°C. Although Widmanstatten precipitation occurs within the bulk for lower aging temperatures, cellular precipitation is considered to be favored below 750°C as it consumed the finer Widmanstatten precipitates. The temperatures at which Widmanstatten precipitation occurs increases for  $\alpha_2+B2$  and super-transus solutionized microstructures. Widmanstatten precipitation was observed upon heating in the  $O+B2$  region (875-975°C) for such cases, see Figures 4.6b and 4.7b. This may be related to the larger  $B2$  grain sizes of such microstructures as smaller grain sizes resulted in lower Widmanstatten-start temperatures for the  $O+B2$  solutionized then aged samples. In addition, small volumes of cellular precipitation were observed for super-transus solutionized samples which were aged within the  $O+B2$  region, see Figures 5.2a and b. This is also depicted in Figure 4.26a. In such cases, chemical segregation may have played a role as the cellular precipitation was not always found at the prior  $B2$  grain boundaries. Rowe (1991) and Rhodes (1997) have also observed discontinuous precipitation for super-transus solutionized samples aged at 870°C and 815°C, respectively. These observations are consistent with the cellular precipitation reasoning as large compositional gradients exist between the  $B2$  phases of super-transus solutionized and  $O+B2$  solutionized microstructures, see Tables 4.2 and 4.3. Thus the

range of temperatures for the lower-temperature aging transformations is dependent on the solutionized microstructure.

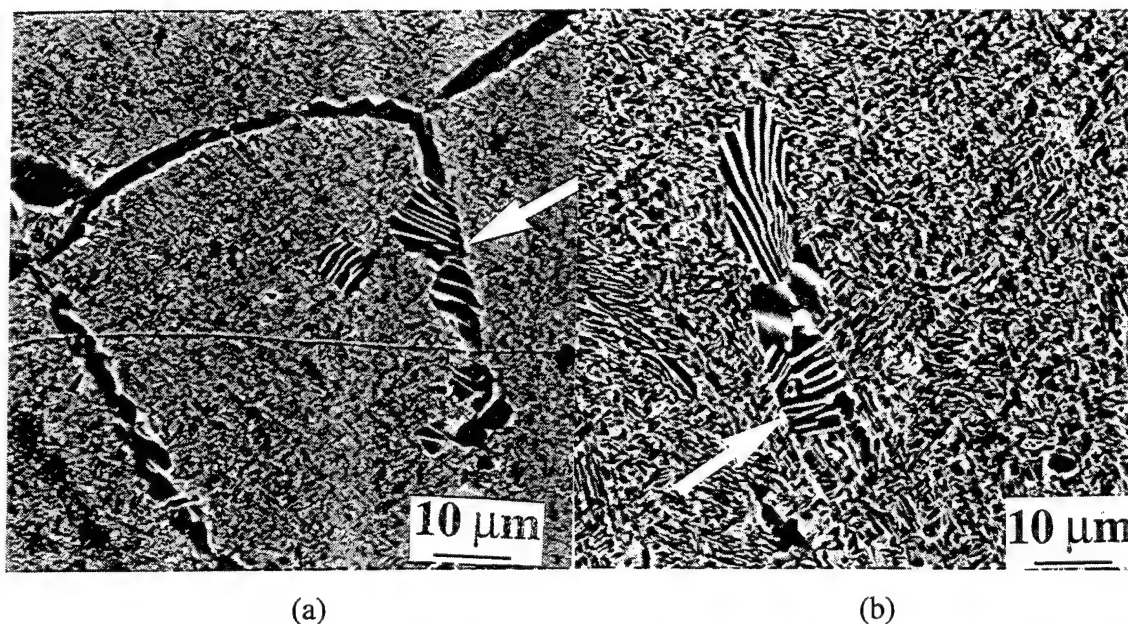


Figure 5.2 Discontinuous precipitation (indicated by arrows) for super-transus Ti-23Al-27Nb samples which were aged within the O+B2 region. The corresponding heat treatments were (a) 1090°C/0.5h/WQ/900°C/8h/WQ and (b) 1090°C/0.5h/WQ/650°C/9h/WQ/900°C/8h/WQ.

### Super-transus Microstructures

Cellular precipitation was not exhibited for super-transus solutionized then slow-cooled samples. In addition, subsequent aging of such samples did not promote cellular reaction. Figure 5.3 depicts the super-transus solutionized then slow cooled microstructure (Figure 4.6a) after subsequent aging at 650°C for 100 hours. Only a slight coarsening of the existing laths occurred. This is consistent with the above reasoning as the B2 phase gradually transformed to O upon cooling and therefore decreased its Al and increased its Nb concentrations along the way. The evolution of the Ti-25Al-27Nb microstructures was also consistent with the above reasoning as slow-cooling of the super-transus processed microstructure did not promote cellular precipitation, see Figure

4.27, and neither did subsequent aging. For the aged microstructure, the B2 structure was retained, see Figure 4.29, which is explained by the previously described slow B2 transformation kinetics as well as the high Al content in the starting B2 structure. Thus even after aging for over 670 hours at 650°C, the non-equilibrium B2 phase had yet to transform. This was also true for the Ti-23Al-27Nb super-transus solutionized then 650°C aged microstructures, see Figure 4.24a. Thus the ability of the B2 structure to disorder depends largely on the B2 composition in the solutionized microstructure. This is in agreement with the observations of Rowe (1991), who identified the discontinuous growth regions containing parallel ribbons of B2 and O in a Ti-25Al-30Nb sample which was super-transus solutionized then aged at 870°C for 100 hours. However, independent of B2 composition, discontinuous coarsening occurred at grain boundaries, where in the current super-transus solutionized then aged microstructures colonies of O-phase grains precipitated then coarsened at transformed-B2 boundaries. This is not unexpected as diffusion across high-angle grain boundaries is usually more rapid than within the bulk, as was depicted for the Ti-12Al-38Nb alloy, see Figure 4.38. Thus grain boundaries, which were the locus of the lower-temperature precipitation events, are quite important to the phase evolution of near  $Ti_2AlNb$  alloys.

The aging transformation behavior of the super-transus solutionized samples was similar to the composition invariant B2-to-O transformation characterized for Ti-24Al-16Nb aged between 800-940°C (Muraleedharan 1995, Muraleedharan *et al.* 1992b) and Ti-24Al-25Nb aged at 700°C (Bendersky *et al.* 1991), where after long aging times the B2 phase reprecipitated in platelet form within the transformed-B2 matrix. For very short aging times ( $t \leq 15$  minutes), these studies have reported the complete transformation of B2-to-O. Because XRD data revealed noticeable shifts from the original B2 peaks for the 15 minute and 2 hour aged conditions of the current work, see Figures 4.21a-c, it is likely that a majority of B2 had already transformed. Thus, the composition invariant transformation from fully-B2-to-fully-O microstructures is probable at 650°C. Within 9



hours fine B2 platelets had reprecipitated throughout the microstructure, which is also indicative that the B2 grains had completely transformed. In agreement with the work of Muraleedharan *et al.* (1992b), colonies of O grains coarsened initially at the transformed-B2 boundaries and then within the bulk. Thus, similar to the sub-transus then aged microstructures, lower aging temperatures promote discontinuous coarsening which initiates at prior B2 grain boundaries. Unlike the sub-transus then aged microstructures, the precipitating phases of the super-transus then aged microstructures were O and B2 (not O and  $\beta$ ), and the fully-B2 microstructure is suggested to have completely transformed to O prior to reprecipitating.

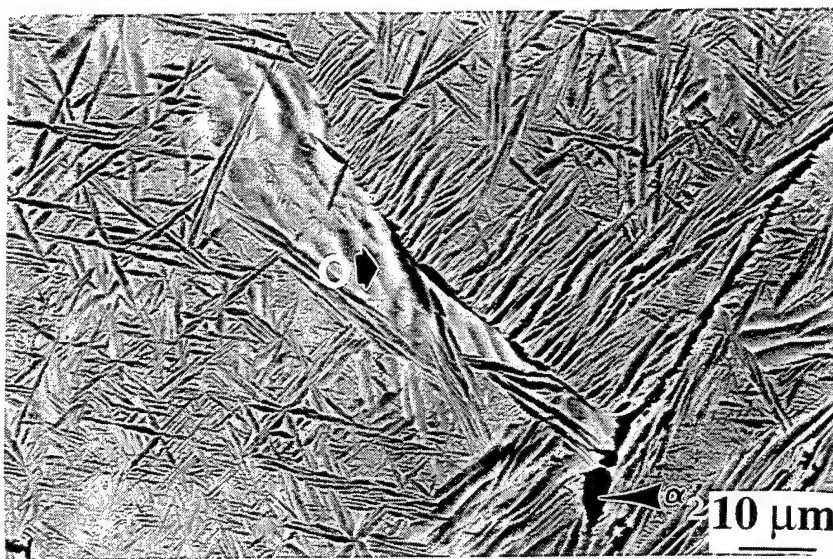


Figure 5.3 Super-transus heat-treated Ti-23Al-27Nb microstructure (1150°C/0.5h/cooled at 15°C/min. to RT) which was subsequently aged at 650°C for 100 hours followed by water quenching. No cellular precipitation was evident.

#### Ti-12Al-38Nb and the Pseudobinary Diagram

As stated in Chapter 2, the Ti-12Al-38Nb alloy was selected based on the phase equilibria work of Rowe *et al.* (1993). At 900°C, this alloy is fully- $\beta$ , yet at lower temperatures the  $\beta$ -phase stability is reduced and the O phase precipitates. Schematic isothermal ternary slices at 900°C and 650°C, depicting the studied alloys which lie along

a Ti=50at.% line, illustrate the lateral shift in the BCC/BCC+O boundary, see Figures 5.4a and b.

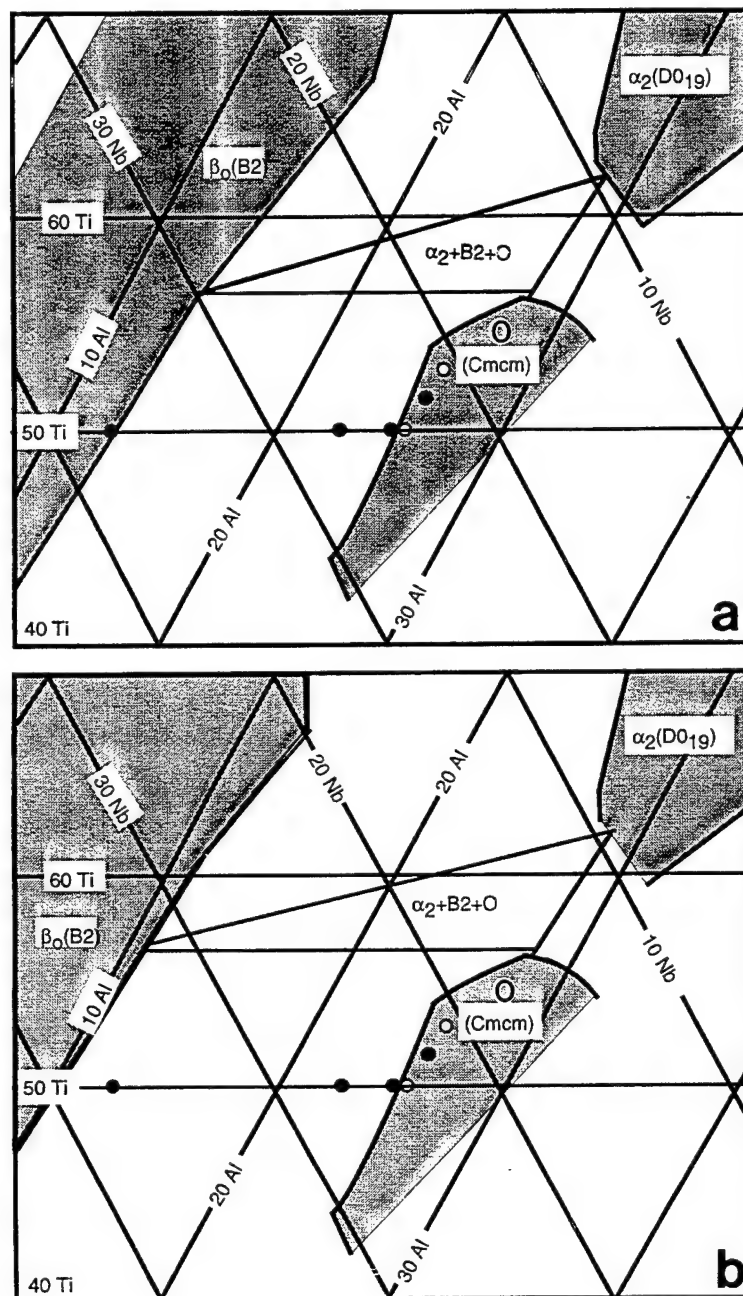


Figure 5.4 Ternary diagrams for the Ti-Al-Nb system. (a) The 900°C isothermal ternary slice taken from Rowe *et al.* (1993) where selected alloys of this work are represented along the constant Ti=50at.% tie-line. Ti-12Al-38Nb borders the BCC/BCC+O phase regimes at the left-hand-side of this line. (b) The schematic representation of a 650°C isothermal ternary slice depicting the lateral shift in the BCC/BCC+O boundary.

The phase evolution of Ti-12Al-38Nb differed significantly from that of the near Ti<sub>2</sub>AlNb alloys. As a result, significantly different microstructures were obtained from similar processing and heat-treatment schedules. The disordered  $\beta$  phase was more stable for Ti-12Al-38Nb than for the near Ti<sub>2</sub>AlNb alloys. This is expected to be a result of the compositional dependence of the BCC structure. The ordered B2 structure was not detected in the as-rolled (932°C) and 650-760°C aged conditions. Although the BCC structure was not investigated for samples heat treated between 760-932°C and above 932°C, the B2 phase is not expected as the BCC composition could not contain more than 13Al and less than 39Nb (the measured composition of the Ti-12Al-38Nb alloy). Thus the temperature range of stable B2-containing microstructures is significantly reduced for lower Al-containing and higher Nb-containing alloys. This is depicted in the pseudobinary diagram for Ti=50at.%, originally developed by Bendersky *et al.* (1991), which has been modified according to the current data, see Figure 5.5. The  $\beta$ -to-B2 transition at high temperatures has been assumed to be second order with no two-phase field. For Ti-12Al-38Nb, the  $\beta$  transus was close to 800°C as determined from the disappearing-phase method. Thus the Ti-12Al-38Nb transus temperature is significantly lower than that of near Ti<sub>2</sub>AlNb alloys. Based on these observations and those previously mentioned for the near Ti<sub>2</sub>AlNb microstructures, the B2 phase is considered to be stable only when it contains more than 12Al. No  $\alpha_2$  phase was observed for Ti-12Al-38Nb and the temperature ranges for the  $\alpha_2$ +B2 and  $\alpha_2$ +B2+O phase fields narrow with increasing Nb and decreasing Al contents, see Figure 5.5. It is noted that for the composition range between TiAl and Ti<sub>2</sub>AlNb, equilibrium involving the  $\alpha_2$ ,  $\gamma$ , and B8<sub>2</sub> phase was excluded. Due to the preliminary nature of the phase diagram work, the diagram was approximated as a quasibinary for simplicity. This is reasonable because experimental results indicated that for temperatures less than 800°C,  $\beta$ -phase volumes were well estimated with tie-line approximations. For example, the maximum O-phase volume predicted for Ti-12Al-38Nb at 650°C is approximately 30%, while the

corresponding value for Ti-25Al-25Nb is nearly 100%. Both these values are close to those observed, see Tables 4.3 and 4.4.

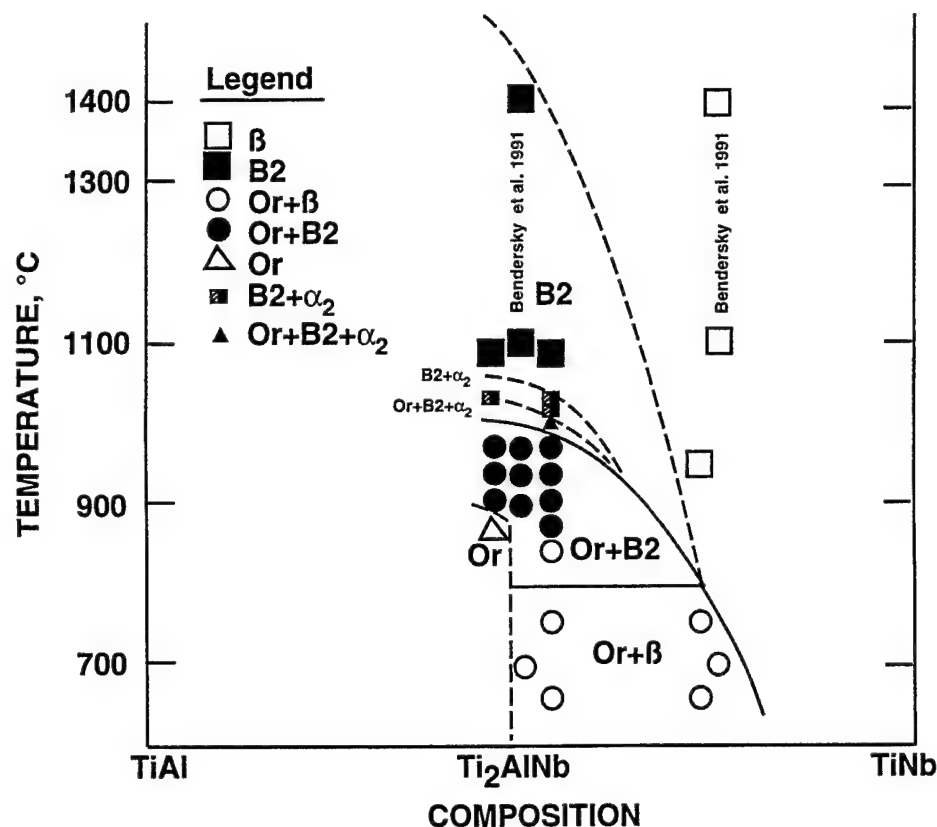


Figure 5.5 The pseudobinary section of the Ti-Al-Nb system at 50 at.% Ti taken from Bendersky *et al.* (1991) with data from the Ti-25Al-24Nb, Ti-23Al-27Nb, and Ti-12Al-38Nb alloys superimposed.

No equiaxed O phase was present in the Ti-12Al-38Nb alloy. This is believed to be a result of the processing temperature chosen for this alloy. Equiaxed primary O grains would be expected if the processing temperatures were below the transus ( $T_{\beta} \approx 800^{\circ}\text{C}$ ), as this was the case for the near Ti<sub>2</sub>AlNb alloys. Nonetheless, from a microstructural design perspective, Ti-12Al-38Nb is less complicated than Ti<sub>2</sub>AlNb because it is easier to change one microstructural feature without affecting others. For example, in order to ascertain grain-size effects on creep, the β grain size was increased through post-processing heat treatments without influencing phase volume fractions or

morphologies. Phase stability is also less complicated in Ti-12Al-38Nb as the O phase equilibrates more rapidly compared to the near Ti<sub>2</sub>AlNb alloys and Widmanstatten precipitation is the dominant transformation mode. No cellular precipitation was observed in Ti-12Al-38Nb. However, O precipitation initiated at  $\beta/\beta$  grain boundaries for short-term aged microstructures, see Figure 4.38. This verifies that higher diffusional rates are exhibited across high-angle grain boundaries in O+BCC alloys. An important observation, based on the aging study of Ti-12Al-38Nb, is that stable, low temperature ( $T < 800^\circ\text{C}$ ) fully- $\beta$  microstructures which contain a majority of Ti are only possible for alloy compositions containing less than 12Al and more than 38Nb, see Figure 5.5. Interpreting the pseudobinary diagram, Ti-10Al-40Nb would border the O+ $\beta/\beta$  regimes at  $650^\circ\text{C}$ . This is in excellent agreement with the  $\beta$ -phase composition measured for a Ti-22Al-27Nb alloy at  $650^\circ\text{C}$  (Rhodes 1997).

## 5.2 Creep Behavior

In order to discuss the creep behavior results, sections devoted to the creep mechanisms and their dependence on microstructure and stress, aging effects, and microstructure-property trends are presented.

### 5.2.1 Creep Mechanisms and Modeling

The creep results indicated that three dominant mechanisms are active for O+BCC alloys at intermediate temperatures ( $650\text{--}760^\circ\text{C}$ ). Coble creep characteristics were exhibited at the lowest applied stresses. Grain boundary sliding was evident at intermediate applied stresses. Dislocation climb behavior was observed at the highest applied stresses. In order to understand the microstructural factors influencing the secondary creep rates, models based on Coble creep, grain boundary sliding, and dislocation climb were investigated.

At low stresses ( $\sigma < 100$  MPa) for the Ti-12Al-38Nb and super-transus solutionized then aged Ti-23Al-27Nb microstructures, the secondary creep behavior was characterized by a stress exponent close to unity, see Figures 4.47a and 4.64a and Tables 4.7 and 4.11. The activation energy corresponding to this regime ranged from 127-178 kJ/mol. Although no activation energies for grain boundary diffusion in O-based Ti<sub>2</sub>AlNb alloys are available, this range corresponds to half the typical activation energies for dislocation climb-controlled creep obtained from the current work as well as the work of others (Nandy *et al.* 1993,1995). Dislocation climb is associated with lattice self-diffusion and typically the activation energy for grain boundary diffusion is half that of lattice self-diffusion. It was therefore concluded that the secondary-stage, low-stress regime corresponds to Coble creep and this conclusion is supported by the lack of significant creep dislocation activity for the described microstructures (see Figure 4.67). N-H and H-D creep were also considered, however, these mechanisms are typically associated with lattice self-diffusion, and therefore they do not apply. In addition, a Langdon-Mohamed type creep deformation mechanism map constructed at 0.5T<sub>m</sub> (Ruano *et al.* 1988) shows that dislocation densities increase the stress range for H-D diffusion controlled-dislocation-creep, while lower dislocation densities are associated with the Coble creep regime, both for stress exponents close to unity. Thus the H-D creep behavior noted for large-grained pure  $\alpha$ -Ti (Ruano *et al.* 1988) is not applicable for the current microstructures, which exhibited relatively low dislocation densities. Interestingly, the measured Q<sub>app</sub> values were between 1-1.5 times greater than those obtained for grain boundary diffusional creep in  $\alpha_2$ -based Ti-24Al-11Nb (Mishra and Banerjee 1990) and pure  $\alpha$ -Ti (Malakondaiah and Rao 1981).

The effective grain size (G<sub>Seff</sub>) for diffusional creep was not immediately obvious. This was because in these microstructures a prior BCC grain exists within which transformation to O took place on aging. The effective grain size could not be the prior BCC grain size as the  $\beta$  grain size was significantly altered for Ti-12Al-38Nb yet

similar minimum creep rates were exhibited (see Table 4.11). From the phase evolution studies, O colony interfaces were the most rapid diffusion sites of the Ti-23Al-27Nb super-transus microstructure. Therefore, the size of the O cells within the colonies was measured and used to obtain an estimate of the frequency factor for grain boundary diffusion,  $D_o$ , in the equation for Coble creep (Coble 1963):

$$\dot{\epsilon}_c = (150/\pi) \cdot \{D_o \cdot \exp(-Q_{app}/RT)\} \cdot \{(W \cdot \Omega \cdot \sigma)/(G_{Seff}^3 \cdot kT)\} \quad (5.2)$$

where  $G_{Seff}$  is 1.74 times the mean-intercept length of the O cell and is equal to 10.1  $\mu\text{m}$ .  $\Omega$  is the activation volume and is estimated to be the Burgers vector ( $b \sim 2.99 \times 10^{-10}\text{m}$ ) cubed.  $W$  is the colony boundary width and is estimated to be  $5 \times 10^{-10}\text{m}$ . Boltzmann's constant is  $k$ , and  $Q_{app}$  is taken as 170 kJ/mol. The equation yields a value of  $D_o$  equal to  $1.9 \times 10^{-6} \text{ m}^2/\text{s}$ , which is six times higher than the frequency factor for grain boundary diffusion ( $D_o = 3.0 \times 10^{-7} \text{ m}^2/\text{s}$ ) in Ti-24Al-11Nb (Mishra and Banerjee 1990) and 40 times lower than the frequency factor for grain boundary diffusion ( $D_o = 7.5 \times 10^{-5} \text{ m}^2/\text{s}$ ) in pure Ti (Malakondaiah and Rao 1981). The size of the B2 platelets located within the O cells was also considered. However, a direct correlation with the B2 platelet size is not possible because the high aspect ratio and the strong directionality of the B2 platelets will alter the grain size dependence  $n$  in a complex manner (Raj and Ashby 1971, Schneibel *et. al.* 1981), which is difficult to evaluate because the platelets are randomly oriented with respect to the stress axis and only the ends of the B2 platelets are expected to possess a "disordered, high-angle" boundary structure while the broad faces are expected to be semicoherent based upon its OR with the O cell. Assuming that diffusion along the O-cell boundaries results in the slope changes leading to creep strain, the Coble creep rates of Ti-23Al-27Nb are compared with the measured values of Ti-24Al-11Nb ( $G_{Seff} = 48 \mu\text{m}$ ) and the extrapolated values for Ti ( $G_{Seff} = 405 \mu\text{m}$ ). Based on the similar creep rates of Ti-23Al-27Nb and Ti-24Al-11Nb and the much faster creep rate of Ti, the

creep strength for the ordered O alloys within the Coble creep regime derives from a considerable increase in the magnitude of the activation energy, a feature perhaps related to the ordered structure of the constituent O phase as well as the high Nb contents in the O and B2 phases. The latter comment is made based on the increasing diffusional activation energies obtained for increasing Nb additions in Ti (Sherman 1963).

Using the minimum creep rates of the Ti-12Al-38Nb microstructures at  $\sigma=50$  MPa and the previously calculated  $D_0$ ,  $G_{\text{Seff}}$  was calculated.  $G_{\text{Seff}}$  is 9.4  $\mu\text{m}$  for the 900°C and 1200°C super-transus then aged microstructures and 7.1  $\mu\text{m}$  for the as-rolled then aged microstructure. These values certainly do not correspond with the  $\beta$  grain size. They more closely resemble the O platelet size within the larger  $\beta$  grains. Though the size of the O platelets could not be estimated for use in the equation for Coble creep, elongated grains can greatly retard creep (Raj and Ashby 1971, Schneibel *et. al.* 1981). Therefore, the fine platelets are expected to provide greater strengthening than equiaxed grains due to their elongated shape. Thus the effective grain size correlated with the Coble creep rates is considered to resemble that of the O platelets and diffusion along (O platelet)-( $\beta$  matrix) interfaces is suggested to result in the slope changes leading to creep strain for Ti-12Al-38Nb. Similar to that for Ti-23Al-27Nb, the creep strength of this alloy derives from the magnitude of  $Q_{\text{app}}$  and the creep resistance of O+BCC microstructures is ranked according to the effective grain size.

For all the microstructures evaluated, at intermediate stresses the secondary creep behavior was characterized by a stress exponent close to two, see Figures 4.47a and 4.64a and Tables 4.7 and 4.11. The activation energies corresponding to this regime ranged from 256-311 kJ/mol. This range contains values intermediate to those within the Coble and dislocation climb regimes. This indicates that the grain boundary and volume diffusion processes are competing at intermediate stresses. The lowest value within this range is significantly higher than the highest value within the Coble regime while the highest value within this regime is relatively close to the value obtained within the



dislocation climb regime. Typically, the activation energy for grain boundary sliding is close to that for lattice self-diffusion. It was therefore concluded that the secondary-creep intermediate-stress regime corresponds to grain boundary sliding and this conclusion is supported by observations of grain boundary offsets, grain boundary cavitation, and the lack of significant creep dislocation activity at midgrain locations.

From the deformation observations, sliding did not appear to be accommodated by plasticity within the grains as suggested by Crossman and Ashby (1975). For FCC and HCP systems, dislocation movement in the grain boundaries has been observed by a combination of glide and climb (Lee *et al.* 1990). Assuming sliding occurs by the climb and glide of extrinsic lattice dislocations in grain boundary zones, where the rate of sliding is governed by the rate of climb, the rate of sliding has been equated by Langdon (1970):

$$\dot{\epsilon}_{gbs} = \{4\pi \cdot p_j \cdot b^2 \cdot (1-\mu) \cdot (z-1) \cdot \sigma^2\} \{D_l \cdot \exp(-Q_{app}/RT)\} / \{GS \cdot G \cdot k \cdot T\} \quad (5.3)$$

where  $p_j$  is the probability of finding a jog on a dislocation (Friedel 1964),  $\mu$  is Poisson's ratio,  $z$  is the coordination number,  $D_l$  is the frequency factor for lattice self-diffusion, and  $G$  is the shear modulus represented by  $(E/(2(1+\mu)))$ . The sliding mechanism proposed by Langdon (1970) is related to the build-up of dislocations near grain boundaries, which was observed at (equiaxed-O)-(equiaxed-O) boundaries for the subtransus Ti-23Al-27Nb microstructures, see Figure 4.60c. The stress concentration caused by grain boundary dislocation pile-up can be relieved by activating grain boundary dislocation sources or by nucleating and propagating an intergranular crack. It was clear from the deformation observations that a portion of the total creep strain was attributed to grain boundary cavitation, see Figures 4.52-4.58. Therefore, the accommodating process for sliding is considered to be the opening of grain boundary cavities and cracks. The nearly identical tension and compression creep rates are in agreement with a grain

boundary sliding mechanism and the similar amount of grain boundary cavitation observed in both cases, compare Figures 4.54a and 4.56, indicated that creep cavitation was not dominating the creep rates.

Similar to several other grain boundary sliding models (Crossman and Ashby 1975, Evans and Wilshire 1985), this model predicts the grain boundary sliding rate is inversely proportional to grain size. It is easily understood that if dislocation motion near the grain boundary contributes to grain boundary shear and promotes sliding, the sliding rate will be a function of grain size in that the grain boundary area per unit volume increases as the grain diameter decreases. An inverse relationship between creep rate and grain size is found in the experimental data, where the corresponding grain size was 1.74 times the mean-linear intercept, measured independent of phase, of the equiaxed grains in the solution-treated microstructures. Unlike the Coble creep regime, the size of the fine precipitating phases within the transformed-B2 grains was not considered as most of the damage accumulated at the larger, equiaxed grains' boundaries. The model assumes the activation energy for grain boundary sliding is close to that of lattice self diffusion. This is considered to be a reasonable assessment as the calculated activation energies are roughly 80% of those found within the dislocation climb regime. Using the data of the O+BCC Ti-23Al-27Nb specimen which exhibited an extensive amount of grain boundary offsets, an estimate of the frequency factor for lattice self-diffusion was obtained. Taking  $p_j=0.01$ ,  $\mu=0.3$ ,  $Q_{app}=265$  kJ/mol, and putting  $z=8$  (for BCC materials),  $D_l$  is equal to  $8.2 \times 10^{-4}$  m<sup>2</sup>/s. Using this frequency factor, the calculated grain boundary sliding rates for the Ti-23Al-27Nb microstructures judged to be within the grain boundary sliding regime are plotted as a function of  $\sigma^2/GS$  in Figure 5.6. The relationship between  $\dot{\epsilon}_{min}$  and  $\sigma^2/GS$  can be represented as:

$$\dot{\epsilon}_{gbs} = A_{gbs} \cdot \{\sigma^2\}/\{GS\} \quad (5.4)$$

where  $A_{\text{gbs}}$  is the slope of the curve and is equal to  $6.66 \times 10^{-29} \text{ m}^5/(\text{N}^2 \cdot \text{s})$ . Also plotted in Figure 5.6 are the measured strain rates. In general, the measured strain rates compare well with those calculated, especially at the lower grain sizes. For the largest grain sized, super-transus microstructure, the deviation between the measured and calculated creep rates was the largest, see Figure 5.6. For smaller grain sizes, creep rates increase rapidly due to the significance of grain boundary sliding (Barrett *et al.* 1967). If larger grain sizes lead to lower contributions from boundary sliding and greater contributions from other creep mechanisms then a larger deviation would be expected for the largest-grained microstructure.

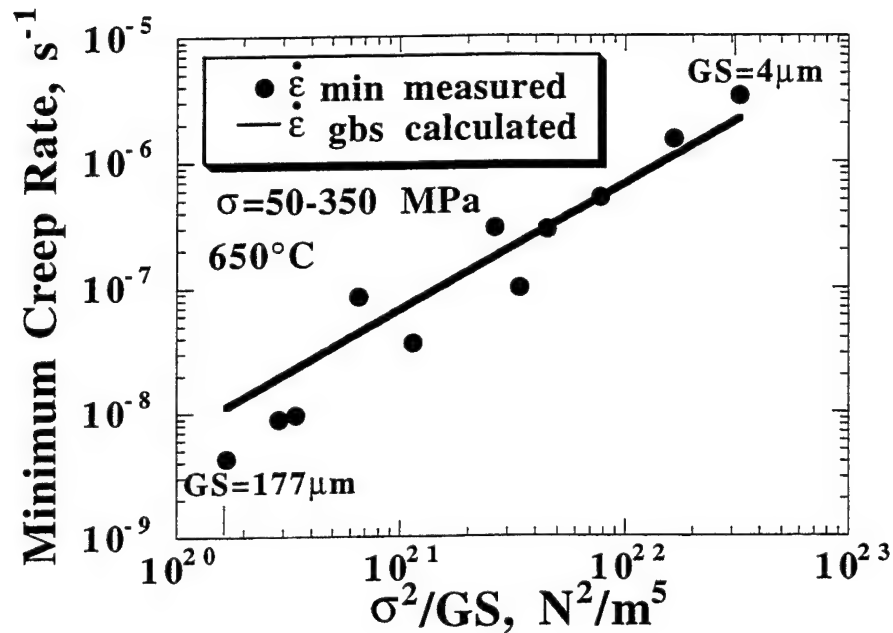


Figure 5.6 The calculated grain boundary sliding rate versus  $\sigma^2/\text{GS}$  for the Ti-23Al-27Nb microstructures judged to be within the grain boundary sliding regime at  $650^\circ\text{C}$ . Also indicated are the measured minimum creep rates for these microstructures.

The model was also compared with all the near  $\text{Ti}_2\text{AlNb}$  and  $\text{Ti-12Al-38Nb}$  minimum creep rate data within the region judged to be dominated by grain boundary

sliding. Both the calculated and measured values are depicted in Figure 5.7. The experimental strain rates are comparable to those calculated over the large ranges of applied stress and grain size for each of the O+BCC alloys studied. The largest deviation between the measured and calculated values was again noted for the largest-grained microstructure, which in this case was that for the 1.3 mm grain size Ti-25Al-27Nb alloy, see the two lowest minimum creep rate data points of Figure 5.7. Both grain size as well as the higher activation energy associated with this microstructure are expected to be responsible for this discrepancy as will now be explained. The calculated grain boundary sliding rates tended to overestimate the actual values for the Ti-25Al-23Nb and Ti-25Al-24Nb microstructures. This was a result of the higher activation energies associated with such microstructures (see Table 4.9). In particular the  $Q_{app}$  for Ti-25Al-23Nb within this regime was 311 kJ/mol, whereas the  $Q_{app}$  for Ti-23Al-27Nb was 265 kJ/mol. Higher  $Q_{app}$  values would decrease the exponential term in equation 5.3 and correspondingly lower the  $A_{gbs}$  term in equation 5.4, thereby resulting in a lower slope for the  $\dot{\epsilon}_{min}$  versus  $\sigma^2/GS$  curve. This would result in a slower calculated grain boundary sliding rate. As noted,  $Q_{app}$  increased with nominal Al content within the grain boundary sliding regime. Higher nominal Al contents were associated with larger O-phase volume percents. Thus, higher O-phase volumes tended to yield higher  $Q_{apps}$ , which resulted in slower grain boundary sliding rates. Therefore, both grain size and O phase volume are considered to be the most influential microstructural features within the grain boundary sliding regime. However, the dominant influence of grain size overrides all other microstructural features including phase volume percent. Although the adopted grain boundary sliding model does a reasonably good job of predicting the grain boundary sliding rates, the most significant finding of the creep behavior of O+BCC alloys in the intermediate stress regime is that the minimum creep rate is proportional to  $\sigma^2/GS$ , where the proportionality constant is relatively independent of nominal alloy composition. This further emphasizes the importance of grain size to the creep behavior of O+BCC alloys.

For high applied stresses ( $\sigma > 352$  MPa), the secondary creep behavior of the near  $\text{Ti}_2\text{AlNb}$  microstructures was characterized by stress exponents greater than or equal to 3.5, see Figures 4.51 and Tables 4.7 and 4.9. The  $Q_{\text{app}}$  value obtained for the supertransus Ti-25Al-27Nb microstructure within this regime was 346 kJ/mol (see Table 4.9), which is twice that obtained within the Coble creep regime for the Ti-23Al-27Nb supertransus microstructure. It was therefore concluded that the secondary-stage, high-stress regime corresponds to dislocation climb-controlled creep, and this conclusion is supported by the observation of higher dislocation densities than those found within the Coble and grain boundary sliding regimes.

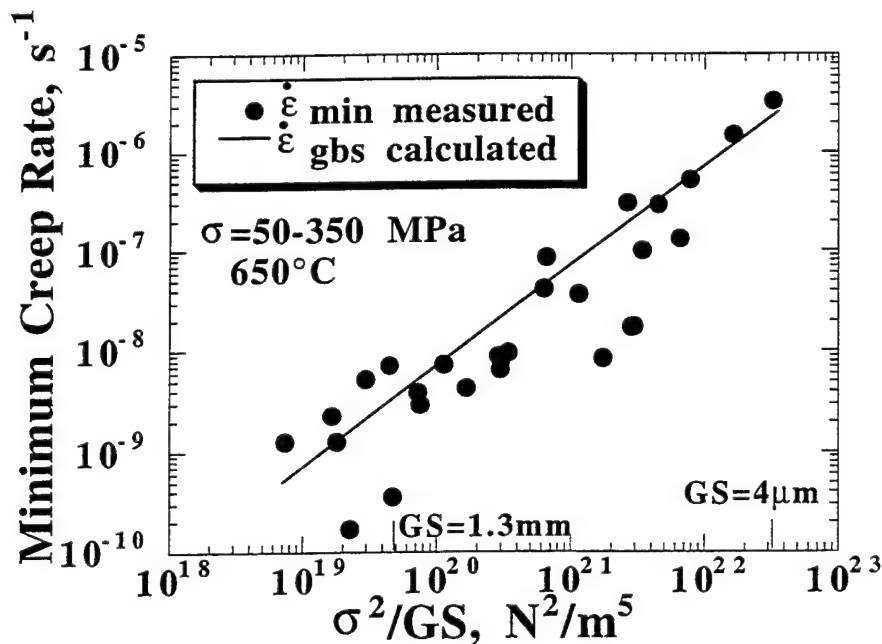


Figure 5.7 The calculated grain boundary sliding rate versus  $\sigma^2/\text{GS}$  for all the near  $\text{Ti}_2\text{AlNb}$  and Ti-12Al-38Nb microstructures judged to be within the grain boundary sliding regime at 650°C. Also indicated are the measured minimum creep rates for these microstructures.

Using the measured minimum creep rate for the Ti-25Al-27Nb microstructure at  $\sigma=394$  MPa and the  $D_l$  used in the grain boundary sliding equation, an estimate was

obtained for the creep constant, A, depicted in the equation for the dislocation climb creep rate (Mukherjee *et al.* 1969):

$$\dot{\epsilon}_{dc} = \{A \cdot G \cdot b / k \cdot T\} \cdot (\sigma / G)^n \cdot \{D_l \cdot \exp(-Q_{app}/RT)\} \quad (5.5)$$

For  $n=5.1$ , the value of A is equal to  $4.3 \times 10^3$ . This is two orders of magnitude lower than that for pure  $\alpha$ -Ti;  $A = 2.4 \times 10^5$  (Malakondaiah and Rao 1981). The value of  $A \cdot D_l$  is equal to  $3.5 \text{ m}^2/\text{s}$ , which is one order of magnitude lower than that for pure  $\alpha$ -Ti;  $A \cdot D_l = 24 \text{ m}^2/\text{s}$  (Malakondaiah and Rao 1981). Using the elastic modulus instead of the shear modulus, the constant  $A \cdot D_l$  was recalculated from equation 5.5 and compared with the data for Ti-24Al-11Nb. In this case, the value of  $A \cdot D_l$  is equal to  $177 \text{ m}^2/\text{s}$ , which is two orders of magnitude higher than that for Ti-24Al-11Nb (Mishra and Banerjee 1990). Because the Ti-25Al-27Nb minimum creep rates were over two orders of magnitude lower than those of the  $\beta$  heat-treated Ti-24Al-11Nb and pure  $\alpha$ -Ti microstructures, the creep strength of this O+BCC alloy in climb-controlled creep is derived from an increase in activation energy for volume diffusion rather than the pre-exponential factor  $A \cdot D_l$ . The secondary creep dislocation structure associated within this regime indicated that dislocation pile-up is occurring at the O/B2 lath interfaces, see Figure 4.62b. In addition the density of dislocations within the lath O phase, see Figure 4.61, was much higher than for specimens deformed in the grain boundary sliding and Coble creep regimes. These observations imply that the Weertman (1968) model, of the climb of the leading dislocations at the head of the pile-up, constitutes the rate-controlling mechanism. In this respect it is felt that lath spacing in regards to the mean-free-slip path is quite important to the creep rate within the dislocation climb regime. The equiaxed grains of the sub-transus microstructures would constitute a larger mean-free-slip path than that for the super-transus lath microstructures. This may explain the lower minimum creep rates exhibited by the super-transus microstructures compared to the projected rates of the sub-

transus microstructures within this regime. The equiaxed grain size of the super-transus microstructures was not significant within this regime as the minimum creep rates of each of the heat-treated Ti-12Al-38Nb microstructures, which ranged in  $\beta$  grain size from 33-337 $\mu\text{m}$ , followed the same curve, see Figure 4.64a. The Ti-12Al-38Nb data is in agreement with the expected importance of lath spacing as the spacing between the O-phase platelets within the large  $\beta$  grains was identical and independent of heat-treatment.

The transition from grain boundary sliding to dislocation climb occurred at different applied stresses for the near Ti<sub>2</sub>AlNb and Ti-12Al-38Nb alloys. The transition between the grain boundary sliding and dislocation climb regimes occurred between 317-360 MPa for Ti-23Al-27Nb and 135-150 MPa for Ti-12Al-38Nb. This large difference in applied stresses for the transition of creep mechanisms may be related to the difference in the 650°C yield strengths of these alloys. The 650°C yield strengths for Ti-23Al-27Nb and Ti-12Al-38Nb were 675 and 391 MPa, respectively (see Table 4.12). The ratios of the creep transition stress to the 650°C YS were 0.47-0.53 and 0.35-0.38 for Ti-23Al-27Nb and Ti-12Al-38Nb, respectively. This suggests that for applied stresses between 0.35-0.53 times the yield strength, the dislocation creep regime initiates for O+BCC alloys at intermediate temperatures ( $T=650^\circ\text{C}$ ). This suggests that the creep rates of O+BCC alloys containing greater BCC volumes accelerates faster at lower applied stress levels due to lower yield stresses. Thus, the elevated-temperature yield strength is a function of microstructure for O+BCC alloys and the ratio of the applied creep stress to the flow stress may be used to predict the creep mechanism.

Combining the creep parameter values of this work with those from published works on O,  $\alpha$ , and  $\alpha_2$ -based systems, the similarities and differences of the creep behavior of such alloys are evident. Table 5.1 compares the  $n$  and  $Q_{\text{app}}$  values for the different alloys. The data shows that the O alloys exhibit the highest activation energy. Each of the Ti alloys compared showed Coble creep characteristics for stresses below 100 MPa, and the highest activation energies were significantly higher for the O alloys

compared with the  $\alpha$  and  $\alpha_2$ -based alloys. For the highest stresses, dislocation climb parameters were observed and again the activation energies were the highest for the O alloys. For intermediate stresses, O alloys exhibit creep parameters characteristic of grain boundary sliding. Although, some studies have noted similar parameters and suggested that such a mechanism exists, prior to this work thorough investigations of grain boundary sliding for Ti-Al-Nb alloys were non-existent. Combining the current data and microstructural observations with those of other studies, the stress range for the grain boundary sliding region is quite large, and therefore grain boundary sliding is a significant contributor to the overall creep behavior of O+BCC alloys.

### 5.2.2 Microstructural Dependence of the Creep Mechanisms

Grain boundary deformation mechanisms were indicated for low-to-intermediate stresses. In agreement, grain boundaries were the locus of cracking and diffusion. From the phase evolution studies, diffusion along BCC grain boundaries was favored over bulk diffusion at 650°C. In the case of the near Ti<sub>2</sub>AlNb alloys, grain boundary precipitates coarsened and migrated from the grain boundary consuming the finer precipitates within the prior B2 grains, see Figures 4.11, 4.12, 4.19 and 4.20. For Ti-12Al-38Nb, O-phase platelets precipitated initially at  $\beta$  grain boundaries, see Figure 4.38, and later precipitated at midgrain locations. The low density of dislocations at midgrain locations indicated that grain interiors were not contributing significantly to the creep rates. Grain interiors were also more resistant to cracking as cracks typically grew intergranularly, see Figures 4.52-4.58. Thus combining the phase evolution, deformation, and strain-rate observations, grain boundary locations were controlling the aging-precipitation and low-to-intermediate stress creep behaviors.



Table 5.1 Comparison of Creep Parameters for Different Ti-Alloys

Alloy Composition (reference)	Heat Treatment	Test Conditions $\sigma$ (MPa)/Temp(°C)	n	Q <sub>app</sub> , kJ/mol
<b>Low-Stress Regime</b>				
Ti (Malakondaiah and Rao (1981))	various	1-2/550-865	1	104-121
Ti-24Al-11Nb (Mishra and Banerjee (1990))	various	50-100/575-725 air	1	107-120
Ti-21Al-22Nb (Smith <i>et al.</i> (1993))	na	30-90/650-760 air	1.4	na
Ti-22Al-23Nb (Woodard and Pollock (1997)))	na	69-110/650 air+vacuum	1.3	187
Ti <sub>2</sub> AlNb (present study)	1090°C/0.5h/WQ +650°C/112h/WQ	50-172/650-760 air	1.2	171
Ti-12Al-38Nb (present study)	various	50-135/650-705 air	1.6-1.9	127-178
<b>Intermediate-Stress Regime</b>				
Ti-22Al-23Nb (Hayes (1996))	996°C/1hr/AQ	69-172/650-760 air+argon	2.8	327
Ti-21Al-21Nb (Woodard <i>et al.</i> (1996))	na	69-172/650 vacuum	2.4	na
Ti-25Al-23Nb (Rowe and Larsen (1996))	815°C/1hr	175-310/650 argon	2.8	na
Ti <sub>2</sub> AlNb (present study)	various	50-352/650-760 air+vacuum	1.8-2.3	265
Ti-12Al-38Nb (present study)	1200°C/5h/WQ + 650°C/53h/WQ	50-135/650-705 air+vacuum	1.9	256
<b>High-Stress Regime</b>				
Ti (Malakondaiah and Rao (1981))	various	1-2/550-865	4.3	241
Ti <sub>3</sub> Al (Mendiratta and Lipsitt (1980))	1000°C/4h/FC	138-312/650-800	4.3	206
Ti-24Al-11Nb (Mishra and Banerjee (1990))	various	100-400/575-725 air	5	260
Ti-27Al-21Nb (Nandy <i>et al.</i> (1993))	1170°C/OQ + 900°C/AQ	240-500/650-750 air	5-6	340
Ti-24Al-16Nb (Nandy <i>et al.</i> (1995))	1150°C/2.5°C/s + 750°C/AQ	150-540/700-750 air	4.2-4.3	371
Ti-27Al-16Nb (Nandy <i>et al.</i> (1995))	1170°C/2.5°C/s + 750°C/AQ	240-660/700-750 air	4.2-4.3	376
Ti-22Al-27Nb (Rowe and Larsen (1996))	815°C/1hr	310-380/650 argon	5.3	na
Ti <sub>2</sub> AlNb present study	various	317-442/650-760 air	3.7-5.1	346
Ti-12Al-38Nb present study	various	135-172/650-705 air	3.5-7.2	na

AQ: air quench; OQ: oil quench; FC: furnace cooled; Ar: cooling performed in static argon gas; na: not available.

The grain boundary creep deformation process was dependent on microstructure and stress. For the large-grained super-transus Ti-23Al-27Nb microstructure, Coble

creep was rate controlling at stresses less than 100 MPa and the creep exponent was close to unity. For applied stresses between 172 and 318 MPa, grain boundary sliding was rate controlling and the creep exponent was two. However, for the fine-grained sub-transus microstructures, grain boundary sliding was dominant for stresses between 50-352 MPa and no transition in the creep exponent was experienced, see Figure 4.47a. The difference in creep mechanisms for the lower applied stresses was supported by the significantly different activation energies obtained. The measured activation energies at  $\sigma=50$  MPa were significantly greater for the sub-transus microstructures compared with the super-transus microstructure, see Figure 4.47b and Table 4.7. Therefore, sub-transus microstructures remained within the grain boundary sliding regime at the lowest applied stresses, and a Coble creep mechanism was not rate controlling. Grain size is considered to be primarily responsible for the change in creep behavior observed below 172 MPa for the super-transus microstructure. For grain sizes smaller than 100  $\mu\text{m}$ , creep rates increase rapidly due to the significance of grain boundary sliding (Barret *et al.* 1967, Sherby and Burke 1968). Smaller grain sizes promote higher strain rates and greater contributions from grain boundary sliding. Therefore, the sub-transus microstructures maintained higher sliding rates than the super-transus microstructure. If the grain boundary creep processes are competing at lower applied stresses, the transition to Coble creep is expected to occur at a higher stress for the super-transus microstructure as for a given applied stress the contribution from grain boundary sliding would be less. It is therefore expected that the sub-transus microstructures would transition to a Coble regime at some  $\sigma < 50$  MPa. Results too recent to be included in this report are in agreement with this statement.

### 5.2.3 Aging Effects

Long-term aging for O+B2 microstructures led to a reduction in primary creep strain and both the primary and minimum creep rates. The difference in creep strain was

more significant in the primary stage as within the first few hours after loading the strains of the unaged specimens had doubled compared with the strain of the aged specimen (see Figures 4.41 and 4.44). Aging reduced the primary creep strains from 0.79% to 0.68% and from 0.77% to 0.56% for the 950°C and 910°C solutionized microstructures, respectively. Thus aging significantly reduces primary strain through O-phase precipitation both within B2 grains and at B2 grain boundaries. This indicates that microstructures containing untransformed B2 are undesirable as primary creep strain, which is used to rank structural materials, is a critical parameter for design purposes. However, in terms of the secondary creep regime, the aging transformation had a relatively small effect as similar minimum creep rates were obtained. A similar result has been found by Rowe and Larsen (1996) for Ti-22Al-27Nb specimens which were heat treated at 815°C, one of which was then aged at 760°C. The 100 hour aged sample had a minimum creep rate that was similar to that of the unaged sample but the primary creep strain after aging was reduced from 0.74% to 0.53%.

The relatively insignificant effect of aging on the minimum creep rates is explained in terms of the secondary creep mechanism, grain boundary sliding. Grain size, rather than phase volume fraction, is the dominant microstructural feature influencing the secondary creep rates within the grain boundary sliding regime. If a majority of the creep deformation is limited to grain boundary locations, transformations occurring at grain interiors would not be expected to have a significant influence on the secondary stage. As concluded from the transformation study, the migrating front of the cellular precipitation continued to grow within the prior B2 grain, even after long aging times, while the platelets at grain boundary locations were relatively stable. Thus the transformation occurring during the creep test for aged specimens is not likely to have significantly effected the secondary creep behavior. However, for unaged specimens, the B2-to-O transformation, which produced a majority of the resulting O phase within the first 24 hours, is expected to generate transformation strains and thereby increase the

measured strains due to transformation strains occurring within the prior B2 grains. This explains the increase in primary-stage strains observed for unaged specimens relative to long-term aged specimens. A smaller effect on the secondary creep rates would be expected as the grain boundary locations, assumed to be controlling the minimum creep rates, stabilize with time.

#### 5.2.4 Microstructure-Property Trends

Combining the observations of this work with published works of O and  $\alpha_2$ -based alloys, important microstructure-property trends are indicated. For both O and  $\alpha_2$ -based alloys, super-transus microstructures are more creep resistant than sub-transus microstructures (Mishra and Banerjee 1990, Majumdar *et al.* 1994 1995, Smith *et al.* 1994a,b 1995, Foster *et al.* 1995, Soboyejo *et al.* 1997). The results for the Ti-23Al-27Nb alloy are quite similar to those of a Ti-24Al-11Nb alloy (Mishra and Banerjee 1995). In both cases the super-transus solutionized microstructure exhibited the best creep resistance, while the two sub-transus microstructures exhibited smaller equiaxed grain sizes and worse creep resistance. The super-transus heat-treated Ti-24Al-11Nb microstructure exhibited a secondary strain rate of  $1.0 \times 10^{-9}$  at 50 MPa/650°C, which is identical to that of the super-transus Ti-23Al-27Nb microstructure. The effective grain size, which is the dominant microstructural feature in Coble creep, for Ti-24Al-11Nb was estimated to be nearly 5 times larger than that of Ti-23Al-27Nb. Although there is a large difference in  $GS_{eff}$ , the slower grain boundary diffusion rate expected for the O+BCC microstructure is suggested to be responsible for the similar resulting creep rates. It is interesting to note that this strain rate is orders of magnitude lower than that for the 405  $\mu\text{m}$  grain size pure  $\alpha$ -Ti microstructure (Malakondaiah and Rao 1981). Thus, ternary Al and Nb additions provide creep strengthening within the Coble creep regime through decreasing the grain boundary diffusional rates. As mentioned previously, this is expected to be a result of the ordered phases present within these alloys.

The most significant relationship discovered in this work is between the equiaxed grain size and the minimum creep rate for intermediate applied stresses. This relationship is also obeyed by first-generation O alloys (Majumdar *et al.* 1994 1995, Smith *et al.* 1995). The creep conditions from those works included 172 MPa/650°C, which is within the grain boundary sliding regime. Originally it was felt that larger volume fractions of O were responsible for the lower creep rates. However, the higher volume of O phase corresponded with a larger prior-B2 grain size due to the higher-temperature solution treatments prior to aging. Thus, for both first and second generation O alloys, higher-temperature solution treatments tend toward larger average, equiaxed grain sizes. This significantly effects the creep behavior in the grain boundary sliding regime as larger equiaxed grain sizes result in lower minimum creep rates. Comparing the current Ti-23Al-27Nb data with data taken from a three-phase Ti-25Al-17Nb alloy (Majumdar *et al.* 1995), whose nominal composition was close to Ti-23Al-16Nb, similar minimum creep rates are achieved for similar average, equiaxed grain sizes. In addition, the Ti-25Al-17Nb data is well represented by the calculated grain boundary sliding rates according to equation 5.4. This observation further emphasizes that grain boundary sliding rates are relatively independent of phase composition and structure. Another important observation from this result is that nominal Nb contents between 16-27at.% do not significantly effect minimum creep rates. A similar result has also been found in a recent investigation by Nandy and Banerjee (1997).

The reason why the higher minimum creep rates were observed for specimens tested in air is believed to be due to environmentally assisted surface cracking. Mishra *et al.* (1995) determined that a critical strain exists for surface cracking, where longer air exposures and lower creep stresses favor lower critical strains for surface cracking. In addition the dynamic nature of environmental embrittlement has been established by Ward (1993). The accelerated growth of cracks in air are expected to lead to larger measured creep strains and minimum creep rates. Surface cracking can therefore

severely impair the load bearing capability of any material. For rotating components, such as those in which Ti-Al-Nb alloys are being targeted for replacements, surface cracking is particularly undesirable.

### 5.3 Tension Behavior

This section discusses the elevated and room-temperature tensile behavior results.

#### 5.3.1 Temperature Dependence

The elevated-temperature yield strength was important for understanding the creep behavior and in particular the transition between the grain boundary sliding and dislocation climb regimes. As described in the creep discussion, the elevated-temperature yield strength was dependent on microstructure. The higher 650°C yield strength was exhibited by Ti-23Al-27Nb and the lower yield strength was exhibited by Ti-12Al-38Nb. Higher elevated-temperature yield strengths corresponded with higher grain boundary sliding-to-dislocation climb transition stresses.

The yield strength decreased with temperature for the near Ti<sub>2</sub>AlNb and Ti-12Al-38Nb alloys, compare data from Tables 4.12 and 4.13. The most significant decrease occurred for the  $\beta$ -dominated alloy, Ti-12Al-38Nb. This indicates that the yield strength of O+BCC alloys containing greater BCC volumes decreases more rapidly with temperature than those alloys containing greater O volumes. Thus the BCC phase is expected to soften more rapidly with temperature than the O phase. This is consistent with the yield stress behavior of the metastable  $\beta$  alloy, Timetal®21S, which dropped more drastically with temperature than the O-based Ti-25Al-17Nb and  $\alpha_2$ -based Ti-24Al-11Nb alloys (Boehlert *et al.* 1997b). Interestingly, the 650°C yield strength for Timetal®21S, which contains  $\alpha$  platelets uniformly dispersed within large  $\beta$  grains, was more than 125 MPa lower than those for the O+ $\beta$  Ti-12Al-38Nb. This suggests that the

O phase provides greater elevated-temperature precipitation strengthening than the  $\alpha$  phase.

### 5.3.2 RT Tensile Behavior

Conventionally processed O+B2 alloys which contain less than 800 ppm oxygen have yielded excellent RT strength, elongation, and fracture toughness (Rowe 1991, Woodfield 1996). However, O+B2 alloys have shown extreme sensitivity to interstitial oxygen content where a dramatic effect on processing was noticed for two ingots which contained 880 ppm oxygen and between 1100-1150 ppm oxygen, respectively (Wojcik *et al.* 1996). In fact the alloy containing between 1100 and 1150 ppm oxygen was not fabricable, relating to its poor ductility. With this respect, interstitial oxygen content is expected to be responsible for the poor RT properties of the higher-oxygen containing Ti-23Al-27Nb and Ti-25Al-23Nb sheet materials of the current work. The poor RT properties of these materials were independent of microstructure. On the other hand, when oxygen content is controlled, microstructure significantly influences the RT tensile behavior. For example, near Ti<sub>2</sub>AlNb alloy microstructures containing greater equiaxed B2-phase volumes exhibit higher strengths and elongations, see Table 4.13. When the B2 content is sufficiently low, however, the O-phase deformation characteristics dominate. Popille and Douin (1996) have shown that the O phase has an insufficient number of independent slip systems active at RT. From this finding it is expected that strain incompatibilities and consequently high stress concentrations would exist at O/O grain boundaries. Such stress concentrations are responsible for the O/O grain boundary cracking, see Figure 4.74, which resulted in poor elongations. This is analogous to the  $\alpha_2/\alpha_2$  grain boundary cracking observed in three-phase O alloys, which led to low RT ductilities (Majumdar *et al.* 1994 1995, Smith *et al.* 1995, Boehlert *et al.* 1997a). Thus, if a sufficient amount of B2 phase is not present to reduce stress concentration effects by

both allowing slip transmittability across O/B2 boundaries and blunting O/O grain boundary cracks, localized failure results at low strain levels.

This work establishes that those alloys containing a high Al concentration do not necessarily exhibit poor ductility, and elongation-to-failure is strongly dependent on microstructure and interstitial oxygen content. For example, solutionizing high in the two-phase O+B2 region will result in larger concentrations of equiaxed B2 phase and provide excellent elongations-to-failure independent of composition. Thereby, in contrast to previous speculation (Banerjee *et al.* 1993, Banerjee, 1994), alloys containing 25at.% Al may exhibit good ductility provided the interstitial oxygen and B2 volumes are controlled. The distribution of the B2 phase appears to also be important as the fully-lenticular O+B2 microstructure exhibited low ductility, even though it contained the same B2 volume as that of the more ductile, equiaxed microstructure. In this case, although slip was transmitted between O/B2 laths, the B2 lath distribution is thought to have been too widespread to successfully disperse slip and blunt O cracks, see Figure 4.78.

For Ti-12Al-38Nb, the fully- $\beta$  microstructures exhibited high elongations ( $\epsilon_f > 27\%$ ). O-phase platelets provided significant strengthening for the  $\beta$ -dominated microstructures with an associated reduction in elongation-to-failure. Excluding the data of the largest-grained microstructure, which is expected to have exhibited inhomogeneous slip due to the exceptionally large grain size, elongations of over 12% were achieved by the O+ $\beta$  microstructures. Thereby, ductility was maintained after aging. In fact, the poorest elongations of the Ti-12Al-38Nb microstructures were over two times larger than those for the most ductile near Ti<sub>2</sub>AlNb alloys. Both the strengths and elongations of the aged Ti-12Al-38Nb microstructures are consistent with an earlier report on a similar alloy, compare row 19 of Table 1.2 with row 27 of Table 4.13. A recognized disadvantage of the higher Nb-containing alloy is its density. In terms of the alloy compositions lying along the constant Ti=50at.% line, lower densities are achieved with lower Nb compositions. Based on data from similar compositions, the density of the Ti-



12Al-38Nb alloy is expected to be 6 g/cm<sup>3</sup>. This is quite unfavorable as weight savings is a vital issue for aerospace applications.

For the near Ti<sub>2</sub>AlNb and Ti-12Al-38Nb alloys, aging resulted in larger O-phase volumes and poorer elongations-to-failure, see Table 4.13. In the case of Ti-12Al-38Nb, adequate ductility ( $\epsilon_f > 12\%$ ) was maintained even though a decrease of over 14% strain was observed. Such debits in elongation could not be afforded for the near Ti<sub>2</sub>AlNb alloy microstructures. In such cases the O-dominated, aged microstructures exhibited less than 1% elongation and this remains a serious concern in terms of practical structural use of these alloys. As depicted in Figure 5.5, nominal composition is vital for maintaining high BCC-phase volumes at 650°C, and therefore it is also important for maintaining adequate RT ductility of aged materials. Thus a balance between creep resistance and ductility must be maintained through proper alloy selection and thermomechanical treatments which control microstructure. Such treatments may be designed for desired structural applications.

## CHAPTER 6

### SUMMARY AND CONCLUSIONS

#### 6.1 Summary

This technical report discussed the results of a systematic study of the physical metallurgy of O+BCC orthorhombic titanium alloys. In particular, the phase evolution, creep, and tensile behavior were investigated. The primary emphasis was on understanding microstructure-creep relations in the low-to-intermediate stress and intermediate temperature regime defined as 35-350 MPa and 650-760°C. Several important observations have been made in this work. The following is provided to summarize the important and relevant findings.

The alloys examined were Ti-25Al-25Nb, Ti-23Al-27Nb, and Ti-12Al-38Nb nominally. The former two were grouped as near Ti<sub>2</sub>AlNb alloys. Each alloy was processed from ingot to sheet form using conventional thermomechanical processes. Another Ti<sub>2</sub>AlNb alloy was processed using an induction melter. The temperature range of the hot-forging and hot-rolling procedures was 932-1000°C. The Ti-12Al-38Nb alloy was the easiest to deform, while the near Ti<sub>2</sub>AlNb alloys were more difficult to deform. This is expected to be a result of two main factors: (i) the flow stress of the near Ti<sub>2</sub>AlNb alloys is significantly higher than that of Ti-12Al-38Nb; (ii) the near Ti<sub>2</sub>AlNb alloys were processed at sub-transus temperatures while Ti-12Al-38Nb was processed within the super-transus  $\beta$  region. In addition, the Ti-25Al-25Nb ingot was more difficult to work than the Ti-23Al-27Nb ingot. This is expected to be a result of the higher nominal Al content.

A variety of microstructures are achievable for near  $\text{Ti}_2\text{AlNb}$  alloys. The achievability of desired microstructures is strongly dependent on the processing and heat-treatment schedules. In particular, a wide variation in grain size was achievable through post-processing heat treatments. Such a variation in grain sizes would not have been possible if super-transus processing temperatures were chosen. The temperature ranges for the  $\alpha_2+\text{B}_2$ ,  $\alpha_2+\text{B}_2+\text{O}$ ,  $\text{B}_2+\text{O}$ , and  $\text{O}+\beta$  phase regions were estimated for the near  $\text{Ti}_2\text{AlNb}$  alloys. The discovery of the three-phase  $\alpha_2+\text{B}_2+\text{O}$  microstructure verified that a narrow three-phase field exists for alloys containing more than 20at.% Nb. Orientation relations, which played a significant role in terms of the RT tensile behavior, existed between sub-transus heat-treated, equiaxed  $\alpha_2/\text{B}_2$  and  $\text{O}/\text{B}_2$  grains. Thus, ORs may be restored in sub-transus worked materials without super-transus heating. For heat treatments above  $875^\circ\text{C}$ , solutionizing followed by quenching resulted in equiaxed-grained microstructures. Below  $875^\circ\text{C}$ , the  $\text{B}_2$  phase transformed into a mixture of  $\text{O}$  and BCC phases with lenticular morphologies. The  $\alpha_2$  phase was more resilient to transformation and once the  $\alpha_2$  was formed, such as through heat treatments within the  $\alpha_2+\text{B}_2$  and/or  $\alpha_2+\text{B}_2+\text{O}$  fields, it was quite difficult to remove without super-transus solutionizing followed by quenching. The  $\text{O}$ -phase volume was dependent on alloy composition and in particular Al content. Higher Al contents tended toward higher  $\text{O}$ -phase volumes.

The dominant aging-transformation mechanism was a function of the solutionizing and aging temperatures. Super-transus solutionizing followed by  $650^\circ\text{C}$  aging resulted in a composition invariant mechanism where fully- $\text{B}_2$  microstructures transformed to  $\text{O}$  within two hours. For longer aging times, fine  $\text{O}$  platelets coarsened initially at prior- $\text{B}_2$  grain boundaries, and then they coarsened within the prior- $\text{B}_2$  grains. Due to the equilibrium conditions, the BCC phase reprecipitated within the  $\text{O}$  grains. Super-transus and  $\alpha_2+\text{B}_2$  solutionized samples, which were aged within the  $\text{O}+\text{B}_2$  regime, exhibited Widmanstätten  $\text{O}$  precipitation within the  $\text{B}_2$  grains. For the  $\alpha_2+\text{B}_2$

solutionized then O+B2 aged samples, the O phase also formed as a rim around the non-equilibrium  $\alpha_2$  phase. This is thought to have provided a barrier to diffusion between the  $\alpha_2$  and B2 regions and therefore deterred  $\alpha_2$  transformation. O+B2 solutionized samples exhibited Widmanstatten O precipitates within equiaxed B2 grains upon aging below 875°C. The size of the Widmanstatten precipitates were related to the aging temperature; coarser precipitates were exhibited at higher aging temperatures. Upon aging O+B2 solutionized samples below 750°C, a discontinuous precipitation reaction occurred at the O/B2 grain boundaries. The precipitates coarsened at the equiaxed prior-B2 grain boundaries and the migrating interface of the coarsening precipitates consumed the finer Widmanstatten precipitates within the bulk of the prior-B2 grain. This reaction was characterized as cellular precipitation according to the reaction:  $B2 \rightarrow \beta + O$ . The  $\beta$ -phase formation was caused by a composition induced disordering of B2 which occurs upon low-temperature aging. The B2 phase is supersaturated with Al compared with the lower temperature  $\beta$  phase. The cellular precipitation reaction was favored by large compositional gradients between the solutionized B2 and equilibrium BCC phases at the aging temperature. Higher solution-treatment temperatures and lower aging temperatures were more conducive to cellular precipitation. Thus, large BCC-phase compositional gradients are the driving force for cellular precipitation at B2 grain boundaries. Cellular precipitation also occurred for  $\alpha_2$ +B2 solutionized samples aged at 650°C. Overall, the cellular precipitation was sluggish and stable equilibrium O+ $\beta$  microstructures were not achieved even after aging times of 28 days at 650°C. In summary, the type of aging-transformation mechanism was strongly dependent on the solutionizing and aging temperatures. It was noted that for all solutionized samples, slow-cooling (instead of quenching than aging) favored Widmanstatten O formation within equiaxed B2 grains, and no cellular precipitation was evident in such cases.

At creep temperatures (650-760°C), the B2 phase undergoes a composition induced disordering and subsequently transforms both homogeneously and through

cellular precipitation. The super-transus solutionized B2 grains, which contained high Al and low Nb levels, were the least likely to disorder to the  $\beta$  phase. Low-temperature equilibrium was more readily obtained for the  $\beta$ -dominated Ti-12Al-38Nb alloy. In this case, Widmanstätten O precipitation occurred for all aging temperatures between 650-800°C and no  $\alpha_2$  phase was present. Above 800°C, fully- $\beta$  microstructures equilibrated and the size of the  $\beta$  grains were controlled by the solutionizing temperature and hold time. Using the heat-treatment data for each of the O+BCC alloys containing Ti=50at.%, the pseudobinary diagram, depicting the phase equilibria of such alloys, was modified.

The phase evolution, including the aging-transformation behavior, significantly influenced the creep response. Long-term aging at 650°C resulted in lower primary creep strains compared to unaged microstructures. In terms of phase volumes and sizes, load did not significantly affect the transformation behavior. The secondary-creep behavior, and in particular the measured minimum creep rates and deformation behavior, were used to identify the dominant creep mechanisms based on the well-established creep theories of single-phase disordered metals. The O+BCC alloys exhibited three distinct secondary creep mechanisms. Coble creep characteristics, including a stress exponent of unity and low calculated activation energies, were exhibited at the lowest applied stress levels ( $\sigma < 100$  MPa). Similar to the phase evolution behavior of the solutionized then aged O+BCC microstructures, grain boundary diffusion appeared to be the rate-controlling process. Based on the calculated activation energies, the activation energy for grain boundary diffusion was estimated to lie between 127-178 kJ/mol. Diffusion across the O cells within the transformed-B2 regions was considered to be significantly contributing to the creep rate of the super-transus solutionized Ti-23Al-27Nb microstructures.

Grain boundary sliding was exhibited at intermediate applied stress levels ( $\sigma = 50$ -352 MPa). Fiduciary-line experiments revealed high local strains at the boundaries of offset grains. Sliding appeared to be accommodated by grain boundary cavitation, which occurred in both tensile and compressive loadings. Little evidence of deformation was

observed at grain interiors, even for specimens unloaded after achieving over 6% creep. The fiducial lines were unaltered at midgrain locations and low dislocation densities were observed within grains. Dislocations were however observed to pile-up at (equiaxed-O)-(equiaxed-O) grain boundaries, which is in agreement with a grain boundary sliding mechanism. Also in agreement with a grain boundary sliding mechanism, the calculated creep exponents were close to two and the apparent activation energies resembled those expected for lattice self-diffusion. A strong correlation between applied stress, equiaxed grain size, and minimum creep rate was exhibited. In particular,  $\dot{\epsilon}_{\text{gbs}} = A_{\text{gbs}} \cdot \{\sigma^2\}/\{\text{GS}\}$ , where the constant  $A_{\text{gbs}}$  was relatively insensitive to alloy composition. This shows the overriding influence of grain size on minimum creep rate. Grain size is the dominant microstructural feature influencing the secondary creep behavior of O+BCC alloys within the grain boundary sliding regime. It was noted that O-phase volume percent is important in that it influences the activation energy, which is incorporated within the  $A_{\text{gbs}}$  term, however, its influence was less significant than that of grain size.

For high applied stresses ( $\sigma > 352$  MPa), characteristics typical of dislocation climb were exhibited. High dislocation densities were observed both within grains and at grain boundaries. The calculated creep exponents ranged between 3.5-7.2 and the activation energies were approximately twice those calculated within the Coble creep regime. Based on the calculated activation energies, the activation energy for lattice self diffusion of O+BCC alloys is between 256-346 kJ/mol. The large range depicted by these values is partially due to the scatter in the data as well as the activation energy dependence on microstructure, and in particular O-phase volume.  $Q_{\text{app}}$  tended to increase with O-phase volume fraction. This is related to alloy composition as the higher Al-containing alloys exhibited higher O-phase volumes at creep temperatures. O-phase volume fraction and lath spacing are considered to be the most influential microstructural features within this regime. More work is necessary to establish which of these factors is more significant. The equiaxed grain size is not playing as significant a role within this

regime compared with the grain boundary sliding regime. This was evidenced by the Ti-12Al-38Nb creep rate data, which showed that independent of grain size the dislocation climb creep rates followed the same curve.

The transition stresses between the regions dominated by separate creep mechanisms were dependent on microstructure. The transition stress between the Coble and grain boundary sliding regimes was higher for the large-grained super-transus solutionized Ti-23Al-27Nb microstructure compared with the finer-grained sub-transus solutionized Ti-23Al-27 microstructures. This appeared to be related to the grain size as larger grain sizes lead to lower grain boundary sliding contributions for a given stress level. For the transition between grain boundary sliding and dislocation climb, higher transition stresses coincided with higher elevated-temperature yield strengths. A near Ti<sub>2</sub>AlNb alloy exhibited significantly higher 650°C yield strength than Ti-12Al-38Nb.

Overall, the creep strength of O+BCC alloys within the Coble creep and dislocation climb regimes was shown to derive from an increase in the activation energies, which are higher than those obtained in  $\alpha_2$ -based Ti-24Al-11Nb and pure  $\alpha$ -Ti. Within the grain boundary sliding domain, those microstructures solution treated to obtain higher initial grain sizes exhibited greater creep resistance. Sub-transus processing and heat treatment degrade creep resistance due to the smaller resulting grain sizes compared to super-transus microstructures. Thus, the intermediate stress creep behavior of O+BCC alloys is quite sensitive to grain size, which is more influential than phase volume fraction, composition, and morphology. This work shows that the low-to-intermediate stress, intermediate-temperature creep behavior of O+BCC alloys is principally dictated by grain size. This is important for the design of microstructures because processing and heat-treatment schedules can be tailored to control grain size which in turn dictates the creep behavior. Coarse-grained microstructures are recommended for creep-driven structural applications, where the alloys experience intermediate stresses and temperatures. Although several deficiencies still exist in our

knowledge of microstructure-creep relationships, this study has provided insight to the creep mechanisms and microstructure-creep relationships for O alloys and bridged the gap from the previous understanding to a more advanced stage.

Similar to the phase evolution and creep behavior, grain boundaries were important to the RT tensile behavior. The near  $\text{Ti}_2\text{AlNb}$  alloys' microstructures were susceptible to O/O grain boundary cracking. When a significant amount of O/O adjacencies existed, poor RT tensile elongations were exhibited. When the number of O/O adjacencies was decreased, such as through solutionizing at temperatures higher in the O+B2 region which results in a higher volume of the B2 phase, higher strengths and elongations were exhibited. The observed slip transmittability across O and B2 grains is expected to have reduced detrimental stress concentration effects at grain boundaries. This work showed that O+B2 alloys containing as high as 25at.% Al can exhibit adequate RT elongations ( $\epsilon_f > 4\%$ ) when the microstructure, and in particular the B2-phase volume, is controlled. The morphology of the B2 phase is also important as equiaxed B2 grained microstructures provided greater elongations than lath-grained microstructures containing identical B2-phase volumes. The near  $\text{Ti}_2\text{AlNb}$  alloys which contained high interstitial oxygen contents ( $> 980$  ppm) exhibited poor elongations independent of microstructure.

Comparing microstructures which exhibited adequate RT elongations, the strengths of the Ti-12Al-38Nb microstructures were lower than those of the near  $\text{Ti}_2\text{AlNb}$  alloys. However, the highest elongations were exhibited by the Ti-12Al-38Nb microstructures. In particular, the fully- $\beta$  Ti-12Al-38Nb microstructure exhibited over 27% strain while the O+ $\beta$  microstructures containing 30% O-phase platelets exhibited over 12% strain-to-failure. Because there was a noticeable increase in strength for the O+ $\beta$  microstructures compared to the fully- $\beta$  microstructure, the O-phase strengthened  $\beta$ -dominated microstructures. Overall, the two-phase O+BCC microstructures exhibited enhanced mechanical behavior compared to their single-phase counterparts as the O-



phase strengthened  $\beta$ -dominated microstructures while the B2 phase toughened O-dominated microstructures. It is important to note that the relatively high elongations of the  $\beta$ -dominated microstructures are lost when the  $\beta$  grain size reaches a certain level. This was indicated by the poor elongations of the largest-grained Ti-12Al-38Nb microstructure, which was expected to have exhibited inhomogeneous slip as reported in another study (Banerjee 1994). Therefore careful consideration of the processing and heat-treatment temperatures is necessary.

The coarsest-grained microstructure examined was that of the super-transus processed Ti-25Al-27Nb alloy. This microstructure exhibited the lowest minimum creep rates. However the RT ductility of this alloy was poor. Overall, the Ti-12Al-38Nb alloy shows the greatest promise for structural application, including applications as a matrix in continuously reinforced titanium matrix composites. This is because of its excellent workability, microstructural stability, and mechanical behavior. In addition, for a given processing or heat-treatment temperature, the grain size was larger for Ti-12Al-38Nb compared with Ti<sub>2</sub>AlNb alloys due primarily to the lower transus temperature for Ti-12Al-38Nb. Its greatest downfalls appear to be its density and environmental sensitivity. It is more susceptible to environmental embrittlement compared with near Ti<sub>2</sub>AlNb alloys. However, the environmental resistance of all O+BCC alloys is suspect, and this is a limiting factor to their aerospace application. Therefore a successful method of protection is necessary. If a compatible, ductile protective layer is developed, the application of Ti-12Al-38Nb is strongly recommended.

## 6.2 Conclusions

The following lists the new and most significant conclusions which may be added to the growing knowledge base of O+BCC alloys.

### 6.2.1 Processing

1. A considerable temperature range comprises the processing window for O+BCC alloys. Adequate microstructural homogeneity may be obtained by hot-forging and hot-rolling at sub-transus temperatures. Fine-grained equiaxed microstructures are only obtainable when work is performed below the transus.

2. Ti-25Al-25Nb is more difficult to process and machine than either Ti-23Al-27Nb or Ti-12Al-38Nb. This is believed to be a result of the higher Al content. Ti-12Al-38Nb was the easiest material to process which is believed to be a result of the excellent ductility of this material and its low Al content.

### 6.2.2 Phase Evolution

1. A wide variety of microstructures are achievable through post-processing solution treatment of sub-transus processed near  $Ti_2AlNb$  alloys. In particular, grain size can be altered significantly. Such a wide range of grain sizes is not possible for super-transus processed O+BCC alloys.

2. A narrow three-phase  $\alpha_2+B_2+O$  field exists between the two-phase  $\alpha_2+B_2$  and O+B2 regions for near  $Ti_2AlNb$  alloys. Sub-transus solution treatments restore orientation relationships between the  $\alpha_2$  and B2 and O and B2 structures.

3. O-phase volume fractions are dependent on heat-treatment temperature and nominal alloy Al content. Higher Al contents favor higher O-phase volumes. Fine-grained, equiaxed fully-O microstructures are achievable through sub-transus heat treatment of near  $Ti_2AlNb$  alloys, provided that the alloy contains at least 25at.% Al.

4. Equiaxed microstructures are exhibited above 875°C for sub-transus processed near Ti<sub>2</sub>AlNb alloys. Below 875°C, aging transformations result in non-equiaxed shapes within B2 grains. The aging-transformation behavior is characterized by three transformation mechanisms which are strongly dependent on the solution-treatment and aging temperatures. A composition invariant mechanism (B2 → O) is exhibited for super-transus solutionized fully-B2 microstructures which are subsequently aged at 650°C. Sub-transus solutionized microstructures exhibit a homogeneous Widmanstatten precipitation transformation and/or cellular precipitation at O/B2 and/or α<sub>2</sub>/B2 boundaries, depending on the solutionizing and aging temperatures. In particular, the solutionizing and aging temperatures determine the compositional gradients between the initial BCC-phase prior to aging and the aged BCC phase. Larger BCC-phase compositional gradients favor cellular precipitation (B2 → O + β). Composition induced disordering of the B2 phase occurs below 750°C for near Ti<sub>2</sub>AlNb alloys. Overall, solutionized and quenched microstructures are susceptible to grain boundary precipitation and subsequent precipitate coarsening occurs at grain boundaries. Stable, low-temperature near Ti<sub>2</sub>AlNb microstructures take long times to equilibrate. Such microstructures depend largely on the processing and heat-treatment schedules.

5. The α<sub>2</sub> phase is more resilient to transformation than the B2 phase. With this regard, once the α<sub>2</sub> phase is formed, it is difficult to remove through subsequent sub-transus heat treatments.

6. For lower Al-containing O+BCC alloys, such as Ti-12Al-38Nb, the BCC transus temperature is lower and the α<sub>2</sub>-phase stability is reduced. The Ti-12Al-38Nb β transus is approximately 800°C. No ordered B2 phase is present in Ti-12Al-38Nb indicating that greater than 12at.% Al is necessary to induce the ordered B2 structure.

The BCC order/disorder transition composition is between Ti-17Al-34Nb and Ti-12Al-41Nb. The existing pseudobinary diagram based on a constant Ti=50at.% was modified.

### 6.2.3 Creep Behavior

1. Creep theories based on the secondary creep rates of disordered, single-phase metals can be used to identify creep mechanisms for ordered intermetallic alloys, including O+BCC alloys. Based on these well-established theories, three separate creep mechanisms are contributing to the creep rates of O+BCC alloys at intermediate temperatures (650-760°C).

2. Coble creep is significantly contributing to the secondary creep rates at low applied stresses for super-transus solutionized then aged O+BCC microstructures. The estimated range of activation energies for grain boundary diffusion was 127-178 kJ/mol.

3. For sub-transus solutionized then aged microstructures, grain boundary sliding is the dominant creep mechanism within the low-to-intermediate stress regime. Super-transus microstructures also exhibit grain boundary sliding characteristics at intermediate applied stresses. Grain size is more influential than phase composition, morphology, and volume fraction within this regime. Overall, the minimum creep rates of the microstructures judged to be within this regime were proportional to the applied stress squared divided by the equiaxed grain size. This was true over the wide ranges of applied creep stresses and grain sizes examined. This shows the overriding influence of grain size on the secondary creep behavior of O+BCC alloys. The grain boundary sliding constant ( $A_{gbs}$ ) is relatively insensitive to alloy composition.

4. Grain boundary sliding leads to grain boundary cavitation which occurs early within the secondary creep stage ( $\epsilon \leq 2.1\%$ ). A similar extent of grain boundary cavitation occurs in both tension and compression creep. Similar creep rates are also observed in tension and compression. Due to the grain boundary cavitation within the secondary creep stage, steady-state creep rates are not applicable and the lowest secondary creep rate can be represented as  $\dot{\epsilon}_{\min}$ .

5. At high applied stresses, dislocation climb is considered to be the rate-controlling process. The estimated range of activation energies for lattice self-diffusion was 256-346 kJ/mol. These values are dependent on alloy composition.

6. The transition applied stresses between the separate creep mechanisms is dependent on microstructure.

7. Microstructural instability, occurring within the B2 phase during creep, increases creep strains and strain rates, and the greatest effect occurs within the primary stage.

8. While all alloys were susceptible to environmental-assisted surface cracking, the lowest Al-containing alloy, Ti-12Al-38Nb, was the most sensitive to the environment.

#### 6.2.4 Tension Behavior

1. Near Ti<sub>2</sub>AlNb fine-grained, fully-O microstructures are susceptible to grain boundary cracking and exhibit poor RT elongations. However, alloys containing 25at.% Al do not always exhibit poor RT ductility. Elongations of greater than four percent are exhibited for heat-treated O+B2 microstructures of such alloys when a sufficient amount

of equiaxed B2 phase is present. In addition, such microstructures exhibit greater strengths than fully-O microstructures. Therefore the B2 phase increases both the RT strength and elongation of near Ti<sub>2</sub>AlNb O-dominated microstructures.

2. For Ti-12Al-38Nb, fully- $\beta$  microstructures exhibit high elongations ( $\epsilon_f > 27\%$ ). O-phase platelets dispersed within  $\beta$  grains provide significant strengthening with an associated reduction in elongation-to-failure, yet ductility remains ( $\epsilon_f > 12\%$ ). Care must be taken to avoid heat treatments which result in extremely large grain sizes as poor RT elongations result.

3. The tensile strength of Ti-12Al-38Nb decreases more rapidly with increasing temperature than that for near Ti<sub>2</sub>AlNb alloys. At all temperatures, near Ti<sub>2</sub>AlNb alloys are stronger than Ti-12Al-38Nb.

4. The tensile properties of near Ti<sub>2</sub>AlNb alloys are sensitive to interstitial oxygen content. Significantly higher elongations were exhibited by alloys containing less than 550 ppm oxygen.

### 6.3 Recommendations

This work has shown that the creep resistance of O+BCC alloys is greater than that for  $\alpha$ ,  $\alpha_2$ , and super  $\alpha_2$ -based alloys at the lowest and highest applied stress levels. This is due to the higher  $Q_{app}$  values within the Coble and dislocation climb regimes, a result which is considered to be related to the diffusivity in the higher Nb-containing ordered O phase. However for the relatively large intermediate stress range, dominated by grain boundary sliding, grain size is the dominant microstructural feature influencing the secondary creep rates. Although higher  $Q_{app}$ s were observed for microstructures

containing greater O volumes, the influence of O volume was less significant than grain size within this regime. With this respect, the creep rates of O and  $\alpha_2$ -based microstructures are more dependent on grain size than phase structure, and similar minimum creep rates result from similar average, equiaxed grain sizes. This implies that in order to obtain greater intermediate-stress creep resistance, the processing and heat-treatment schedules are more important than alloy composition. This is an important observation as creep resistance may be maintained while the alloy density is decreased. For example, decreasing the Nb contents from 27-16at.% Nb will result in a significant weight savings. Microstructures subjected to higher temperature processing and/or post-processing solution treatments, which result in larger equiaxed grain sizes, exhibit lower minimum creep rates. (However, as seen in the study of Ti-12Al-38Nb, there is a critical grain size above which the benefits of larger prior-BCC grained microstructures are negligible.) Thus the processing and heat-treatment schedules become important issues for applications targeted within the grain boundary sliding regime.

A disadvantage of very large-grained super-transus microstructures is the poor RT elongation. This work has shown that large-grained super-transus microstructures fail intergranularly and exhibit RT elongations less than 1%. This is unacceptable for most structural applications, including matrices in MMCs. (The poor RT elongation and high coefficient of thermal expansion of  $\gamma$ -based alloys exclude such alloys from most applications within TMCs.) Thus, solving the problem of poor RT ductility in large-grained super-transus Ti-Al-Nb microstructures would be beneficial for obtaining a better combination of RT tensile and elevated-temperature creep properties.

In terms of the RT properties, high  $\alpha_2$  concentrations are detrimental as  $\alpha_2/\alpha_2$  boundaries are susceptible to cracking. This is also true for O/O boundaries of O-dominated microstructures. By obtaining a minimum of 20% BCC phase in O-based microstructures, the RT elongations and strength are improved. Careful alloy selection is necessary to maintain higher BCC-phase volumes. For example, O+BCC alloys

containing less than 23Al will exhibit at least 20% BCC by volume at 650°C. Thus, alloy selection becomes quite important for structural applications requiring stringent creep and RT tensile requirements. For these reasons it is considered that O+BCC alloys containing between 12-23at.% Al and 17-38at.% Nb are optimal for applications requiring a balance of properties.  $\alpha_2$ -based alloys, which contain less Nb than O-based alloys, are especially attractive on a density-normalized basis, however their poor RT elongations significantly disrupt the balance of properties. Although the densities of O alloys are larger than those for  $\alpha_2$ -based systems, a more attractive balance of properties is maintained. For better density-normalized properties, the density can be decreased in going from higher Nb contents to those closer to 17at.%. On the other hand, Al concentrations of less than 23at.% significantly reduce the elevated-temperature strength and environmental resistance of O+BCC alloys and are therefore not recommended. Thus in attempting to optimize density-normalized properties, alloy compositions close to Ti-23Al-17Nb are quite attractive. However, a significant gap is present in our understanding of the mechanical behavior and phase evolution of alloys containing 12-23Al and 27-38Nb. Based on the microstructure-property relationships found in the current work, such alloys are expected to provide higher strengths than Ti-12Al-38Nb while maintaining adequate RT ductilities and lower densities. As previously mentioned, the intermediate-stress creep resistance is a function of grain size, which is controlled through the processing and heat-treatment schedules. In particular, conservative sub-transus processing schedules could be utilized for more dependable control of the grain size through post-processing heat-treatment. However, for many structural applications, the processing and heat-treatment schedules are dependent on component fabrication and are therefore relatively inflexible. In such cases, O+BCC alloys of the indicated range of compositions are expected to be manageable as they contain  $\leq 23\text{Al}$ . Overall, the author feels that O+BCC alloys, due to the attractive combination of their mechanical behavior and processability, are feasible replacement materials for intermediate-temperature, low-to-intermediate



stress applications. Yet, more work is necessary to properly understand and optimize microstructures for specific structural components.

Although it is recognized that several deficiencies still exist for our knowledge of microstructure-property relationships, this study has provided insight to the creep mechanisms and microstructure-creep relationships for O+BCC alloys and bridged the gap from the previous understanding to a more advanced stage. The following lists the recommendations for future research based on the findings of the current work.

1. Future work is recommended toward characterizing the compositional gradient across the cellular precipitation migrating front. In addition, establishing the composition of the fine phases resulting from the Widmanstätten and cellular transformations of the aged microstructures would be beneficial to pinpoint the order/disorder transition composition. In order to accomplish these tasks, careful microprobe work using high-resolution TEM is necessary.

2. Future work is recommended toward understanding the primary creep mechanisms and microstructure-property relations within this stage as typically design requirements, such as time to 0.2% creep strain, fall within the primary stage.

3. Diffusion data for O alloys is necessary to confirm both the grain boundary and volume diffusion activation energies.

4. More work should be directed toward “optimizing” O+BCC alloy microstructures for obtaining a better balance of the density-normalized RT and elevated-temperature properties. In particular, alloy compositions between 12-23Al and 27-38Nb are expected to provide higher strengths than Ti-12Al-38Nb while maintaining adequate RT ductilities and lower densities. Phase evolution studies of such alloys would also improve the understanding of the phase equilibria for the alloy composition gap between Ti-23Al-27Nb and Ti-12Al-38Nb.

## BIBLIOGRAPHY

Aaronson HI, Furuhashi T, Rigsbee JM, Reynolds, Jr. WT and Howe JM, 1990, Metallurgical Transactions, 21A, 2369-2409.

Akkurt AS, 1990, MS Thesis, New Mexico Institute of Mining and Technology.

Akkurt AS, Liu G and Bond GM, 1991, High Temperature Ordered Intermetallic Alloys-IV, L.A. Johnson, D.P. Pope, and J.O. Stiegler, eds., (Pittsburgh, PA: Materials Research Society) vol. 213, 455-60.

Albert DE and Thompson AW, 1991, Microstructure/Property Relationships in Titanium Aluminides and Alloys, Y-W. Kim and R.R. Boyer, eds., (Warrendale, PA: The Metallurgical Society) 399-406.

Albert DE and Thompson AW, 1992, Metallurgical Transactions, 23A, 3035-43.

Austin CM, Dobbs JR, Fraser HL, Konitzer DG, Miller DJ, Parks MJ, Schaeffer JC and Sears JW, 1992, Rapidly Solidified Oxidation Resistant Niobium Base Alloys, WL-TR-93-4059, GE Aircraft Engines, Cincinnati, OH.

Balsone SJ, Maxwell DC and Broderick TF, 1993, Fracture Mechanics: Twenty-Third Symposium, ASTM STP 1189, ed. Ravinder Chona, American Society for Testing and Materials, Philadelphia) 551-67.

Banerjee D, Nandy TK and Gogia AK, 1987, Scripta Metallurgica, 21, 597-600.

Banerjee D, Gogia AK, Nandy TK and Joshi VA, 1988, Acta Metall., 36 no. 4, 871-882.

Banerjee D, Nandy TK, Gogia AK and Muraleedharan K, 1989, Titanium '88 Science and Technology, ed. The Minerals, Metals, and Materials Society, 1989, 1091-96.

Banerjee D., Gogia AK and Nandy TK, 1990, Metallurgical Transactions, 21A, 627-39.

Banerjee D, Rowe RG and Hall EL, 1991, High Temperature Ordered Intermetallic Alloys-IV, L.A. Johnson, D.P. Pope, and J.O. Stiegler, eds., (Pittsburgh, PA: Materials Research Society) vol. 213, 285-90.

Banerjee D and Rowe RG, 1993, Titanium '92 Science and Technology, ed. F.H. Froes and I. Caplan, The Minerals, Metals, and Materials Society, 1147-53.

Banerjee D, Gogia AK, Nandy TK, Muraleedharan K and Mishra RS, 1993, Structural Intermetallics, ed. R. Darolia, J. J. Lewandowski, C. T. Liu, P. L. Martin, D. B. Miracle, and M. V. Nathal (The Minerals, Metals, and Materials Society) 19-33.

Banerjee D, 1994, Intermetallic Compounds Principles and Practice, J.H. Westbrook and R.L. Fleischer, eds., John Wiley & Sons Ltd., New York, N.Y., vol. 2, 91-131.

Banerjee D, 1995, Phil. Mag., 72 no. 6, 1559-1587.

Bao G, Hutchinson JW and McMeeking RM, 1991, Acta Metall. Mater, 39 no. 8, 1871-82.

Barrett CR, Lytton JL and Sherby OD, 1967, Trans. Metall. Soc. A.I.M.E., 239, 170-80.

Bendersky LA, Boettinger WJ and Roytburd A, 1991, Acta Metall. Mater, 39, 1059-69.

Bendersky LA and Boettinger WJ, 1993, Journal of Research of the National Institute of Standards and Technology, 98 no. 5, 585-606.

Blackburn MJ and Smith MP, 1989, WRDC-TR-89-4095, Wright-Patterson Air Force Base, OH.

Boehlert CJ, 1993, MS Thesis, University of Dayton.

Boehlert CJ, Majumdar BS, Krishnamurthy S and Miracle DB, 1997a, Metallurgical Transactions, 28A, 309-23.

Boehlert CJ, Majumdar BS and Eylon D, 1997b, Key Engineering Materials, 127-131 Part I, 843-50.

Boehlert CJ, Majumdar BS and Seetharaman V, 1997c, Deformation and Fracture of Ordered Intermetallic Materials, W.O. Soboyejo, H.L. Fraser, and T.S. Srivatsan, eds., (Warrendale, PA: The Metallurgical Society) 565-82.

Boehlert CJ, Majumdar BS, Seetharaman V and Miracle DB, 1997d, Orthorhombic Titanium Matrix Composites II, AF TR# WL-TR-97-4082, ed. P.R. Smith, 212-27.

Boehlert CJ, Majumdar BS, Seetharaman V, Miracle DB and Wheeler R, 1997e, Structural Intermetallics, ed. M.V. Nathal, R. Darolia, C.T. Liu, P.L. Martin, D.B. Miracle, R. Wagner, and M. Yamaguchi (The Minerals, Metals, and Materials Society) 795-804.

Burgers WG, 1934, Physica, 1, 561.

Chesnutt JC, Amato RA, Austin CM, Fleischer RL, Gigliotti MFX, Hardwick DA, Huang SC, Konitzer DG, Lee MM, Martin PL, Rhodes CG, Rowe RG, Scarr GK, Shih DS and Zomcik PA, 1993, Very High Temperature Titanium-Base Materials Research, WL-TR-91-4070, GE Aircraft Engines, Cincinnati, OH.

Cho W, Thompson AW and Williams JC, 1990, Metallurgical Transactions, 21A, 641-51.

Coble RL, 1963, Journal of Applied Physics, 34 no. 6, 1679-82.

Conrad H, Doner M, and de Meester B, 1973, Titanium Science and Technology, ed. R.I. Jaffee and H.M. Burte, vol. 3 (Plenum Press, New York) 969-1005.

Crossman FW and Ashby MF, 1975, Acta Metall., 23, 425-40.

Dary FC and Pollock TM, 1996, Material Science and Engineering, A208 no. 2, 188.

Dary FC, Woodard SR and Pollock TM, 1996, Titanium '95, P.A. Blenkinsop, W.J. Evans, and H.M. Flower, eds., (Cambridge, UK: The University Press) vol. 1, 396-403.

Davis LC and Allison JE, 1995, Metallurgical Transactions, 26A, 3081-9.

Denquin A and Naka S, 1996, Acta Metall., 44 no. 1, 353-65.

Doner M and Conrad H, 1975, Metallurgical Transactions, 23A, 853-61.

Emura S, Liu J, Hagiwara M, Kawabe Y and Okada A, 1996, Titanium '95, P.A. Blenkinsop, W.J. Evans, and H.M. Flower, eds., (Cambridge, UK: The University Press) vol. 1, 404-10.

Evans RW and Wilshire B, 1985, Creep of Metals and Alloys, ed. D. McLean, (The Institute of Metals) 295-307.

Evans AG, Hutchinson JW and McMeeking RM, 1991, Scripta Metallurgica, 25, 3-8.

Eylon D, Hall JA, Pierce CM and Ruckle DL, 1976, Metallurgical Transactions, 7A, 1817-26.

Foster MA, Smith PR and Miracle DB, 1995, Scripta Metallurgica, 33 no. 6, 975.

Friedel J, 1964, Dislocations (Oxford: Pergamon Press) 104-117.

- Gandhi C and Raj R, 1981, Metallurgical Transactions, 12A, 515-20.
- Gogia AK, 1990, Ph.D. dissertation, Banaras Hindu University, Varanaji, India and the Defense Metallurgical Research Laboratory, Hyderabad, India, 1990.
- Gogia AK, Nandy TK, Muraleedharan K and Banerjee D, 1992, Material Science and Engineering, A159, 73-86.
- Gupta SP, 1975, Material Science and Engineering, 21, 211-20.
- Hartman GA and Russ SM, 1989, Metal Matrix Composites: Testing, Analysis, and Failure Modes, ASTM STP 1032, ed. W.S. Johnson (Philadelphia, PA: American Society for Testing and Materials) 43-53.
- Hayes RW, 1989, Scripta Metallurgica, 23 no: 11, 1931.
- Hayes RW, 1991, Acta Metall. Mater, 39 no. 4, 569-77.
- Hayes RW, 1996, Scripta Metallurgica, 34 no: 6, 1005-12.
- Herring C, 1950, Journal of Applied Physics, 21, 437-45.
- Hertzberg RW, 1976, Deformation and Fracture Mechanics of Engineering Materials, (New York, NY: John Wiley and Sons).
- Higgins GT, Wiryolukito S and Nash P, 1992, Grain Growth in Polycrystalline Materials, G. Abbruzzese and P. Brozzo, eds., Trans Tech Publications, Aedermannsdorf, Switzerland.
- Hu H and Rath BB, 1970, Metallurgical Transactions, 1, 3181-84.
- Kestner-Weykamp HT, Ward CW, Broderick TF and Kaufman MJ, 1989, Scripta Metallurgica, 23, 1697-1702.
- Koss DA, Banerjee D, Lukasak DA and Gogia AK, 1990, High Temperature Aluminides and Intermetallics, ed. S.H. Whang, C.T. Liu, D.P. Pope, and J.O. Stiegler, (Warrendale, PA: The Metallurgical Society) 175-195.
- Krishnamurthy S and Gupta SP, 1977, Material Science and Engineering, 30, 155-65.
- Krishnamurthy S and Miracle DB, 1997a, Metal Matrix Composites, Proc. Eleventh International Conference on Composite Materials, M.L. Scott, ed., vol. 3, 399-408.

Krishnamurthy S and Miracle DB, 1997b, UES, Inc. and WPAFB, unpublished research, 1997.

Krishnamurthy S, Smith PR and Miracle DB, 1994, Scripta Metallurgica, 31 no. 6, 653-8.

Kumpfert J and Leyens C, 1997, Structural Intermetallics, ed. M.V. Nathal, R. Darolia, C.T. Liu, P.L. Martin, D.B. Miracle, R. Wagner, and M. Yamaguchi (The Minerals, Metals, and Materials Society) 895-904.

Langdon, TG, 1970, Phil. Mag., 22, 689-700.

Langdon TG, 1972, Metallurgical Transactions, 3, 797-801.

Langdon, TG, 1982, Metallurgical Transactions, 13A, 689-701.

Lee TC, Robertson IM, and Birnbaum HK, 1990, Philosophical Magazine A, 62 no. 1, 131-53.

Luetjering S, Smith PR and Eylon D, 1997, Orthorhombic Titanium Matrix Composites II, AF TR# WL-TR-97-4082, ed. P.R. Smith, 228-42. (100)

Majumdar BS, Newaz GM and Brust FW, 1992, Constitutive Behavior of High Temperature Composites, Proc. ASME Winter Annual Meeting MD-40, ed. B.S. Majumdar, G.M. Newaz, and S. Mall, 77-90.

Majumdar BS, Boehlert CJ and Miracle DB, 1994, WL-TR-95-4068, Wright Patterson Air Force Base, OH, 65-83.

Majumdar BS, Boehlert CJ, Rai AK and Miracle DB, 1995, High Temperature Ordered Intermetallic Alloys-VI, J. Horton, I. Baker, S. Hanada, R.D. Noebe, and D.S. Schwartz, eds., (Pittsburgh, PA: Materials Research Society) vol. 364, 1259-65.

Malakondaiah G and Rao PR, 1981, Acta Metall. Mater, 29, 1263-75.

Malakondaiah G, Prasad N, Sundararajan G, and Rao PR, 1988, Acta Metall. Mater, 36 no. 8, 2167-81.

Martin JM and Doherty RD, 1976, Stability of Microstructure in Metallic Systems (Cambridge: Cambridge University Press).

Melton RN and Edington JW, 1974, Acta Metall., 22, 1457-62.

Mendiratta MG and Lipsitt HA, 1980, Journal of Material Science, 15, 2985-90.

- Miller WH Jr., Chen RT and Starke EA Jr., 1987, Metallurgical Transactions, 18A, 1451-68.
- Miracle DB, 1993, Acta Metall., 41 no. 3, 649-84.
- Miracle DB, Rhodes CG and Foster MA, 1996, Titanium '95, P.A. Blenkinsop, W.J. Evans, and H.M. Flower, eds., (Cambridge, UK: The University Press) vol. 1, 372-9.
- Mishra RS and Banerjee D, 1990, Material Science and Engineering, A130, 151-64.
- Mishra RS and Banerjee D, 1994, Scripta Metallurgica, 31 no. 11, 1555-60.
- Mishra RS and Banerjee D, 1995, Material Science and Engineering, A192/193, 756-62.
- Mishra RS, Banerjee D and Mukherjee AK, 1995, Material Science and Engineering, A192/193, 763-8.
- Mozer B, Bendersky LA, Boettinger WJ and Rowe RG, 1990, Scripta Metallurgica, 24, 2363-8.
- Mukherjee AK, Bird JE and Dorn JE, 1969, Trans. Am. Soc. Metals, 62, 155-79.
- Muraleedharan K, Nagender SV and Banerjee D, 1990, Scripta Metallurgica, 24, 27-32.
- Muraleedharan K, Gogia AK, Nandy TK, Banerjee D and S. Lele, 1992a, Metallurgical Transactions, 23A, 401-15.
- Muraleedharan K, Nandy TK, Banerjee D and Lele S, 1992b, Metallurgical Transactions, 23A, 417-31.
- Muraleedharan K, 1995, Ph.D. dissertation, Banaras Hindu University, Varanaji, India and the Defense Metallurgical Research Laboratory, Hyderabad, India.
- Muraleedharan K, Banerjee D, Banerjee S and Lele S, 1995a, Phil. Mag., 71 no. 5, 1011-36.
- Muraleedharan K, Nandy TK, and Banerjee D, 1995b, Intermetallics, 3, 187-199.
- Nandy TK, Mishra RS and Banerjee D, 1993, Scripta Metallurgica, 28, 569-74.
- Nandy TK, Mishra RS, Gogia AK and Banerjee D, 1995, Scripta Metallurgica, 32 no: 6, 851-6.
- Nandy TK and Banerjee D, 1997, Structural Intermetallics, ed. M.V. Nathal, R. Darolia, C.T. Liu, P.L. Martin, D.B. Miracle, R. Wagner, and M. Yamaguchi (The Minerals, Metals, and Materials Society) 777-86.

Nix WD and Ilshner B, 1980, Strength of Metals and Alloys, ed P. Haasen, V. Gerold, and G. Kosterz, vol. 3 (Pergamon Press, New York) 1507-30.

Popille F and Douin J, 1996, Phil. Mag., 73, 1401-18.

Popille-Puissochet F, Courret A and Douin J, 1997, Titanium '96 Science and Technology, ed., The Minerals, Metals, and Materials Society,, 380-7.

Porter DA and Easterling KE, 1981, Phase Transformations in Metals and Alloys (Berkshire, UK: Van Nostrand Reinhold Company Limited) 322-30.

Raj R and Ashby MF, 1971, Metallurgical Transactions, 2, 1113-27.

Rhodes CG, Graves JA, Smith PR, and James MR, 1993, Structural Intermetallics, ed. R. Darolia, J. J. Lewandowski, C. T. Liu, P. L. Martin, D. B. Miracle, and M. V. Nathal (The Minerals, Metals, and Materials Society), 45-52.

Rhodes CG, 1997, Orthorhombic Titanium Matrix Composites II, AF TR# WL-TR-97-4082, ed. P.R. Smith, 83-100.

Rowe RG and Bendersky LA, 1995, Mechanical Properties and Phase Transformations of Multi-Phase Intermetallic Alloys III, ed. A.F. Giamei, H.R.P. Inoue, and Y. Mishima (Warrendale, PA: The Metallurgical Society).

Rowe RG and Gigliotti MFX, 1990, Scripta Metallurgica, 24, 1209-14.

Rowe RG and Hall EL, 1991, High Temperature Ordered Intermetallic Alloys-IV, ed. L.A. Johnson, D.P. Pope, and J.O. Stiegler (Pittsburgh, PA: Materials Research Society) vol. 231, 449-54.

Rowe RG, Konitzer DG, Woodfield AP and Chesnutt JC, 1991, High Temperature Ordered Intermetallic Alloys-IV, ed. L.A. Johnson, D.P. Pope, and J.O. Stiegler (Pittsburgh, PA: Materials Research Society) vol. 231, 703-8.

Rowe RG, 1991, Microstructure/Property Relationships in Titanium Aluminides and Alloys, Y-W. Kim and R.R. Boyer, eds., (Warrendale, PA: The Metallurgical Society) 387-98.

Rowe RG, Siemers PA and Larsen M, 1992, Advances in the Processing, Synthesis, Characteristics, and Applications of Aerospace Metal Based Materials, Proceedings Third International SAMPE Metals and Metals Processing Conference.

Rowe RG, 1993a, Physical Metallurgy Laboratory, GE Report#93CRD030.

Rowe RG, 1993b, Titanium '92 Science and Technology, ed. F. H. Froes and I. Caplan, The Minerals, Metals, and Materials Society, vol 1, 343-50.



Rowe RG, Banerjee D, Muraleedharan K, Larsen M, Hall EL, Konitzer DG and Woodfield AP, 1993, Titanium '92 Science and Technology, ed. F. H. Froes and I. Caplan, The Minerals, Metals, and Materials Society, 1259-66.

Rowe RG and Larsen M, 1996, Titanium '95, P.A. Blenkinsop, W.J. Evans, and H.M. Flower, eds., (Cambridge, UK: The University Press,) vol. 1, 364-71.

Ruano OA, Wadsworth J, and Sherby OD, 1988, Acta Metall., 36 no. 4, 1117-28.

Russ SM, Boehlert CJ and Eylon D, 1995, Materials Science and Engineering, A192/193, 483-9.

Sagar PK, Banerjee D, Muraleedharan K and Prasad YVRK, 1996, Metallurgical Transactions, 27A, 2593-2604.

Saqib M, Apgar LS, Eylon D and Weiss I, 1995, Material Science and Engineering, A201, 169-81.

Schneibel JH, Coble RL and Cannon RM, 1981, Acta Metall, 29, 1285-90.

Schwenker SW and Kim YK, 1995, Gamma Titanium Aluminides, eds Y-K Kim, R. Wagner, and M. Yamaguchi (TMS Warrendale, Pa.) 985-92.

Seetharaman V and Semiatin SL, 1997, Metallurgical Transactions, 28A, 947-54.

Semiatin SL and Smith PR, 1995, Material Science and Engineering, A202, 26-35.

Sherby OD and Burke PM, 1968, Mechanical Behavior of Crystalline Solids at Elevated Temperature (Oxford: Pergamon Press) 353.

Sherman PG, 1963, Diffusion in Solids, (McGraw-Hill Book Co., New York) 61-94.

Shyue J, Hou DH, Johnson SC, Aindow M and Fraser HL, 1993, High Temperature Ordered Intermetallic Alloys-V, I. Baker, R. Darolia, J.D. Whittenberger, and M.H. Yoo, eds., (Pittsburgh, PA: Materials Research Society) vol. 288, 243-8.

Smith PR, Khobaib M and Graves JA, 1993, Scripta Metallurgica, 29, 1313-18.

Smith PR, Graves JA and Rhodes CG, 1994a, Metallurgical Transactions, 25A, 1267-83.

Smith PR, Porter WJ, Kralik WJ, and Graves JA, 1994b, WL-TR-95-4068, Wright Patterson Air Force Base, OH, 371-85.

- Smith PR, Porter WJ, Kralik WJ and Graves JA, 1995, Metal Matrix Composites, Proc. Tenth International Conference on Composite Materials, A. Poursartip and K.N. Street, eds., vol. 2, 731-8.
- Soboyejo WO, Lederich RJ and Schwartz DS, 1997, Journ of Mater. Sci., 32, 1877-87.
- Subramanian PR, 1997, UES, Inc., unpublished research.
- Szaruga A, Saqib M, Omlor R and Lipsitt HA, 1992, Scripta Metallurgica, 26, 787-90.
- Takag S and Ouchi C, 1997, Materials Transactions, JIM, 38 no. 4, 285-91.
- Thomas M, Naka S and Khan T, 1996, Titanium '95, P.A. Blenkinsop, W.J. Evans, and H.M. Flower, eds., (Cambridge, UK: The University Press) vol. 1, 388-95.
- Thompson AW and Pollock TM, 1991, ISIJ International, 31 no. 10, 1139-45.
- Tu, 1972, Metallurgical Transactions, 3, 2769-76.
- Van Thyne RJ and Kessler HD, 1954, Trans. AIME, 200, 193-9.
- Vasudevan VK, Yang J and Woodfield AP, 1996, Scripta Metallurgica, 35 no. 9, 1033-7.
- Ward CH, 1993, International Materials Reviews, 38 no. 2, 79-101.
- Weertman J, 1968, Trans. Am. Soc. Metals, 61, 681-94.
- Williams JC, 1973, Titanium Science and Technology, ed. R.I. Jaffee and H.M. Burte, vol. 3 (Plenum Press, New York,) 1433-94.
- Wojcik CC, Roessler R and Zordan R, 1996, Advances in the Science and Technology of Titanium Alloy Processing, I. Weiss, P. Bania, and D. Eylon, eds., (Warrendale, PA: The Metallurgical Society).
- Woodard SR, Pollock TM and Dary FC, 1996, Carnegie Mellon University, Final Report for Grant#F3360194MT488.
- Woodard SR and Pollock TM, 1997, Orthorhombic Titanium Matrix Composites II, AF TR# WL-TR-97-4082, ed. P.R. Smith, 265-76.
- Woodfield AP, 1996, Progress Report No. 5, General Electric Aircraft Engines, Cincinnati, Ohio.
- Worth BD, Jones W and Allison JE, 1995, Metallurgical Transactions, 26A, 2947-59.